Imagerie tridimensionnelle nanométrique de matériaux et dispositifs à semi-conducteurs par tomographie électronique

Georg Haberfehlner

To cite this version:

Georg Haberfehlner. Imagerie tridimensionnelle nanométrique de matériaux et dispositifs à semi-conducteurs par tomographie électronique. Autre [cond-mat.other]. Université de Grenoble, 2013. Français. NNT : 2013GRENY017 . tel-00952978

HAL Id: tel-00952978
https://theses.hal.science/tel-00952978

Submitted on 28 Feb 2014

UNIVERSITÉ DE GRENOBLE

THÈSE

Pour obtenir le grade de

DOCTEUR DE L'UNIVERSITÉ DE GRENOBLE

Spécialité : **Nanophysique**

Arrêté ministériel : 7 août 2006

Présentée par

Georg HABERFEHLNER

Thèse dirigée par **Pierre BLEUET**

préparée au sein du **Laboratoire d'Électronique et de Technologies de l'Information (CEA, LETI)**
et de **l'Ecole Doctorale de Physique**

3D nanoimaging of semiconductor devices and materials by electron tomography

Thèse soutenue publiquement le **24 Septembre 2013**,
devant le jury composé de :

Thierry EPICIER
Directeur de Recherches CNRS, MATEIS INSA Lyon, Président
Paul A. MIDGLEY
Professeur, University of Cambridge, Rapporteur
Filadelfo CRISTIANO
Chargé de Recherches CNRS, LAAS Toulouse, Rapporteur
Laurent DESBAT
Professeur, Université Joseph Fourier Grenoble, Examinateur
Laurens KWAKMAN
Ingénieur de Recherche, FEI Company, Examinateur
Pierre BLEUET
Ingénieur de Recherche, CEA, LETI, Grenoble, Directeur de thèse

It is an important and popular fact
that things are not always what they seem.

DOUGLAS ADAMS
The Hitchhiker's Guide to the Galaxy

Acknowledgments

There is a large number of people who have contributed in many different ways to the success of this thesis and I hope to forget not too many of them here.

First and foremost I want to thank *Pierre Bleuet*, who directed this thesis. I want to thank you Pierre for being always available with your expertise, for excellent advises and for a better working relationship than I would have ever hoped for.

I want to thank all my fellow microscopists at the "Plateforme Nanocaractérisation" for helping me to explore the world of fast electrons and for support and exciting discussions. Thanks in particular to *David Cooper*, *Armand Béché*, *Thibaud Denneulin*, *Adeline Grenier* and *Pascale Bayle-Guillemaud*, who first taught me, which buttons not to push. To *Raphaël Serra*, *Miguel Lopez-Haro* as well as *Tony Printemps*, for joining up in Grenoble's tomography team, who helped greatly in finding out how to best spin around samples. With Raphaël, Tony, *Guillaume Brunetti* and *Matthieu Vigouroux* I had the pleasure of sharing an office over the years. Thanks to *Vincent Delaye* as the team leader of LETI's microscopy team, who was always there with help and advise. I want to thank also all other microscopists at the platform:

- *Dominique Lafond*, *Robert Truche*, *Anne-Marie Papon*, *Francisco de la Peña* and *Cyril Guedj* at LETI
- *Jean-Luc Rouvière*, *Yannick Martin*, *Eric Prestat*, *Pierre-Henri Jounneau*, *Hanako Okuno*, *Eric Gautier* and *Aurélien Masseboeuf* at INAC
- *Donatien Robert*, *Laure Guetaz*, *Adrien Boulineau* and *Cyril Cayron* at LITEN
- *Martien den Hertog* and *Catherine Bougerol* at the CNRS

For teaching me how to do "nanobricolage" using focused ions I am indebted to *Guillaume Audoit* and *Geoffroy Auvert*. Geoffroy first taught me how to use a FIB and later on Guillaume was always eager to try out new impossible experiments, which still often happened to work out.

For interesting discussions about tomography and sharing ideas and results, I want to thank the tomography team at STMicroelectronics: *Kevin Lepinay* and *Frédéric Lorut.*

A part of this thesis was carried out in the frame of a collaboration with the MIT and supported by the MIT-France MISTI seed fund. I want to thank *Silvija Gradečak* and her research group for giving me the chance to working with them on their excellent samples. With *Matthew Smith* I had the chance of working on laser-doped silicon – developed at Harvard University by *Meng-Ju Sher*, *Mark Winkler* and *Eric Mazur* – and with *Sam Crawford* and *Sung-Keun Lim* I could work on their heterostructure nanowires. I want to thank Matt in particular for the great time spent together in Boston and Grenoble.

For the silicon nanowire samples, my gratitude goes to *Paul-Henry Morel*, who developed these devices during his PhD thesis and in the frame of the CARNOT CAPAFIL project, together with *Vincent Jousseaume*, *Murielle Fayolle-Lecocq*, *Thierry Baron* and *Thomas Ernst.* For the Trigate transistor I am grateful to *Sylvain Barraud* for providing these samples, which were developed in the frame of the IBM/ST/LETI joint project.

This thesis was carried out at the "Service de Caractérisation des Materiaux et Composants (SCMC)" at LETI, which is part of the "Plateforme Nanocaractérisation (PFNC)", supported by the French "Recherche Technologique de Base (RTB)" project. I am grateful to all the people, who keep this lab running and provided an excellent environment for this thesis. *Jean-Claude Royer* and *Frédéric Laugier* as head and deputy of the SCMC, *François Bertin* as scientific director, *Narciso Gamborcorti*, being responsible for the programs, and *Amal Chabli.* I also want to thank the assistants of the laboratory, *Sophie Riondet* and *Marie-Andrée Lesbre* for all their help with administrative tasks.

Thanks to my all fellow PhD students, interns, postdocs as well as the permanent staff at the SCMC for nice moments and coffee breaks: *Julien*, *Paul*, *Pauline*, *Sylvain*, *Tanguy*, *David*, *Robert*, *Riccardo*, *Viktoriia*, *Daario*, *Hokwon*, several *Matthieu's*, *Maylis*, *Claire*, and all others.

I want to thank the members of the jury, who took the time to evaluate my thesis and make the way to Grenoble for my defense: *Paul Midgley* and *Fuccio Cristiano* as "rapporteurs", *Thierry Epicier* as "président" as well as *Laurent Desbat* and *Laurens Kwakman* as "examinateurs".

Life in Grenoble would have been very boring without all my friends, with whom I shared an apartment, beers or the mountains. I had a great time with *Manue*, *Thomas*, *Djo*, *Seb* and *Emiline* as "collocataires" over the years as well as with

Marina, *Toux* and *Emilie*. For exploring the mountains around Grenoble in all different forms and for getting back safe to work each time great thanks *Peter*, *Yannick*, *Alex*, *Markus*, Thomas and Marina.

I am grateful to my parents and my family, who have supported me in all my choices and throughout my studies.

I am hoping to stay in contact with many among you and to have the possibility to work together again and to meet you at many occasions. Merci!

Contents

1 Introduction

Transistors are modern workhorses of today's society. Large-scale integration of transistors enabled efficient data processing and thereby computers, the internet and mobile communication devices. Transistors are based on semiconductor materials, together with other semiconductor devices, such as lasers, light-emitting diodes or solar cells, these devices are the basis for a large part of modern electronic devices.

The processes used for creating semiconductor devices need to be controlled with an accuracy down to the atomic level. Understanding and optimizing semiconductor devices requires characterization: Electrical and optical characterization of the finished devices to verify their behavior as well as local morphological, chemical and structural characterization to understand the roots of device behavior and to optimize manufacturing processes and device design.

Most of these physical and chemical characterization techniques can provide only two-dimensional (2D) or one-dimensional (1D) representations of the original three-dimensional (3D) object such as 2D images or 1D depth profiles. As in many cases the three-dimensional structure is relevant for device behavior though, 3D characterization techniques are necessary. Such techniques have been developed at different length scales for 3D morphological, chemical and structural imaging.

The transmission electron microscope (TEM) is among the most important tools for semiconductor materials and device characterization. With electron tomography TEM has been extended to three dimensions allowing 3D imaging with nanometer down to atomic resolution.

This thesis deals with the application and development of electron tomography for semiconductors. Electron tomography is applied on semiconductor materials and devices to answer open questions about 3D morphology and chemistry. With this background tomographic techniques have been studied in detail to introduce technical improvements necessary for the investigated applications. As such different contrast techniques are investigated and routes towards improved spatial resolution are studied.

1.1 Research Environment for this Work

This thesis was carried out at CEA, LETI in Grenoble. CEA, the "Commisariat à l'énergie atomique et aux énergies alternatives" , is a French national institution for fundamental and applied research, located at several sites all over France. It was originally founded for nuclear research, and later extended to several domains, such as renewable energies or information technology. LETI, the "Laboratoire d'électronique et de technologies de l'information" is the largest of CEA's laboratories in Grenoble and is concerned with research in nanoelectronics and other types of semiconductor nanotechnology.

Semiconductor research requires characterization, which is why a number of instruments for this purpose are required. For this purpose the "Plateforme Nanocaractérisation" (PFNC), where this thesis was carried out, was installed in Grenoble. The PFNC is a shared facility between three of CEA's laboratories – LETI, working on information technology, INAC, working on fundamental materials research, and LITEN, working on renewable energies and energy efficiency. One of the competence centers of the PFNC is concerned with electron microscopy and comprehends several state of the art transmission electron microscopes – e.g. a double spherical aberration corrected FEI Titan Ultimate microscope and a probe-corrected FEI Titan microscope – and about 15 permanent researchers as well as a similar number of PhD students and postdoctoral researchers.

In this framework the goal of this thesis was to establish and further develop electron tomography techniques at the PFNC, in particular for LETI's applications - electron devices and semiconductor materials.

1.2 Outline of this Work

This thesis is split into four major parts. Part I constitutes an introduction to the domain of this thesis, in Part II the experimental methods are presented and Parts III&IV illustrate and discuss results of this thesis. Part III is concerned with different contrast mechanisms usable for electron tomography, while Part IV deals with improving resolution of a reconstruction.

In Part I, Chapter 2 gives an introduction to semiconductor materials and devices and highlights challenges, which need to be addressed by 3D characterization techniques. Chapter 3 introduces different 3D characterization techniques for micro- and nanoscale investigations in materials science and discusses strengths, limitations and applications of each technique.

Part II is an introduction to the used methods. In Chapter 4 the principles of tomographic reconstruction are discussed, together with different tomographic reconstruction algorithms and data pre- and postprocessing. Chapter 5 gives an introduction to TEM and in particular to TEM-techniques used for electron tomography. In Chapter 6 requirements for sample preparation for electron tomography and methods applied in this thesis are discussed.

In Part III two different types of semiconductor nanowires as well as selenium hyperdoped silicon is studied. This part highlights applications of different TEM contrast techniques for electron tomography. Chapter 7 deals with the application of high-angle annular dark field (HAADF) scanning transmission electron microscopy (STEM) tomography for morphological and compositional studies of nanowires as well as to investigate selenium dopant distribution in femtosecond laser-doped silicon. Chapter 8 deals with an application, where HAADF STEM tomography failed due to too small mass contrast. For this reason low-loss energy-filtered transmission electron microscope (EFTEM) tomography is applied for the characterization of nanowire-based capacitors and the potential of spectral low-loss EFTEM tomography is investigated.

Part IV deals with routes towards improving resolution in electron tomography. In Chapter 9 dual-axis electron tomography is applied to tri-gate transistors for the purpose of improving resolution in the reconstruction for all gate surfaces of the transistor. Chapter 10 extends the principle of dual-axis tomography to multiple tilt-axis and shows perspectives of resolution improvements by such multiple-axis tomographic schemes. Finally Chapter 11 shows examples of reconstruction algorithm-based resolution improvements. Compressed sensing based algorithms are applied to the reconstruction of GaAs nanowires.

The thesis finishes with conclusions and perspectives in Chapter 12 and a “Résumé” in French language in Chapter 13.

For the reader’s convenience a list with used abbreviations can be found on page 239, the used notations are summarized on page 243 and used physical constants on page 247.

Part I

Background

2 Semiconductor Materials and Devices

Semiconducting materials form the basis for a large number of applications today. Their success started in 1947 with the creation of the first transistor. While previously switching of electron currents was done mechanically, transistors allowed for the first time pure electrical switching. This first transistor was a bipolar transistor made of germanium, the first silicon bipolar transistor was produced seven years later in 1954 and the first silicon field-effect transistor (FET) in 1960.

Transistors allowed the creation of integrated circuits (ICs), functionalized assemblies of transistors. The number of transistors in integrated circuits quickly increased. Based on observations of the development of integrated circuits in the preceding years, this caused Gordon Moore in 1965 to predict an exponential growth of the number of components on an integrated circuit, doubling every two years (Moore, 1965). This prediction is now popularly known as “Moore’s law” and turned out to work up to today. Fig. 2.1 shows Moore’s original prediction and its extrapolation until today. In the same article Gordon Moore also predicted “(...) such wonders as home computers (...) automatic controls for automobiles, and personal portable communications equipment”.

The method for increasing the number of components on a chip is scaling: Reducing the size of a single component reduces the space and power consumption of each transistor, allowing more components to be integrated on a single chip. The forefront of scaling is built up by complementary metal-oxide-semiconductor (CMOS) technology. Metal-oxide-semiconductor field-effect transistors (MOSFETs) allow the highest integration rate of all devices, currently around a billion transistors are integrated on a single chip.

While scaling of CMOS technology is a major driving force for semiconductor research and development of processes, a large number of other devices based on silicon or other semiconductors have been developed and gained importance for a wide range of applications. While classical CMOS scaling is now often referred to as “More Moore”, a part of this diversification, which is based on processes developed

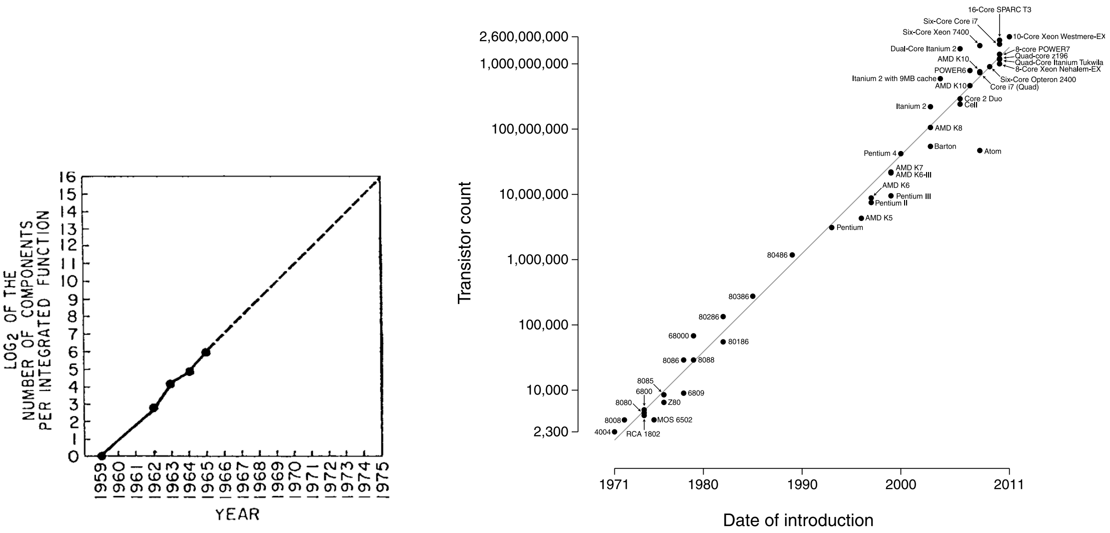

(a) **(b)**

Figure 2.1: Moore's law: (a) Graph originally published by Gordon Moore in 1965 (Moore, 1965) (b) Extrapolation until 2011 showing important microprocessors (Wikipedia, 2013).

for CMOS technology is summarized as being "More than Moore" (Arden et al., 2010). Fig. 2.2 shows these trends.

Apart from CMOS, semiconductor-based nanotechnology covers a wide field. Relatively close to CMOS technology are other transistor technologies, for example for power applications or high frequency application, based on silicon or on other semiconductors. Examples of transistors used for such applications are bipolar transistors, double-diffused metal-oxide-semiconductor (DMOS) transistors based on silicon or high-electron mobility transistors high-electron mobility transistors (HEMTs) based on III-V materials.

Based on silicon technology microelectromechanical systems (MEMS) and nanoelectromechanical systems (NEMS) have been developed, which are used as sensors and actuators towards the environment of the chips. Accelerometers or gyroscopes are popular examples.

III-V, II-VI, but also organic semiconductors have become important in particular for optical applications. Laser diodes and light emitting diodes are commercially very successful devices based on these materials. Photovoltaics are another optical application of semiconductors, based most frequently on silicon, using a semiconductor's capability to create active charge carriers from photons. They range among the most promising technologies for exploiting regenerative energy sources.

In this chapter an overview about important semiconductor devices and processes for creating these devices is given to illustrate the potential of semiconductors and

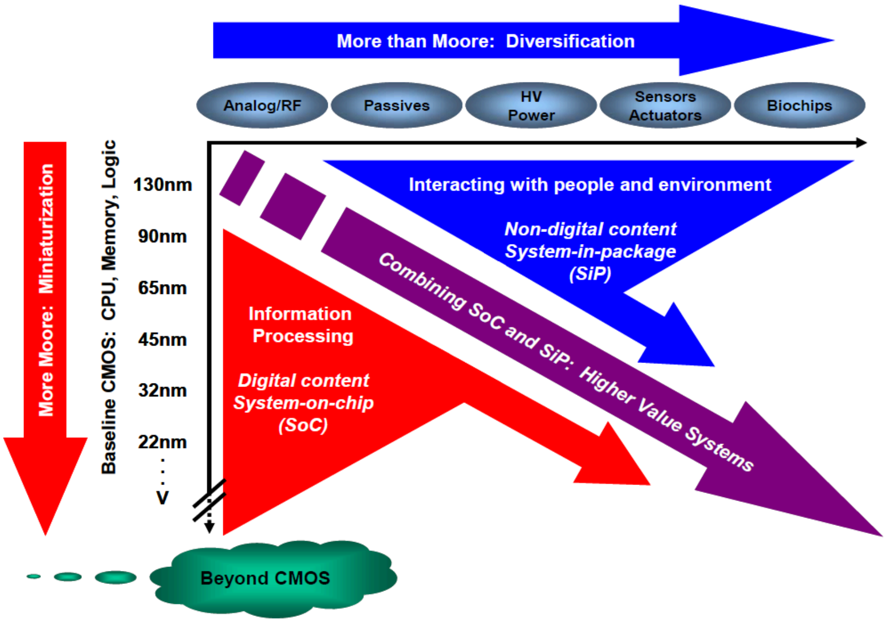

Figure 2.2: The trends of "More than Moore" as compared to "More Moore" (Arden et al., 2010).

the necessity of using advanced nanoscale characterization techniques. Additionally some basic physics of semiconductors and their electrical and optical properties are discussed in Appendix A. There exist a large number of books extensively covering semiconductor physics, processes and devices (Balandin and Wang, 2009, Doering and Nishi, 2008, Sze, 1981, Yu and Cardona, 2004).

2.1 Processes in Semiconductor Technology

The production of semiconductor devices requires complicated, precise and expensive processes. Semiconductor processing requires a well-controlled environment and is therefore usually done in cleanrooms, which contain a large number of machines for doing all necessary processes. While in research and development the conception and demonstration of a small number of nanoscale objects can be done on smaller machines, which allow human interaction in or between different process steps, industrial fabrication of semiconductor devices is done on a large scale in a semiconductor fabrication plant (often called fab). In these plants a large number of chips is processed at the same time and human interaction in the manufacturing process is reduced as far as possible. The purpose of production at a large scale is reduction of the cost per chip, a well controlled environment is necessary to limit the number of defective devices and chips. While the parallel production of many chips reduces the cost per chip, it increases the cost of machines and manufacturing

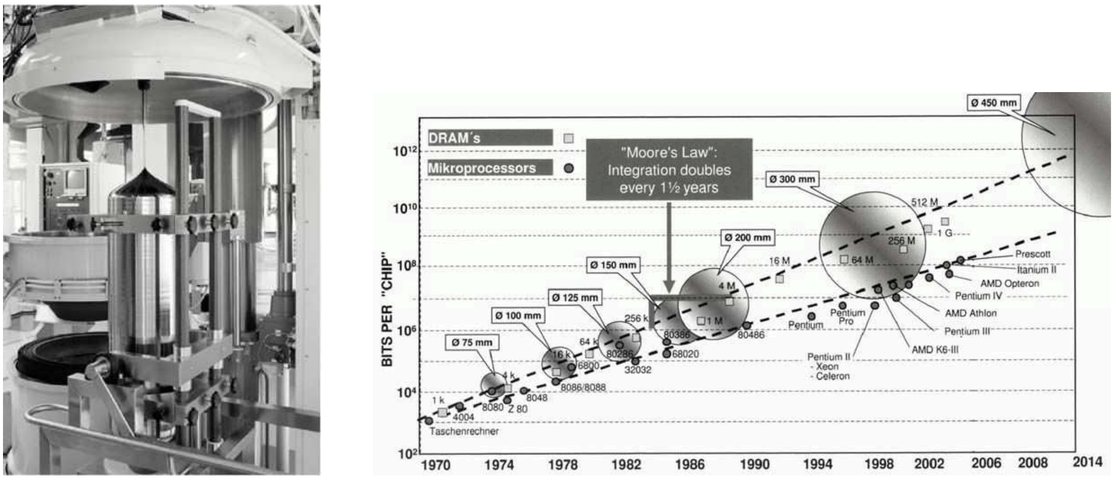

(a) (b)

Figure 2.3: Silicon wafer growth: (a) Czochralski puller for growth of silicon wafers (b) Evolution of wafer sizes overlaid with the evolution of integrated circuits following Moore's law. Source: Siltronic AG, reproduced from (Müller, 2007).

plants, the cost of a new fab is in the range of a few billion Euro. The complexity of semiconductor devices and their cost explains, why serious efforts are necessary for their characterization, for controlling the different processes and device design. In the following the most important processes used in semiconductor technology and processes used for the samples investigated in this thesis are described.

2.1.1 Wafer Production

The most important method for the production of semiconductor substrates is the Czochralski method. The principles of this method were found by Jan Czochralski in 1917 (Czochralski, 1918). The material, silicon or another material is melted and a crystal is grown starting from a seed crystal, which is dipped into the melt and slowly lifted out of the melt. The diameter of the crystal is controlled by the temperature of the melt, by the pulling speed and by rotation of the crystal (Müller, 2007). After growth the crystal is sliced into wafers, which are polished. The first semiconductor crystal grown was germanium (Teal and Little, 1950), today silicon is by far the most frequently used substrate. Currently silicon wafers with a diameter of 300 mm are in use, the transition to even larger wafers with a diameter of 450 mm is in discussion. Fig. 2.3 shows a Czochralski puller and the evolution of silicon wafer diameter. The challenge in the growth of wafers consists in the need for growing high purity crystal with very small amounts of defects and contamination. Apart from silicon and germanium also several other semiconductor substrates can be grown. When compound semiconductors are grown a major challenge is to prevent dissociation of

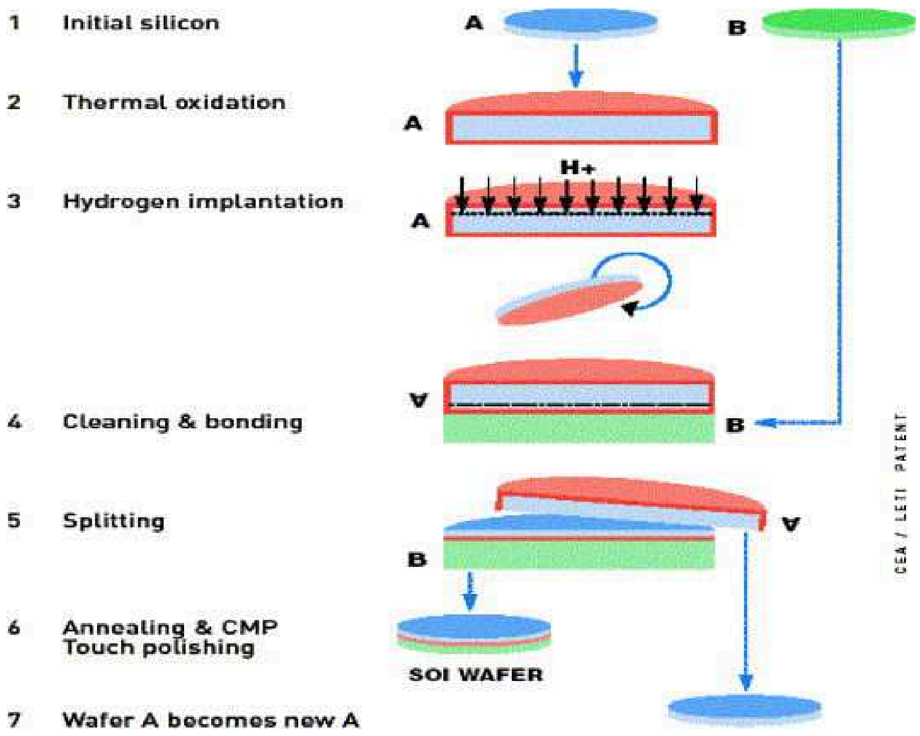

Figure 2.4: SmartCut$^{\text{TM}}$ process for manufacturing SOI wafers (Allibert et al., 2001).

the compound (Müller, 2007). Several techniques to encapsulate the melt have been developed. Examples for compound substrates are GaAs or InP.

For some devices substrates, which contain an insulating layer (SiO_2), are necessary. The most frequently used process to create such silicon on insulator (SOI) wafers is the SmartCut$^{\text{TM}}$ process (Bruel, 1995). The SmartCut$^{\text{TM}}$ process is shown in Fig. 2.4. One wafer (wafer A) is thermally oxidized. After oxidation hydrogen is implanted to create a layer of defects at a controlled depth, which will serve to cut the wafer. The wafer is bonded to a second pure silicon wafer. After bonding the wafer is split at the level of the defects leaving a thin homogeneous wafer of silicon on SiO_2. The wafer is now polished and can be used a SOI wafer. The remaining part of the first wafer, which was split of can be polished an reused. SOI wafers are of importance for transistors with improved performance, as discussed in Section 2.2.1.

2.1.2 Lithography

Photolithography or optical lithography is the most important process for lateral structuring in semiconductor technology (Seisyan, 2011). It is used to transfer structures from a mask to a photoresist on a sample. These structures can then be used to selectively manipulate parts of the sample by doping, etching or growth of a material. The smallest feature size which can be transferred onto a photoresist on the

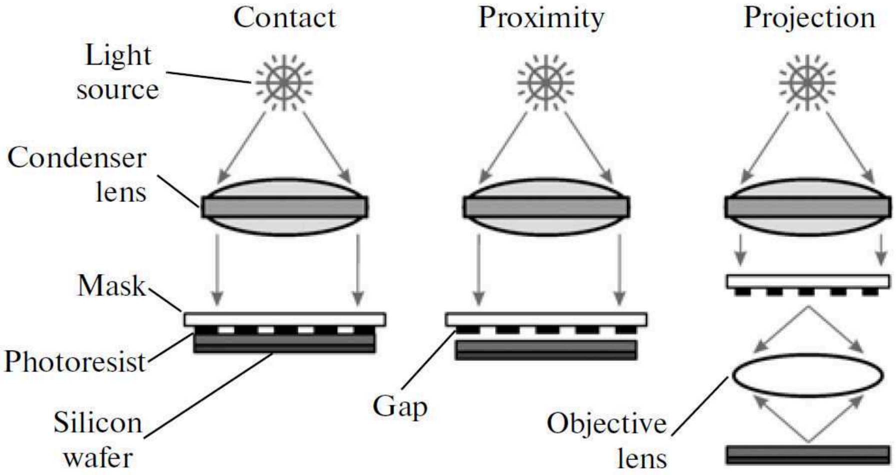

Figure 2.5: Basic operation modes of optical lithography: In contact lithography the mask is in direct contact with the resist, in proximity lithography there is a small gap in between. Projection lithography uses a lens system between the mask and the sample (Seisyan, 2011).

sample is one of the main limiting factors for the integration density of nanoscale devices. In the photolithography process first a resist is deposited on the wafer surface. Then the mask is aligned with the wafer and exposure takes place. Exposure changes the chemistry of the exposed surface. The photoresist is then developed and the exposed photoresist is removed. The structured resist can now be used as mask for a process. Fig 2.5 shows the principle of optical lithography in different operation modes. Originally contact and proximity lithography were used, current systems use projection lithography.

The smallest possible feature size, which can be created by lithography is influenced first of all by the wavelength of the used radiation for exposure. Classically Hg-lamps have been used for optical lithography, which emit at wavelengths around 400 nm. These were later replaced by excimer lasers emitting in the deep ultra-violet region, first by Krypton fluoride (KrF) lasers (248 nm) and later argon fluoride (ArF) lasers (193 nm). However reduction of the wavelength alone was not sufficient for continued scaling for microelectronics. Several techniques are being employed to create structures with sizes well below the used wavelength such as phase-shift masks, off-axis resolution, lenses with high aperture and finally fluid immersion systems.

Many efforts have been put into pushing the resolution using 193 nm, due to technological challenges in switching to lower wavelengths. One major challenge at lower wavelength is that air and all materials become absorbing at wavelengths below about 185 nm. Therefore photolithography at lower wavelength requires operation under vacuum as well as reflective optics. Systems emitting in the extreme ultraviolet (EUV), around 13.5 nm have been developed, based on emission from plasma. Currently their main limitations, which still prevent from industrial applications, are a relatively low power of the light source, as well as very high cost.

There exist several alternatives to optical lithography, such as electron beam (e-beam) lithography or nanoimprint lithography. E-beam lithography is currently much in use for research and development. In e-beam lithography a resist sensitive to electrons is used and writing of the resist is done without a mask by scanning of the electron beam. Due to the small wavelength of electrons very small features can be written. In research e-beam lithography is of interest as it allows writing without the need for masks. For industrial application the serial writing by the electron beam is a major drawback leading to a low throughput compared to optical lithography. Systems have been developed which use a large number (several thousands up to a million) parallel electron beams for writing. These tools are a possible candidate for replacing optical lithography tools. Nanoimprint lithography is based on mechanical transfer from the mask to the resist, based on similar principles as a simple stamp (Schift, 2008). The mask is mechanically pressed into a resist, which is deformed by the pattern of the mask. In an anisotropic etching step the mask is completely removed from the compressed areas and can then serve as mask for other processes.

2.1.3 Doping

Doping is the process of introducing impurities into an intrinsic semiconductor to modify its bandstructure and thereby its electrical properties. Dopants are divided into acceptors, elements with three or less outer shell electrons and donators, elements with five or more outer shell electrons. Acceptors remove electrons from the crystal giving rise to holes, which serve as positively charged carriers (p-type doping). Donators provide additional free electrons which serve as negatively charged carriers (n-type doping). In silicon technology the most common dopants are boron for p-doping and arsenic or phosphorus for n-type doping.

The most common processes for doping are thermal diffusion and ion implantation. For thermal diffusion the dopant is provided at the surface of the semiconductor, either in gaseous, liquid or solid form. At elevated temperature the dopants can diffuse into the semiconductor driven by a gradient of their concentration. For ion implantation the dopant is ionized and accelerated towards the surface. The kinetic energy defines the depth at which the dopants are introduced.

Ion implantation allows a more precise control of the dopant profile than thermal diffusion. Dopant concentration and depth can be well adapted to specific needs. However ion implantation damages the crystal structure, so an annealing step is required after implantation. During this step generally also thermal diffusion of dopants occurs. On a process level the throughput of ion implantation is lower than using thermal diffusion.

Some samples investigated in the frame of this thesis were doped by a particular process, called optical hyperdoping (Sher et al., 2011). In this process the crystal (e.g. silicon) is irradiated by a train of laser pulses in the presence of a dopant precursor. This precursor can be either a gas-phase precursor like sulfur hexafluoride (SF_6) (Wu et al., 2001, Younkin et al., 2003) or a thin solid film precursor (e.g. a selenium or tellurium film) (Sheehy et al., 2007). Laser irradiation causes fast melting and resolidification of the surface of the material, which traps dopant atoms. This process yields very high dopant concentrations, however solid segregation and loss of crystalline order can occur.

In addition to the incorporation of dopant atoms the laser pulses can also modify the surface structure and induce surface texturing. Of particular interest is femtosecond laser-doping of silicon with chalcogens (S, Se, Te) as doping and texturing provides a material with near-unity optical absorptance in the visible and infrared range, which is of interest for photovoltaics and optical detectors.

2.1.4 Etching

Etching is used as process to remove material from a surface (Lang, 1996, Radjenović and Radmilović-Radjenović, 2010). An etching process is characterized by its properties and by the type of etchant used. The two large groups of etching are liquid-phase (or wet) etching and vapor-phase (or dry) etching. Furthermore etching processes are categorized by their isotropy and their selectivity. Isotropic etching refers to a process, which removes material equally in all direction, anisotropic etching has a preferred direction. The selectivity of an etching process denotes the differences of the etch rate of different materials.

In wet etching the surface to etch is put inside a bath of the etchant where the material is removed. The process can be stopped by removal and cleaning of the sample or by dilution of the etchant. Wet etching provides usually a high amount of selectivity, but is generally isotropic, which is often unwanted.

Dry etching is done using gas molecules, which are split into free radicals under the influence of a plasma. Fig. 2.6 shows different types of dry etching. In classical plasma etching the etchants coincide with the surface from all directions, typically giving an isotropic and selective process. Sputtering and reactive ion etching are other types of dry etching, with higher anisotropy. Sputtering is done at much lower pressures than plasma etching, ions are accelerated towards the surface of the

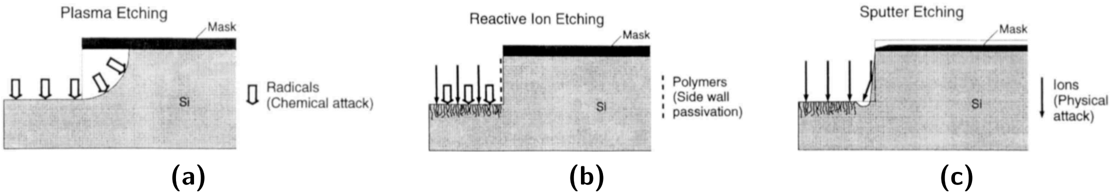

Figure 2.6: Dry-etch methods: (a) Plasma etching, (b) reactive-ion etching, (c) sputtering (Lang, 1996).

sample, where they knock out atoms. Sputtering provides high anisotropy but poor selectivity. Reactive ion etching is an intermediate process between plasma etching and sputtering, being generally anisotropic but more selective than sputtering.

2.1.5 Thermal Oxidation of Silicon

To create films of SiO_2 an important process is the thermal oxidation of a silicon surface (Atalla et al., 1959). This process provides a high-quality dielectric, which for many years formed also the core of CMOS technology as gate oxide. Silicon can be oxidized purely thermally in an O_2 environment (dry oxidation) or hydrothermally in a gaseous H_2O environment (wet oxidation). Oxidation uses up a part of the silicon surface to create SiO_2. The SiO_2-layer is approximately two times as thick as the layer of used Si. Though SiO_2 is now being replaced by high-κ dielectrics in the gate stack a thin layer of SiO_2 is still necessary and SiO_2 is in use for many purposes. In contrast to SiO_2 high-κ dielectrics cannot be grown from Si, but are deposited, using methods as discussed in the next section.

2.1.6 Layer Deposition

Several techniques exist for the deposition of thin solid films on a surface. Here we will shortly discuss chemical vapor deposition (CVD) including atomic layer deposition (ALD) and molecular beam epitaxy molecular beam epitaxy (MBE).

In CVD processes carrier gases react on a heated surface leaving a stable solid on the surface (Choy, 2003). Fig. 2.7 shows this principle. A wide range of materials can be deposited by CVD, which exists in several variants. While in classical CVD the reaction is activated thermally, plasma-enhanced chemical vapor deposition (PECVD) uses a plasma to activate the chemical reaction on the surface, enabling operation at low temperatures. metal-organic chemical vapor deposition (MOCVD) is classified by the use of metalorganic precursors. These are compounds, which

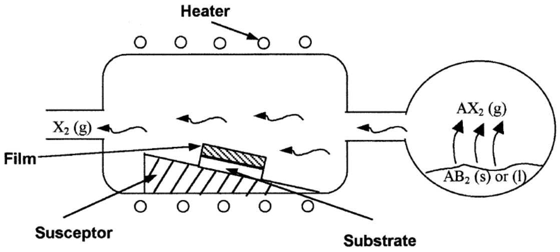

Figure 2.7: Principle of CVD deposition. The material to deposit A is transferred to a gaseous precursor AX_2 from a solid or a liquid source. On the heated surface the precursor reacts and the material is deposited (Choy, 2003).

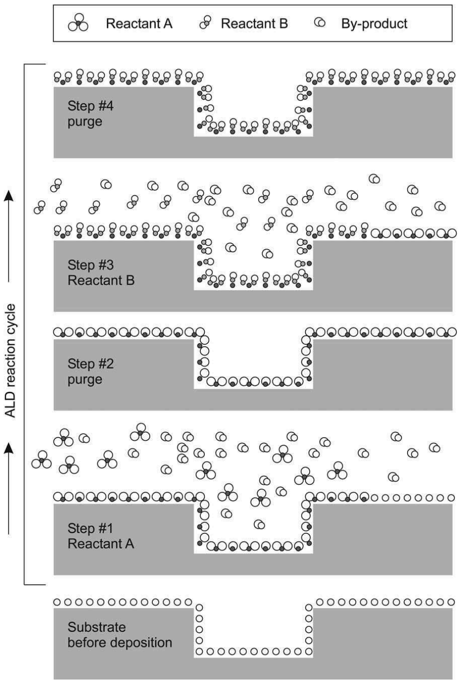

Figure 2.8: Illustration of one reaction cycle of ALD (Puurunen, 2005).

contain metal atoms being bonded to organic radicals. MOCVD is of interest as these compound decompose at relatively low temperatures.

ALD is another special mode of CVD (Puurunen, 2005). The particularity of ALD is the use of self-terminating reactions, which allow the growth of monoatomic layers. ALD uses several cycles consisting of two distinct reactions. Such a reaction cycle is illustrated in Fig. 2.8. The first reaction forms a monolayer on the surface. Once the whole surface is covered the reaction terminates. The chamber is purged and a second self-terminating reaction or a surface treatment activates the surface again for the first reaction. In this way high quality thin films can be deposited and the thickness can be controlled exactly by counting atomic layers.

MBE is another method for deposition of high quality thin films, which is of particular importance for compound semiconductors. MBE allows the deposition of thin films on a heated surface from molecular beams of different elements under ultra-high vacuum. Molecular beams can be created by thermal evaporation from Knudsen sources. MBE is a popular method for the growth of semiconductor heterostructures, in particular for optoelectronic devices, such as lasers. It is also an important method for the formation of quantum dots. For this purpose a thin layer of a material with a larger lattice constant is grown on a material with a smaller constant. Relaxation of the thin layer leads to the formation of quantum dots (Franchi et al., 2003).

2.1.7 Nanowire Synthesis

Nanowires are one type of nanostructures, which are gaining significant attention in semiconductor research (Lu and Lieber, 2006, Schmidt et al., 2009). Nanowires are structures, which are small in two dimensions and larger in the third dimension. Their diameter is usually below 100 nm, their length is generally in the range of a few micrometers. They can be therefore considered one-dimensional systems. The elaboration of nanowires is divided into top-down and bottom-up approaches. Top-down refers to processes which start from a continuous layer or a substrate of material, which is then patterned to create nanowire structures. Vertical nanowires can be created in this way by defining their position by lithography followed by anisotropic etching. The elaboration of horizontal nanowire structures is possible for example by using combinations of anisotropic and isotropic etching or by starting from thin layers of a material, for example from an SOI substrate.

In bottom-up approaches nanowires are grown from precursors, which are provided most frequently in gaseous form, but can be also liquid or solid. Generally catalyst particles are used, which favor directional and localized growth. The catalyst can be either liquid or solid during growth. The most frequently used approach for bottom-up elaboration of nanowires is the vapor-liquid-solid (VLS) method, where a gaseous precursor is supplied, which is incorporated in the liquid catalyst particle (Wagner and Ellis, 1964). From the catalyst the supplied atoms precipitate into a solid phase to form the nanowire. If a molecular precursor is used, which reacts at the surface of the catalyst this process is also described to be CVD. Another important method for bottom-up growth is the elaboration by molecular beam epitaxy. In this case the precursor is directly provided in its atomic form as a molecular beam. Those atoms are more readily deposited via the catalyst particle than directly on the surface. A large range of materials can be grown as nanowires. Silicon, germanium, III-V as well as II-VI composite semiconductors. Other materials, which can be grown as nanowires are for example metallic oxides or different types of silicides.

An interesting option when nanowires are synthesized is the possibility to create heterostructures consisting of different materials. Such heterostructures are classified into axial heterostructures, where the material composition changes along the direction of the nanowire and radial or core/shell heterostructures, where the composition changes from the center of the nanowire towards its exterior. Axial heterostructure nanowires are grown by modulating the supply of precursors during growth. Radial heterostructures can be formed by homogeneous deposition on the nanowire surface after its growth. Such structures provide combinations of several one-dimensional or zero-dimensional systems, where electrical and optical properties can be adjusted by adapting the size of different elements. Core/shell nanowires can be also obtained by layer deposition onto a nanowire, which was elaborated in a top-down method. An interesting feature, when semiconductor heterostructures are grown is that due to the small lateral size of nanowires they can accommodate a large lattice mismatch without defects. Therefore material combinations, which cannot be grown on full layers can be often still grown as nanowires. In particular this allows also a wide range of materials to be grown directly on silicon. When nanowires devices should be included in integrated circuit for many concepts a limitation are used materials or temperatures necessary for growth, which are often not compatible with IC technologies.

2.2 Semiconductor Devices

Eventually the goal of semiconductor research is to create devices. Understanding of physics and control of processes are necessary for this task and allow the conception of new devices and devices with improved performance. There exist a huge number of semiconductor devices. Electronic applications require many different types of transistors, but also resistors, capacitors or diodes. Well known optical devices are light-emitting diodes, laser-diodes, solar cells or optical detectors. Integrated optics are a newer field in semiconductor technology, which require devices for guiding and modulating light. Apart from these applications semiconductor technology has also been expanded to new fields, microelectromechanical and nanoelectromechanical systems are one such example. Here we will give an overlook over a few semiconductor devices, in particular such, which are of relevance for this thesis.

2.2.1 CMOS Transistors and New Transistor Concepts

CMOS technology combines negative metal-oxide-semiconductor (NMOS) and positive metal-oxide-semiconductor (PMOS) transistors to form logic circuits. NMOS transistors allow conduction of electrons between source and drain, if a positive voltage is applied on the gate, PMOS transistors conduct holes, if a negative voltage is applied on the gate. Combination of NMOS and PMOS transistors gives logic circuits, which became the dominant technology for very large scale integration, in particular due to a low power consumption in static states.

Since their first integration the materials used in metal-oxide-semiconductor (MOS) transistors have changed only little, but huge changes have taken place regarding their size. In the end of the 1960s the classical MOSFET gate stack consisting of SiO_2 and polycrystalline silicon (poly-Si) was developed (Faggin and Klein, 1969). This material combination proved very successful, in particular the easy fabrication of a high-quality oxide by thermal oxidation was a major advantage for silicon compared to germanium and a basis for the success of silicon MOS transistors (Atalla et al., 1959). The material combination Si/SiO_2/Poly-Si formed the basis of MOS transistors for over 30 years until finally SiO_2 was replaced, first by nitrided SiO_2 (SiON) and later by high-κ gate dielectrics (Wilk et al., 2001).

The core of a MOSFET is built up by a metal-oxide-semiconductor capacitor (Wong et al., 1999). In the case of a classical MOSFET poly-Si is the conductor, SiO_2 the insulator and silicon the semiconductor. The semiconductor body region is p-doped for an NMOS transistor and n-doped silicon for a PMOS transistor. Fig. 2.9 shows a classical NMOS transistor. An applied voltage on the poly-silicon gate creates an external electrical field which bends the bandstructure in the semiconductor body region and thereby changes the carrier statistics through the field-effect. If a positive voltage is applied to the gate of an NMOS transistor the density of holes is reduced at the interface to the insulator. This is called depletion. If the voltage is high enough the bands in the semiconductor bend far enough to shift the conduction band below the Fermi-level, which then allows current transport by electrons in a thin region at the interface. This state is called inversion, the conducting region is referred to as channel. In a NMOS transistor the n-doped source and drain regions are located on both sides of the channel and under inversion conditions electrons can move between source and drain through the channel. In a PMOS transistor n- and p-regions are inverted. A large enough negative voltage causes inversion in the n-doped channel of the transistor and allows the transport of holes between the p-doped source and drain.

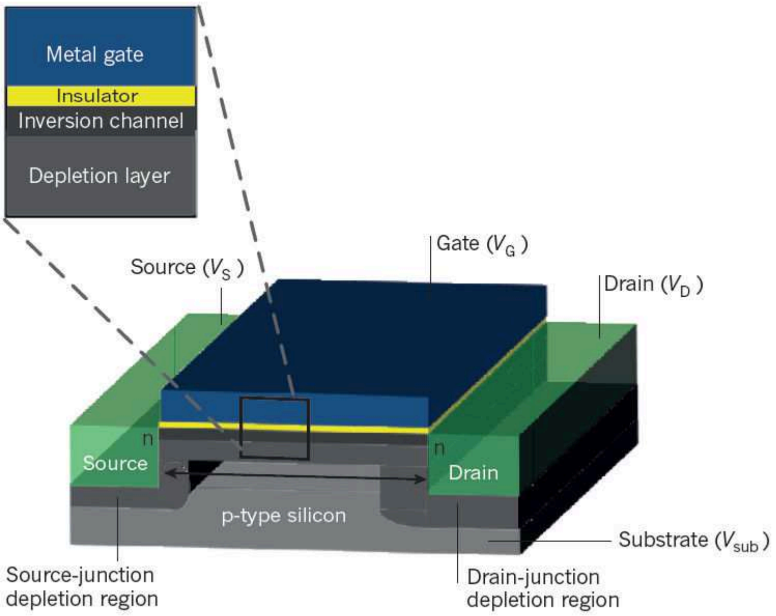

Figure 2.9: Schematic of a classical NMOS transistor, inversion and depletion layers in its active state are shown (Ferain et al., 2011).

While the basic design of MOSFET devices has not changed over the years, their size was continuously reduced, which allowed increasing the number of devices on a chip. This reduction of the size is known as scaling. For scaling all geometrical sizes of a transistor, the gate length, gate width and oxide thickness as well as the operating voltage are reduced. For many years scaling provided faster transistors with lower power consumption. Simple scaling came to its end, when physical limits became important. By reducing the oxide thickness the insulating power of SiO_2 came to its limits and gate leakage became too high to allow further reduction of the oxide thickness. This limit was overcome by replacing SiO_2 by high-κ dielectrics. Several oxides were under research for this purpose, finally hafnium-based oxides, either HfO_2 or HfSiON, were chosen to replace SiO_2. These oxide have a relative permittivity of 20-25 compared to SiO_2, which has a relative permittivity of only 3.9. This higher permittivity allows using thicker oxide films to get the same capacitance. Practically SiO_2 is not completely removed from the gate stack, but a thin layer is grown before deposition of the high-κ dielectric as this gives oxides with higher quality (Gusev et al., 2003). Since several years now also strain is employed in the channel of MOSFET transistors to improve the mobility of carriers (Fischetti and Laux, 1996). Electron mobility in silicon can be improved by tensile strain, while the mobility of holes increases by applying compressive strain.

Short channel effects became important in the last years and are putting an end to using conventional planar transistors on bulk substrates. Two strategies are currently

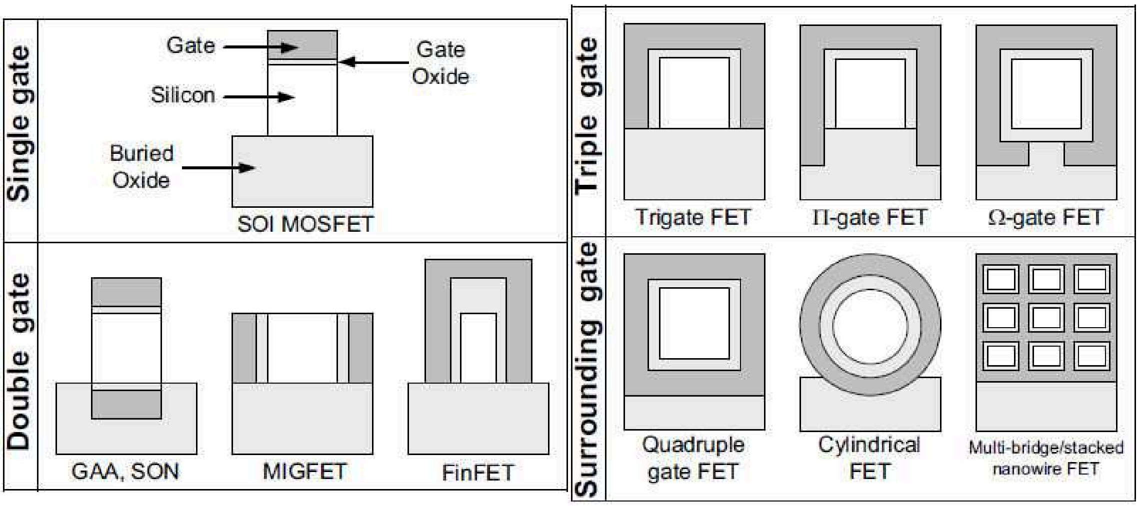

Figure 2.10: Different concepts for multi-gate transistors on SOI (Colinge, 2007).

being followed for overcoming this challenge, which can eventually also be combined: The first one is switching from bulk to SOI devices (Takagi et al., 2008), the second one is the use of thin multi-gate devices (Colinge, 2007, Ferain et al., 2011). The main motivation for these approaches is to create fully-depleted devices, where the whole silicon body region is depleted. Those devices provide significantly better performance compared to bulk transistors. Multi-gate transistors are characterized by the number of active gate surfaces around the channel as double-gate, tri-gate or gate-all-around transistors. An overview of these concepts is given in Fig. 2.10. Several names exist for particular types of multi-gate devices: FinFET transistors are a special type of a double-gate transistor with a thin channel. Ω- or Π- gate transistors are special types of tri-gate transistors, where underetching of the channel is used to allow a partial control also from the fourth side of the channel. There exist several ideas for further device performance improvements, one such concept is to replace silicon as material in the channel by semiconductors with higher carrier mobility (Takagi et al., 2008, Wu et al., 2008a). Germanium provides higher mobility for both electrons and holes, and for NMOS transistors GaAs would be even better providing again higher electron mobility.

The question whether to overcome limitations of scaling by multi-gate devices or by switching to SOI devices is currently dividing semiconductor manufacturing companies. Most notably Intel has chosen the path of multi-gate transistors, current high-end processors contain FinFET devices. A company using SOI devices is for example STMicroelectronics.

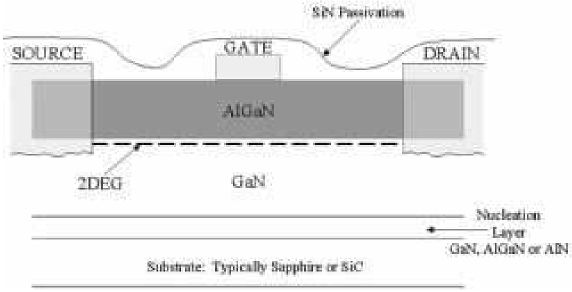

Figure 2.11: Schematic of an InGaN/GaN HEMT (Mishra et al., 2002).

2.2.2 Other Types of Transistors

Apart from CMOS transistors several other types of transistors are in use in integrated circuits. Important types of applications, which cannot be covered by classical CMOS devices are high-frequency and power applications. Bipolar transistors are of importance for high-frequency applications and are frequently integrated together with CMOS technology in BiCMOS processes. A silicon device used for power applications are DMOS transistors, cointegration of bipolar, CMOS and DMOS devices is known as BCD or Smart Power technology (Baliga, 1991). An important type of transistors based on III-V materials are HEMTs (Mimura et al., 1980). Such a device is shown in Fig. 2.11. In HEMTs a heterostructure of different III-V materials is used in the gate stack of the device. A material with a smaller bandgap is used in the channel, while a larger bandgap material is used as insulator in the gate stack. Impurity atoms for doping are introduced in the material with the larger bandgap, but electrons or holes provided by the dopant move into the smaller bandgap material, where they localize at a thin layer close to the interface between the two materials and form a two-dimensional electron gas (2DEG). Carriers in the 2DEG have a very high mobility due to the absence of scattering from ionized impurities. This makes them interesting devices for very high frequency applications and they are therefore in use for communication systems, e.g. in cell phones, satellite receivers or radar. The first HEMTs were based on heterostructures of GaAs and GaAlAs, later also GaN-based HEMTs have gained significant attention, the large bandgap is of interest in particular for high power applications (Kuzmik, 2001, Mishra et al., 2002).

2.2.3 Optoelectronic Devices

Optoelectronics are a field where semiconductor materials are being successfully used for a large number of devices exploiting interactions between photons and electrons. Examples for such devices are solar cells, optical detectors, light-emitting diodes

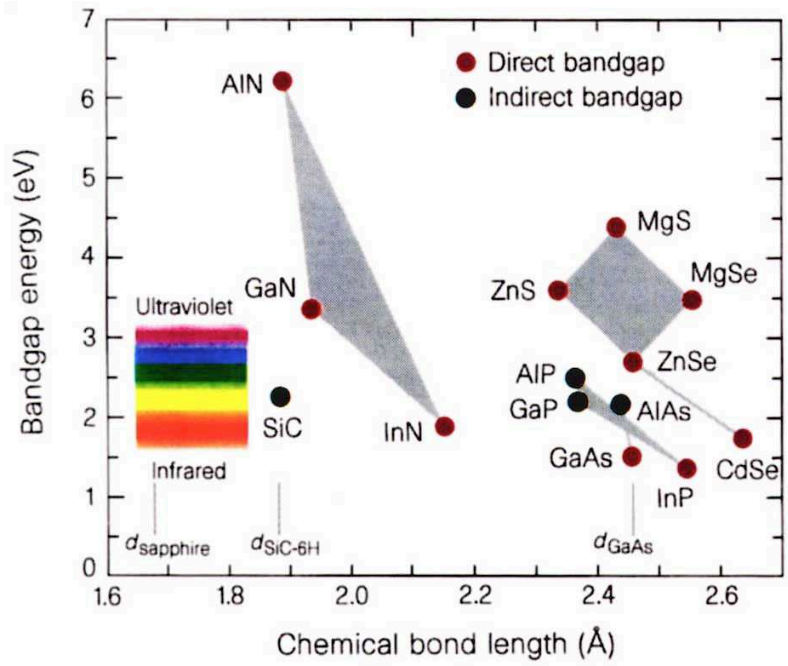

Figure 2.12: Band gap and lattice constant of different compound semiconductor. The visible spectrum is indicated (Ponce and Bour, 1997).

(LEDs) and semiconductor lasers. The most important semiconductor property for such devices is the bandgap of a semiconductor, which for most devices corresponds to the minimum photon energy, which is necessary for absorption or to the energy of photons, which are emitted.

For light-emitting optoelectronic devices, compound semiconductors, in particular III-V compounds are important as they offer a wide range of available band gap energies. Many of them are direct semiconductors, and they allow adjusting the band gap by using mixtures of compound semiconductors. Fig. 2.12 shows an overview of the bandgap and the lattice constant of different compound semiconductors as well as domains, where mixtures are possible. The lattice constant is of importance when heterostructures are formed as generally only materials with low lattice mismatch can be grown on top of each other without structural defects.

Light-emitting diodes are based on a simple p-n junction of a direct semiconductor material (Black et al., 1963). With forward biasing of the diode electrons and holes flow towards the junction, where they can recombine, creating photons by spontaneous emission. The first light-emitting diodes were based on GaAs and on materials allowing emission in the infrared up to green light region. An important step was the development of LEDs based on III-V nitrides (Ponce and Bour, 1997). Those materials allow emission in the blue range and provided thereby coverage of the full visible spectrum. Blue light-emitting diode are necessary for lighting application, creating white light either by mixing of several differently colored LEDs or by downconversion of the energy of a part of the photons to lower energies.

Semiconductor laser diodes are based on stimulated emission in direct semiconductors (Dupuis, 1987, Holonyak and Bevacqua, 1962, Renk, 2012). Laser diodes basically require a resonating cavity as well as a pumped direct semiconductor which is excited to be in optical inversion. As resonating cavity, in the simplest cases two cleaved surfaces of a semiconductor can be used, in other concepts Bragg-mirrors based on heterostructures on both sides of the cavity are employed. The cavity governs the resonant modes of the laser-diode. Pumping is most frequently done electrically by inserting electrons and holes into a p-n junction. In principle the p-n junction can be a homogeneous semiconductor made of a single material, but such homojunction lasers are very inefficient. Generally a heterojunction is used, where the active region is made of a semiconductor with a smaller bandgap, so the active zone is reduced to this zone. When the active zone is thin enough, the density of states becomes two-dimensional, which provides again more efficient diodes, due to the abrupt changes of the density of states in a 2D system. Such devices are known as quantum-well lasers. There exist several other types of semiconductor laser diodes. One interesting concept is the quantum-cascade laser, which uses interband transitions, based on a large number of quantum wells (Faist et al., 1994). Such lasers are emitting photons with a large wavelength in the far-infrared and THz regime.

Solar cells (or photodiodes) are optoelectronic devices, which are used to convert energy from photons to electrons (Goetzberger et al., 2003). As other optoelectronic devices, solar cells are based on p-n junctions. Photons which arrive in the p-n junction can create an electron-hole pair by absorption. These electrons and holes can then be separated and provide electrical energy. As absorption happens also in indirect semiconductors, these can be also used for solar cells, even though the are less efficient. Many different concepts exist for solar cells and a wide range of materials is used, in particular also organic semiconductors (Günes et al., 2007). Commercially currently the most frequently used material is silicon, in different crystalline phases due to its relatively low price. The main goal when developing solar cells is to improve the energy efficiency of conversion from photons to electrons. This efficiency depends on the solar cells reflectance, on the efficiency of the creation of electron-hole pairs, on their separation efficiency as well as on conduction losses in the solar cell.

2.2.4 Nanowire-Based Devices

Several different types of devices based on nanowires have been demonstrated (Li et al., 2006a). Transistors have been created based on nanowires both from top-down as well as from bottom-up approaches. Using top-down approaches is of interest as the controlled structuring allows high integration densities. In fact many multi-gate concepts, in particular gate-all-around transistors can be seen as nanowire transistors. Transistors using bottom-up synthesis of nanowires have been also demonstrated. Several groups have demonstrated horizontal nanowire transistor by contacting nanowires after deposition on a substrate (Xiang et al., 2006). This approach is of interest to show the performance of nanowires for transistors, but it can be only used for single devices and cannot be integrated. A more interesting approach in terms of integration is to leave the nanowires as grown and construct transistors on this basis. In this way vertical nanowire transistors have been grown (Goldberger et al., 2006, Schmidt et al., 2006).

Composite semiconductor nanowires are of interest for optical applications (Yan et al., 2009). LEDs as well as lasers based on nanowires have been demonstrated (Qian et al., 2005, 2008). Furthermore sensors have been developed based on grown nanowires with a functionalized surface (Cui et al., 2001), as well as silicon nanowire-based batteries (Chan et al., 2008). Recently nanowire-based capacitors have been demonstrated (Morel et al., 2012), which have been characterized in the frame of this thesis (see Chapter 8).

2.2.5 NEMS

The processes developed for micro- and nanoelectronics are being used for a wide range of applications apart from classical transistor manufacturing. One large field, which is mostly concerned with sensors and actuators towards the surroundings of a chip are microelectromechanical systems (MEMS) and nanoelectromechanical systems (NEMS). These use lithography, etching and other processes to form devices which are converting mechanical into electrical signals at the nanoscale and vice versa. Classically such devices have been known as MEMS. MEMS are now in use for a wide range of applications, as pressure sensors, accelerometers, gyroscopes, for bio-chips and the manipulation of micro-fluids or for communication applications (Ko, 2007).

The advances of silicon technology to feature sizes well below the micrometer has lead to electromechanical systems with very small sizes, which are now referred to as NEMS (Ekinci and Roukes, 2005). NEMS are usually created on compound

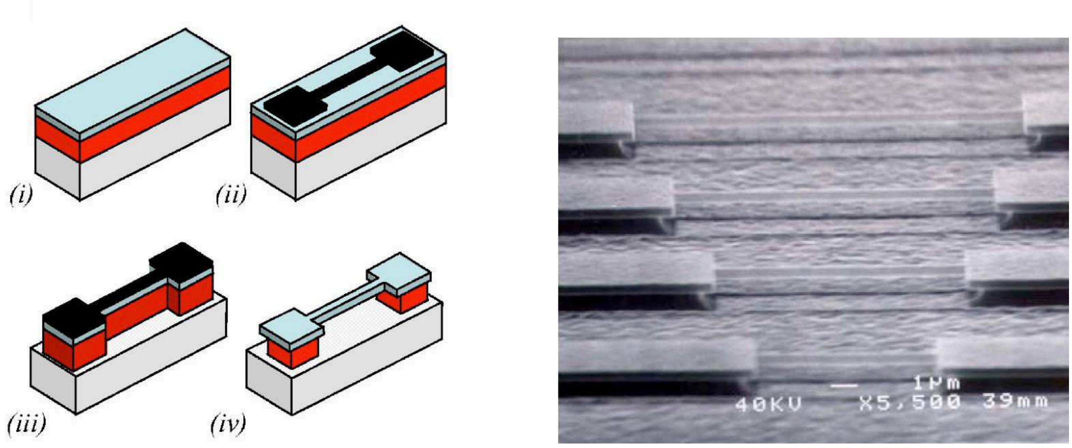

(a) **(b)**

Figure 2.13: NEMS: (a) Surface nanomachining of a NEMS: (i) The process is starting from a composite (e.g. SOI) substrate. (ii) Definition of the NEMS by lithography. (iii) Anisotropic etching transfers the structure. (iv) Selective isotropic etching is applied to remove the sacrificial layer below the NEMS and liberate it. (b) SEM image showing finished NEMS (Ekinci and Roukes, 2005).

substrates, for example on SOI, GaAs/AlGaAs or SiC on silicon. The fabrication process it then referred to as surface nanomachining. In this process suspended nanostructures, for example cantilevers or nanowires, are created by patterning followed by anisotropic and isotropic etching. An example for such a process is shown in Fig. 2.13.

Such suspended structures can mechanically interact with the environment. They are generally classified into resonant and quasistatic NEMS. Resonant NEMS are much more frequently used. These are excited by an electrical signal to resonant modes. This excitation can happen for example by magnetic forces or by capacitive forces. Influences from the environment can modify these vibrational characteristics, these changes need to be detected. For the detection several schemes are possible, based on magnetic or electric forces or on optical schemes. Resonant frequencies can change due to changes of the NEMS' mass or due to external forces. Sensitivity to the mass can be employed for sensing in chemistry or biology, by applying functionalized layers on the NEMS, which are sensitive for example to a specific molecule, cell or virus (Eom et al., 2011).

2.3 3D Characterization Needs for Semiconductor Devices

Several technological issues in semiconductor devices need to be addressed by three-dimensional (3D) characterization techniques. In transistors two major questions when morphological and chemical characterization is concerned are the positioning of dopant atoms and characteristics of different materials in the gate stack, in particular the gate oxide. Information is required about roughness of these layers in different directions. Transmission electron microscopy (TEM) techniques have always played a significant role for addressing these issues, high-resolution TEM and scanning transmission electron microscopy (STEM) allow morphology investigations on thin lamella prepared by the focused ion beam (FIB). Electron energy-loss spectroscopy (EELS) or energy-dispersive x-ray spectroscopy (EDS) are methods for imaging of dopants, though with limited chemical resolution (Clement et al., 2011). A limitation of these two-dimensional (2D) TEM techniques is, that they do not allow observations of variations along the thickness of the prepared samples, as they provide only projections of the device. One technique, which can reconstruct the roughness of different layers in all directions is atomic force microscopy (AFM). However AFM can be only applied directly after deposition of a specific layer and cannot be used to investigate the morphology of the finished device. Tomographic techniques, which are therefore of interest for investigating transistors are electron tomography and atom probe tomography. Atom probe tomography provides high chemical sensitivity and offers thereby great perspectives for 3D characterization of dopants (Inoue et al., 2009, Lauhon et al., 2009). Electron tomography by contrast is of interest for morphological studies, to see variations of layers in the gate stack in all three dimensions on finished devices. In this thesis tri-gate transistors have been studied by electron tomography for this purpose (see Chapter 9).

When optically active semiconductors, in particular solar cells, are concerned, it is often their internal material structure, which governs their optical properties. Localization of impurities, or compositional characterization of compound material systems are tasks, which can require 3D characterization at different length scales (Herzing et al., 2010). In this thesis one such example is the investigation of femtosecond laser-doped silicon, where the distribution of selenium dopants was analyzed by electron tomography to understand optical material properties (see Section 7.2).

For nanowires and nanowire-based devices the morphology and composition of nanowires governs their electrical and optical properties. Therefore these parameters need to be controlled when nanowires are grown. To understand growth parameters, characterization techniques are required, which allow recovering morphology and composition. Electron tomography is a useful technique for this purpose, which allows recovering the shape of nanowires and the distinction of different materials in many nanowire heterostructures (see Section 7.1 and Chapters 8&11). When doping of nanowires is concerned atom probe tomography can be a useful tool.

For NEMS characterization, similar to nanowires, characterization of their morphology can be important. Another issue, which may be addressed by 3D characterization techniques is the analysis of functionalized layers for sensor applications. Furthermore electron tomography can be useful for the exploration of any other materials relevant for semiconductor technology. For example investigation of porous materials – porous silicon or porous low-κ dielectrics – can be of interest or different types of composite nanoparticles or other nanostructures.

2.4 Conclusion

This chapter gave an introduction to semiconductor physics, technology and devices. Properties of semiconductors depend on their morphology and chemical composition at the atomic scale. With ever shrinking devices, this local material composition is governing the behavior of devices. Understanding and controlling device behavior therefore requires knowledge about their composition. A large range of characterization techniques exist for this purpose, most of them providing either images of the surface or averaged signals (projections) over one or two dimensions. Though some of these techniques, notably TEM or AFM provide atomic resolution, the loss of information by recording only reduced representations of the three-dimensional object can prevent from seeing important compositional information. This explains the need for three-dimensional characterization techniques, for understanding and optimizing nanoscale devices.

3 3D Characterization for Nanotechnology

While real objects are always three-dimensional, detectors generally loose information about these objects collecting only representations in two, or even less dimensions. Tomography in its widest sense includes techniques, which try to recover properties of the original object from such reduced representations, often called projections. Tomography is done over a large range of length scales for many different types of applications using different types of detectors for collecting information. Tomography is generally best known from medical applications such as computed x-ray tomography or magnetic resonance tomography. One extreme example of tomography at a very large scale is seismic tomography, which gives insight into the mantle of the earth (Rawlinson et al., 2010). Another rather exotic example of tomography is network or internet tomography, where the properties of a computer network are reconstructed from observations about its behavior (Castro et al., 2004, Coates et al., 2002).

Important tomographic techniques for three-dimensional imaging at microscopic and nanoscopic length scales are, ordered from large to small scale, x-ray tomography, serial sectioning in a dual-beam FIB/scanning electron microscope (SEM), electron tomography and atom probe tomography. Here the focus is on application of these techniques for investigations of materials, but they are also of importance in other scientific fields, in particular for life science applications. Table 3.1 gives an overview of 3D characterization techniques for micro- and nanoscale materials characterization and their typical field of view and resolution. As x-ray tomography is also done at a larger scale, microscopic application of this technique is referred to as x-ray micro- and nanotomography. The resolution limits given are indicative for typical applications of the technique, but can depend significantly on the size and type of investigated samples. For electron tomography for example, atomic resolution has been demonstrated, but only for very small samples of materials strongly scattering electrons. As to atom probe tomography, while in principle it provides atomic res-

	Sample cross-section	Resolution
X-ray microtomography	mm	µm
X-ray nanotomography	10 µm	<100 nm
FIB/SEM serial sectioning	µm-mm	10 nm-µm
Electron tomography	few 100 nm	nm
Atom probe tomography	100 nm	atomic resolution

Table 3.1: Approximate field of view and resolution of tomographic techniques for microscopic materials characterization.

olution, the resolution can be seriously reduced for complex samples consisting of several materials due to uncertainties in the reconstruction.

In this chapter a short overview of tomographic methods for materials applications is given. The principles of the different techniques are explained, capabilities and limitations of each technique are given. For each technique typical applications are referenced and a special focus is put on the techniques relevance for semiconductor materials and device application.

3.1 X-ray Tomography

The first tomography systems were based on x-rays. In 1968 Godfrey Hounsfield constructed the first system for computed x-ray tomography, which earned him the Nobel prize in Physiology or Medicine in 1979 together with Allan McLeod Cormack who had founded the theoretical basis for the application (Cormack, 1963). The first applications of tomography were found in medicine to obtain 3D images of the interior of a human body. While medical applications remain among the most important applications of tomography until today, the same principles were extended to a large field of applications. For materials science in particular tomography systems providing higher resolution are of importance. X-ray tomography for high resolution applications is known as x-ray microtomography (Landis and Keane, 2010) and x-ray nanotomography (Withers, 2007) classified by the achievable resolution.

X-ray tomography is done with laboratory-based equipment or in beamlines on synchrotrons, where x-rays are created by bending of a high-energy electron beam in a magnetic field (Baruchel et al., 2006). Synchrotrons provide beams 10 orders of magnitude brighter than conventional sources. Furthermore the x-ray beams can be tuned to be highly monochromatic and parallel beams can be provided. X-ray tomography can be done with several types of projection geometries, fan-beam, cone-beam or parallel beam geometries. The main limitation for the resolution in x-ray tomography is generally the source size: If the source is large a specific pixel on the detector, will collect information from several beam paths through the sample, which leads to blurring in the image.

For x-ray nanotomography focusing optics are used to improve the achievable resolution (Withers, 2007). For lower beam energies of few keV diffractive optics, in particular Fresnel zone plates can be used to focus x-ray beams (Vila-Comamala et al., 2012), at higher beam energies refractive or reflective optics, for example Kirpatrick-Baez mirrors have to be used (Bleuet et al., 2009). Using such optics tomographic reconstructions with spatial resolution up to 20 nm have been demonstrated (Vila-Comamala et al., 2012). A method, which has been used to acquire high-resolution tomographic reconstructions in a lens-less system is the combination of ptychography and tomography. With this technique reconstructions with a resolution better than 100 nm have been demonstrated (Dierolf et al., 2010).

The most frequently used contrast method for x-ray tomography is to acquire a series of 2D radiographs, which give contrast depending on the x-ray absorption along the beam path (Landis and Keane, 2010). The absorption of x-rays travelling through a sample is a logarithmic function of the absorptivity of the material. The absorptivity depends on the number and types of atoms. Generally atoms with lower atomic mass absorb less than atoms with a higher atomic mass. The absorptivity decreases with increasing energy of the x-rays, except for energies close to x-ray absorption edges, which are characteristic for each element.

Apart from pure absorption also other contrast mechanisms can be used for x-ray tomography. Phase contrast is of interest in particular for samples with small atomic mass, which provide only little amplitude contrast. Tomographic reconstruction based on phase imaging has been done by interferometric methods (Momose, 2003, Momose et al., 1996) and by projection methods, where several tomographic series are acquired at different focal distances to the sample, which allows retrieval and reconstruction of phase maps (Cloetens et al., 1996, 1999). This approach is also called holotomography. Phase imaging generally requires synchrotron radiation as a coherent beam is needed.

In fluorescence tomography the photons, which are created due to excitation by the x-ray beam are recorded on an energy dispersive detector (de Jonge and Vogt, 2010). For fluorescence tomography the x-ray beam needs to be focused and scanned over the sample, to acquire 2D projections of the fluorescence spectra. The detector is usually located at the side of the sample at an angle of 90° to the specimen. Fluorescence tomography is interesting due to its chemical sensitivity but is quite time consuming.

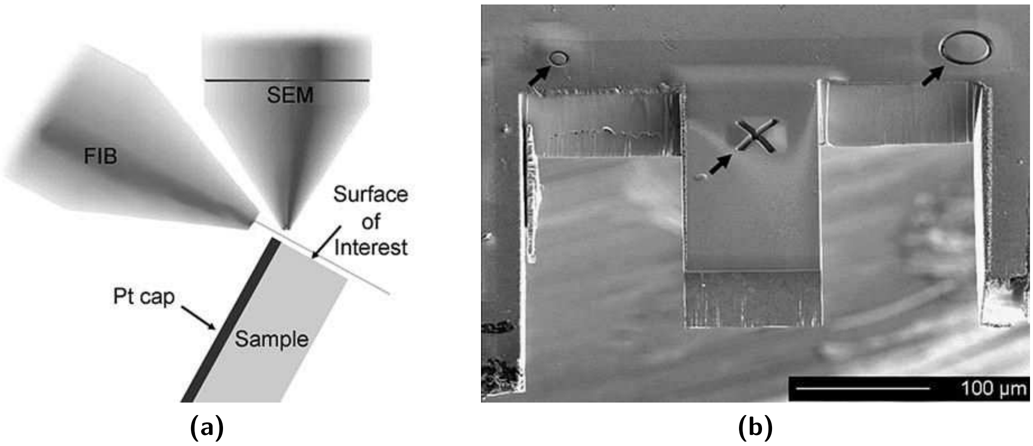

Figure 3.1: Principle of serial sectioning in a FIB/SEM instrument: (a) Geometry of sample with respect to the FIB and SEM column (b) Sample prepared for serial sectioning. On this example markers are indicated, which are used for alignment if the sample is rotated (Uchic et al., 2007).

Diffraction tomography is another mode of x-ray tomography (Bleuet et al., 2008, Larson et al., 2002). As with fluorescence tomography the beam is scanned along the sample and diffraction patterns are acquired for each position. From these projections local three-dimensional diffraction patterns can be reconstructed, which give information about local structural properties.

3.2 Serial Sectioning in a Dual-Beam FIB/SEM

Dual-beam focused ion beam/scanning electron microscope instruments offer a platform for three-dimensional imaging by serial sectioning (Uchic et al., 2007). Fig. 3.1a shows the typical geometry of a dual-beam FIB/SEM system and the positioning of a sample for serial sectioning. For investigating a volume of a sample, the FIB is used to remove the surface of the material one layer at a time by ion milling. The imaging capabilities of the SEM or of the FIB itself can then be used to acquire an image of each exposed surface. This provides a series of two-dimensional images, which can be assembled to a 3D stack providing information about the full investigated volume. The resolution of this technique is limited in two dimensions by the resolution of the acquired images and in the third dimension by the precision of FIB milling. These parameters are usually adapted to the size of the sample to perform experiments within a reasonable amount of time. For large samples generally thicker slices are cut and images are acquired at lower resolution, while for smaller samples the resolution can be improved. This technique requires no reconstruction in a classical sense, but it is generally necessary to shift images to be aligned to each other.

While in principle no specific sample preparation is necessary, it is generally advantageous to liberate the region of interest before the beginning of the image acquisition for the experiment. An example of a sample prepared for serial sectioning is shown in Fig. 3.1b. This type of preparation limits the redeposition of removed material on the sample and prevents shielding of detectors by the surrounding material. For image acquisition the FIB column itself can be used to acquire scanning ion microscopy images or secondary ion mass spectroscopy maps. Using the SEM, conventional SEM images can be acquired, but it is also possible to acquire EDS maps or electron backscatter diffraction (EBSD) maps. While for SEM or EDS imaging the geometry of dual-beam systems allows imaging with the SEM and cutting with the FIB without repositioning the sample, for ion-based images or EBSD the sample needs to be rotated between the cutting and imaging steps. For this purpose realignment is necessary after each rotation, which can be done based on pattern recognition of markers as shown in Fig. 3.1b.

FIB/SEM tomography has been used extensively for the investigation of solid-oxide fuel cells (Iwai et al., 2010, Smith et al., 2009, Wilson et al., 2009). Of the available imaging modes, in particular EBSD has gained significant attention, due to its capability of imaging three-dimensional structural material properties (Groeber et al., 2006, Zaefferer et al., 2008). In semiconductor device applications, FIB/SEM tomography is of interest for applications requiring the investigation of volumes in the micrometer range, but at a resolution, which can not be achieved by x-ray tomography. One example is the investigation of copper vias and lines in the interconnect level of integrated circuits (Clement et al., 2011).

3.3 Electron Tomography

Electron tomography refers to tomographic techniques which use contrast mechanisms in a transmission electron microscope as basis for tomographic reconstruction. As electron tomography is the technique mostly applied in this work a detailed description of TEM techniques used for tomography, sample preparation methods and of the principles of reconstruction applied in electron tomography is given in Part II. Here the discussion will be limited to a rough overview of imaging techniques, important technical advances and targeted applications.

Historically the development of electron tomography started around the same time as x-ray computed tomography (De Rosier and Klug, 1968, Hart, 1968, Hoppe et al., 1968). First applications were focused in particular on symmetrical particles (Crowther et al., 1970a,b) but soon the principle was extended to non-symmetrical objects (Hoppe, 1974, Hoppe et al., 1974). The computational problems involved in tomography limited spreading of the technique until the beginning of the 1990s. In this period charge-coupled device (CCD) cameras for electron microscopes and computers capable of tomographic data processing became affordable for a larger community. This lead to automation of image acquisition and data processing and made electron tomography more widely available (Dierksen et al., 1993, 1992, Koster et al., 1992).

Up to the end of the 1990s applications targeted by electron tomography were almost exclusively found in life sciences (Baumeister et al., 1999, Grimm et al., 1997, 1998a,b, Koster et al., 1997), where electron tomography is still an important tool (Anderson et al., 2008, Frank et al., 2002, Leapman et al., 2004). The transfer of the principle to materials science happened relatively late (Koster et al., 2000, Midgley and Weyland, 2003, Midgley et al., 2001, Möbus and Inkson, 2001, Weyland and Midgley, 2003). The main limitation for this step was the need for an imaging technique which fulfils the projection requirement. For biological applications bright-field (BF) TEM imaging can be used as basis for a reconstruction, as the contrast depends on the type and density of material encountered by electrons in the sample. For crystalline samples however diffraction contrast is dominant in BF TEM imaging, which gives a signal strongly dependant on the orientation of the crystal relative to the electron beam, making reconstruction unreliable or even impossible. Electron tomography in materials science was enabled by the introduction of imaging techniques based on the detection of incoherently scattered electrons. These techniques are high-angle annular dark field (HAADF) STEM (Midgley et al., 2001), where electrons scattered incoherently and elastically to large angles are detected and energy-filtered transmission electron microscopy (EFTEM) as well as later also EELS, where incoherently, inelastically scattered electrons are detected (Möbus et al., 2003, Möbus and Inkson, 2001) and EDS where x-rays created in the scattering process are detected.

Another TEM technique, which has been combined with tomography is nanobeam electron diffraction (NBED), to do diffraction tomography (Kolb et al., 2007, 2008, 2011). Diffraction tomography allows reconstruction of local 3D crystallographic information.

Furthermore also 3D imaging of dislocations has been demonstrated by using contrast techniques, which are sensitive to diffraction contrast originating from dislocations, but still fulfil within a good approximation the requirements necessary for tomographic reconstruction. The first technique, which was applied for dislocation tomography was weak-beam dark-field imaging (Barnard et al., 2006a,b) and later it was realized than medium-angle annular dark field (MAADF) STEM imaging using smaller collection angles than in HAADF STEM can provide even better reconstructions of dislocations (Barnard et al., 2010).

Electron tomography has been applied in many fields of materials science. One of the first applications was the study of heterogeneous catalysts (Florea et al., 2010, Grothausmann et al., 2011, Midgley et al., 2001, Ward et al., 2007). Many different types of nanostructures are investigated by electron tomography. It has been used for example for recovery of the shape of tetrapod shaped (Arslan et al., 2006) and octapods shaped particles (Brescia et al., 2011), for investigation of plasmonic nanostructures (Chuntonov et al., 2012, Perassi et al., 2010), palladium nanoparticles (Benlekbir et al., 2009), or hollow nanospheres (Stagg et al., 2011).

Another type of investigated materials are carbonaceous structures, for example the distribution of metallic particles in carbon nanotubes has been analyzed (Ersen et al., 2007), catalyst particles of carbon nanotubes (Bals et al., 2007) or carbon nanotubes inside cells (Porter et al., 2007). Electron tomography has been used for morphological studies in porous structures (Bals et al., 2009, de Jong and Koster, 2002, Shen et al., 2012) and for precipitation studies in metallic alloys and semiconductors (Feng et al., 2011, Hata et al., 2008, Kaneko et al., 2008, Schierning et al., 2011).

Nanowires, in particular semiconductor nanowires are other frequently investigated samples (Hemesath et al., 2012, Tourbot et al., 2011, Verheijen et al., 2007). Tomography is employed to get information about the shape of catalyst particles, as well as about nanowire morphology and chemical composition. Embedded quantum dots have also been observed by electron tomography (Inoue et al., 2009, Wu et al., 2008b). For microelectronics applications several investigations have been done on different types of transistors (Bender et al., 2007, Cherns et al., 2010, Yaguchi et al., 2008), copper interconnects (Ercius et al., 2009, 2006) as well as on rather exotic interconnects based on carbon nanotubes (Ke et al., 2010). Another type of material relevant for microelectronics, where characterization with electron tomography has been attempted are low-κ dielectrics (Huolin et al., 2010, Xin and Muller, 2010).

Advances in electron tomography have been made within the last two decades in improving resolution and in the application of new imaging methods. Concerning imaging methods electron tomography has been extended towards several imaging methods based on inelastic scattering (Goris et al., 2011). The first of these techniques used was EFTEM tomography, in particular in the core-loss range (Florea et al., 2010, Jin-Phillipp et al., 2011, Midgley and Weyland, 2003, Möbus et al., 2003, Möbus and Inkson, 2001). Core-loss EFTEM is chemically sensitive and allows elemental identification. Its drawbacks are long acquisition times in particular for elements with absorption edges at high energy losses, and problems if absorption edges of different elements are located at energy losses close to each other. EFTEM tomography in the low-loss range has been applied for materials, which have little differences in mass, but can be distinguished by their volume plasmons (Gass et al., 2006, Herzing et al., 2010, Yurtsever et al., 2006). Compared to core-loss EFTEM, EFTEM tomography in the low-loss range has the advantage of requiring much shorter image acquisition times, which also allows spectral tomographic imaging (Gass et al., 2006).

EELS is based on the same physical principles as EFTEM, but a full energy-loss spectrum is acquired for each pixel. This generally requires longer acquisition times than EFTEM, even so EELS was combined with tomography for three-dimensional reconstruction (Jarausch et al., 2009, Yedra et al., 2012). Another technique based on inelastic scattering is EDS. In EDS x-rays created by inelastic scattering processes are detected (Kotula et al., 2007, 2006, Saghi et al., 2007). EDS tomography is gaining attention with the recent advent of more efficient x-ray detectors (Lepinay et al., 2013). EDS tomography provides elemental identification in an easily accessible manner, however even with new x-ray detectors acquisition times remain long.

Resolution improvements in electron tomography are based on improved acquisition schemes as well as on advanced reconstruction algorithms. For many years a major problem in electron tomography have been missing wedge artifacts, which refers to artifacts appearing, when a sample can not be tilted over a full tilt range of 180°. This leads to loss of resolution and elongation of sample features in the reconstruction along one direction. To reduce these artifacts dual- and multiple-axis tomography has been introduced, for biological applications (Mastronarde, 1997, Messaoudi et al., 2006, Penczek et al., 1995) as well as for materials applications (Arslan et al., 2006, Sugimori et al., 2005, Tong et al., 2006).

Many samples, in particular FIB-prepared samples can be prepared in needle-shape instead of as a thin lamella, as usual for TEM. This provides advantages as for such needle-shaped samples the sample thickness along the beam path does not increase with the tilt angle. Additionally sample holders have been developed, which allow rotation over a full tilt range of 180° and eliminate the missing wedge in this way (Kawase et al., 2007, Ke et al., 2010).

Recent developments of reconstruction algorithms focus on including prior knowledge about the sample in the reconstruction process and improving the resolution in this way. The first such technique, which was employed in electron tomography is discrete tomography (Bals et al., 2009, 2007, Batenburg et al., 2009, Jinschek et al., 2008). In discrete tomography it is assumed that only a limited number of discrete grey levels exist in the reconstruction, in the simplest case only two levels.

Compressed-sensing based reconstruction is based on similar ideas as discrete tomography. Mathematically it is founded on the sparsity of signals. It assumes that either the reconstruction itself or more frequently a transformation, e.g. the gradient of the reconstruction consists mostly of zero values (Goris et al., 2012b, Saghi et al., 2011). If sparsity of the gradient is assumed, this technique is referred to as total-variation minimization reconstruction. It assumes the grey-levels of the reconstruction to be locally constant, an assumption closely related to discrete tomography.

Based on discrete tomography and total-variation minimization techniques atomic resolution tomography has been demonstrated. The first demonstrations were based on discrete schemes, in combination with very strong prior assumptions about the object (Bals et al., 2010, Van Aert et al., 2011). With more relaxed assumptions near-atomic resolution has been demonstrated on polycrystalline samples (Scott et al., 2012) and atomic resolution based on compressed-sensing in single-crystalline samples (Goris et al., 2012a). All these demonstrations have in common that very small particles consisting of strongly scattering materials have been investigated.

3.4 Atom Probe Tomography

Atom probe tomography has its origins in field ion microscopy. In atom probe tomography atoms are ionized from the surface of a tip-shaped sample located in ultrahigh vacuum (Blavette et al., 1993, Kelly and Miller, 2007, Miller and Forbes, 2009). A high voltage is applied, which leads to a very high electric field at the apex of the needle. This ionizes atoms on the surface, which are projected towards a position-sensitive detector. From the position of the ions impact on the detector the original position of the atom can be reconstructed. The atom can be identified by time of flight mass spectroscopy from the time difference between the evaporation event and the impact on the ion on the detector.

Classically in atom probe tomography a pulsed voltage is used, which causes evaporation by an electric field. This technique works well for good conductors, in particular metals have been extensively studied by this method (Blavette et al.,

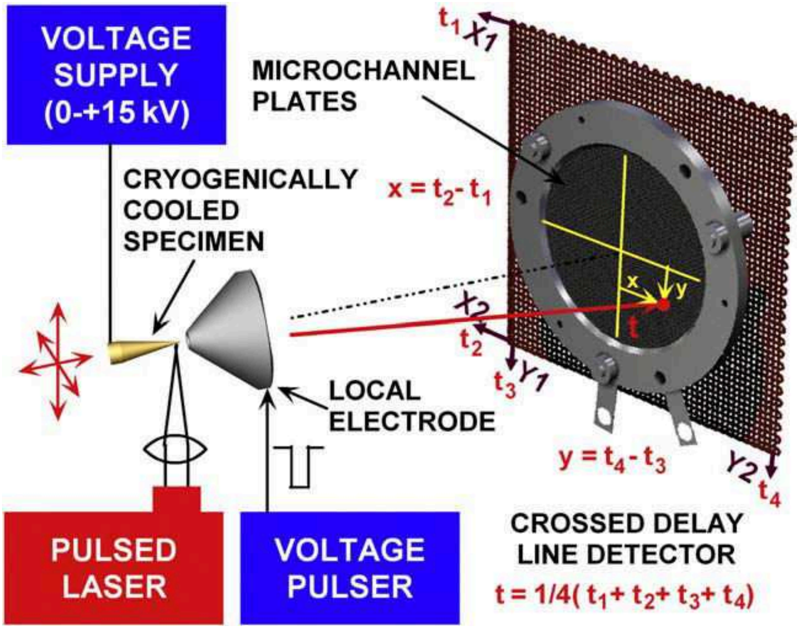

Figure 3.2: Schematic of a laser-assisted atom probe (Miller and Forbes, 2009).

1996, Miller et al., 2005a, 2003). For semiconductors or insulators pure electric field evaporation does not work, which lead to the development of laser-assisted atom probe tomography. In this technique a constant voltage is applied on the sample and short laser pulses are used to evaporate atoms from the tip. An example of a laser-assisted atom probe is shown in Fig. 3.2. Evaporation in this case is assumed to be driven mostly by thermal excitation though other mechanisms can also play a role (Gault et al., 2007).

While earlier applications of atom probe tomography were mostly concerned with metals, due to their good electrical conductivity, since the introduction of laser-assisted atom probe tomography, this technique has received significant attention within the semiconductor community (Lauhon et al., 2009, Thompson et al., 2005). Nanowires have been investigated (Perea et al., 2005, 2008) and for electron devices, in particular for transistors the perspective of three-dimensional detection of the position of dopant atoms is of considerable interest (Inoue et al., 2009, Kambham et al., 2011, Ronsheim et al., 2010)

Though in principle atom probe tomography inherently provides atomic resolution, the resolution is reduced to some degree by uncertainties and artifacts. One limitation is the efficiency of detectors, which usually detect around 60% of all atoms. Sample fracture is another issue, which seriously limits the number of successful experiments. Another limitation are reconstruction uncertainties, in particular for complex samples, consisting of several materials: If materials have different evaporation properties the shape of the tip no longer has a uniform radius, as is generally assumed for atom probe tomography. This leads to an uncertainty about the original position of a detected atom, which introduces distortions in the reconstruction. Considerable effort is currently put into understanding and correcting these artifacts. While simulations and modelling are one important point, another contribution towards improving atom probe results is the correlation with other techniques. In particular combined electron tomography and atom probe tomography is an exciting perspective (Arslan et al., 2008). Electron tomography can provide reliable three-dimensional geometric information, as resolution limits and artifacts are rather well understood, while atom probe tomography provides excellent chemical sensitivity.

3.5 Conclusion

In this chapter an overview of different techniques for 3D micro- and nanoscale characterization was given. The choice of a characterization technique for a specific application depends on many different factors. The size of the sample and its composition determine whether a technique is applicable or not. The spatial resolution needs to be high enough to retrieve the required detail quality. The type of information, whether chemical, structural or just geometrical information is required will determine the used imaging mode. In this context electron tomography is currently the most reliable technique for 3D morphological characterization at the nanoscale. A large range of materials can be analyzed and success rate is relatively high, compared in particular to atom probe tomography. Contrast between different materials can be an issue, but eventually the imaging mode can be adapted to the materials. Reconstruction artifacts can be another issue, but for complex material systems their effect is smaller than in atom probe tomography. By contrast for acquiring 3D nanoscale chemical information, atom probe tomography is generally better suited than electron tomography. Altogether the discussed techniques build up a large framework of methods for 3D material characterization, which will be continuously extended towards the utopic goal of identifying and locating each single atom (or its components) in a millimeter- (or meter-) sized sample.

Part II

Experimental Methods

4 Principles of Tomography

Tomography in its classical sense deals with the reconstruction of a three-dimensional (3D) object from its two-dimensional (2D) projections, which are measurements of some physical, chemical or other property of the sample integrated over straight lines through the object. Electron tomography is a tomographic technique in this classical sense, the same as x-ray tomography. Other techniques, referred to as tomography are not, notably atom probe tomography or focused ion beam (FIB)/scanning electron microscopy (SEM) serial sectioning. For this classical type of tomography the problem of reconstruction consists of recovering the original 3D parameters of the investigated sample from the measured 2D projections. This chapter deals with the formulation of this problem and different approaches to solve it. While the mentioned methods are applicable to several types of tomography, this chapter concentrates on the techniques, which are relevant for electron tomography in a transmission electron microscope. Detailed descriptions about principles of tomography and reconstruction can be found for example in (Frank, 2005, Kak and Slaney, 1987).

4.1 Projections and the Radon Transform

For the mathematical formulation of tomographic problems, line integrals are used. These describe the integral over some function, which depends on parameters of the object, over a straight lines through the object. Line integrals can be defined through 3D representations of the object, for the following considerations 2D cases are considered, which can represent a slice through the 3D object.

The formulation of a line integral through an object, represented by the function $f(x, y)$, is given for the parameters θ and t (Kak and Slaney, 1987). These parameters define the line as

$$x \cos(\theta) + y \sin(\theta) = t \tag{4.1}$$

This is illustrated in Fig. 4.1a. The line integral along such a line is then defined as

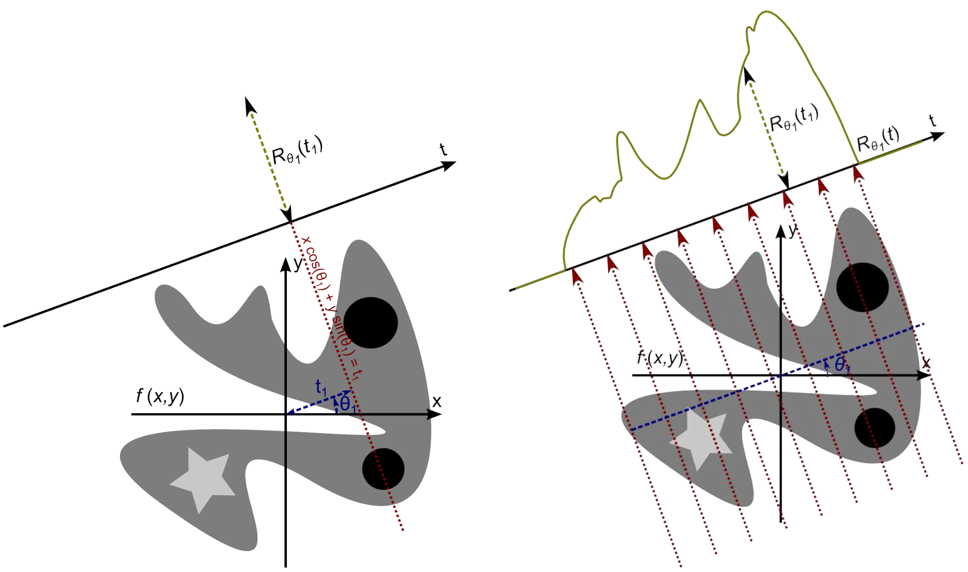

(a) **(b)**

Figure 4.1: (a) Line integral $R_{\theta_1}(t_1)$ through an object $f(x,y)$. (b) Parallel projection $R_{\theta_1}(t)$ of an object $f(x,y)$ constituted of a set of line integrals.

$$R(\theta,t) = \int_{(\theta,t)line} f\,(x,y)\,ds \tag{4.2}$$

This function is the Radon transform. It was first formulated by the Austrian mathematician Johann Radon in 1917 (Radon, 1917). The Radon transform maps data from its real space representation in (x,y)-coordinates to its Radon transform in (θ,t)-coordinates. From the Radon transform a projection can be defined as a collection of several line integrals. In the case of electron tomography the relevant type of projections are parallel projections. Many imaging techniques in the transmission electron microscope (TEM) provide such parallel projections, at least to a good approximation. In a parallel projection source and detector have the same size and each projection consists of line integrals at a constant θ with several values for t. An example of such a parallel projection is shown in Fig. 4.1b. Several other types of projections exist like fan-beam or cone-beam projections, but as they are of no relevance for electron tomography, only parallel projections are considered.

4.2 The Central Slice Theorem

The central or Fourier slice theorem gives a relationship between the Radon transform and the Fourier transform of an object and has great importance for all reconstruction procedures. The central slice theorem is illustrated in Fig. 4.2.

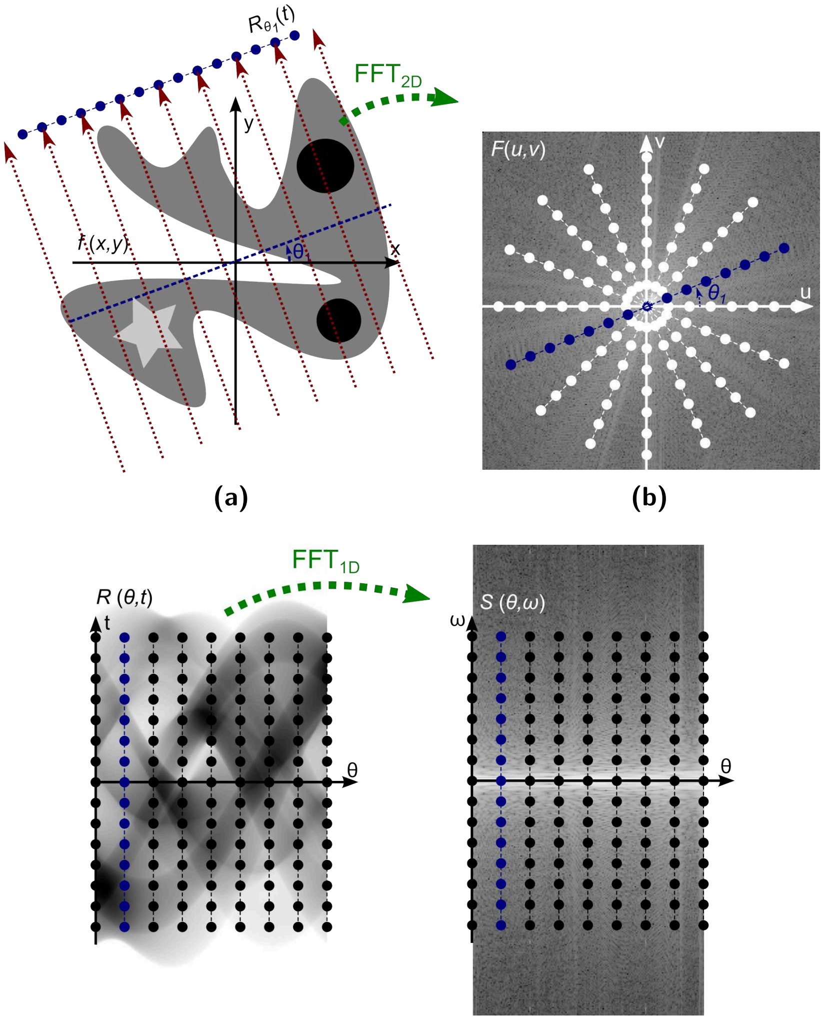

(a) **(b)**

(c) **(d)**

Figure 4.2: Central slice theorem: (a) 2D object $f\,(x, y)$, (b), 2D Fourier transform $F(u, v)$ of (a), (c) projections $R(\theta, t)$ of the 2D object (a), (d) 1D Fourier transform $S\,(\theta, w)$ of the projections (c) along the direction t. The 1D Fourier transform $S\,(\theta_1, w)$ of a projection $R_{\theta_1}(t)$ is equal to a central slice through the 2D Fourier transform $F(u, v)$ of the object $f(x, y)$ lying at an angle θ_1 to the u-axis.

With the two-dimensional Fourier transform $F(u,v)$ of an object $f(x,y)$ defined as

$$F\left(u,v\right)=\int_{-\infty}^{\infty}\int_{-\infty}^{\infty}f\left(x,y\right)e^{-j2\pi(ux+vy)}dxdy \tag{4.3}$$

and the Fourier transform $S(\theta,w)$ of a projection $R(\theta,t)$

$$S\left(\theta,w\right)=\int_{-\infty}^{\infty}R(\theta,t)e^{-j2\pi wt}dt \tag{4.4}$$

it can be shown that the Fourier transform of a projection at an angle θ is equal to a central slice through the 2D Fourier transform of the object, which is lying at the same angle θ to the u-axis (Kak and Slaney, 1987):

$$S\left(\theta,w\right)=F\left(w\cos\theta,w\sin\theta\right) \tag{4.5}$$

In this way projections acquired at different tilt angles give information about the Fourier transform of the object along central slices. If enough projections are acquired the full information about the object can be recovered.

From these considerations it can be understood that in principle the reconstruction can be done by an inverse Fourier transform in two dimensions. Such methods are known as direct Fourier reconstruction methods (Stark et al., 1981). However this requires an interpolation in Fourier space to transform the discrete data from polar coordinates to Cartesian coordinates, which can cause errors. It is therefore generally preferred to reformulate the problem in a way which requires an interpolation in real space rather than in Fourier space.

4.3 Backprojection Operations

Starting from the formula for the inverse Fourier transform

$$f\left(x,y\right)=\int_{-\infty}^{\infty}\int_{-\infty}^{\infty}F\left(u,v\right)e^{j2\pi(ux+vy)}dudv \tag{4.6}$$

substitution of the Cartesian coordinates for polar coordinates gives

$$f\left(x,y\right)=\int_{0}^{2\pi}\int_{-\infty}^{\infty}F\left(w,\theta\right)we^{j2\pi wt}dwd\theta \tag{4.7}$$

t has been defined previously in (4.2).

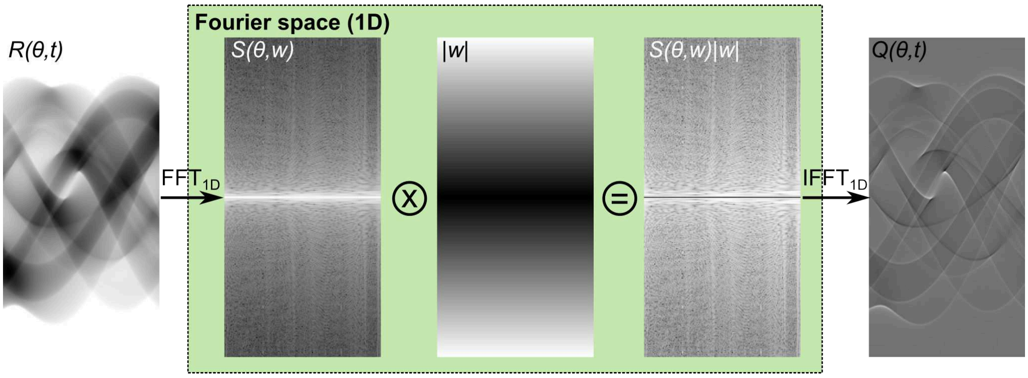

Figure 4.3: Filtering of a sinogram with a ramp-filter in Fourier space.

As the projections from 0° to 180° are equal to the projections from 180° to 360° and using the central slice theorem (4.7) can be written as

$$f\left(x,y\right)=\int_{0}^{\pi}\int_{-\infty}^{\infty}S\left(w,\theta\right)\left|w\right|e^{j2\pi wt}dwd\theta \tag{4.8}$$

This is the basic formula for the weighted backprojection (WBP) or filtered backprojection (FBP). The operation can be split up into two parts. The inner, filtering operation is defined as

$$Q\left(\theta,t\right)=\int_{-\infty}^{\infty}S\left(w,\theta\right)\left|w\right|e^{j2\pi wt}dw \tag{4.9}$$

which provides $Q\left(\theta,t\right)$, the filtered projection, which is filtered in Fourier space by a ramp filter given by $|w|$. This operation of filtering the projections is illustrated in Fig. 4.3. The necessity of filtering can be also intuitively seen in the Fourier domain (see Fig. 4.2b). As the data is sampled more densely at low frequencies, close to the center of the Fourier space, weighting is necessary to equalize the impact of different frequency components.

The outer operation is the backprojection, which can be written as

$$f\left(x,y\right)=\int_{0}^{\pi}Q\left(\theta,x\cos\left(\theta\right)+y\sin\left(\theta\right)\right)d\theta \tag{4.10}$$

The backprojection is illustrated in Fig. 4.4. In the backprojection operation the filtered projections for all angles are summed to reconstruct an estimate of the original object $f\left(x,y\right)$. Each filtered projection will contribute equally to all points, which are on lines through the object in the direction of this projection.

Though for the case of continuous signals the filtered backprojection using a ramp-filter is mathematically exact, for practical discrete cases it often needs to be adapted. In practice only limited often noisy data is available. For this purpose

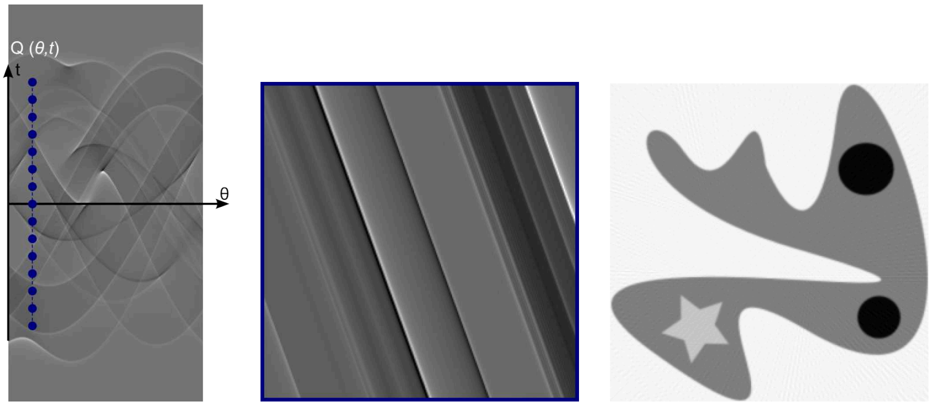

(a) (b) (c)

Figure 4.4: Filtered backprojection: (a) Filtered sinogram, (b) filtered backprojection of one projection, (c) filtered backprojection from all projections.

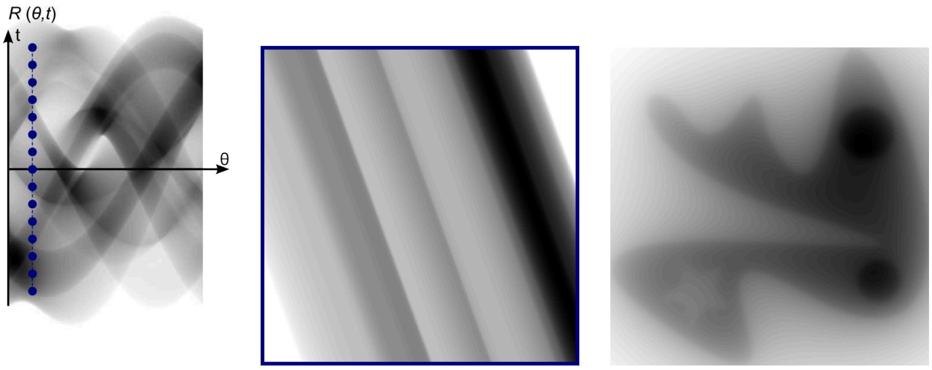

(a) (b) (c)

Figure 4.5: Unfiltered backprojection: (a) Unfiltered sinogram, (b) unfiltered backprojection of one projection, (c) unfiltered backprojection from all projections.

the filter can be adapted to reduce high frequency noise, or iterative reconstruction methods can be used. In particular also an unfiltered backprojection operator (usually referred to simply as backprojection) can be useful. This operator is formulated as

$$f\left(x,y\right)=\int_{0}^{\pi}R\left(\theta,x\cos\left(\theta\right)+y\sin\left(\theta\right)\right)d\theta \tag{4.11}$$

with $R\left(\theta,t\right)$ being the unfiltered projections of the object. Fig. 4.5 illustrates this operation. It can be clearly seen that low frequency contributions to the signal are overestimated, due to the absence of a filter, which directly transfers the dense sampling in the central part of the Fourier domain to the reconstruction.

Though the backprojection operation cannot correctly reconstruct the original object it is often useful, in particular in combination with iterative reconstruction algorithms. The operation allows a stronger weighting of low-frequency components,

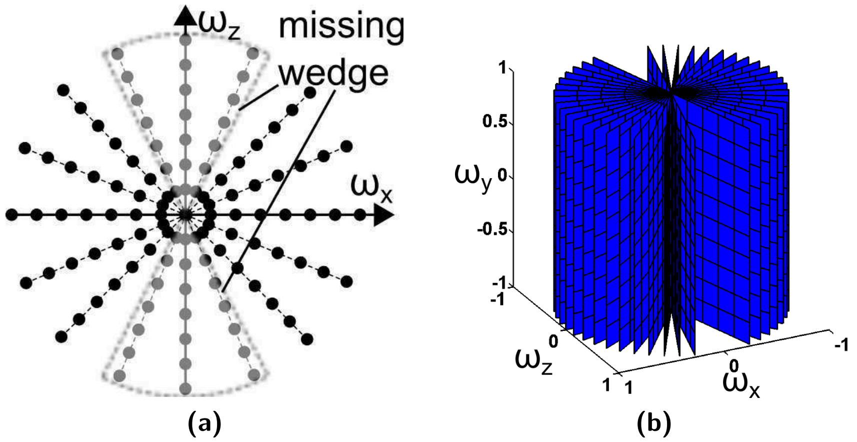

Figure 4.6: (a) Sampling in 2D Fourier space, (b) sampling in 3D Fourier space.

which can be used in the initial reconstruction and can then be corrected using high frequency contributions up to the amount of available data. Such iterative algorithms reduce artifacts due to missing information, which cause high frequency contributions to the reconstruction. These artifacts and algorithms will be discussed in the next sections.

4.4 Resolution and Artifacts

The central slice theorem allows estimating the possible resolution in tomography and understanding artifacts, which appear in the reconstruction. An important point about the resolution in tomography is that it is generally anisotropic. It is different along different directions of space and depends on the original resolution of the imaging technique as well as on acquisition parameters of the projections. In this section, we will consider only the effect of acquisition parameters, such as the number of projections, on the resolution of the reconstruction. The resolution of the imaging techniques is discussed in the corresponding sections.

For this simplified approach, we assume that the resolution of the individual projections is limited only by their pixel size. Projections with an image size $W \times W$ and a number of pixels $N \times N$ along both dimensions have therefore a 2D resolution of one pixel $(W/N)^2$. In the optimal case the reconstruction can then have the same resolution as the projections along all three dimensions.

From the central slice theorem we know, that each projection provides information on a central slice through the 3D Fourier transform of the object. Fig. 4.6 shows schematically the sampling of the Fourier space by a typical electron tomography experiment. Recovery of the information of the object with a resolution equal to the resolution of the projection requires that the spacing between central slices is smaller than the voxel size of the 3D Fourier transform of the objects at least in the central sphere of the Fourier transform. To fulfil this criterion the number of projections n_{proj} necessary for reconstructing a volume of the size $N \times N \times N$ from projections of the size $N \times N$ with the same resolution as the projections is

$$n_{proj} = \frac{N * \pi}{2} \tag{4.12}$$

The projections need to be equally spaced over a range of 180°. For projections with a size of 1024 × 1024 pixels therefore 1600 projections would be necessary to fulfil this criterion.

While for example in x-ray tomography it is feasible to acquire such a large number of projections, in electron tomography this is practically impossible. Limitations arise due to beam sensitivity of the samples, due to precision of the sample stage as well as due to time restrictions. In practice projections are typically acquired every degree or every few degrees, giving 180 projections or less. A resolution limit is given by the Crowther criterion (Crowther et al., 1970b) for the resolution in the xz-plane without a missing wedge[1]. The resolution can be estimated by the spacing of the central slices through the number of projections n_{proj} as well as by the diameter of the object D as

$$d_x = \frac{D * \pi}{n_{proj}} \tag{4.13}$$

It should be noted however that the resolution depends also on the shape and orientation of the object. Eventually higher resolution could be achieved, if the spatial frequencies composing the object happen to match the information sampled by the projections. Fig. 4.7a illustrates the effects of the limited number of projections for the reconstruction of a circle.

Another limitation in the resolution of electron tomography arises from the so-called missing wedge. Due to the geometry of the sample or the sample holder it is often not possible to tilt the sample over a full tilt range of 180°. This leads to missing projections in a part of the tilt range and in consequence to missing information in a wedge-shaped part of the Fourier domain (see Fig. 4.6). This missing information leads to an elongation of features in the reconstruction in the direction of the missing wedge. The impact of missing wedge artifacts depends on the missing tilt range and on the size of features in the direction perpendicular to the missing wedge. Fig. 4.7b illustrates the effects of the missing wedge for the reconstruction of a circle.

---

[1] In this thesis the direction of the tilt axis is denoted with y. z is the direction of the electron beam at 0° tilt. x is perpendicular to y and z.

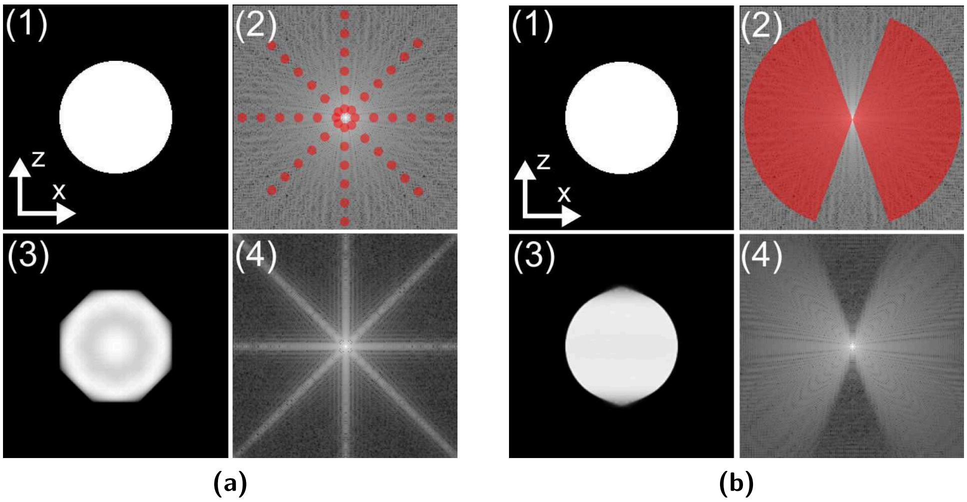

Figure 4.7: Effects of (a) limited number of projections (4 projections) and (b) missing wedge (range ±70°) in a reconstruction of a circle. Images show (1) original images, (2) FFT of the original images and Fourier domain covered by the projections, (3) reconstructions from projections taken as indicated in (2) using a SIRT algorithm (see Section 4.5), (4) FFT of the reconstructions.

To quantify the impact of the missing wedge on resolution frequently an elongation factor, first introduced by Radermacher, is used (Radermacher, 1988). In his work he used the point spread function to calculate an elongation factor, which gives the elongation of a single point in the reconstruction in the direction of missing wedge (z-direction). This elongation factor can be calculated as

$$e_{xz} = \sqrt{\frac{\alpha + \sin\alpha\cos\alpha}{\alpha - \sin\alpha\cos\alpha}} \tag{4.14}$$

for a maximum tilt angle α expressed in radians. Based on this elongation factor Radermacher gives the degradation of the resolution z-direction as a function of the resolution in the x-direction as

$$d_z = e_{xz} d_x \tag{4.15}$$

an estimation frequently reproduced in literature. As example for a tilt range of ±70° this would give an elongation factor of 1.3, indicating that in the direction of the missing wedge resolution is only slightly worse than outside of the missing wedge. Furthermore this resolution estimation suggests, that improving the resolution in the x-direction, for example by using a large number of projections, leads to resolution improvements in the z-direction, affected by the missing wedge. From practical experience it is well known that this is not the case and that the resolution of features affected by missing wedge artifacts is frequently much worse than given by Radermacher's estimation, in particular for features having high aspect-ratio.

Eventually the error in Radermacher's estimation lies in concluding from the elongation of the point-spread function to the degradation in the resolution. Such a conclusion would require linearity. However while forward projection is a linear operation – the projection of two objects being equal to the sum of the individual projections – the reconstruction operation is generally not linear, at least in the case of limited data. The sum of the reconstructions from two different sets of projections is not necessarily equal to the reconstruction from the sum of the sets of projections. What can actually be derived from the elongation factor is the elongation of a circle relative to its diameter in the z-direction (see Fig. 4.7b).

To re-examine considerations on resolution an useful approach is to consider the sampling of an object in 3D Fourier space by its 2D projections taken around a single tilt axis (see Fig. 4.6b). First of all the missing wedge has an impact on all features with dominating frequency components in the z-direction. These can not be reconstructed correctly and will be reconstructed with an additional frequency component in the x-direction. The worst resolution will appear for thin lines or planes oriented in the x-direction. Depending on its size along the x-direction s_x with the maximum tilt angle α such an object will be elongated to

$$e_z = \frac{s_x}{\tan\alpha} \tag{4.16}$$

in the z-direction as can be estimated from geometrical considerations. As an example $\alpha = 70°$ and $s_y = 100\text{nm}$ lead to $e_z = 30\text{nm}$. This is illustrated for a simulation in Fig. 4.8.

Features with high frequency components along the xz-plane can loose resolution depending on the spacing between the different slices caused by the limited number of projections. This is illustrated in Fig. 4.9. In the y-direction the resolution is independent of the spatial frequency. The quality of the reconstruction depends therefore only on the x- and z-frequency components. Features with low spatial frequency components along these directions can be therefore reconstructed with the original image resolution along the y-direction.

4.5 Iterative Reconstruction Techniques

The most commonly used reconstruction algorithms in electron tomography are iterative algebraic reconstruction methods, most frequently the simultaneous itera-

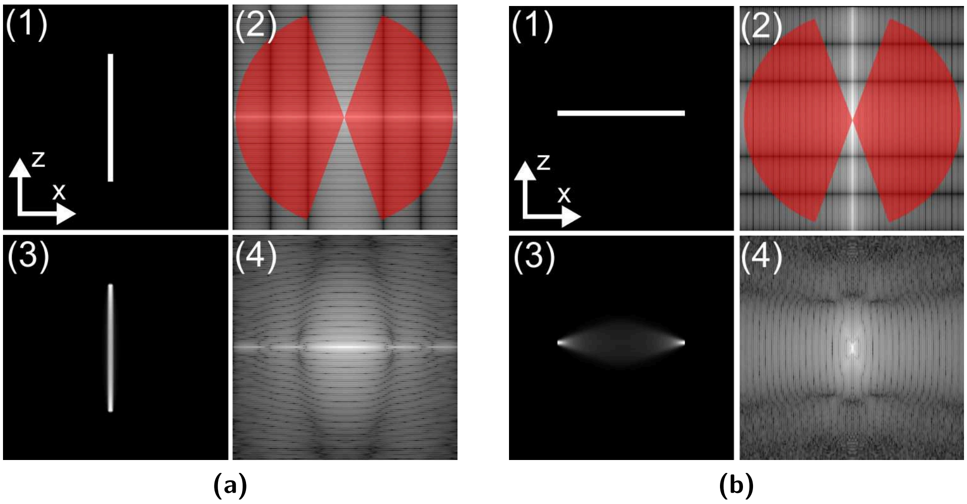

Figure 4.8: Effects of the missing wedge in a reconstruction of a thin line (a) oriented favorable with respect to the missing wedge, (b) oriented not favorable with respect to the missing wedge. Images show (1) original images, (2) FFT of the original images and range of Fourier domain covered by the projections, (3) reconstructions from projections taken with a step of 1° over a range of ±70° as indicated in (2) using a SIRT algorithm (see Section 4.5), (4) FFT of the reconstructions.

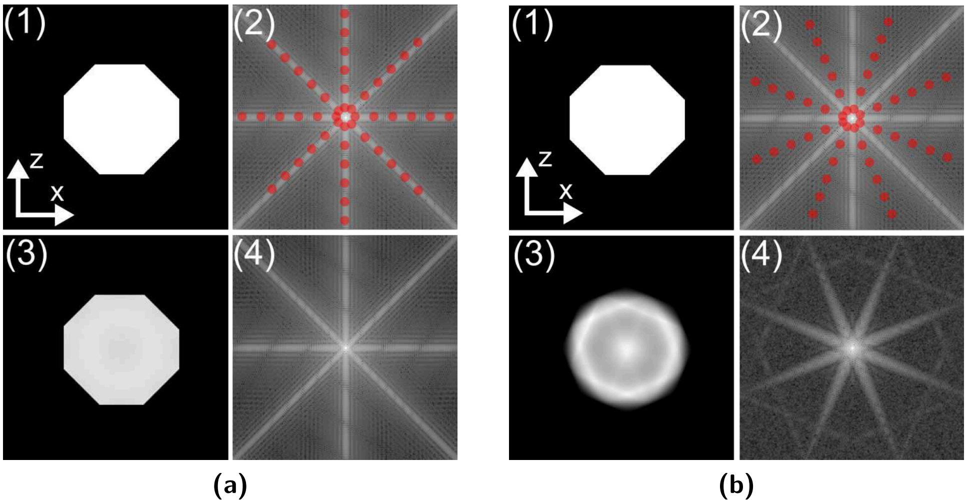

Figure 4.9: Effects of the limited number of projections (a) for projections acquired at tilt angles favorable for the reconstruction, (b) for projections acquired at tilt angles not favorable for the reconstruction. Images show (1) original images, (2) FFT of the original images and sampling by 4 projections used for the reconstruction, (3) reconstructions from projections as indicated in (2) using a SIRT algorithm (see Section 4.5), (4) FFT of the reconstructions.

tive reconstruction technique (SIRT) (Gilbert, 1972), less frequently the algebraic reconstruction technique (ART) (Gordon et al., 1970) as well as variants of these techniques such as simultaneous algebraic reconstruction technique (SART). These algorithms are generally less sensitive to noise than weighted backprojection and reduce the impact of artifacts from limited number of projections and missing wedge in the reconstruction.

Algebraic methods are based on setting up a system of equations, which links the unknown object data to the measured projections (Kak and Slaney, 1987). The object, or image $f(x, y)$ consists of j pixels (or voxels) f_j, each of which is assumed to be constant. Through these pixels rays are defined, the sum over each ray p_i is the result of a linear equation. The system of equations given by all ray sums can be written as

$$\sum_{j=1}^{N} w_{ij} f_j = p_i \tag{4.17}$$

where w_{ij} are weighting factors. To calculate the weighting factors, one possibility is assume rays with a thickness corresponding to the size of a pixel of the detector. The weighting factors then denote the area of an image pixel, which is intercepted by a ray. Most of these factors are zero.

To solve this equation system an iterative algorithm is applied. At each iteration n the value of each pixel $f_j^{(n)}$ is updated based on its current value $f_j^{(n-1)}$ with a calculated *difference reconstruction* value $\Delta f_j^{(n)}$ as

$$f_j^{(n)} = f_j^{(n-1)} + \lambda \Delta f_j^{(n)} \tag{4.18}$$

where λ is a relaxation factor, which affects the convergence speed and stability (Herman and Lent, 1976). $\Delta f_j^{(n)}$ is calculated from the values of all pixels $f_k^{(n-1)}$ for each projection value p_i with

$$\Delta f_j^{(n)} = \frac{p_i - q_i}{\sum_{k=1}^{N} w_{ik}^2} w_{ij} \tag{4.19}$$

where

$$q_i = \sum_{k=1}^{N} f_k^{i-1} w_{ik} \tag{4.20}$$

In these equations q_i are the sums along a ray through pixels in the current iteration. These are compared to the measured ray sums p_i. This gives a *difference projection*, which is normalized by the weighting factors over the ray with $\sum_{k=1}^{N} w_{ik}^2$ and by the weighting factor of the corresponding pixel w_{ij}. It should be noted that in principle the calculation of the ray sums q_i is a Radon transform, while the calculation of the normalized differences Δf_j is an inverse Radon transform.

Different types of algebraic algorithms are distinguished by the moment, when the pixels f_j are updated. (4.19) actually provides a difference reconstruction Δf_j^i for each pixel f_j from each projection value p_i. In ART the update is done for each projection using the sum of the difference projections from all detector pixels. One iteration of an ART update is finished, when all projections have been used to update the reconstruction one time. Updating the estimate after each projection is advantageous in terms of convergence speed, however it is more sensitive to noise in the projections. Approximations, which are generally used for the weighting factors w_{ij} can introduce *salt and pepper* noise, noise and errors of single projections are directly transferred to the reconstruction. Furthermore projections, which are used for the update at the end of an iteration generally have a larger impact on the reconstruction than projections, which have been used earlier. This is in particular an issue, when the single projections are used in the order of the tilt angles, so frequently random or alternating orders are used.

An algorithm, which is more robust than ART is SIRT. In SIRT the pixels of the reconstruction are updated using all projections at once. For this purpose from each projection the changes Δf_j^i for each pixel j from each equation i are calculated. The update of the individual pixel is done only after all changes for all projections have been calculated, by a mean value of the changes calculated for each pixel from each projection. Eventually instead of calculating the difference between the measured and calculated projections, also their quotient can be used to calculate the *difference projection*. The update by the *difference reconstruction* is then done with a multiplication.

Fig. 4.10 illustrates the principle of a SIRT algorithm with a multiplicative update. First the reconstruction is initialized. In the present case this is done with a simple backprojection, but eventually the reconstruction can be also initialized with a constant value for all pixels. This *initial reconstruction* is used as first *temporary reconstruction* in the iterative loop. The ray sums q_i, the *re-projections* of the *temporary reconstruction* are calculated by a Radon transform. These are compared to the measured ray sums p_i, the acquired *tilt series*, to get the *difference projections*. From these difference projections the changes Δf_j for each pixel, the *difference reconstruction* is calculated. The *temporary reconstruction* is updated with the *difference reconstruction*. In this work for most reconstructions a SIRT algorithm with a multiplicative update was used with 20 to 30 iterations.

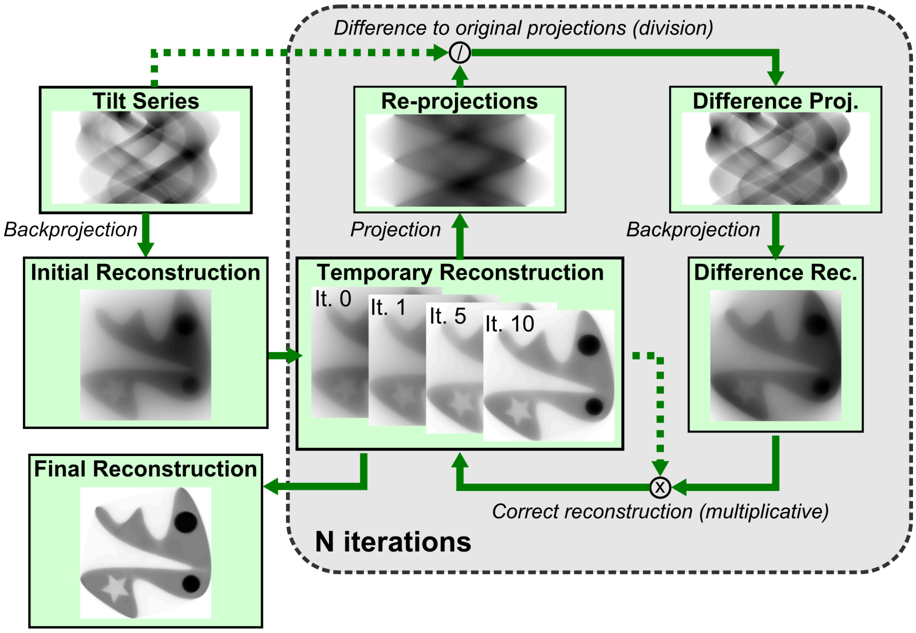

Figure 4.10: Principle of the SIRT algorithm.

4.6 Constrained Reconstruction Techniques

In electron tomography generally the number of unknowns is larger than the number of measurements, so the reconstruction represents an underdetermined problem, which does not have a unique solution. Algebraic reconstruction techniques are generally designed to treat these uncertainties using the available measurements for filling up the information about the object from low spatial frequencies to higher spatial frequencies as far as information is available. This provides relatively smooth reconstructions, which suffer however from a limited resolution. To improve the resolution, prior knowledge can be introduced as constraints in the tomographic problem. Two techniques using prior knowledge have received significant attention for electron tomography applications, which are discrete tomography and compressed sensing based tomographic reconstruction. Discrete tomography directly introduces constraints to the reconstruction, while compressed sensing is based on minimizing a feasible norm calculated from the reconstruction.

4.6.1 Discrete Tomography

Discrete tomography is based on the assumption that the investigated object contains only a discrete number of grey levels (Herman and Kuba, 1999). This is an assumption, which is often valid in materials science, as frequently relative large parts of a volume consist of the same material. The number and values of these grey levels are used as constraints for the reconstruction. A practical implementation of a discrete scheme is for example given in (Batenburg et al., 2009). In this case SIRT is used as basis for the reconstruction. After a certain number of SIRT iterations the reconstruction is discretized by using thresholds between the different discrete grey levels. In the discretized reconstruction boundary pixels are identified, which are subject to new SIRT iterations, while non-boundary pixels are kept constant. After a certain number of new SIRT iterations these boundary pixels are again discretized and new boundary pixels are identified, finishing one iteration of the discrete algorithm.

Discrete reconstruction is of particular interest for reconstruction from very limited data, where only a small number of projections are available. Practically the prior definition of the grey values can be problematic, it is generally based on a non-discrete reconstruction, which is done before starting the discrete algorithms. Discrete tomography can not reconstruct small differences between different regions, which could represent for example changes in the relative concentration of a composite material.

4.6.2 Compressed Sensing

Compressed sensing is based on the assumption that a signal or the transformation of a signal is sparse (Candes et al., 2006, Candes and Wakin, 2008, Donoho, 2006). This signal f is observed by a measurement p, with A being a linear mapping matrix as

$$Af = p \tag{4.21}$$

In tomography f is the image or volume containing all pixels (or voxels), p are the values of all acquired projections, the linear equation system for tomography has been defined in (4.17). If $\dim(p) < \dim(f)$ the system is underdetermined, allowing an infinite number of possible solutions. In compressed sensing it is assumed that f is sparse, and therefore the optimal solution for f can be found by minimizing its l_1-norm as

$$\min \|f\|_1 = \min \sum_i f_i \tag{4.22}$$

In electron tomography the l_1-norm has been directly applied to the volume for reconstruction with atomic resolution, as for this purpose it can be assumed that most of the values of f are zero, c.f. do not contain an atom (Goris et al., 2012a). More frequently however not f itself, but rather its gradient is assumed to be sparse


(a) **(b)**

Figure 4.11: Illustration of the sparse gradient assumption: (a) Sheep-Logan phantom and (b) its gradient. The gradient image is a sparse matrix.

(Goris et al., 2012b, Saghi et al., 2011). This can be written with $f(x, y)$ being an image represented in pixels as

$$\min \|f\|_{TV} = \min \left(\sum_{x,y} \sqrt{\frac{\partial f(x,y)}{\partial x}^2 + \frac{\partial f(x,y)}{\partial y}^2} \right) \tag{4.23}$$

This is also known as total variation (TV)-minimization. A sparse gradient image assumes a piecewise constant image $f(x, y)$. This assumption is illustrated in Fig. 4.11 for the case of a Sheep-Logan phantom. This is an assumption closely related to discrete tomography, however it is not necessary to define the number of grey levels and their values. Additionally TV-minimization does not necessarily force the reconstruction to discrete values, but prefers these solution, if multiple solutions are available. Eventually, if enough measurements are acquired, TV-minimization should be also able to reproduce non-discrete objects.

Practical approaches to minimize the TV-norm most frequently solve either the problem

$$\min \|f\|_{TV} \;\; s.t. \; Af = p \tag{4.24}$$

or the problem

$$\min \|f\|_{TV} + \frac{\mu}{2} \|Af - p\|_2^2 \tag{4.25}$$

where μ is a regularization parameter. The second formulation has advantages as μ can be set accordingly to suppress noise present in the projections, though too low values of μ can lead to loss of high frequency information.

It should be noted though, that while TV-minimization works usually perfectly for simulations with low noise level, it has been also shown that it can loose information

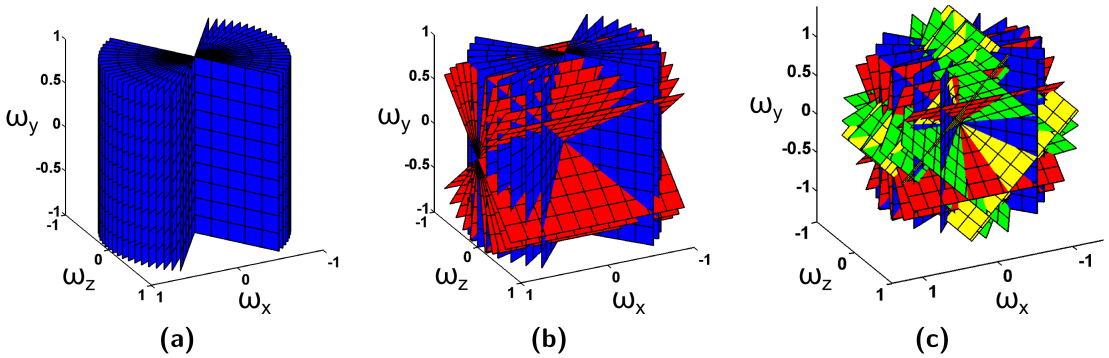

Figure 4.12: Sampling of the Fourier domain by different acquisition schemes: (a) single-axis tomography, (b) dual-axis tomography, (c) multiple-axis tomography using four tilt axes.

in the case of projections with higher noise levels, as compared to conventional reconstruction techniques (Herman and Davidi, 2008).

Apart from the signal itself or its gradient also other transformations of the signal can be assumed to be sparse. In classical image processing often the wavelet transform of an image is assumed to be sparse, such algorithms are being used for image recovery (Candes and Wakin, 2008).

4.7 Dual- and Multiple-Axis Tomography

Dual- and multiple- axis tomography are being principally used to reduce effects of missing wedge artifacts. For dual-axis tomography, after acquisition of a first tilt series the sample is rotated by 90° in the plane perpendicular to the direction of the electron beam to acquire a second tilt series around a second axis (Mastronarde, 1997, Penczek et al., 1995, Tong et al., 2006). For multiple-axis tomography several rotations in the plane perpendicular to the electron beam are done between the acquisition of the different tilt series (Messaoudi et al., 2006). The impact of using two or more axis can be best understood by considering sampling in the Fourier domain. Fig. 4.12 compares sampling by single-axis, dual-axis and multiple-axis tomography. It can be seen that in dual-axis tomography the missing wedge is reduced to a missing pyramid, in the case of multiple-axis tomography it is reduced even further towards the shape of a missing cone. Practically this has the advantage that the resolution degradation by the missing data affects only features which are small in the z-direction, and large in both the x- and the y-direction, while if they are small in either the x- or the y-direction they can be well reconstructed. As discussed previously, in single-axis tomography features need to be small in the x-

direction to be well reconstructed in the z-direction, the size in y-direction does not have an impact on the resolution in the z-direction.

Several methods exist for the reconstruction of tilt series acquired in a dual-axis scheme. The first applications used simple real-space combination of the two individual reconstructed series (Penczek et al., 1995), later it was realized that combination in Fourier-space generally works better than real-space combination (Mastronarde, 1997). In particular it allows using only the information of one tilt series, in parts of the Fourier domain, which lie in the missing wedge of the other tilt series. Finally the two tilt-series can be also combined directly in the reconstruction by combination with iterative reconstruction algorithms. As such an alternating dual-axis SIRT algorithm has been proposed, which uses the two tilt-series alternating in each iteration (Tong et al., 2006) and in this work we will describe a combined dual-axis SIRT algorithm, which uses both series at the same time (see Chapter 9).

Apart from the reduction of missing wedge artifacts, dual- and multiple-axis tomography changes the sampling conditions also for all spatial frequencies outside of the missing wedge. Notably frequency components in the direction of the different tilt axis are very densely sampled. This effect has been investigated only little so far, but in this thesis experiments have been done which take advantage of this dense sampling. It will be therefore not discussed further here, but will be detailed in Part IV.

4.8 Alignment

Alignment of the projections is a critical step in electron tomography. Due to the small size of samples, the stability of sample stages for TEMs is generally not sufficiently high to keep a common tilt axis in the center of all projections during the acquisition of a tilt series. Acquisition of a tilt series in a TEM generally requires re-centering of the sample before the acquisition of each projection, which is usually done by shifting the electron beam. While this allows keeping the region of interest inside the field of view, the projections are generally not aligned to each other after acquisition, i.e. there is no common line (tilt-axis) in the center of the projections around which sample features are rotating. Therefore before reconstruction electron tomography necessitates an alignment step.

Alignment is frequently split into two parts. In the first part, the shift alignment, the shift between the projections is calculated with the goal of finding alignment parameters, for which a common tilt-axis exists for all projections. The second step is the alignment of this tilt-axis, the position of which needs to be identified, its shift

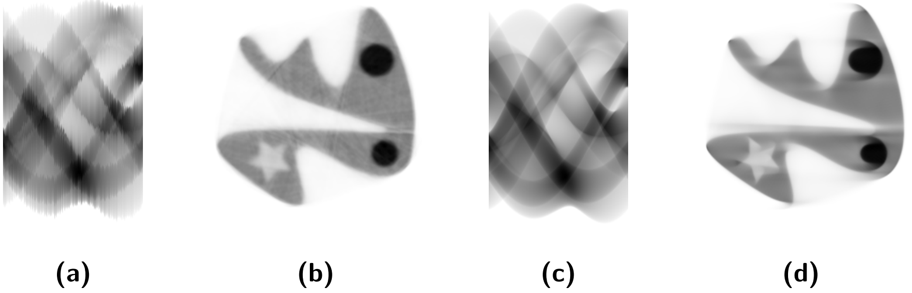

Figure 4.13: Effects of misalignment: (a) Projections with erroneous shift alignment, (b) Reconstruction from the misaligned projections shown in (a). (c) Projections with erroneous alignment of the tilt-axis, (d) Reconstruction from the misaligned projections shown in (c).

with respect to the center of the images and its angle with respect to the y-axis of the images. Fig. 4.13 shows effects from both erroneous shift alignment and erroneous alignment of the tilt axis.

For shift alignment the most commonly used techniques are alignment by cross-correlation (Owen and Landis, 1996) of subsequent tilt images and marker-based alignment (Brandt et al., 2001, Ress et al., 1999). For cross-correlation methods the cross-correlation between two subsequent images is calculated and the position of the maximum of the cross-correlation gives the shift between the images. Frequently before calculation of the cross-correlation, filters are applied to the images to improve the quality of the result. Filters can be used to enhance specific features of the sample, which then impact the cross-correlation calculation. In the case of needle-shaped samples frequently the boundaries of the needle are enhanced for this purpose, to be used as reference for the shift alignment. It is usually necessary to do several iterations of cross-correlation alignment, in particular if filters are used. Generally alignment by cross-correlation is done on a trial and error basis: Filters are applied, the shift is calculated and the result is controlled by visual inspection. If the result appears satisfying it is kept. Therefore eventually alignment can introduce errors in the reconstruction, which are hard to estimate as they depend on subjective verification of the alignment task. Even so for many samples cross-correlation is currently the best working alignment method and was used almost exclusively in the experiments presented in this thesis.

An alignment method, which is used frequently in tomography for life science applications is the alignment based on markers (Brandt et al., 2001, Ress et al., 1999). For this purpose markers, usually gold beads, are deposited onto the sample. In the alignment step the trajectories of these markers are recorded and based on these trajectories the shift between images and the position of the tilt axis can be calculated. The same principle can be also applied without artificially introduced markers, if the sample contains easily identifiable local features. In the frame of this work such approaches have been tested on samples containing high contrast features. Generally however these features were too large in one or two dimensions to make such algorithms work. Another alignment method, which has been proved useful for atomic resolution reconstruction of isolated particles is alignment based on center of mass calculations (Goris et al., 2012a, Scott et al., 2012).

Marker-based alignment methods also provide directly the alignment of the tilt axis, while the other methods in particular cross-correlation based methods do not. There exist several possibilities to find the correct position of the tilt axis. The technique mostly used in this work is to test several different alignment parameters manually and to find the parameters for which “banana-shaped” artifacts are reduced (Kobayashi et al., 2009). These artifacts appear especially for round features, if the position of the tilt axis is not correct. For needle-shaped samples the exterior surface of the sample can be generally well used for this purpose. Other methods, which can be applied for finding the tilt axis are the tracking of features throughout the tilt series, either manually or automated, to find the direction along which they move, or the calculation of rotational center from the center of mass of individual sinograms (Azevedo et al., 1990). These methods were in some cases employed to verify or improve alignment of the tilt axis.

Eventually alignment and reconstruction could be combined to improve the alignment. With certain alignment parameters a reconstruction can be done, which could then be re-projected and compared to the original projections to calculate misalignment of the individual projections.

4.9 Post-Processing

The reconstruction process provides a volume, with voxels containing grey values. This volume can be displayed by showing slices through the volume or by volume rendering, where to each voxel a color and transparency is attributed according to its grey value. Often however, the goal is to display interfaces between different materials, or even to extract quantitative information about sample morphology. For this purpose individual voxels need to be attributed to a specific material, giving a volume with discrete values, the number of discrete levels corresponding to the number of different materials, often referred to as phases. Previously discrete tomography was discussed as a method, which includes discretization in the reconstruction, if the discretization is done independently after reconstruction, this step is known as segmentation.

4.9.1 Filtering

It can be advantageous to filter a volume before segmentation, to reduce noise. There exist a large number of filters known in image processing, which can be in principle applied for this task. One group of filters, which are frequently used in tomography are anisotropic diffusion filters, which are also known as edge-preserving smoothing filters (Black et al., 1998, Perona and Malik, 1990, Weickert et al., 1998). These filters are iterative filters, based on gradient measures and on conduction coefficients calculated from these gradient measures, which weight how strong each neighboring value changes a specific value in each iteration.

In an example for a 3D implementation of this algorithm (Perona and Malik, 1990) in each iteration the value of a specific voxel $I_{i,j,k}$ is updated by the formula

$$I^{(t+1)}_{i,j,k} = I^{(t)}_{i,j,k} + \lambda \sum_{d=N,S,E,W,U,D} \left(c\left(\nabla_d I^{(t)}_{i,j,k}\right) \nabla_d I^{(t)}_{i,j,k} \right) \tag{4.26}$$

where $\nabla_d I^{(t)}_{i,j,k}$ gives the difference to the nearest neighbors of a voxel (in north, south, east, west, up, down) and λ is a weighting factor.

The difference to the northern neighbor for example is calculated as

$$\nabla_N I^{(t)}_{i,j,k} = I^{(t)}_{i-1,j,k} - I^{(t)}_{i,j,k} \tag{4.27}$$

$c(\nabla I)$ is the diffusion coefficient, which is calculated by a non-linear function. Examples for such functions are

$$c(\nabla I) = e^{-\left(\frac{\|\nabla I\|}{K}\right)^2} \tag{4.28}$$

or

$$c(\nabla I) = \frac{1}{1 + \left(\frac{\|\nabla I\|}{K}\right)^2} \tag{4.29}$$

The diffusion coefficient approaches 1 for small values of $\|\nabla I\|$ and 0 for large values. Practically this means that the filter reduces the differences between neighboring voxels, which have only a small difference (which is assumed to correspond to noise), while it keeps differences between neighboring voxels, if the differences are large (which is assumed to correspond to the edge of a sample feature). The constant K needs to be chosen to describe the boundary between differences, which should be interpreted as noise as compared to what should be interpreted as edge. The weighting factor λ needs to be chosen accordingly to guarantee stability and influences the convergence speed of the algorithm. The number of iterations can be chosen to define how strongly the volume should be filtered.

4.9.2 Segmentation

Segmentation generally refers to two tasks in image processing, to identifying different distinct components in an image and to identifying connected regions in an image (Ohser and Schladitz, 2009). For most applications in this thesis the first task is relevant, to distinguish between different materials inside a reconstructed volume. Identifying connectedness is of importance for example for porous materials and similar types of samples.

A large number of possibilities exist for segmentation. Segmentation can be done manually, semi-automated or fully automated. A problem with manual methods is their subjectivity, which can make results dependent on the person performing the segmentation. However still it is frequently employed as human experience can often identify sample features better than computer vision.

The simplest method for segmentation is segmentation based on absolute threshold values. All voxels with values below a certain threshold are attributed to one phase, while all voxels above the threshold are attributed to another phase. Thresholds for such a segmentation can be chosen manually, but there exist also several criteria for choosing a threshold, mostly based on evaluation of the histogram of an image (Otsu, 1979, Ridler and Calvard, 1978, Sezgin and Sankur, 2004). These methods work relatively well, if different phases are well separated by their grey value and if the noise is much lower than their differences. In other cases, noise will lead to erroneous voxels in the different regions and the boundary between materials will not be well defined. Apart from such global thresholding methods there exist also methods using local thresholds, which are useful, if the image intensity varies between different regions (Trier and Jain, 1995).

Region growing methods are another important family of segmentation methods (Ohser and Schladitz, 2009). These methods usually use seed pixels. Starting from these seed pixels neighboring pixels are added to a specific region, if they fulfil a homogeneity criterion. Such a criterion can be based for example the mean grey value and variance of the current grey values of the region or on an edge-detection algorithm. Apart from seeded region growing also algorithms for region growing without seeds exist (Revol-Muller et al., 2002).

A useful tool for image segmentation is the watershed transform (Vincent and Soille, 1991, Volkmann, 2002). For the watershed transform in two dimensions an image can be interpreted as a topological surface where the height is defined by the grey-value of a pixel. Starting from local minima this surface is flooded and the water rises with growing grey-values. Now pixels where water from different sources meet are denoted as watershed pixels and can be used to define the interface between different regions.

While the watershed transform can be applied directly on the image to distinguish for example between different pores in a porous material it can be also applied on the gradient of an image to distinguish between different materials. Such a method combined with seeded region growing was applied for some experiments presented in this thesis (Adams and Bischof, 1994). For this purpose first of all the gradient of the volume is calculated. Based on the gradient volume a mask is defined by applying a threshold in the gradient volume. All voxels above a certain threshold are masked. Such high gradient regions generally correspond to transition regions between different materials. In the remaining volume seed regions, which belong to a specific material, are defined. In our applications this was done based on absolute threshold values. However it is possible to leave gaps between the ranges of grey values which are attributed to the specific materials. In this way only voxels, which certainly belong to a specific material are attributed in this step. Additionally voxels which were masked before are not attributed to a specific material, independent of their grey value. After these steps, which necessitate input from the user the actual segmentation takes place. For this purpose a watershed transform is applied to the gradient volume, to allocate masked voxels and voxels lying between the thresholded intervals and set the boundary between regions of different materials. The watershed transform sets the boundary between seed regions of different materials to the position of the highest gradient.

4.10 Conclusion

In this chapter principles and relevant techniques for reconstruction in electron tomography have been discussed. The main goal in tomographic reconstruction is to get the best possible reconstruction from the available data. To compensate for practical limits, such as limited number of projections and missing projections imposed by the imaging system and the sample, two principal approaches are being followed: The adaption of the acquisition geometry to dual- or multiple-axis tomography, and the development of reconstruction algorithms, in particular algorithms including prior knowledge. Eventually these approaches can also be combined. Apart from the reconstruction itself also pre- and post-processing of the data is of importance in electron tomography. Alignment before reconstruction is necessary to even allow the reconstruction of a tilt series, while filtering and segmentation after the reconstruction are important, when quantitative information should be recovered.

5 Transmission Electron Microscopy for Tomography

A transmission electron microscope (TEM) is a versatile instrument, which allows the recovery of morphological, structural and chemical information down to the atomic scale. There are a large number of operation modes for different applications and many modern microscopes allow relatively easy switching between these modes. Where tomography is concerned images need to fulfil specific conditions to allow tomographic reconstruction from a series of images. In this chapter principles of transmission electron microscopy are reviewed and techniques applicable to tomography are discussed in more detail. Several books exist with detailed introductions to transmission electron microscopy (Pennycook and Nellist, 2011, Reimer and Kohl, 2008, Williams and Carter, 2009).

5.1 Electron-Matter Interaction in a TEM

Contrast in a TEM stems from interactions between the fast electrons which traverse the sample and the nuclei and shell electrons of the atoms in the sample. Electrons can be scattered when traversing the sample and such scattering can be elastic or inelastic, depending on whether energy is transferred in the scattering process. Furthermore it can be distinguished between coherent and incoherent scattering, designating whether a phase relation exists between the electron wave before and after the scattering event. Generally elastic scattering is usually coherent, while inelastic scattering is usually incoherent. For larger scattering angles however elastic scattering is getting incoherent. For tomographic applications, we are particularly interested in incoherent scattering, which is why we will discuss these processes in more detail. In inelastic scattering processes energy is transferred to the sample and this excess energy can lead to the creation of secondary signals.

Fig. 5.1 gives an overview of the most important signals which arise from electron-matter interactions in a TEM. In TEM several of these signals are used for characterization of the sample. The direct beam, elastically scattered and inelastically

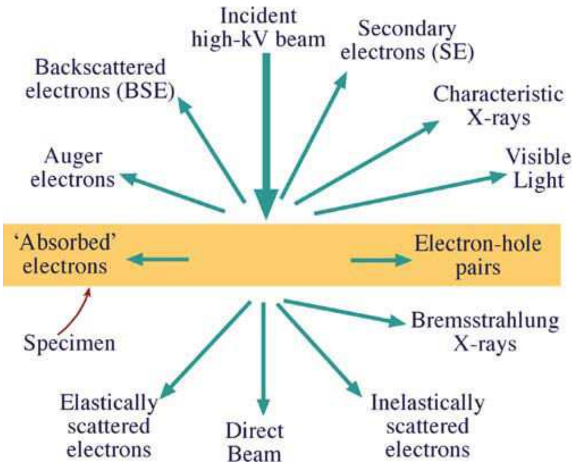

Figure 5.1: Signals arising due to fast electrons in a sample (Williams and Carter, 2009).

scattered electrons are recorded on different detectors located below the sample. X-rays created by electron-matter interaction can be detected in energy-dispersive x-ray spectroscopy (EDS) by detectors located in the vicinity of the sample. Here the main interest is in characteristic x-rays, which can be used for elemental identification and quantification. Another signal which is sometimes used in a TEM is the visible light emitted from the sample. This is known as cathodoluminescence.

5.1.1 Elastic Scattering

As samples prepared for TEM are quite thin, it can be usually assumed that single-scattering is the dominant process, while it is much less likely that electrons are scattered more than once, while traversing the sample. This assumption simplifies the analysis of scattering processes. To analyze scattering, first of all it is important to know the probability of an electron being scattered from a single atom. To quantify this probability atomic scattering cross sections are used (Williams and Carter, 2009). The cross section is defined from an effective radius of an atom r as

$$\sigma_{atom} = r^2\pi \tag{5.1}$$

Generally different cross sections are used for different scattering processes. Usually one is not interested into the overall scattering from a single atom, but into scattering to a specific angular range. For this purpose a differential scattering cross section $d\sigma/d\Omega$ is introduced, which defines scattering towards a differential solid angle $d\Omega$. It is usually more convenient to use a scattering angle θ with respect to the direction of the incident beam. The relation between the differential scattering cross section with respect to a solid angle and to a scattering angle can be derived from geometrical considerations and is given as

$$\frac{d\sigma}{d\Omega} = \frac{1}{2\pi \sin\theta} \frac{d\sigma}{d\theta} \tag{5.2}$$

Integration of this expression gives the scattering cross section over a specific angular range. From the scattering cross section of a single atom the total cross section σ_{total} per unit distance of a beam traversing a sample can be calculated as

$$\sigma_{total} = \frac{N_0 \sigma_{atom} \rho}{A} \tag{5.3}$$

with the Avogradro number $N_0 = 6.022 \times 10^{23}$ atoms mol^{-1}, A the atomic weight of the scattering atoms (in kg mol^{-1}) and the density ρ (in kg m^{-3}). The scattering cross section is linked to another frequently used property, the electron mean free path, which is generally denoted by λ but should not be confused with the electron equivalent wavelength. The mean free path is given in units of length as

$$\lambda = \frac{1}{\sigma_{total}} \tag{5.4}$$

It gives the mean distance between two scattering events.

When considering scattering processes, these can be caused by electron-electron interactions between the fast electrons traversing the sample and the electrons in the sample or by electron-nucleus interactions. Generally electron-electron interactions lead to relatively small scattering angles and coherent scattering. As such the wave character of the incident electron beam needs to be considered, which interacts with the sample as a whole and leads to diffraction, depending on the crystal structure of the sample. In contrast electron-nucleus interactions generally lead to larger scattering angles and dominate over electron-electron scattering for larger scattering angles. Electrons scattered by the nucleus generally have no phase relation to the electron wave before the scattering event, it can be therefore considered as incoherent scattering. The contrast arising from electron-nucleus interactions is therefore not affected by diffraction, which is of interest for tomography.

Electron-nucleus interactions can be described as Rayleigh scattering and the differential scattering cross section can be approximated by the Rutherford cross section

$$\sigma_R(\theta) = \frac{e^4 Z^2}{16 \left(4\pi\varepsilon_0 E_0\right)^2} \frac{d\Omega}{\sin^4\left(\frac{\theta}{2}\right)} \tag{5.5}$$

where $e = 1.602 \times 10^{-19}$C is the elemental charge, $\varepsilon_0 = 8.854 \times 10^{-12}$A^2 s^4 kg^{-1} m^{-3} the vacuum permittivity, Z the atomic number, and E_0 the electron beam energy in eV. (5.5) is non-relativistic and neglects the so-called screening effect of the electron cloud, which affects the charge distribution and is important for scattering of electrons relatively far from the nucleus. Additionally at least for acceleration voltages above 100 kV also relativistic effects should be included (Williams and Carter, 2009).

The differential cross section can be integrated to get the scattering cross section for electron-nucleus scattering to angles greater than θ as

$$\sigma_{nucleus} = 1.62 \times 10^{-24} \left(\frac{Z}{E_0}\right)^2 \cot^2 \frac{\theta}{2} \tag{5.6}$$

It can be seen that the scattering cross section depends on the atomic number Z as well as on the beam energy E_0. This is the basis for high-angle annular dark field (HAADF) scanning transmission electron microscopy (STEM), which is also called Z-contrast imaging as images display the proportionality to the atomic number.

5.1.2 Inelastic Scattering

When fast electrons interact with a sample they can loose energy in inelastic scattering events due to electron-electron collisions or collective excitation with outer-shell electrons. Such collisions reduce the energy of the fast incident electron and transfer energy to the sample. This excess energy can generate different detectable signals such as x-rays, secondary electrons or visible light. Some of these signals have been displayed in Fig. 5.1. The probability of these events and the energy lost contain a large amount of information about sample properties, such as their chemistry and electronic structure. Information can be retrieved either by recording the secondary signal or by recording the energy-loss spectrum of the incident electrons, which have traversed the sample. Several techniques deal with recording the secondary signal, depending on which type of signal is recorded. In EDS x-rays are recorded, in cathodoluminescence visible light is recorded, in Auger electron spectroscopy secondary electrons are recorded.

Techniques based on analysis of the energy-loss spectrum of electrons traversing the sample are electron energy-loss spectroscopy (EELS) (Egerton, 2009, Egerton and Malac, 2005, Kociak et al., 2011) and energy-filtered TEM (EFTEM) (Hofer et al., 1997, Hofer and Warbichler, 1996, Verbeeck et al., 2004). Fig. 5.2 shows an example of an energy-loss spectrum including some important features. It should be noted that counts are displayed in logarithmic scale. The spectrum is generally divided into a low-loss and high-loss (or core-loss) region with the boundary be-

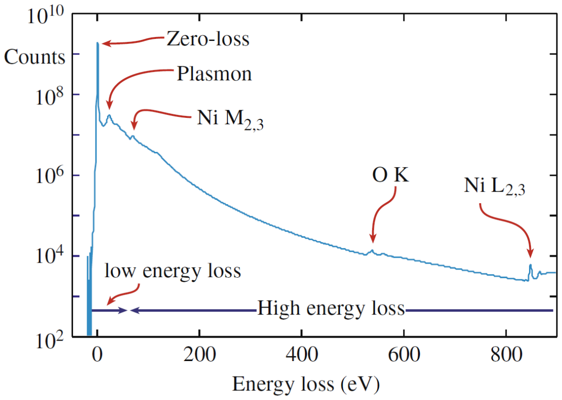

Figure 5.2: Example of an electron energy-loss spectrum (Williams and Carter, 2009).

tween these two regions being at about 50 eV. The first feature of the energy-loss spectrum is the zero-loss peak, which contains all unscattered and elastically scattered electrons. The zero-loss peak is very intense compared to all other features of the spectrum. In the low-loss region the dominating features are plasmon peaks. These and other features of the low-loss region are caused by weakly bound outer shell electrons. The signal in the low-loss region is still quite intense, in particular compared to the signal in the high-loss region. The high-loss region contains ionization edges, features of the high-loss regions are mostly linked to strongly bound inner-shell electrons.

The Low-Loss Spectrum

The low-loss spectrum is dominated by interactions of fast electrons with outer-shell electrons in the sample. The features dominating the low-loss spectrum are plasmon peaks, caused by the creation of volume plasmons and surface plasmons in the sample. Plasmons are pseudoparticles, created due to an oscillatory response of outer-shell electrons to a passing fast-moving electron. The outer shell electrons are weakly bound to the atoms and coupled to each other due to electrostatic forces. Therefore the Coulomb force of a passing electron causes an oscillatory response with alternating positive and negative space charge regions. The frequency of these oscillations can be calculated from the density n of the outer-shell electrons and their effective mass m^* (Egerton, 2009)

$$2\pi f_p = \omega_p = \left(\frac{ne^2}{\varepsilon_0 m^*}\right)^{1/2} \tag{5.7}$$

The energy of a plasmon is therefore given by

$$E_p = hf_p \tag{5.8}$$

with Planck's constant $h = 4.135 \times 10^{-15}\text{eV s} = 6.626 \times 10^{-34}\text{J s}$ and is typically in the range of few tens of eV. Plasmon peaks arise at energy losses which correspond to multiples of the plasmon energy E_p.

The probability of the creation of N plasmons by a fast electron in a sample of thickness t is given by Poisson statistics

$$P_N = \frac{1}{N!}\left(\frac{t}{\lambda_p}\right)^N e^{-t/\lambda_p} \tag{5.9}$$

with the plasmon mean free path λ_p.

Being caused by the electric field of the incident electron, plasmon generation can be also related to the dielectric properties of the sample. One such formulation, which also allows energy-loss spectra to be simulated is the Drude-model. From this model the complex permittivity ε can be written as

$$\varepsilon = 1 - \frac{E_p^2}{E^2 + jE\Gamma} \tag{5.10}$$

with the plasmon damping Γ, which corresponds approximately to the full width at half maximum of the plasmon peak. From the complex permittivity an energy-loss function can be defined as the imaginary part of its negative inverse:

$$\Im\left(-\frac{1}{\varepsilon(E)}\right) = \frac{E\Gamma E_p^2}{\left(E^2 - E_p^2\right)^2 + (E\Gamma)^2} \tag{5.11}$$

This loss-function can be used as an approximation for the shape of a plasmon peak.

Surface plasmons occur at interfaces between different materials as the surface is polarized. This gives a longitudinal wave with a frequency satisfying the condition

$$\varepsilon_a(\omega) + \varepsilon_b(\omega) = 0 \tag{5.12}$$

with $\varepsilon_a(\omega)$ and $\varepsilon_b(\omega)$, the relative permittivity of the two materials. One simple example is the interface between vacuum and a metal, where the free electron approximation is valid. Here $\varepsilon_a(\omega) = 1$ for vacuum and $\varepsilon_b(\omega) = 1 - \omega_p^2/\omega^2$ giving a surface plasmon peak at an energy E_s related to the energy of the volume plasmon peak in the metal E_p

$$E_s = E_p/\sqrt{2} \tag{5.13}$$

Surface plasmon scattering is strongly dependent on the incident angle of the electron beam on the surface. Its contribution is small compared to bulk plasmons at normal incidence, but grows with inclination of the surface with respect to the incident electron direction, and dominates over bulk plasmons for large incidence angles. The intensity of surface plasmons reduces the intensity of volume plasmons. This is called *begrenzungs*[1] effect. Surface plasmon fields of different surfaces can also be electrostatically coupled which leads to the generation of Čerenkov radiation.

In addition to collective plasmon excitation valence electrons can be also excited individually by a fast electron and be lifted to a higher energy state. In semiconductors these excitations can be in principle used to get information about their bandstructure.

The Core-Loss Spectrum

The core-loss spectrum is dominated by ionization edges from the excitation of inner shell electrons. These electrons have binding energies in the range of hundreds to thousands of electron volts. A fast electron can ionize an atom, elevating an electron to an energy state above the Fermi level. These transitions are characterized by a minimum energy necessary typical for each element and type of shell and follow a specific transition law. Therefore these transitions give rise to ionization edges in the energy-loss spectrum, which can be used for elemental identification. They are therefore denoted by the atomic shells, for example as K, L_1 edges or as L_{23} or M_{45} edges, if neighboring edges give an overlapping signal. The ionization edges are superimposed on a background, which is caused by transitions occurring at lower energies, such as plasmon excitation or ionization edges at lower energy losses. The shape of ionization edges depends on the type of elements, on the shell and on the density of states in the initial and final energy levels. Analysis of the shape of ionization edges is known as energy-loss near-edge spectroscopy (ELNES) and can be used to probe the electronic structure and thereby the structural and chemical environment of atoms (Radtke and Botton, 2011).

An important application of energy-loss spectroscopy in a TEM is elemental analysis. From the intensity of ionization edges elemental concentrations can be calculated or even absolute quantification is possible. For this purpose first a background

---

[1] Begrenzung is a German word for limitation

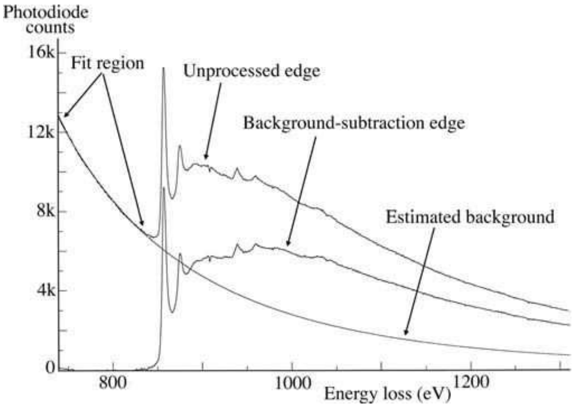

Figure 5.3: Principle of background subtraction for elemental quantification (Kociak et al., 2011).

subtraction is necessary to extract the total intensity due to the given transition. The most common method for background subtraction is to fit the background to a suitable function at energy losses below the absorption edge. This function is then extrapolated to energies above the absorption edge and subtracted from the actual signal (Egerton, 2009). The most frequently used function for fitting the background is a power law of the form

$$I = AE^{-r} \tag{5.14}$$

where A and r are fitting parameters. An example for background extrapolation and subtraction is shown in Fig. 5.3.

After background subtraction the areal density of an element N can be approximately recovered from the formula

$$I_c(\theta, \Delta) \approx N I_1(\theta, \Delta)\sigma(\theta, \Delta) \tag{5.15}$$

if scattered electrons up to an angle θ are collected over an energy range Δ. $\sigma(\theta, \Delta)$ is a partial cross section for a specific element and edge, which can be either calculated from simulations or measured experimentally. $I_1(\theta, \Delta)$ is the integral over the low-loss spectrum up to an energy Δ including the zero-loss peak, $I_c(\theta, \Delta)$ is integral over the same energy range over the signal from the ionization edge after background subtraction. The concentration of a specific element can be calculated if the thickness of the sample t is known as $n = N/t$.

While (5.15) provides absolute quantification, relative quantification to compare the ratio between different elements is often more useful and accurate. The ratio of the concentration of two different elements n_a/n_b can be calculated as

$$\frac{n_a}{n_b} = \frac{I_{c,a}(\theta, \Delta)}{I_{c,b}(\theta, \Delta)} \frac{\sigma_b(\theta, \Delta)}{\sigma_a(\theta, \Delta)} \tag{5.16}$$

5.2 The Instrument

A transmission electron microscope can be divided into three parts: An illumination system, the objective lens region, including the sample and its holder and the imaging system (Williams and Carter, 2009).

The illumination system consists of an electron gun and the condenser system, which are used to create an electron beam and to form it into its desired shape on the sample. Additionally in a modern microscope it may contain further elements like a monochromator or a probe-aberration corrector. Traditionally as electron source tungsten and later LaB_6 was used, with operation based on thermionic emission. If a material is heated to sufficiently high temperature, to allow electrons to overcome a barrier specified by the work function Φ, electrons leak out of the material and can be accelerated to form an electron beam. LaB_6 sources are still in use in many TEMs though they are now being frequently replaced by field-emission guns (FEGs). A FEG is a fine needle consisting for example of tungsten. An applied electric field is significantly increased at the sharp tip and this high electric field lowers the work function to allow tunnelling of electrons out of the tip. FEGs can be operated either under ultra-high vacuum (UHV) ($<10^{-9}$ Pa) under ambient temperature (cold FEGs) or at elevated temperature at a worse vacuum (Schottky FEGs).

Comparing different electron sources, FEGs have the advantages of providing higher brightness and higher spatial and temporal coherence, which are of importance for high spatial resolution and energy resolution for spectroscopy. Cold FEGs are superior to Schottky FEGs in all these matters, but their emission is less stable over time and they need to be operated in ultra-high vacuum. Even in UHV contamination builds up on a cold FEG, which reduces the current over time and requires periodic “flushing” of the point by inversion of the current or by heating of the point to remove the contamination layer. All the instruments used in this work operated on Schottky FEGs.

Electrons, which are pulled out of the source are accelerated by an electric field to a specific energy, which is defined by the operating voltage of the microscope. In a FEG two distinct anodes are used for extraction and acceleration. Typical operation

Acceleration voltage (kV)	Non-relativistic wavelength (nm)	Relativistic wavelength (nm)	Mass ($\times m_0$)	Velocity ($\times 10^8$ ms^{-1})
100	0.00386	0.00370	1.196	1.644
200	0.00273	0.00251	1.391	2.086
300	0.00223	0.00197	1.587	2.330

Table 5.1: Properties of electrons for different acceleration voltages, $m_0 = 9.11 \times 10^{-31}$kg is the electron rest mass (Williams and Carter, 2009).

voltages for a TEM are in the range of few tens to a few hundred keV, the microscopes used for this thesis can be operated between 80 kV and 300 kV. Higher acceleration voltages provide electrons with higher energy and thereby a shorter equivalent wavelength and a higher mean free path. Table 5.1 shows electron properties for different acceleration voltages. Higher energies are useful as spatial resolution (or more important for tomography the resolution/depth of field product) can be higher and thicker samples can be analyzed. However some mechanisms of beam damage become more important for higher electron energies. For most investigations in this thesis an acceleration voltage of 200 kV was used, which provides sufficiently high values for resolution and depth of field but usually leads to no observable beam damage for the investigated samples.

The condenser system consists of several optical elements, lenses, apertures and scan coils, which allow bringing the beam into its desired shape before interaction with the sample. This defines two basic operation modes of a TEM, which are parallel beam operation (used for conventional TEM), where a parallel (or almost parallel) beam illuminates the sample, and convergent beam operation (used for scanning TEM), where the beam is focused, and a convergent beam interacts with the sample. Fig. 5.4a shows the condenser system in the so-called nanoprobe mode for these two operation modes for the example of a FEI Titan microscope, as was used in this thesis. Between the two modes the excitation of the C3 lens is changed to switch between convergent and parallel illumination. The condenser system of this microscope can be also operated in the so-called microprobe mode (see Fig. 5.4b). In this mode the minicondenser (MC) lens which is just above the objective lens is used to compensate the upper objective lens. This is useful for TEM, if large areas should be illuminated, and for STEM, when a larger probe with a small convergence angle is desired.

In the condenser system several parameters of the beam can be adapted thanks to the use of three condenser lenses. The excitation of the gun lens influences, how many of the extracted electrons are used to form the beam. The same can be achieved by changing the position of the crossover between the C1 and C2 lens

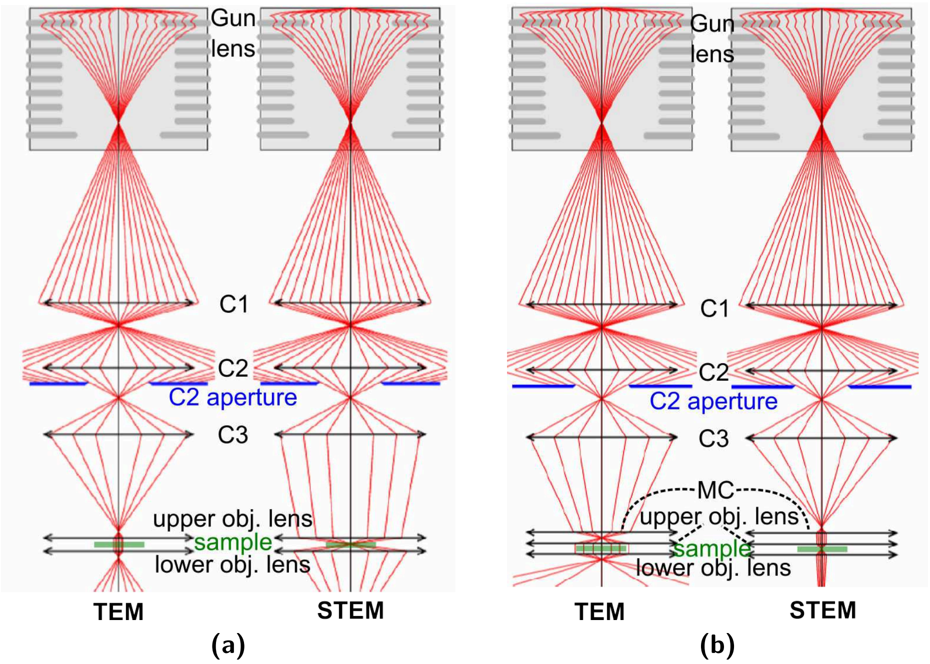

Figure 5.4: Parallel (TEM) and convergent beam (STEM) operation for the example of an FEI Titan microscope in (a) nanoprobe mode and (b) microprobe mode (Tiemeijer, 2005).

(referred to as spot size in FEI microscopes). These settings change the intensity of the beam, but also the spatial coherence of the beam. The diameter of the C2 aperture and the position of the crossover between the C2 and C3 lens are used to define the illuminated area in case of parallel illumination and the convergence angle in case of convergent beam illumination.

Between the illumination system and the imaging system the sample is located. The sample is fixed on a sample holder, which is used to transfer the sample into its position and to position it in the microscope with the help of a sample support stage. Generally the sample stage allows positioning of the sample along the three dimensions of space and allows tilting of the sample around one axis. The two directions perpendicular to the beam directions are usually referred to as x and y, the direction parallel to the electron beam as z, the tilt along the first axis, which can be done using the stage of the microscope is usually denoted with α. Additionally sample holders are available, which allow tilting around a second axis perpendicular to the first one (referred to as β) as well as sample holders which allow rotation of the sample. A TEM is usually aligned for a reference plane along the z-direction at which the sample should be positioned during operation. This plane is known as the eucentric plane and a sample which is located at the eucentric plane will not move or move only a little along x and y, when the sample is tilted around α.

For tomography the most important feature of a stage and sample holder is the maximum tilt range available. Standard tomography holders and sample stages allow tilt ranges up to ±80°, though if conventional TEM grids are used, shadowing of the region of interest often occurs already at lower tilt angles. Additionally when electrons scattered to large angles are recorded, a part of these scattered electrons can already suffer from shadowing even before the incident beam. For needle-shaped sample geometries special sample holders are available, which do not suffer from shadowing and can be used to tilt over a full range of ±90° using an internal mechanism of the sample holder. This allows rotation of the sample with respect to the holder in addition to the tilt mechanism of the sample stage.

The imaging system of a TEM consists of all optical elements between the specimen and the fluorescent screen of a TEM. There are usually several lenses, known as intermediate and projector lenses, and apertures which can be introduced if needed, the objective aperture and the selected area diffraction (SAD) aperture. Additionally the imaging system may also contain an image aberration corrector, which compensates for spherical aberrations of the imaging system and improves the resolution in TEM imaging. The imaging system can be operated in two basic operation modes, in imaging and diffraction mode. Fig. 5.5 shows the imaging system for these two modes.

In diffraction mode the lenses are set in a configuration to project the back focal plane of the objective lens, i.e. the diffraction pattern of the illuminated area on the fluorescent screen. With parallel illumination this gives discrete diffraction spots and a SAD aperture can be introduced to acquire the diffraction pattern of a specific area. This is known as selected area diffraction and is a standard method for acquiring diffraction patterns in a TEM. If the specimen is illuminated by a convergent focused beam the diffraction spots become discs, the size of the discs depending on the convergence angle of the beam. Such diffraction patterns are collected in convergent beam electron diffraction (CBED). If a beam with a very small convergence angle is used the spots become again discrete and the operation is then known as nanobeam electron diffraction (NBED). In STEM imaging the imaging system is also operated in diffraction mode. STEM images are formed by integrating the intensity of diffraction plane over specific angles for each scan position on the sample.

In imaging mode the lenses project the image plane of the objective lens and an image of the sample appears on the screen. This mode is used for TEM imaging in combination with parallel beam illumination. An objective aperture can be introduced to select only a specific part of the diffraction pattern for imaging. Such

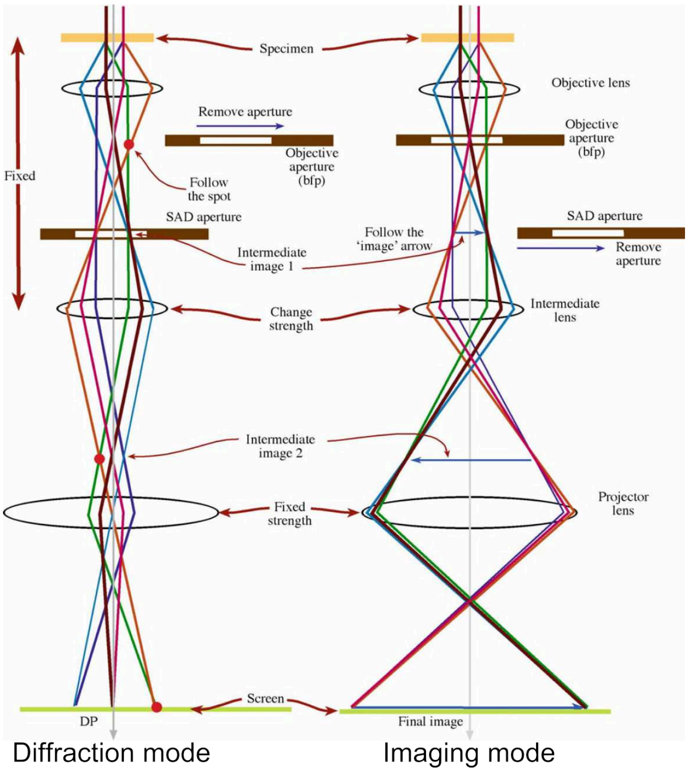

Figure 5.5: The imaging system of a TEM in diffraction and in imaging mode (Williams and Carter, 2009).

operation is known as bright-field (BF) or dark-field (DF) TEM imaging. In BF TEM only the direct beam is selected by the objective aperture to form the image, in DF TEM a diffracted beam is selected.

5.2.1 Energy Filters

To record energy-loss spectra and filtered images in a TEM, energy filters are used. These are based on energy-dispersive magnetic prisms, which function similar to glass prisms in optics. Such a magnetic prism uses the Lorentz force

$$\tilde{\mathbf{F}} = q\left(\tilde{\mathbf{E}} + \vec{v} \times \tilde{\mathbf{B}}\right) \tag{5.17}$$

where a particle with a charge q moving at a velocity $\vec{v}$ is deviated from its trajectory due the the magnetic field $\vec{B}$. The principle of such a magnetic prism is shown in Fig. 5.6 for a post-column energy filter (Gubbens et al., 1995). Electrons which pass through an entrance aperture are deflected by a magnetic field by approximately 90°, where electrons with a lower energy (which have lost energy due to inelastic scattering processes) are deflected further than electrons which have lost no energy. In addition to being energy dispersive the magnetic prism also works as a lens.

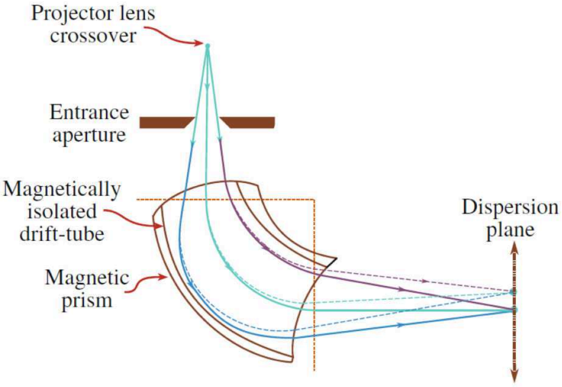

Figure 5.6: Principle of an energy-dispersive magnetic prism (Williams and Carter, 2009).

Altogether this has the effect that all electrons, which have lost a certain energy are focused at the same height in the dispersion plane of the prism, regardless of the angle they have been scattered to and the point of their origin. This allows two basic modes of operation of an energy-filter which are known as electron energy-loss spectroscopy (EELS) and energy-filtered transmission electron microscopy (EFTEM).

In EELS a detector – usually a charge-coupled device (CCD) camera – is put at the position of the energy dispersion plane. This allows recording an energy loss spectrum of the area illuminated by the electron beam. In EFTEM an energy-selecting slit is put in the dispersive plane to select a specific range of energy-loss, and an image is recorded after the slit at an image plane. The most frequently used post-column energy filters are manufactured by Gatan, and are named Gatan imaging filter (GIF). Switching between EFTEM and EELS is done by changing the optics of the energy filter. Apart from post-column energy filters also in-column filters exist, which can be used for EFTEM and EELS. These are known as Ω-filters, as the electron beam is deviated from its axis by prisms along an Ω-shaped beam path. Furthermore for dedicated STEM microscopes, filters are available, which allow only EELS operation. The microscopes used in this work were equipped with post-column energy filters.

5.3 The Projection Requirement

For tomographic reconstruction to be applicable to a series of images, the images need to be monotonically varying functions dependent on properties of the samples along straight lines through the sample (Hawkes, 1992). This condition is known as projection requirement. The projection requirement limits the number of TEM techniques, which are applicable for tomography, in particular for crystalline samples. The contrast in many imaging techniques is largely influenced by diffraction effects, which depend on the orientation of the crystal lattice to the direction of the electron beam.

Diffraction contrast leads to different image intensities from objects with the same properties and thickness, but different orientations with respect to the electron beam. Such contrast does therefore not fulfil the projection requirement. Diffraction contrast is dominant in images of crystalline samples, which are based on the detection of coherently scattered electrons. Therefore imaging techniques, which can be used for tomography need to be based on the detection of incoherently scattered electrons. Such techniques are HAADF STEM, where the contrast is mainly due to elastic incoherent scattering and techniques based on inelastic incoherent scattering, such as EELS and EFTEM. Additionally also EDS fulfils at least to a good approximation the projection requirement.

5.4 Imaging Techniques for Tomography

Several imaging techniques are available based on the discussed scattering processes and secondary signals created in the electron-matter interactions. Here the imaging techniques, which can be used as basis for tomographic reconstruction on crystalline samples are discussed. These are HAADF STEM, EELS, EFTEM and EDS. While BF TEM is the most common method for tomography in life sciences, in material science usually diffraction contrast is too large to allow reconstruction.

It should be noted that apart from imaging, also diffraction modes of TEMs have been combined with tomography (Kolb et al., 2007, 2008, 2011). Furthermore – even though diffraction contrast in images is usually unwanted for tomography – it has been used for tomographic reconstruction of dislocations. For this purpose the diffraction contrast stemming from dislocations in weak-beam dark-field imaging (Barnard et al., 2006a,b) has been used and more recently also medium-angle annular dark field (MAADF) STEM, where an annular detector located at smaller collection angles than for HAADF STEM is used (Barnard et al., 2010). However these techniques were not applied in the frame of this thesis and they will therefore not be discussed further.

5.4.1 HAADF STEM

In STEM the sample is illuminated by a convergent beam. Detectors record signals in a diffraction plane, which depend on the sample properties in the illuminated

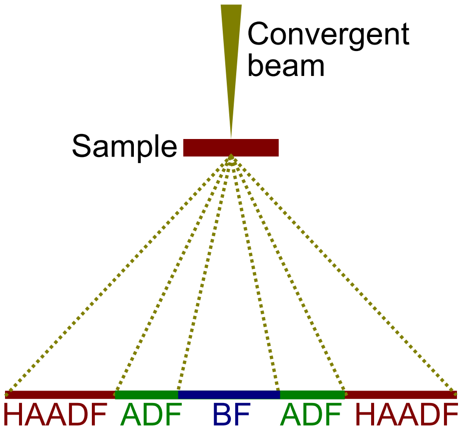

Figure 5.7: Schematic of detectors in STEM.

region. The spatial resolution of STEM imaging depends therefore not on the imaging system, but on the size of the convergent beam. To record images, the beam is scanned over the sample using scan coils in the condenser system which shift the convergent beam parallel along the x- and y-directions. Signals are recorded for each beam position.

Similar to TEM, STEM can also be done in bright-field or dark-field modes. For STEM however no aperture is necessary, but the shape and size of the detector selects which part of the diffraction pattern is recorded. Fig. 5.7 shows a schematic of different STEM detectors. In BF STEM the direct beam is recorded, in the center of the diffraction pattern. In DF STEM scattered electrons are recorded in regions outside of the direct beam. Most frequently annular detectors are used, which are ring-shaped detectors, recording electrons scattered to a specific angular range in all directions. Such imaging is known as annular dark field (ADF) STEM, if the detector is located to detect only electrons scattered to relatively high angles it is also called HAADF STEM.

Different types of detectors exist to collect the electrons. In the microscopes used in this thesis a scintillator-photomultiplier detector is as HAADF detector. It is based on a yttrium aluminum perovskite (YAP) scintillator optically coupled to a photomultiplier tube.

As mentioned previously scattering to high angles can be approximated by the Rutherford cross-section and is proportional to Z^2 (see (5.5) & (5.6)). Practically this idealized approximation is never reached as several other factors influence the contrast which gives a proportionality of the HAADF signal I_{HAADF}

$$I_{HAADF} \propto Z^{\alpha} \tag{5.18}$$

with $\alpha \approx 1.6 - 2$. For qualitative investigations, as are usually done by electron tomography knowledge about this proportionality is sufficient, for quantitative HAADF STEM investigations the factor α needs to be known.

Though (5.18) fulfils the projections requirement, there are further effects, which can give rise to additional contrast contributions. Electron channelling occurs, when a crystal is oriented close to a major zone axis (Pennycook and Nellist, 2011). This gives rise to stronger scattering as would be expected from (5.18), leading to brighter images for crystal orientations close to a zone axis. In practice usually only few images of a tilt series are affected by channelling effects. If this contrast contribution appears too large on specific images, it is often useful to remove these images from the tilt series before reconstruction.

An important issue for tomography is how well a probe can be focused in STEM and how much of the sample remains in focus along the depth. Ideally for classical tomography the whole sample should be in focus when an image is acquired. These parameters are governed by the convergence angle of the focused electron beam. They can be approximately calculated by formulas known from optics (Biskupek et al., 2010). With a convergence angle α_c the resolution limit d is defined by the Rayleigh criterion

$$d = \frac{0.61\lambda_e}{\sin\alpha_c} \tag{5.19}$$

with the electron wavelength λ_e. The depth of field DOF, defines the thickness of the layer in focus for which this resolution d can be achieved and can be calculated as

$$DOF \approx 2\frac{d^2}{\lambda_e} \tag{5.20}$$

Fig. 5.8 shows the convergence angle and the Rayleigh resolution limit as a function of depth of field (DOF). This relation gives the convergence angle, which should be used for a specific sample thickness to have optimal focus for the whole sample: a low convergence angle is necessary to get high DOF. It should be noted that for samples more than 100 nm thick the convergence angle should be significantly smaller than typical settings for STEM, which are in the range of 10-20 mrad. However, while a small convergence angle has advantages in terms of depth of field there are few drawbacks of using a very small convergence angle: Residual diffraction contrast due to elastic scattering becomes more important as a small convergence angle reduces the angular range over which the signal is averaged. Additionally if the microscope is operated in nanoprobe mode the beam intensity is decreased as a small C2 aperture needs to be used. For very thick samples therefore operation of the microscope in microprobe mode can be useful, which allows using very small conver-

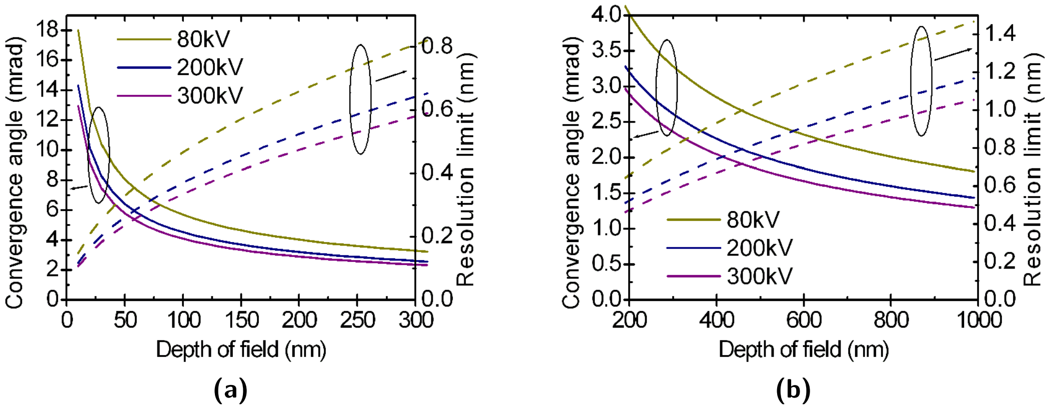

Figure 5.8: Convergence angle and resolution limit vs. depth of field (DOF) for acceleration voltages of 80 kV, 200 kV and 300 kV, (a) for DOF up to 300 nm, (b) for DOF between 200 nm and 1000 nm.

gence angles while keeping sufficiently high beam intensity (Hyun et al., 2008). So a compromise between current and convergence angle has to be found to get optimum acquisition conditions.

5.4.2 STEM-EELS

The main interest when investigating inelastic scattering in a TEM is to get spatially resolved spectral information. The information, which should be acquired is often referred to as the EELS data cube. Such a data cube contains information along two dimensions of space, x and y and along the energy loss E. The principal methods for acquiring the information in such a datacube are STEM-EELS and the imaging-spectroscopy method by EFTEM. Eventually also other methods are possible such as tomographic reconstruction of the data cube from projections but are not commonly used (Van den Broek et al., 2006).

In STEM-EELS the data cube is sampled serially along x and y, one spectrum at a time. For this purpose the microscope is operated in STEM mode, with a convergent beam, and energy-loss spectra are acquired on the camera of the energy filter for each scan position. The spectral resolution in EELS is limited by the monochromaticy of the incident electron beam and by the energy resolution of the spectrometer. The energy dispersion of the beam depends on the type of electron gun used. It is in the range of 0.6-0.8 eV for a Schottky FEG and in the range of 0.3-0.5 eV for a cold FEGs. It can be reduced by a monochromator, the best values which have been achieved are as low as 30 meV (Krivanek et al., 2013). In the spectrometer the energy range and resolution needs to be adapted to the application. This is set as energy dispersion (in eV/pixel) and energy offset. Generally only a part of the spectrum is recorded on an ultrafast CCD camera (2048×2048 pixel), to improve the resolution over the desired range and because changes in intensity over the spectrum are very large, so acquisition times necessary for recording ionization edges in the core-loss region would often lead to saturation of the camera in the low-loss range and in particular for the zero-loss peak. As it can be very useful to have information about the low-loss range and core-loss range at the same time recently systems have been developed – named dual-EELS systems by Gatan –, which allow parallel recording of two spectra with different energy and exposure settings.

5.4.3 EFTEM

In EFTEM energy-filtered images are acquired, which provides sampling of the EELS data cube one energy at a time. In principle the full data cube can be recorded in this way with an energy resolution given by the energy range recorded in each image. This approach is known as imaging spectroscopy (Thomas and Midgley, 2001a,b). Often however it is sufficient to record images at just a few energy losses. For example for analysis of ionization edges by EFTEM, frequently only two or three filtered images are recorded in the vicinity of the ionization edge one is interested in.

For EFTEM the microscope is operated in TEM mode, a relatively large area of the sample is illuminated by a parallel beam. The energy filter is used to select a specific energy range and record an image at this energy. For investigations of ionization edges by EFTEM the most frequently used methods are the three-window method and the jump-ratio method (Hofer and Warbichler, 1996, Verbeeck et al., 2004). The three-window method can be used for elemental quantification. For this purpose two images are acquired at energies below an ionization edge to fit the background. A third image is recorded at an energy window above the ionization edge. Subtracting the extrapolated background gives the element specific signal and allows absolute or relative elemental quantification based on (5.15) or (5.16). Fig. 5.9 illustrates the principle of the three-window method.

The jump-ratio method is based on taking just two images, one before and one after the ionization edge and on calculating their ratio. This can be useful for low elemental concentrations, where the three-window method can lead to noisy images (Hofer et al., 1997). However the jump-ratio method allows only qualitative investigation, quantification is not possible in this way.

Imaging-spectroscopy by EFTEM is of interest to improve the quality of elemental quantification compared to the three-window method, but also to investigate other

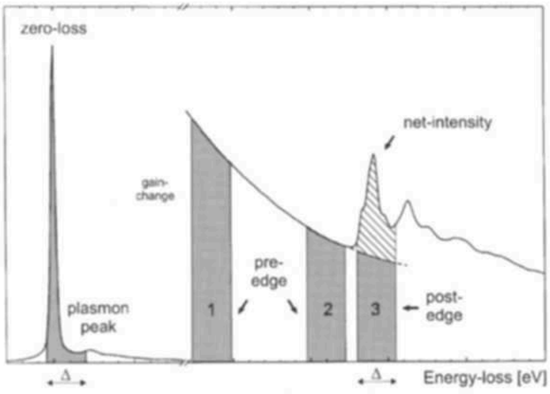

Figure 5.9: Principle of quantification by the three-window method: Two pre-edge images (1,2) and one post-edge image (3) need to be taken. For absolute quantification also an image in the low-loss region needs to be recorded (Hofer and Warbichler, 1996)

features of the energy-loss spectrum apart from the intensity of ionization edges, such as their shape or to get information about the low-loss spectrum as it was employed in this thesis (see Chapter 8).

5.4.4 EDS

EDS is another technique based on inelastic scattering, which has been combined with tomographic reconstruction. In EDS x-rays emitted from the sample are recorded. Inelastic scattering of electrons can produce two types of x-ray radiation in a sample: *characteristic* x-rays and *bremsstrahlung* x-rays (Williams and Carter, 2009). The main interest is generally in characteristic x-rays as they can be used for elemental identification. When a fast electron ejects an electron from an inner shell of an atom an ionized atom remains. This atom will almost immediately return to its lowest energy state by filling the empty state with an electron from an outer shell. In this process from the excess energy either an x-ray or an Auger electron can be emitted. For each atom several such transitions are possible, which are characterized by their energy an by a specific probability. Analysis of the energy of emitted x-rays can be used for chemical identification and eventually also for quantification. Characteristic x-rays are emitted as a spherical wave from their origin. X-ray detectors are therefore positioned around the sample and their efficiency depends on the angular range covered. For this purpose recently microscopes have been developed which combine several detectors to maximize the interception of x-rays.

5.5 Conclusion

In this chapter requirements and applicable imaging techniques for doing tomography in a TEM were reviewed. As such HAADF STEM, EELS, EFTEM and EDS are in principle applicable. Of these techniques HAADF STEM tomography is by far the most widely used technique due to its relative simplicity and relatively short acquisition times. Other contrast techniques based on inelastic scattering are of interest, when the contrast between different materials from HAADF STEM is not sufficient, or when elemental identification is required. Furthermore there exists also the perspective of 3D elemental quantification, which remains however a significant challenge.

6 Sample Preparation

Many sample preparation methods, which are used for standard TEM investigations, can be also used for electron tomography. However for electron tomography there exists the additional requirement, that the sample geometry should allow image acquisition over as large a tilt range as possible and that the sample thickness along the beam path should remain small also for large tilt angles. Therefore for electron tomography a sample should be ideally needle-shape as compared to the lamella-shape preferable for other TEM techniques.[1]

6.1 FIB-Based Preparation

Most of the samples investigated in this thesis were prepared using a dual-beam FIB-SEM instrument. The FIB is an important tool for TEM preparation, in particular for site-specific preparation from substrates, for example in microelectronics (Giannuzzi and Stevie, 1999). Dual-beam FIB-SEM instruments consist of an FIB and an SEM column, which are located at a specific angle to each other (52° for the instruments used in this thesis). The sample is located at the position, where the beams between the two columns intersect, on a sample support stage which can be shifted, tilted and rotated. Operation of the FIB column is most frequently based on Ga^+-ions. To extract ions a liquid gallium reservoir is used, which is in contact with a sharp tungsten tip. Liquid gallium wets the needle and a high electric field is used to extract Ga^+-ions by field ionization and accelerate the ions in the FIB column. Acceleration voltages of ions are usually in the range of 500 V to 50 keV. In addition the current of the FIB column can be chosen to define how many ions are extracted and interact with the sample. In the FIB column ions can be focused to fine probe sizes below 10 nm.

Ions can be used for imaging by scanning the ion beam over the sample and detecting either secondary electrons or secondary ions. The main interest for sample preparation is though, that additionally the FIB allows localized sputtering and matter deposition. The imaging capabilities of both the SEM and the FIB allow

---

[1] Parts of this chapter are reproduced from (Bleuet et al., 2013)

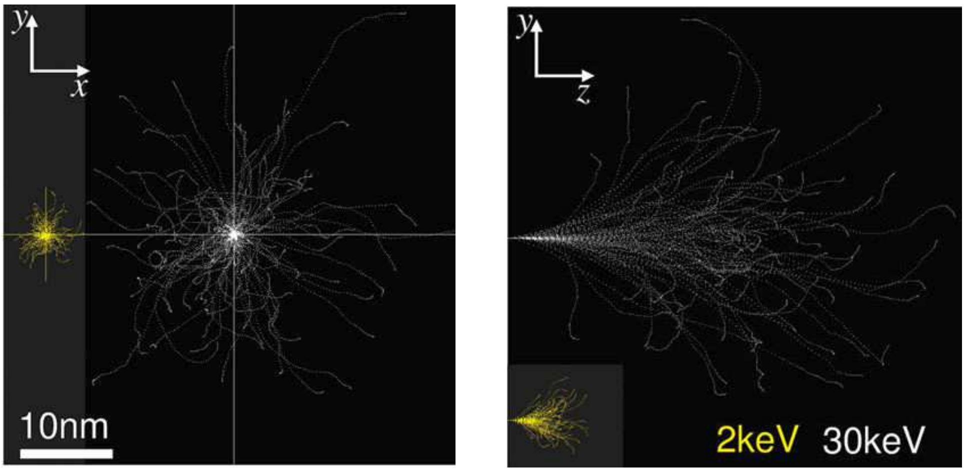

(a) (b)

Figure 6.1: Collision plots of 30 keV and 2 keV gallium ions (white and yellow, respectively). The beam is along the z-axis. Both lateral (a) and depth profiles (b) show that a 2 keV milling limits damage to the first 5 nm.

precise control of the position for sputtering or deposition. Ions, which are accelerated towards the surface of a sample lead to a series of interactions with the sample, which lead to ejection of atoms or ions from the sample as well as to the implantation of Ga^+-ions. Therefore the FIB is efficient for removing matter, but it also affects the remaining material in several ways, which is known as ion beam damage. The most important of these damaging effects are amorphization, implantation and stress. Ion beam damage can be reduced by using lower acceleration voltages, which reduces the penetration depth of ions. As such a rule of thumb is that each kV of acceleration voltage adds 1 nm thickness to the damaged layer. Fig. 6.1 shows collision plots for gallium ions in silicon based on Monte Carlo simulations (Ziegler et al., 2010).

Matter deposition in the FIB is done by beam assisted chemical vapor deposition. A needle-shaped gas injector is inserted close to the surface of the sample, which is used to inject a gas precursor, which absorbs on the surface. Ga-ions, but also electrons from the SEM can decompose the precursor and lead to deposition of material on the surface. If ions are used this is referred to as ion-beam induced deposition (IBID), if electrons are used as electron-beam induced deposition (EBID) (Randolph et al., 2006). EBID takes more time than IBID but is less invasive. The chemical composition and associated mechanical, thermal, or electrical properties of the deposited materials are also quite different when EBID or IBID is used. In TEM preparation methods deposition is frequently used to protect the region of interest before extraction of the sample. For this purpose usually EBID is performed as

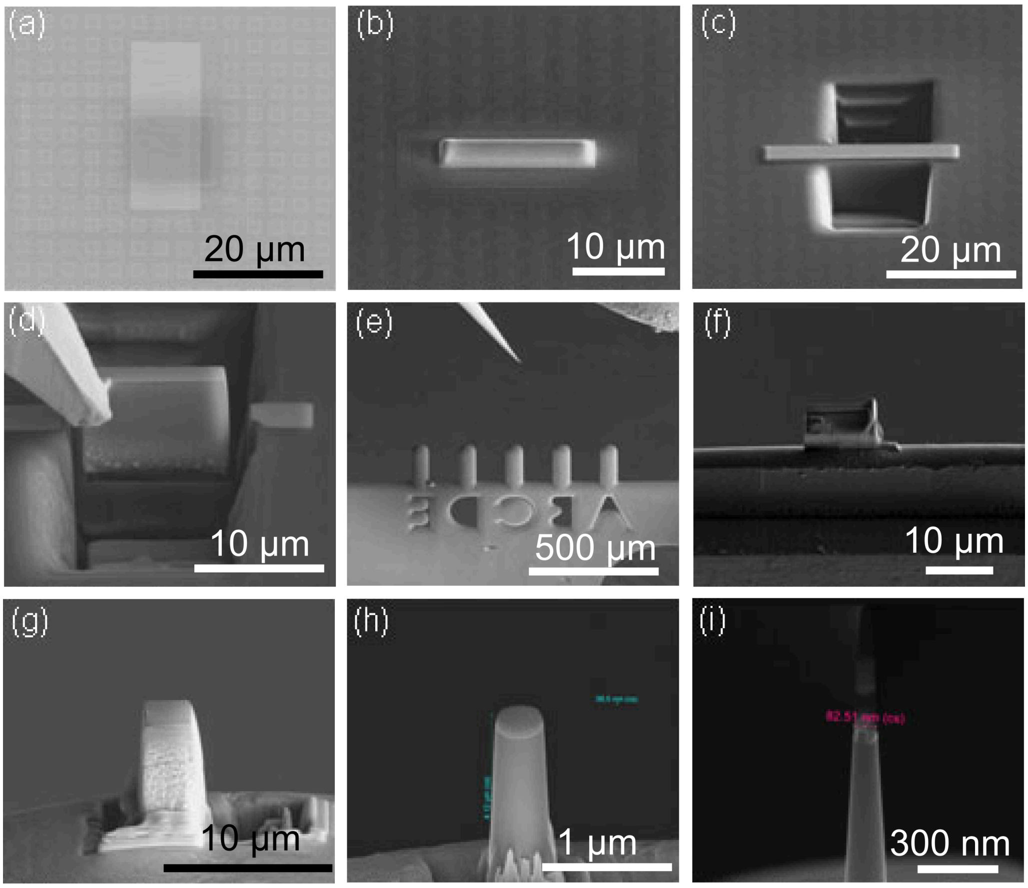

Figure 6.2: Sample preparation in an FIB for electron tomography (a) ROI before preparation, (b) after deposition of a protective tungsten layer (rotated 90° to previous image), (c) cutting of basins above and below the sample, (d) extraction with micromanipulator, (e) Omniprobe support grid, (f) lamella glued to a supporting post of the grid, (g) reduction of lamella size to a pillar, (h) sample after the first steps of annular milling, (i) finished sample containing the transistor.

a first step and is then followed by IBID to prevent damage to the surface. For deposition several materials are available, the most frequently used are W and Pt, as metals, and SiO_2 as insulator.

To extract matter from a larger sample, micromanipulators can be introduced in the vacuum chamber of the instrument. A sample can be glued to such a micromanipulator and be thereby extracted and glued to a support for TEM investigation.

As mentioned before, for electron tomography investigations, samples should be ideally needle-shaped. Techniques for FIB-based preparation of needle-shaped samples have been first developed for atom probe tomography (Miller et al., 2005b, Thompson et al., 2004, 2007), and the same methods were transferred to sample preparation for electron tomography (Kawase et al., 2007, Ke et al., 2010, Yaguchi et al., 2004). Fig. 6.2 shows an example for such a sample preparation. The lift-out procedure is similar to standard TEM preparation: first of all, the region of interest is covered by a protective stack, in this case consisting of electron deposited SiO_2, electron deposited tungsten and ion-deposited tungsten. Once the sample is protected, basins are cut on the top and bottom sides of the protected area, and a lamella with a thickness of few micrometers is extracted with a micromanipulator. The extracted sample is then glued to a support. Eventually also multiple samples can be prepared from a single extracted lamella. In the present case an Omniprobe FIB grid was used, which is the standard sample support in electron microscopy. Glueing the sample to the top of one of the supporting posts reduces shadowing effects in the TEM. Recently developed specific tomography sample holders use needle-shaped sample supports, some of these supports can be used for electron tomography as well as for atom probe tomography, which allows both techniques to be performed on the same sample. The sample preparation process for needle-shaped supports is similar to the presented case, with the sample being glued to a needle instead of an Omniprobe grid.

After the sample is glued to a support, its size is reduced. This can be done using annular milling in the FIB. The inner diameter of the circular milling pattern is reduced in several steps until the desired diameter is achieved. In the present case, milling needs to be controlled precisely to keep the device inside the needle. This can be done by taking images with the SEM at high acceleration voltage, where the device becomes visible before it is actually at the surface. Reduction of sample diameter is usually done at a high tension of 30 kV on the FIB. This provides steep side walls but creates an amorphous layer of about 30 nm thickness. A way to reduce the amorphous layer is to finish the sample at lower high tension, e.g., at 5 kV. However this reduces also the inclination of the side walls. The decision whether to perform this last step will therefore depend on the application. If information over a large depth is required, steep side walls are preferable, at the expense of the presence of an amorphous layer. For the present example of the transistor, the ROI is only about 100 nm deep, so the steepness of the side walls is of less importance.

6.2 Other Preparation Methods

In many cases preparation for TEM is done by transfer of the sample to specific grids, usually consisting of copper, with a diameter of a few millimeters and a mesh of a few hundred squares. Depending on the application these grids may be covered with a thin carbon film, or with a lacey carbon mesh. The preparation methods using such grids are manifold. Examples which have been used during this thesis are the deposition of nanoparticles directly from a solution, or sonication of nanowires in an ultrasonic bath, to get a solution, which can then also be deposited on the grid. For nanowires another possibility is to place the grid directly on the substrate and to swipe it slightly. In this way nanowires are transferred directly from the substrate to the grid.

Generally the distribution of the deposited sample on the grid is random. Therefore, a challenge when doing tomography on such samples is finding a suitable region for doing tomography in the TEM. As one example in the case of nanowires deposited on a grid, a nanowire needs to be found that is located close to the center of a mesh square and additionally also oriented along the tilt axis. The location of the sample is important, as large tilt angles are only possible close to the center of a window. A drawback of using these grids in comparison to FIB preparation is that missing wedge artifacts cannot be avoided. Typical tilt ranges that can be achieved are about ±70°.

6.3 Conclusion

Sample preparation methods for electron tomography need to be optimized to maximize the available tilt range. For this purpose, in particular for semiconductor materials and devices, FIB-based preparation is usually the best method. It allows site specific preparation of needle-shaped samples, where the diameter of the needle can be optimized. The acceleration voltage of the FIB for the final preparation steps can be set accordingly to either reduce surface damage or to prepare long thin needles. Conventional TEM preparation methods are useful for samples, which can not be prepared by FIB. In this case samples, or parts of a sample need to be found, which are located suitably for electron tomography investigations, to allow a large tilt range, and also the orientation of the sample with respect of the tilt axis can be of importance.

Part III

Getting Contrast

7 HAADF STEM Tomography

When a contrast technique for use with tomography is considered the two major questions are whether a specific contrast mechanism fulfils the projection requirement and whether the selected technique can provide contrast for the desired application. After these two essential requirements other important questions are the time necessary for image acquisition and possible further information desired such as chemical identification or quantification. For crystalline samples high-angle annular dark field (HAADF) scanning transmission electron microscopy (STEM) generally fulfils the projection requirement and image acquisition times are relatively short, allowing a tomography experiment to be performed within a reasonable timeframe. Therefore, if HAADF STEM tomography can provide the desired information, there is usually little need for using another contrast technique.

In this chapter HAADF STEM tomography is applied to two types of samples. First we investigate nanowire heterostructures, to explore faceting of nanowires and the evolution of their cross section linked to changes in growth conditions as well as to analyze their composition. The shape and composition of nanowires governs their electrical and optical properties and knowledge about these parameters is therefore necessary to understand their behavior.[1]

In the second section of this chapter electron tomography is used for compositional analysis of Se-doped silicon. Doping of silicon with chalcogens (S, Se, Te) by femtosecond (fs)-laser irradiation to concentrations well above the solubility limit leads to near-unity optical absorptance in the visible and infrared (IR) range and is a promising route toward silicon-based IR optoelectronics. However, open questions remain about the nature of the IR absorptance and in particular about the impact of the dopant distribution and possible role of dopant diffusion. The higher mass of selenium compared to silicon allows using HAADF STEM tomography for acquiring information about local changes in dopant concentration in the material. We extract information about the three-dimensional distribution of selenium dopants

---

[1] This work presented in Section 7.1 was done in collaboration with Sam Crawford, Sung-Keun Lim and Silvija Gradečak (MIT). Nanowire growth and characterization apart from electron tomography were performed at MIT, parts of this section are reproduced from (Lim et al., 2013).

in silicon and correlate these findings with the optical properties of selenium-doped silicon. We quantify the tomography results to extract information about the size distribution and density of selenium precipitates.[2]

7.1 Nanowire Morphology and Composition

Semiconductor nanowires are quasi-one-dimensional single crystals that have emerged as promising materials for the development of photonic and electronic devices with enhanced performance (Li et al., 2006a, Thelander et al., 2006, Yan et al., 2009). Control of the nanowire composition and morphology is an ultimate goal in designing novel nanowire devices with functionalities that are superior to those of current thin film technologies. Spatial variation of the composition forms the basis of many functional devices, light-emitting diodes (LEDs) (Qian et al., 2005), lasers (Qian et al., 2008), high electron mobility transistors (Li et al., 2006b), and multijunction solar cells (Hamzaoui et al., 2005). Furthermore, diameter modulations along the nanowire axis could be used to enhance device performance, including improved light trapping by minimizing reflection and maximizing absorption (Fan et al., 2010), efficient thermoelectric conversion through increased phonon scattering in structures with multiple diameter modulations (Zianni, 2010), or enhanced field emission from thin nanowire regions with increased curvature (Pan et al., 2010). Simultaneous control over both composition and morphology would further expand the realm of possible nanowire architectures, but achieving this goal has so far been challenging or elusive.

Particle-mediated nanowire growth, by either the vapor-liquid-solid (Wagner and Ellis, 1964) or vapor-solid-solid (Persson et al., 2004) mechanism, is a versatile technique in which the nanowire morphology depends on the size and shape of the metal seed particle. Using this approach, nanowire morphology can be modulated in several ways including self-organized oscillatory motion of the seed particle due to energetic instability at the vapor/liquid/solid (v/l/s) triple-phase boundary (Caroff et al., 2009, Ross et al., 2005), which can be promoted by impurities (Algra et al., 2008) and results in a high density of stacking faults (Caroff et al., 2009) or by using a template that confines the seed particle and limits the size of the particle/nanowire interface (Fan et al., 2010). Diameter changes have also been related to changes in

---

[2] This work presented in Section 7.2 was performed in collaboration with Matthew Smith and Silvija Gradečak (MIT) as well as Meng-Ju Sher, Mark Winkler and Eric Mazur (Harvard University). Sample preparation and optical characterization was done at Harvard University, cross-sectional TEM characterization was done by Matthew Smith (MIT) and Juan-Carlos Idrobo (Oakridge National Lab). This section is reproduced from (Haberfehlner et al., 2013b).

nanowire kinetics, but the fluctuations were attributed to the presence of defects (Chiaramonte et al., 2011).

On the nanowires investigated by electron tomography in this work, controlled modulation of both the diameter and the composition along individual (In,Ga)N nanowires was demonstrated through the modulation of the seed particle size by tuning the supply of precursors during the growth. This is a simple and versatile approach, which requires neither a template nor the introduction of impurities or other defects detrimental to the device performance. This idea was applied to demonstrate diameter modulation of binary InN and GaN nanowires and extended to grow composition- and diameter-modulated InN/InGaN axial heterostructure nanowires in the nonpolar [1-100] m-direction. III-V nitrides are of interest because of their superior optoelectronic properties and broad-range bandgap tunability that make them attractive material systems for a variety of heterostructure-based optoelectronic devices (Hamzaoui et al., 2005, Li et al., 2006b, Lim et al., 2009, Qian et al., 2005, 2008). In addition, nonpolar heterojunctions are predicted to play a critical role in realization of high-efficiency nitride-based optoelectronic devices (Koester et al., 2011, Speck and Chichibu, 2009, Waltereit et al., 2000), as they mitigate effects associated with the quantum-confined Stark effect observed in polar heterojunctions. III-V nitride axial heterostructures have been previously only reported in the polar [0001] c-direction (Guo et al., 2011, Rigutti et al., 2010); therefore the demonstration focuses on the synthesis of axial heterostructures in the nonpolar [1-100] m-direction. Analyzing composition, morphology, and growth rate of the (In,Ga)N heterostructures allows elucidating the underlying mechanisms controlling the structural evolution, which can be readily extended to other nanowire materials systems.

7.1.1 Investigated Samples

The samples investigated by electron tomography were grown after previous experiments have shown that adjusting the supply of group III precursors as well as group V precursors can be used to modify growth rate and diameter of GaN and InN nanowires and that trimethylgallium (TMG) pulses during InN nanowire growth influence both the diameter of the nanowire as well as its chemical composition (Lim et al., 2013).

For synthesis of the investigated nanowires quasi-periodic TMG pulses were applied during m-directional InN nanowire growth. This process provided “caterpillar” shaped nanowires, with quasi-periodic diameter variations along the nanowire axis.

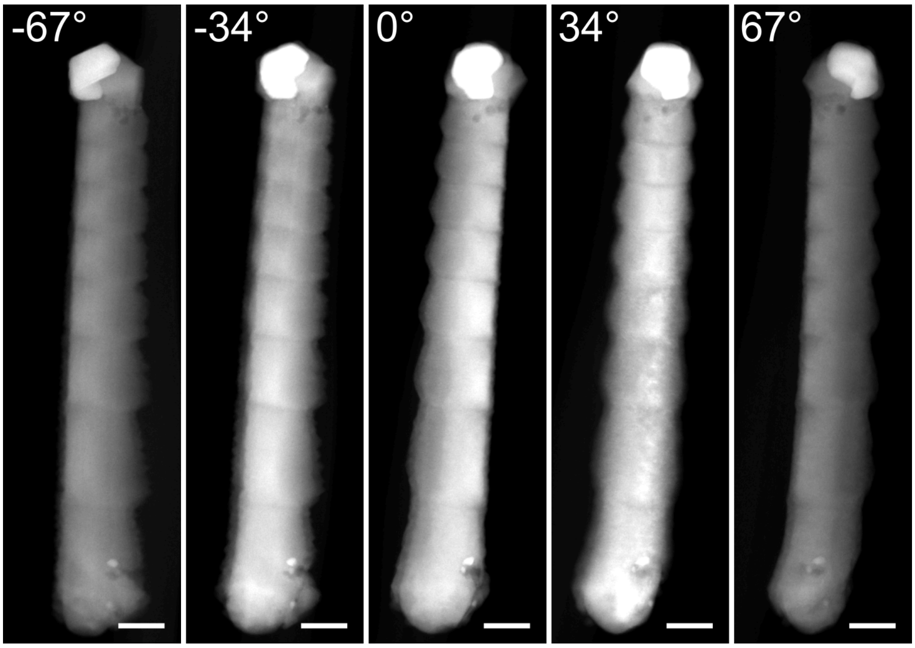

Figure 7.1: Projections acquired of periodic InGaN heterostructure nanowire. All scale bars represent 50 nm.

7.1.2 Electron Tomography Investigations

To understand the evolution of the nanowire diameter changes during growth and changes in the chemical composition, electron tomography was applied. For this purpose nanowires were transferred on a lacey-carbon grid and a tilt series of HAADF STEM images of a caterpillar-shaped nanowire was acquired over a tilt range of ±67° with a tilt step of 1°. Fig. 7.1 shows some images of the acquired tilt series.

Alignment of the tilt-series was done by cross-correlation methods and reconstruction was performed with a SIRT algorithm using 20 iterations. Fig. 7.2 illustrates results from the tomographic reconstruction together with scanning electron microscopy (SEM) images acquired on a similar nanowire. Fig. 7.2a shows the timing of the TMG pulses applied during InN nanowire growth, Fig. 7.2b-e show surface rendered tomographic results and SEM images from different viewing angles. These results show that the volume changes in these nanowires heterostructures are accommodated by changes in relative nanowire facet lengths, which consequently alter the cross-sectional geometry along the nanowire in two distinctive steps (Fig. 7.2f). At position 1, the nanowire has a truncated triangular cross-section consisting of two {11-22} facets and a {0001} facet. Small truncated facets of the same family of planes ({11-22} and {0001}) in the corners of the nanowire become more dominant upon diameter reduction, first yielding a diameter reduction along the <11-22> direction (step I in Fig. 7.2g). Next, the upper {0001} facet broadens in addition

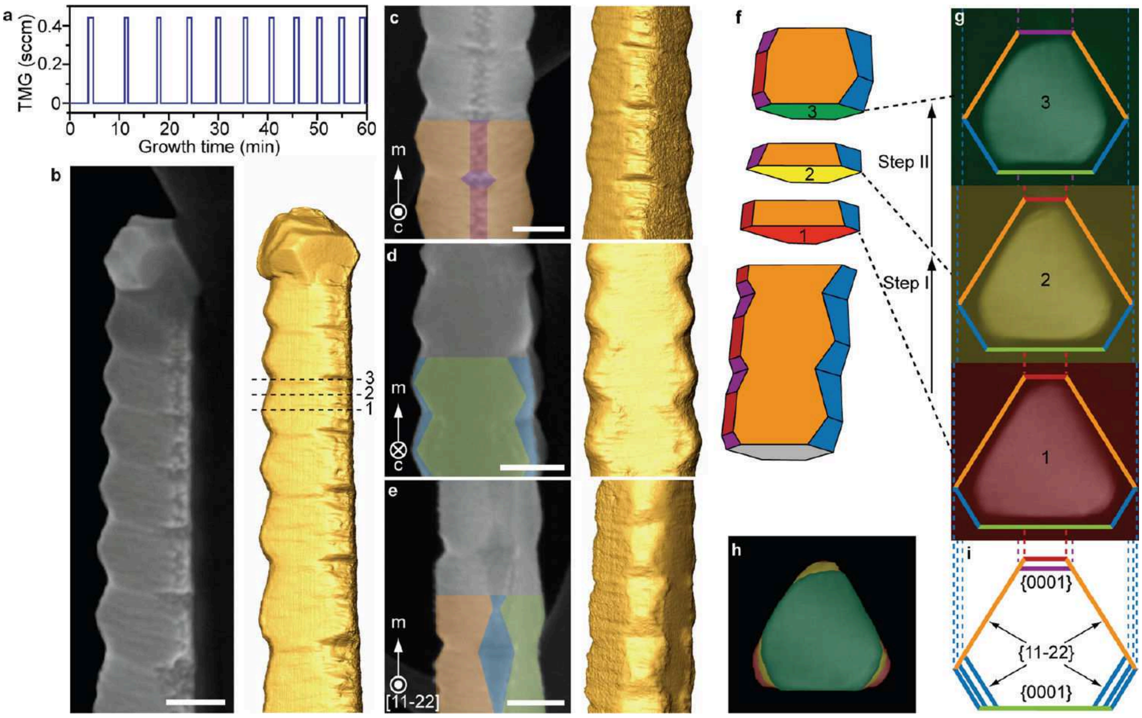

Figure 7.2: (a) TMG flow during nanowire growth of m-directional, caterpillar-shaped InN/InGaN axial heterostructures (in sccm, standard cubic centimeter per minute). (b) SEM image (left) and corresponding tomography reconstruction (right) of a caterpillar-shaped nanowire. (c-e) SEM images (left) and corresponding tomography reconstruction (right) of caterpillar-shaped InN/InGaN nanowires taken along two <0001> directions and one <11-22> direction, described by insets. Colors represent different facets defined in (i). (f) Reconstructed model of the nanowire morphology using the same facet color scheme as in (c-e). (g) Cross-sections at positions 1-3 extracted from the tomography results at the positions labelled in (b) and illustrated in (f). Colors of cross-sections and facets correspond to those in (c-f). The facet inclination in the upper left corner of the reconstructed cross-sections is an artifact resulting from the limited tilt range of the tomography series. (h) Overlaid cross-sections shown in (g) emphasize the evolution during steps I and II. (i) Identification of the nanowire facets and their two-step evolution. The "upper" {0001} and {11-22} facets are shown in red/purple and orange, respectively. The "lower" {0001} and {11-22} facets are shown in green and blue, respectively. All scale bars represent 50 nm.

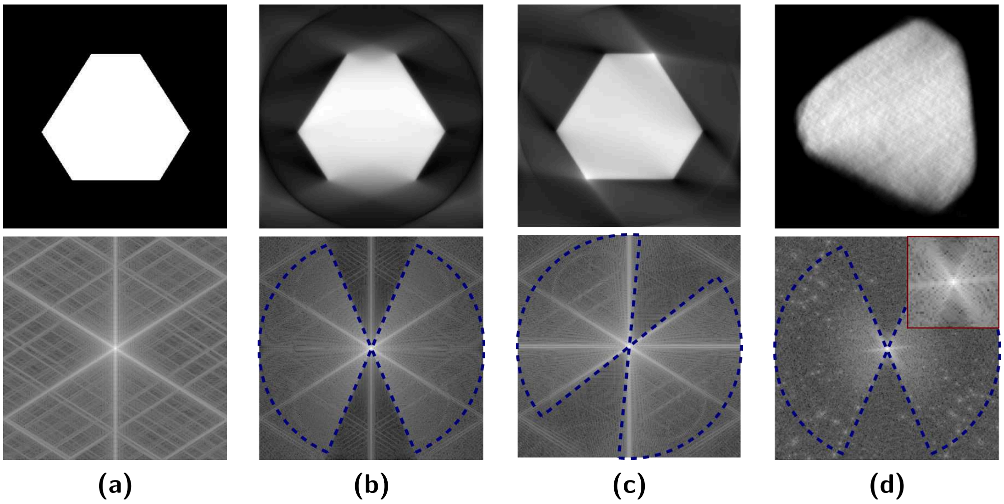

Figure 7.3: Evaluation of the impact of the missing wedge on cross sections of the caterpillar-shaped InN/InGaN nanowire. (a) Phantom created for simulations to evaluate the missing wedge artifact corresponding to modelled cross-sectional shape of the nanowire (top) and corresponding 2D Fourier transform (bottom). (b) Reconstruction of the phantom shown in (a) from projections taken over a tilt range of ±67° with the phantom oriented not favorable with respect to the missing wedge (top) and corresponding Fourier transform of the reconstruction (bottom). The sampled range of the Fourier space is indicated in the Fourier transform. (c) Reconstruction of the phantom shown in (a) from projections taken over a tilt range of ±67° with the phantom oriented favorable with respect to the missing wedge (top) and corresponding Fourier transform of the reconstruction (bottom). The sampled range of the Fourier space is indicated in the Fourier transform. (d) Slice through the experimental reconstruction of the nanowire in its original orientation (top) and corresponding Fourier transform (bottom) with a zoom on the central part (inset). The orientation of the sample with respect to the missing wedge is close to the most favorable orientation shown in (c).

to the lower corner {11-22} facets, yielding a highly truncated (almost hexagonal) nanowire cross-section in step II (Fig. 7.2g).

It is notable that, even though the tilt range for the tomographic series was only ±67°, the impact of the missing wedge in the reconstruction of the nanowire appears quite limited. To investigate this closer we did simulations on a phantom object corresponding to the modelled cross section of the InN/InGaN nanowire (see Fig. 7.3a). From the Fourier transform of this phantom object it is visible that the object is mainly defined by three lines through the spectrum oriented perpendicular to the orientations of the object's surfaces in real space. The phantom can therefore be well reconstructed if these frequency components are well sampled. For the given example of a tilt range of ±67° there exist two extreme cases for bad and good sampling conditions, which are shown in Figs. 7.3b & 7.3c respectively. In the first case

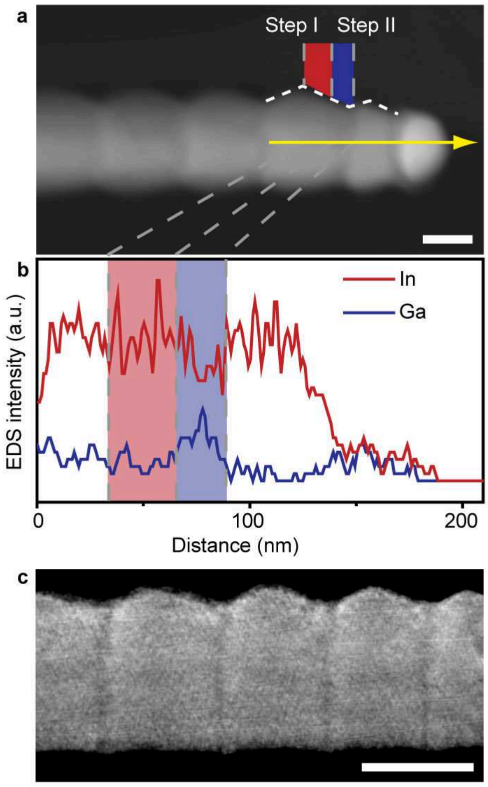

Figure 7.4: (a) DF-STEM image of an m-directional caterpillar-shaped InN/InGaN nanowire taken along the [0001] zone axis. (b) EDS linescan profiles of In and Ga along the yellow arrow in (a). The regions corresponding to Steps I and II of the cross-sectional shape evolution are indicated by red and blue, respectively, which also corresponds to regions with greater In (red) and Ga (blue) content, respectively. (c) Slice along the tomographically reconstructed nanowire. The darker contrast in the thin-diameter regions indicates greater Ga content. All scale bars represent 50 nm.

(see Fig. 7.3b) surfaces of the nanowire are oriented exactly perpendicular to the electron beam at a tilt angle of 0°. The frequency components defining these surfaces lie therefore inside the missing wedge and cannot be reconstructed. In the second case (see Fig. 7.3c) the nanowire is rotated by 30° with respect to the electron beam at a tilt angle of 0°. Therefore none of the major three lines in the spectrum lies inside the missing wedge and the nanowire can be well reconstructed. In the present experiment the conditions were very close to this favorable case as is illustrated for a cross-section from the experimental reconstruction in Fig. 7.3d.

In addition to morphological information electron tomography also allows recovery of compositional information. Fig. 7.2 shows a slice through the tomographic reconstruction as well as results from an energy-dispersive x-ray spectroscopy (EDS) line scan along a nanowire. Both results show that Ga is localized within the thin diameter regions (Fig. 7.4), corresponding to step II of the morphology evolution. In the tomographic reconstruction the slightly darker areas in these regions can be attributed to a higher Ga content due to its smaller atomic mass compared to In.

These results allow explaining the two-step cross-section evolution and associated volume changes along the axial heterostructure nanowires. It is suggested that step I occurs during Ga incorporation into the seed particle, while step II occurs during InGaN solidification. In step I, TMG is introduced and Ga incorporates into the seed particle, but InGaN is not yet formed. The lower {11-22} facets expand at the expense of the upper {11-22} facets and the lower {0001} facet. Due to the inherent c-directional polarity in nitrides, the polarity of the upper and lower facets is opposite. The relative abundance of III and V species on surface facets affects the relative stability of facets of different polarity within the same family (Joyce et al., 2011) as well as the stability of {0001} facets (Northrup and Neugebauer, 1999). Thus the presence of Ga adatoms on the side wall facets is presumably responsible for the changes observed in step I. In step II, the formation of InGaN yields abrupt changes in facet energies and is coincident with the broadening of the upper {0001} facet. The most stable {0001} facets for InN and GaN have been observed to be (000-1) and (0001), respectively (Hiramatsu et al., 2000, Jain et al., 2008). It is therefore suggested that the lower facet is (000-1), and the upper (0001) facet is stabilized as Ga is incorporated into the nanowire.

7.2 Selenium Segregation in Femtosecond-Laser Hyperdoped Silicon

Enabling silicon to absorb in the infrared range is of great interest for silicon-based infrared optoelectronic devices (Carey et al., 2005). One route toward tailoring of the optoelectronic properties of silicon is doping with chalcogens (S, Se, Te) to concentrations well above the solubility limit. This process, known as optical hyperdoping, can produce broad-band absorption in the IR range. Optical hyperdoping can be obtained by the irradiation of silicon with fs-laser pulses in the presence of a dopant precursor, either a gas-phase precursor such as sulfur hexafluoride (SF_6) (Wu et al., 2001, Younkin et al., 2003) or a thin film precursor (Sheehy et al., 2007, Smith et al., 2011a, Tull et al., 2009). When doping is done with conventional methods - for example, vapor diffusion or ion implantation (followed by annealing) - the dopant concentration is limited by their equilibrium solid solubility limit to $10^{16} - 10^{17}$ cm^{-3} (Vydyanath et al., 1978), while optical hyperdoping can yield concentrations in the range of $10^{19} - 10^{20}$ cm^{-3} (Sher et al., 2011).

It has been shown that the supersaturated concentrations of chalcogens give rise to strong sub-band gap absorptance in silicon (Sheehy et al., 2007), but the nature of the IR absorptance is still poorly understood. A useful approach to understanding how the dopant distribution influences the absorptance is through monitoring the decay in sub-band gap absorptance with annealing (Tull et al., 2009). It has been shown that the reduction of sub-band gap absorptance scales with both annealing time and temperature in a way that is proportional to the diffusion length of the dopant at a given annealing condition. The evolution of the chemical state of selenium with annealing has also been investigated by extended x-ray absorptance fine structure (EXAFS) spectroscopy and showed a shift in the chemical state of selenium with annealing that is closely related to the observed decay in sub-band gap absorptance (Newman et al., 2009). Despite the improved understanding of the diffusion-limited kinetics and changes in chemical state that occur during the annealing of selenium-hyperdoped silicon, no direct structural evidence of dopant diffusion or phase segregation has been observed.

Electron tomography based on STEM using a HAADF detector is an efficient method to distinguish between materials with differences in their atomic number and provides nanometer resolution in three dimensions (Midgley and Dunin-Borkowski, 2009, Midgley and Weyland, 2003). The sensitivity of HAADF STEM to the atomic number allows for the detection of heavy atoms in a lighter environment and is thereby well suited for studying the distribution of dopants with sufficient mass contrast. Segregation has been studied using electron tomography at a larger scale for the identification of germanium precipitates in an Al-Ge alloy using HAADF STEM (Kaneko et al., 2008) and for the studies of oxide precipitates in silicon using bright-field (BF) transmission electron microscopy (TEM) tomography (Schierning et al., 2011). Another frequently used method for studies of dopant segregation is atom probe tomography (Duguay et al., 2010, Jin et al., 2012, Thompson et al., 2005), but atom probe tomography is not suited for the present case due to the strong structural disorder caused by the doping process, which makes evaporation of the material difficult. For very small samples electron tomography has been shown to provide near-atomic resolution (Scott et al., 2012) and even atomic resolution in combination with prior assumptions about the object (Bals et al., 2010, Goris et al., 2012a, Van Aert et al., 2011). For larger samples measuring few 100 nm, the achievable resolution is in the nanometer range.

In this work we investigate the distribution of selenium in fs-laser doped silicon before and after annealing using HAADF STEM structural characterization. Cross-sectional investigations show inhomogeneous dopant distribution arising during fs-

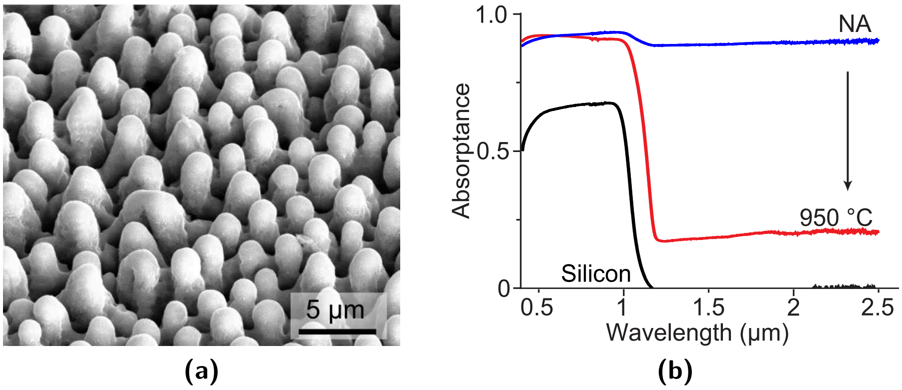

(a) (b)

Figure 7.5: (a) SEM image of fs-laser doped silicon before annealing. The surface is covered by micron-scale peaks, which are formed during laser irradiation. (b) Absorptance of Se-hyperdoped silicon without any post-treatment annealing (blue, from (Smith et al., 2011a)) and after a 30 min anneal at 950 °C (red), with the absorptance of an untreated silicon wafer for reference (black). Post-treatment annealing reduces the infrared absorptance.

laser doping and provide initial observations of selenium segregation with annealing. Next, electron tomography is used to measure the three-dimensional (3D) distribution of selenium before and after annealing. A segmentation process is developed for quantifying the density and size distribution of precipitates, which takes into account the inhomogeneous dopant distribution in the starting material. Comparing these segmented reconstructions allows for confirmation of a large increase in the density of small (radius ≈ 10 nm) precipitates and a decrease in the amount of selenium remaining in silicon as a solute.

7.2.1 Material Synthesis and Optical Characterization

To prepare selenium-hyperdoped silicon samples for this investigation, first a 75 nm film of selenium was deposited on boron-doped Si (100) wafers (resistivity $\rho = 1 - 20\ \Omega$ cm. Then, the wafers were irradiated with a 1 kHz train of 80 fs, 800 nm laser pulses with a fluence of 4 kJ/m^2 using 88 pulses per area. Post-irradiation annealing was done in a forming gas (5% H_2) environment. In this work, we compare the dopant distribution before and after annealing for 30 min at 950 °C. A more detailed description of the hyperdoping process has been published elsewhere (Tull et al., 2009). Fig. 7.5a shows a SEM image of the sample after doping. In addition to the incorporation of dopants, fs-laser doping also modifies the surface, producing a rough surface covered by periodic micron-scale peaks (Tull et al., 2006). Crystalline silicon in the doped surface is transformed to different types of polycrystalline silicon, which is attributed to pressure-induced phase transformations (Smith et al., 2011b, 2012).

Optical properties of the samples before and after annealing have been investigated by measuring the IR absorptance with a UV-VIS-NIR (ultraviolet-visible-near infrared) spectrophotometer equipped with an integrating sphere (Smith et al., 2011b, Tull et al., 2009). The diffuse and specular reflectance (R) and transmittance (T) were measured, in 1 nm increments, to determine the absorptance ($A = 1 - R - T$) at each wavelength. Fig. 7.5b shows the measured absorptance for the investigated samples. The modified sample morphology influences the optical properties of silicon, increasing the absorptance due to enhanced geometrical light trapping (Sher et al., 2011). More importantly, the nonannealed sample shows near-unity absorptance for the whole investigated spectral range, extending well below the band gap, while for the 950 °C annealed sample the sub-band gap absorptance is reduced to below 0.25. This annealing condition represents the extreme case; lower annealing temperatures and shorter annealing times provide samples with intermediate absorptance (Tull et al., 2009).

7.2.2 Sample Preparation

Cross-sectional TEM samples were prepared using a South Bay Technology Model 590 tripod polisher and diamond polishing films on a Struers Labopol-4 polishing wheel. Final thinning of cross sectional samples was carried out with an Ar^+-ion mill at 5 kV in a Gatan Precision Ion Polishing System.

Sample preparation for electron tomography was done in a FEI Strata dual-beam focused ion beam (FIB)/SEM. The instrument is equipped with an in situ gas injection system with sources for deposition of silicon dioxide and tungsten as well as with a micromanipulator for extraction of the sample. The principles of sample preparation are shown in Fig. 7.6. The goal of the preparation was to prepare a needle-shaped sample from the center of one of the peaks of the material, with a diameter of about 150 nm and a height of few micrometers. This type of sample preparation is now commonly used in electron tomography (Kawase et al., 2007, Ke et al., 2010, Yaguchi et al., 2004) as needle-shaped samples maximize the tilt range for tomography while keeping the sample thickness along the electron beam path small for all tilt angles. Preparing a relatively long needle allows the extraction of information about changes in sample composition with depth.

A protective stack, consisting of electron deposited silicon dioxide, electron deposited tungsten, and finally ion deposited tungsten, was deposited on one of the micronscale peaks on the surface prior to milling. Then a standard lift-out technique

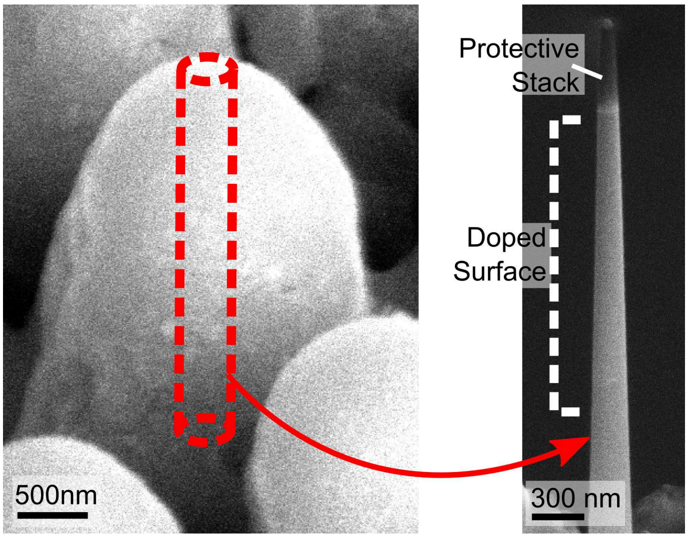

Figure 7.6: Principle of the sample preparation for electron tomography: Needle-shaped samples are prepared from the center of peaks of the structured surface using a FIB/SEM instrument. The finished needle-shape samples contain a cylinder through the doped silicon surface.

is used to extract a lamella with a thickness of 1-2 µm containing the protected peak. The extracted lamella is glued to an Omniprobe TEM support grid. In contrast to standard TEM preparation, where the sample is usually glued to the side of one of the supporting posts of the TEM grid, we glued the lamella to the top of a support to prevent shadowing from the support at high tilt angles and to allow milling to a circular shape. To obtain a needle-shaped sample, annular milling at 30 kV was used, where the diameter of the milling pattern is reduced in several steps until a sample with a diameter of about 100 nm at the top remains. We abstained from finishing with ion milling at lower high tension, as this would reduce the inclination of sidewalls, thereby leading to a much larger sample diameter at the base of the peak. Our sample preparation produced samples with an inclination of the sidewalls of approximately 1.38°, causing the sample diameter to increase by 45 nm every 1 µm along the depth.

7.2.3 Cross-Sectional TEM Investigations

Cross-sectional HAADF STEM characterization was conducted in a probe aberration-corrected FEI Titan 80-300 s microscope operated at 300 kV. The HAADF STEM image in Fig. 7.7a provides insights into the selenium distribution in a Se-hyperdoped region prior to annealing. Although HAADF STEM does not directly give chemical information, comparing Fig. 7.7a with previous investigations show that contrast changes observed in HAADF STEM images correspond to changes in the selenium

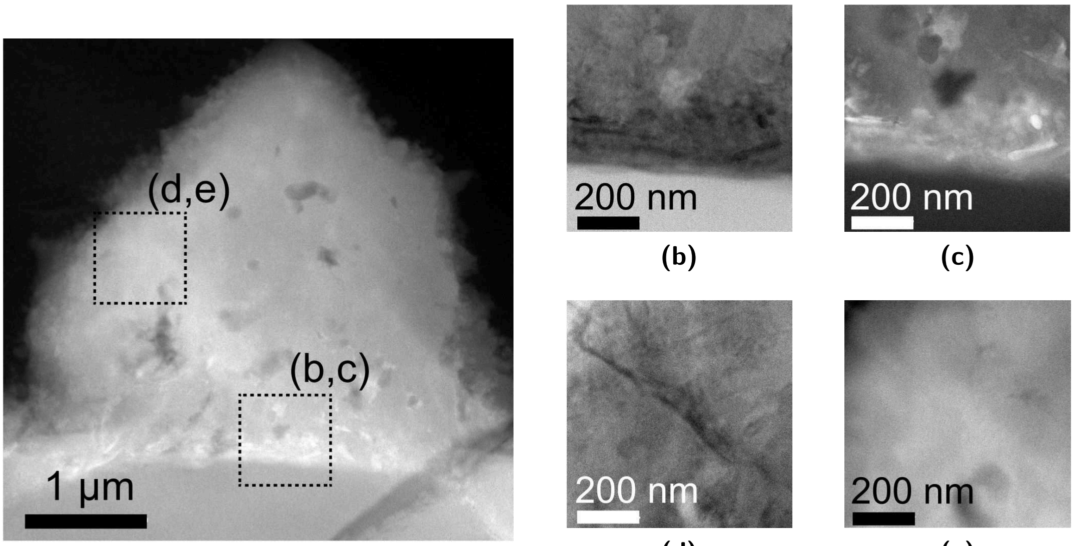

(a) **(b)** **(c)** **(d)** **(e)**

Figure 7.7: (a) HAADF STEM image of a peak on the non-annealed surface of selenium-hyperdoped silicon. Brighter contrast within the peak is due to increased concentrations of selenium. (b) Bright-field STEM image of the interface between the polycrystalline hyperdoped region and the undoped silicon substrate, from region indicated in (a). (c) HAADF STEM image of the interface in (b), showing diffuse contrast due to increased selenium concentrations, with some segregation already visible. (d) BF-STEM image of a grain boundary within the polycrystalline region. (e) HAADF STEM image of the grain boundary in (d), showing no visible signs of segregation. The dark spots visible in the HAADF STEM image are voids.

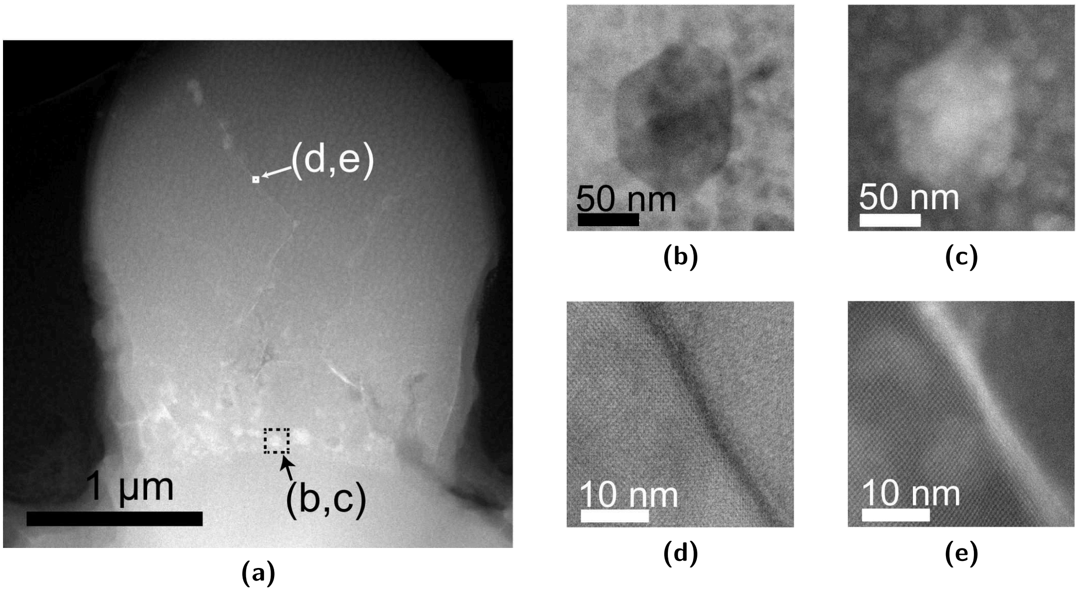

Figure 7.8: (a) HAADF STEM image of a peak on the surface of selenium-hyperdoped silicon that was annealed for 30 minutes at 950 °C. The base of the peak contains precipitates of selenium-rich material and segregation to grain boundaries in the body of the peak is also visible. (b) Bright-field STEM image of a faceted Se-rich precipitate, from region indicated in (a). (c) HAADF STEM image of the precipitate in (b), confirming that it is selenium rich. (d) BF-STEM image of a grain boundary within the polycrystalline region. Region indicated in (a) is a best estimate of the image position. (e) HAADF STEM image showing selenium segregation to grain boundary in (d). Lighter contrast visible in (c) and (e) is ion beam damage due to sample preparation.

concentration in silicon (Sheehy et al., 2007, Smith et al., 2011a). Se-rich regions give brighter contrast due to the higher atomic number of selenium compared to silicon. The selenium concentrations are highest at the base of the peak, where the image contrast is diffuse and noticeably inhomogeneous (Figs. 7.7b&7.7c). The contrast is also inhomogeneous throughout the body of the peak, though this may be exaggerated by changes in sample thickness. Close investigation of a grain boundary prior to annealing suggests no visible grain boundary segregation (Figs. 7.7d&7.7e).

Annealing at 950 °C for 30 min produces significant selenium segregation to grain boundaries and the precipitation of selenium-rich material, as shown in Fig. 7.8a. At the base of the peak, where there was diffuse contrast before annealing, there is now a high density of selenium-rich precipitates, some of which exhibit faceting (Figs. 7.8b&7.8c). A HAADF STEM image of a grain boundary, from the region indicated in Fig. 7.8a, shows selenium segregation into a region that is ~3 nm thick (Figs. 7.8d&7.8e).

Comparing cross-sectional HAADF STEM images of the nonannealed selenium-hyperdoped silicon reveals an inhomogeneous selenium distribution within the surface peak. After annealing for 30 min at 950 °C, we see evidence of selenium segregation and precipitation with annealing. However, due to the complex 3D distribution of dopants, it is difficult to extract quantitative information about size and distribution of Se-rich regions from these cross-sectional images. To confirm and improve our understanding of selenium segregation with annealing, we therefore use HAADF STEM tomography to map the selenium distribution in three dimensions.

7.2.4 Electron Tomography Investigations

Electron tomography was performed on a probe aberration corrected FEI 80-300 Titan microscope operated at 200 kV in HAADF STEM mode. A small convergence angle of 5 mrad was used to improve the depth of field (Hyun et al., 2008). Projections of the needle-shaped samples were acquired over a tilt range of ±78° using a linear tilt step of 1°. The tilt range was limited by the used sample holder. Projections were acquired with a size of 2048 × 512 pixels at a pixel size of 1.03 nm. The voxel size of the reconstructed volumes is equal to the pixel size of the projections. Alignment of the tilt series was done by cross correlation using the FEI Inspect3D software. For the reconstruction a Matlab-based implementation of the simultaneous iterative reconstruction technique (Gilbert, 1972) with 20 iterations was used. For processing and visualization of the reconstructed volumes Matlab, ImageJ, and Avizo were employed.

To enable the comparison of different reconstructions, we normalized the contrast in each reconstruction relative to two reference values; the mean value of the vacuum outside of the sample (set to 0) and the mean value of the undoped region in the bottom of the peaks (set to 1). The values of all voxels were normalized relative to those two values. Quantification of the selenium concentration would require both an exact knowledge of the Z-dependence of the contrast (Van Aert et al., 2009, Van den Broek et al., 2012) and detailed understanding of how selenium is incorporated in the silicon crystal structure. Therefore, in this investigation we concentrate on qualitative observations and, in particular, on the evolution in dopant distribution with annealing.

Fig. 7.9 shows volume rendered views and slices through the reconstruction of the nonannealed sample. In agreement with the observations of the cross-sectional sample, the concentration of dopants is highest at the base of the peak. In the nonannealed sample, we observe diffuse contrast throughout the doped region, indicative of solid solution selenium incorporation and also some clusters of selenium-rich material. After a 30 min 950 °C anneal (Fig. 7.10), the dopant distribution is strongly inhomogeneous. We observe selenium segregation to grain boundaries as well as a

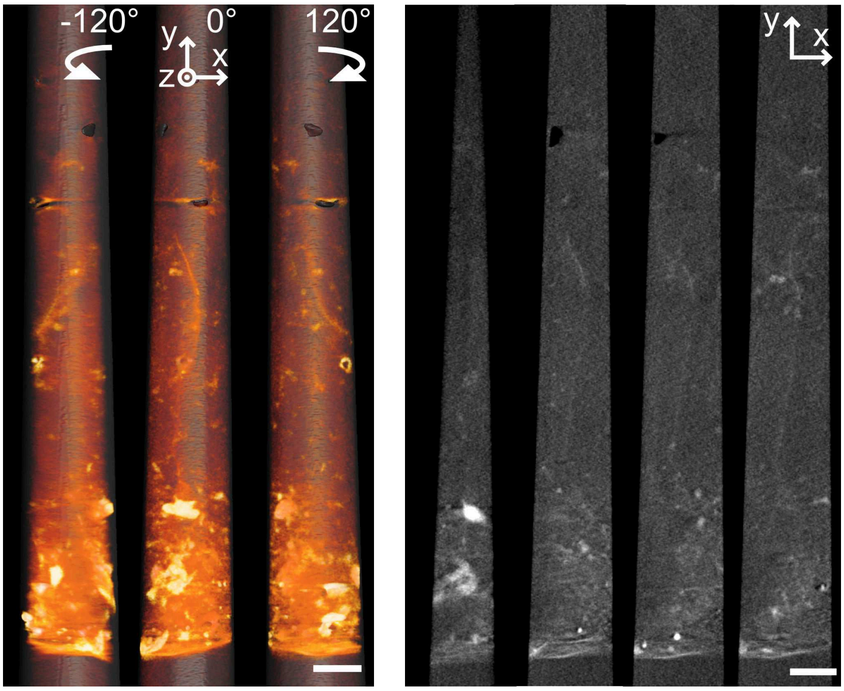

(a) (b)

Figure 7.9: 3D reconstruction of the non-annealed sample: (a) Volume-rendered view from different viewing angles. Brighter regions correspond to higher selenium concentration. (b) Slices through the reconstructed volume at different locations along the z-direction. Diffuse contrast is visible at the base of the sample with some Se-rich precipitates. The selenium concentration increases towards the base of the sample. Scale bars are 100 nm.

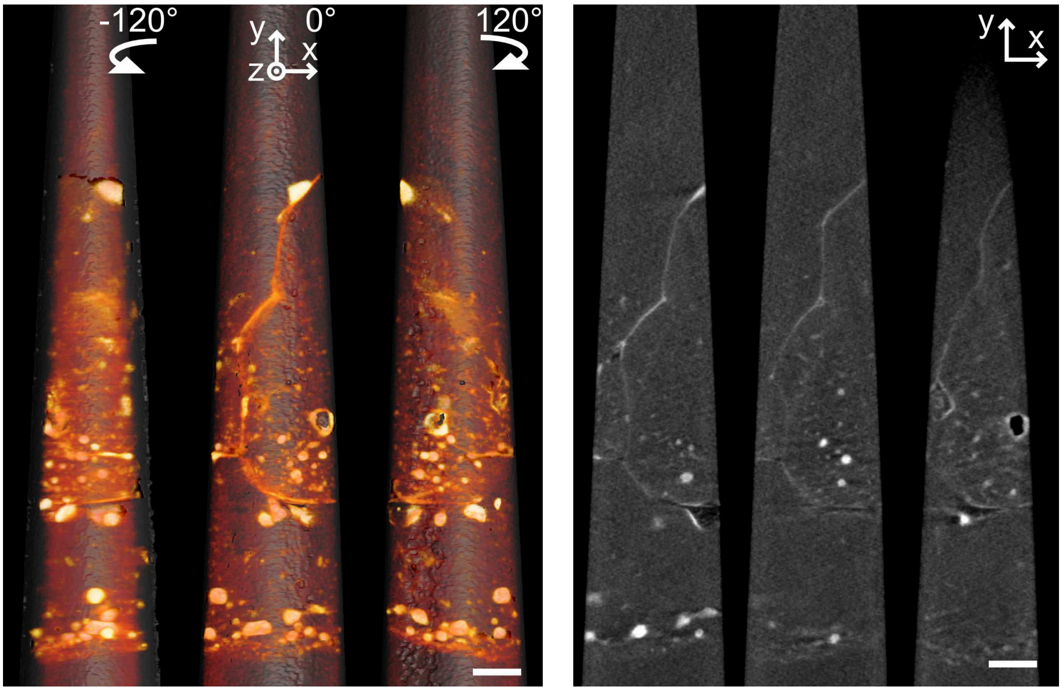

(a) (b)

Figure 7.10: 3D reconstruction of the sample annealed at 950 °C for 30 min: (a) Volume-rendered view from different viewing angles. Brighter regions correspond to higher selenium concentration. (b) Slices through the reconstructed volume at different locations along the z-direction. Strong signs of precipitation and segregation to grain boundaries as well as to voids are visible. The diffuse contrast is reduced compared to the non-annealed sample. Scale bars are 100 nm.

large number of selenium-rich precipitates, in particular at the base of the peak, but also in the vicinity of the grain boundaries. Furthermore, the collection of this high resolution structural information in three dimensions enables the quantification of dopant segregation with annealing.

7.2.5 Segmentation of Dopant Segregation

To extract quantitative information about the different types of segregation – to grain boundaries, and to voids – and precipitation we must first segment the reconstructed volumes into selenium rich and non selenium rich regions. For the segmentation procedure, we used preprocessing steps for the normalization and filtering of the volumes combined with a gradient watershed segmentation algorithm (Adams and Bischof, 1994, Fernández, 2012). An evaluation of the proposed segmentation method and on effects of missing wedge artifacts for a simulated object can be found in Appendix B.

Other methods – such as discrete tomography (Bals et al., 2007, Batenburg et al., 2009) or total variation (TV)-minimization based reconstruction (Goris et al., 2012b, Saghi et al., 2011) – use prior knowledge about discreteness of the material phases in the sample to combine reconstruction and segmentation or to obtain a filtered volume in the case of discrete tomography and TV-minimization based reconstruction, respectively. In our case, we decouple reconstruction and segmentation, as no discrete interfaces of selenium-rich material throughout the sample are expected due to the nature of the dopant incorporation and segregation. In addition, in the segmentation process we focus on regions with bright contrast relative to their close surroundings, rather than defining a specific dopant concentration threshold of interest.

To more clearly illustrate this segmentation process designed for quantifying dopant segregation in a disordered environment and from an initially inhomogeneous distribution, Fig. 7.11 shows slices through the reconstructed volume before and after each step of the segmentation routine. The intensity profile, extracted along the indicated intersection, illustrates the evolution in signal noise from this segmentation process. Our segmentation routine consists of the following steps:

- *Normalization along height* (Fig. 7.11 (1) → (2)): Starting from the original reconstructed volumes, in the first step we compensate for changes in overall dopant concentration with height of the sample (y-direction), visible in particular for the nonannealed sample. With this normalization, we put the gray level of regions between precipitates to approximately constant values for the

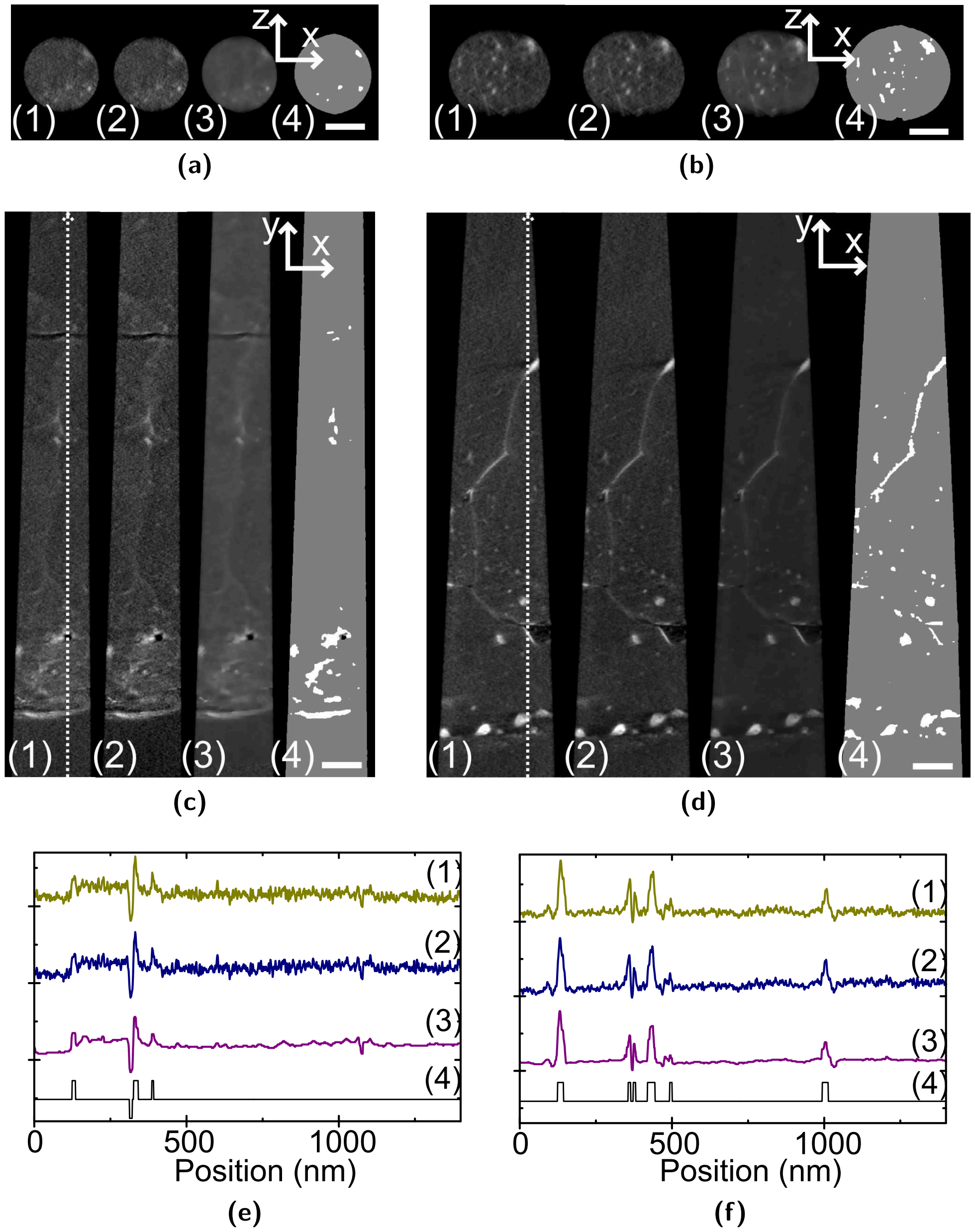

Figure 7.11: Steps of the data segmentation process (a) Slices through the non-annealed sample along an xz-plane, (b) Slices through the 950 °C annealed sample along an xz-plane. The slices along the xz-planes illustrate also effects of missing wedge artifacts. (c) Slices through the non-annealed sample along an xy-plane, (d) Slices through the 950 °C annealed sample along an xy-plane, (e) Intensity profiles along z-direction at the position indicated by a dashed arrow in (c), (f) Intensity profiles along z-direction at the position indicated by a dashed arrow in (d). The segmentation process starts from the original volume (1), to a volume normalized along the depth (2), to a volume filtered using an anisotropic diffusion filter (3) and finishes with the final segmented volume (4). Scale bars are 100 nm.

whole sample, thus compensating for the increasing concentration of selenium in solid solution toward the base of the peaks. This normalization allows emphasis on the regions that have a high dopant concentration relative to their close surroundings. For this purpose we calculate the mean intensity at each height in the sample and do a linear interpolation along the height. Then we normalize all values at a given height with the value extracted from the interpolation. This provides a volume with relatively constant gray values in the region between the Se-rich regions, which facilitates the following segmentation step.

- *Filtering* (Fig. 7.11 (2) → (3)): After the normalization we apply an anisotropic diffusion filter (Perona and Malik, 1990) to the volume to reduce noise in the reconstruction. A 3D version of the filter proposed by Perona and Malik, implemented in C, was used for filtering. Anisotropic diffusion filtering has been shown to be an efficient tool for edge-preserving denoising of electron tomograms and is frequently used in biological applications (Fernández et al., 2008, Fernández and Sam, 2005, Frangakis and Hegerl, 2001). The effects of filtering can be seen in the profiles, as the strong signals from segregated regions are conserved, while regions in between are smoothed.

- *Segmentation* (Fig. 7.11 (3) → (4)): For the actual segmentation we use a gradient watershed algorithm (Adams and Bischof, 1994). Related segmentation methods have been proven efficient for segmentation of electron tomograms of biological samples (Fernández-Busnadiego et al., 2010, Salvi et al., 2008, Volkmann, 2002). Segmentation is done using the Avizo software. First, regions with a large gradient are masked in such a way that transition regions between the materials are defined and will be subject to automated segmentation. In the remaining volume, seed regions, which belong to a specific material, are defined based on absolute threshold values. These two steps necessitate input from the user to define the threshold for the gradient mask and to set the ranges for the threshold value. For the actual segmentation a watershed transform is applied to the gradient volume to allocate masked voxels and voxels lying between the thresholded intervals. The watershed transform sets the boundary between seed regions of different materials to the position of the highest gradient.

This process produces volumes in which Se-rich regions are discretely separated from other regions of silicon. We can identify precipitation of selenium, segregation at grain boundaries and segregation toward the exposed surfaces of voids. Fig. 7.12

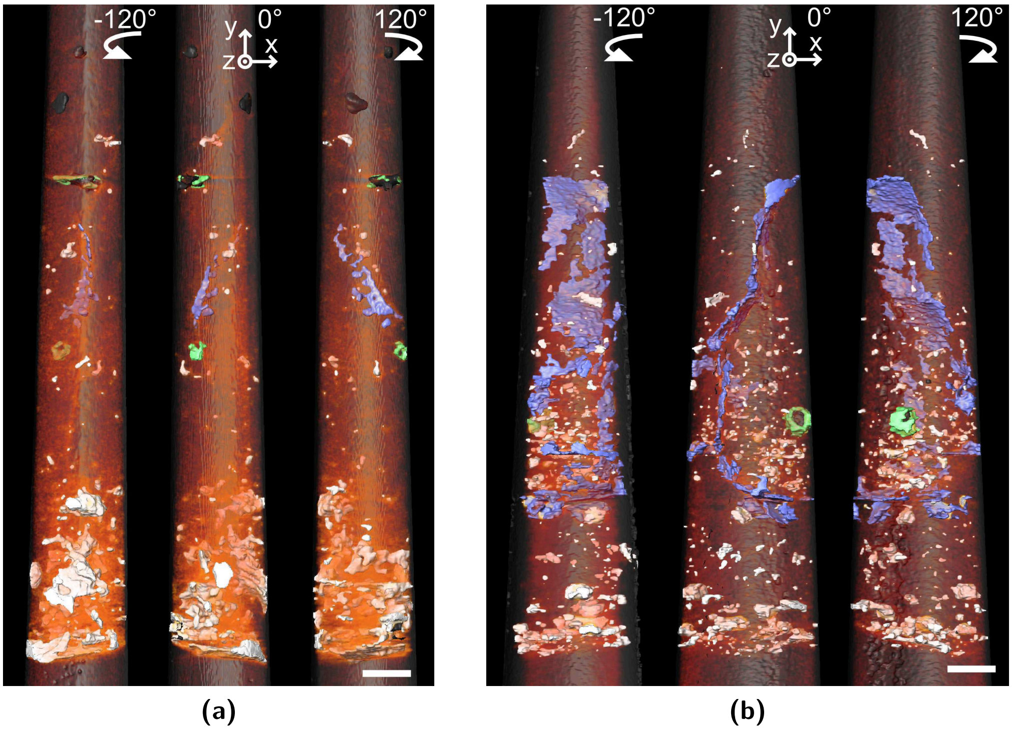

Figure 7.12: Surface rendered views of segmented reconstructions overlaid with volume-rendered views for (a) non-annealed sample, (b) 950 °C annealed sample seen from different viewing angles. The volumes shows precipitates (white), segregation at grain boundaries (blue) and segregation at voids (green). Scale bars are 100 nm.

shows the results of the segmentation, using different colors for the three types of segregation. This segmentation allows us to move forward quantifying the effect of annealing on segregation of selenium from the supersaturated silicon.

7.2.6 Quantification of Dopant Segregation

Qualitative inspection of the volumes reconstructed before and after annealing reveals results consistent with the previous cross-sectional TEM investigations: differences can be observed in the number of precipitates, which increases significantly with annealing, and also in the contrast observed in the material between the Se-rich regions, which is significantly lower in the annealed sample. Motivated by these qualitative observations, we extract quantitative information about the size and density of precipitates and the change in selenium concentration in solid solution in the regions between precipitates.

- *Precipitate size and density:* For this measure we focus only on precipitates to get information about their size and distribution, excluding segregation to

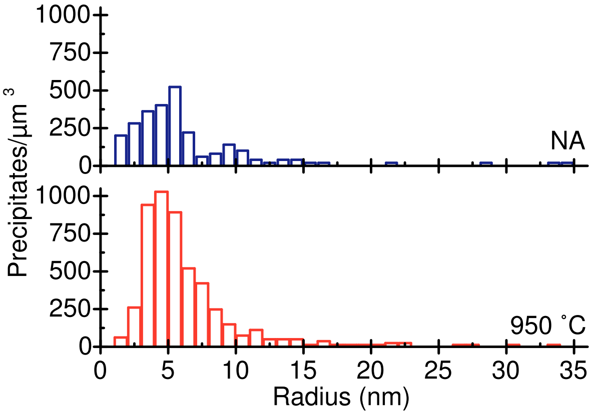

Figure 7.13: Size distribution of precipitates before annealing (blue) and after a 950 °C anneal for 30 minutes (red). The number of precipitates has been normalized by the overall volume measured to take into account the slightly different volumes characterized. The size distribution shows a significant increase in the density of precipitates with annealing.

grain boundaries and voids. For this purpose the volume of each precipitate is extracted using the 3D object counter plugin for ImageJ. The volume of each precipitate is transformed to an equivalent radius of a sphere with the corresponding volume. The number of precipitates is converted to a precipitate density distribution by normalizing the number of precipitates with respect to the total volume of the investigated sample. The resulting size distribution for both samples is shown in Fig. 7.13. We observe a significant increase in the density of precipitates with annealing, in particular a large number of relatively small precipitates is present after annealing, with 67% of the precipitates having a radius $r = 5 \pm 2\text{nm}$. A drawback of this technique is that the sample volume is too small to get a sufficient amount of data to quantify the evolution of larger precipitates $r > 10\text{nm}$ with annealing.

- *Background dopant concentration:* The segmented volumes can also be used to extract information about the dopant concentration in the regions between segregates. This process is shown in Fig. 7.14a. We create a mask of all voxels that are attributed to silicon but which are not identified as being Se-rich. Then a morphological erosion operator in 3D is applied several times on this mask using the ImageJ plugin 3D Toolkit. This step removes voxels close to the boundary of the volume and close to segregates. This mask is overlaid with the original reconstructed volume. The masked volume then contains only regions that are not Se-rich and therefore provides information about

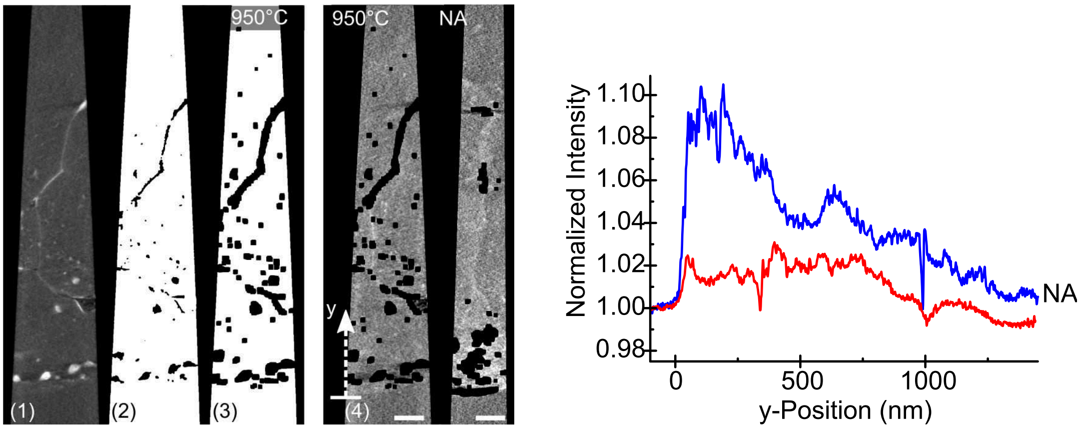

(a) **(b)**

Figure 7.14: (a) Quantification of dopant concentration in the region between segregates: (1) Slice through the original volume, (2) slice through the mask containing background voxels, (3) slice through the mask after morphological erosion for the 950 °C annealed sample, (4) slices through the masked volume for both samples (brightness/contrast settings are adapted compared to previous images): these voxels are used to calculate the normalized background intensity. (b) Normalized background intensity for the non-annealed sample (blue) and for the 950 °C-annealed sample (red) as a function of height. The distance is given from the interface to the undoped region towards the top of the samples as indicated in (a)(4). The extracted background intensity shows changes of dopant concentration with height for both samples and a reduction of dopant concentration in the region between segregates with annealing. Scale bars are 100 nm.

changes in the amount of selenium in this area. Fig. 7.14b shows the average intensity of each slice of the masked volume along the height for the two samples. The comparison of this background intensity shows clearly the changes of dopant concentration with height in both samples as well as the reduction of dopant concentration with annealing in the regions between precipitates, grain boundaries and voids.

We note, however, that the values extracted from quantification of electron tomography reflect only the behavior in a small volume, and this makes correlation of the observed trends on the nanoscale with bulk properties a challenge. However, complementary experiments, using a more global probe such as EXAFS spectroscopy, can be used to confirm the trends on a larger scale (Newman et al., 2009). Finally, very small precipitates ($r < 1 - 2$nm) cannot be detected due to the spatial resolution limit, which can be estimated to approximately 3 nm for the used number of projections (Midgley and Weyland, 2003). Therefore, segregation on atomic length scales is below the detection limits of electron tomography.

7.2.7 Results and Discussion

Our initial HAADF STEM investigations provide direct evidence of selenium precipitation and segregation with annealing, which supports previous hypotheses that diffusion-limited segregation is responsible for the optical deactivation of selenium with annealing (Tull et al., 2009). The HAADF STEM results highlight the potential significance of the nucleation and growth of a Se-rich phase during the optical deactivation process.

Characterization of a nonannealed sample using both cross-sectional TEM investigations and electron tomography allows for the identification of a representative microstructure and dopant distribution. Using Z-contrast to monitor the selenium distribution, we find an inhomogeneous distribution of dopants even before annealing. We observe an increasing concentration of dopants toward the base of the peak, until it reaches a relatively sharp interface with the unmodified silicon wafer underneath. A diffuse bright contrast is visible in the nonannealed sample, which indicates a solid solution of selenium in silicon (Figs. 7.7&7.9). Se-rich precipitates can also be observed, in particular at the base of the peak (Fig. 7.12a). The initial segregation of selenium from the supersaturated solid solution is likely a consequence of the annealing that occurs during scanning of the pulsed laser beam over the surface (Smith et al., 2012).

After annealing for 30 min at 950 °C, we observe more localized Se-rich regions, providing direct evidence of dopant precipitation and segregation in both cross sectional (Fig. 7.8) as well as in tomography investigations (Fig. 7.10). Electron tomography reveals a large number of small precipitates (Fig. 7.12b) and allows for quantification of their density and size distribution. Tomography shows that the size and number of these precipitates decreases toward the top of the peak, where there was less selenium observed in solid solution in the nonannealed sample. Quantification of the size distribution and density of precipitates (Fig. 7.13) confirms the formation of a large number of precipitates with annealing. The precipitates form throughout the investigate volume and in a larger number in the region with a higher initial supersaturation (bottom of the peak). In addition to the formation of new precipitates possibly also segregation to existing precipitates can occur.

Grain boundary segregation is observable by comparing the Z-contrast of a grain boundary in the nonannealed and 950 °C annealed samples. Close investigation of grain boundaries in the cross-sectional nonannealed sample (Figs.7.7d&7.7e) showed no signs of segregation, while in the annealed sample a few-nm-thick Se-rich layer is visible at the grain boundary (Figs. 7.8d&7.8e). Similar trends are observed in the tomography reconstructions. Though here the reconstruction of the nonannealed sample (Figs. 7.9&7.12a) shows weak signs of segregation at a grain boundary, in the annealed sample (Figs. 7.10&7.12b) segregation is significantly enhanced and a Se-rich layer is clearly visible at the grain boundary.

It is understood that the sub-band gap absorptance shown in Fig. 7.5b arises due to high concentrations of chalcogens being incorporated into silicon as a metastable, supersaturated, solid solution (Sheehy et al., 2007). Therefore, it is the decrease in supersaturation of silicon that is directly related to the optical properties of the material. The quantification of the contrast in the silicon matrix (Fig. 7.14) shows a significant reduction with annealing, which corresponds to a lower amount of selenium supersaturation in the annealed sample as compared to the nonannealed sample. In particular in the most highly doped regions, toward the base of the cylinder, this contrast arising due to selenium supersaturation is several times higher in the nonannealed sample than in the annealed sample.

The studies performed here provide elemental confirmation of chalcogen diffusion and segregation occurring as sub-band gap optical absorptance decreases. Previously this theory enjoyed only circumstantial support (Tull et al., 2009). We observe the precipitation of dopants and segregation toward grain boundaries and voids, while at the same time the concentration of dopants in the material between the precipitates, grain boundaries and voids decreases. The observations support the theory of diffusion-limited segregation being a major driving force behind the reduced sub-band gap absorptance with annealing, specifically during relatively long annealing at high temperatures.

Combined with volume segmentation methods, electron tomography can be used for quantitative investigation of a large number of small precipitates and also to monitor changes in contrast of the surrounding matrix. With a proper calibration sample, it may be possible to use the contrast observed in HAADF STEM tomography to quantify the composition of the segregating phase and the surrounding supersaturated matrix.

7.3 Conclusion

In this chapter electron tomography based on HAADF STEM contrast has been used for understanding the mechanisms behind a flow-controlled approach for the growth of diameter- and composition-modulated nanowire heterostructures and to reveal selenium segregation in fs laser-doped silicon.

The described flow-controlled approach to nanowire growth provides a foundation for controlled synthesis of complex nanowire architectures, by varying both III and V sources during nanowire growth. In the exploration of the process, electron tomography served as an important tool, which allowed recovery of the faceting of the nanowire and thereby the proposition of a growth model for the nanowire.

Selenium segregation and precipitation observed with annealing in fs laser-doped silicon is likely a critical mechanism behind the reduced IR absorptance of silicon hyperdoped with chalcogens with annealing. Through 3D investigations using electron tomography based on HAADF STEM, we observed precipitation and segregation to grain boundaries and to voids. Quantification of the distribution of dopant-rich regions can provide insight into the kinetics of dopant precipitation and segregation, and eventually such methods could be also extended toward absolute quantification of dopant concentration.

HAADF STEM tomography is demonstrated as a useful technique for both morphological and compositional 3D analysis, if mass contrast is sufficiently large. This is not always the case as will be shown on an example in the next chapter. Applications with little mass contrast therefore require the application of other TEM contrast techniques for tomography.

8 Low-Loss EFTEM Tomography

As shown in the previous chapters HAADF STEM tomography is a useful tool for distinguishing different materials, if they provide sufficient contrast by their mass difference. However not all material systems fulfil this criterion. When HAADF STEM contrast is too low, other contrast mechanisms need to be applied. In this chapter we investigate Si/Al_2O_3/TiN core-shell nanowires, which form the basis of nanostructured capacities. While these materials have only small differences in their mass, their electronic structure is quite different, which gives rise to differences in their bulk plasmon peaks. We used these differences for 3D elemental characterization by low-loss energy-filtered transmission electron microscopy (EFTEM) tomography doing four-dimensional spectral tomography of the nanowire-based capacitors. This method allows reconstructing local low-loss spectra within the whole device giving access to the chemical distribution. We used this capability to extract information about plasmon peaks from the different materials within the nanowire leading to the reconstruction of a three-dimensional model of the device. Additionally the reconstructed low loss spectra are compared to spectra acquired in classical two-dimensional (2D) scanning geometries across the whole nanowire and across a thin FIB-prepared lamella of the nanowire.[1]

8.1 Introduction

Silicon nanowires (Hayden et al., 2008, Lu and Lieber, 2007) have been proposed as promising candidates for device miniaturization in nanoelectronics. Their specific geometries are ideal to build 3D nanostructured devices like gate-all-around transistors (Nam et al., 2009), nanosensors (Cui et al., 2001), large capacitors or energy storage devices (Chan et al., 2008), which could be integrated or stacked on the same complementary metal-oxide-semiconductor (CMOS) chip (Lu, 2009).

---

[1] Nanowire growth, device elaboration and electrical characterization has been performed by Paul-Henry Morel, Vincent Jousseaume, Murielle Fayolle-Lecocq, Charles Leroux, Thiery Baron, and Thomas Ernst. Sample preparation of cross sectional samples and 2D EFTEM investigation have been done by Guillaume Audoit and Dominique Lafond. Parts of this chapter are reproduced from (Haberfehlner et al., 2012) and (Morel et al., 2012)

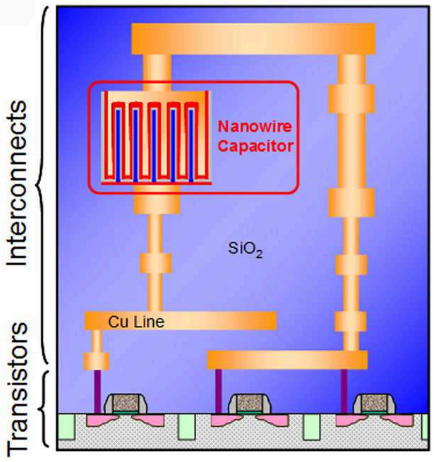

Figure 8.1: Nanowire capacitor in the interconnect level above the transistors in a microelectronic chip

For decoupling capacitors or energy storage devices, the capacitance density should be maximized, to minimize the chip area needed for their integration. One scheme for the integration of such capacitors, which can provide high capacitance densities is to use vertically grown silicon nanowires as basis for a capacitor, which can be located in the interconnect level of an integrated circuit (IC), as shown in Fig. 8.1. However to allow the integration of such devices all processes used need to be compatible with CMOS technology. This implies in particular the use of low temperature processes (< 450 °C), as well as the use of compatible materials. Previous demonstrations of integrated interconnect level capacitors feature capacitance densities up to 3.5 µF/cm^2 using high-κ dielectrics combined with 3D structuring (Bajolet et al., 2005). Using such capacitors, an area of about 3.8×3.8 mm^2 would be required for a decoupling capacitor of 0.5 µF (Black et al., 2004), which means a very large area consumption on today's integrated circuits. Indeed, the capacitance density (C_d) of a planar structure is given by

$$C_d = \frac{\varepsilon\ S}{d\ A} \tag{8.1}$$

where ε is the dielectric constant, S the electrode surface, d the dielectric thickness, and A the top view area occupied by the device. The electrodes nanostructuration combined with a high-κ dielectric is thus a great opportunity to increase the capacitance density by making three dimensional large surface devices. Up to now, many techniques have been reported using either silicon etching (Chang et al., 2007, Huang et al., 2011, Klootwijk et al., 2008, Morton et al., 2008, Zschech et al., 2007) or nanostructure growth (Li et al., 1999, Lu and Lieber, 2007, Wagner and Ellis, 1964, Wang et al., 2006). In principle, these techniques provide high density capacitors since they improve the S/A ratio. However, when silicon substrate etching is used, some of these approaches are limited by the substrate surface consumption, which should be dedicated to transistors. Moreover, nanostructures are either composed of carbon nanotubes (Choi et al., 2010) with a maximum reported capacitance density of 0.62 µF/cm^2, or nanoporous alumina (Banerjee et al., 2009) with 100 µF/cm^2. Unfortunately, the latter is not easily compatible with integration in the CMOS interconnections since its formation uses an anodization process which requires a backside electrical contact. Moreover, the reported devices work only at a frequency lower than 100 Hz.

The devices investigated here make use of silicon nanowires grown in the interconnect levels of an integrated circuit. This concept takes advantage of the highly developed surface of a nanowire assembly grown on a metal to get high density metal-oxide-semiconductor (MOS) capacitors. The nanowires have been grown using a low temperature growth (< 425 °C) with copper as a catalyst (Renard et al., 2009) to be compatible with CMOS interconnects. The obtained devices with alumina and conformal metallisation have a capacitance density of 18 µF/cm^2. This demonstration prefigures a next generation of energy storage components (Arico et al., 2005) or ultra-dense decoupling capacitors (Detalle et al., 2010, Roozeboom et al., 2000) for integrated circuits. This architecture with integrated high density capacitors will result in smaller and faster circuits and improved power management.

The fabrication of such nanodevices is challenging and involves many technological steps that must be controlled using the most advanced characterization techniques. Typically, probes enabling nanometer resolution and chemical sensitivity are required. Furthermore, the 3D arrangement of these devices imposes to have 3D imaging capabilities to measure the 3D elemental distribution at the nanometer scale. For the investigated devices in particular conformity of the alumina deposition is of importance for device performance.

Electron tomography is a well suited technique for this purpose. For materials science investigations, the most widely used imaging mode in a TEM for tomography is obtained by scanning the electron probe and using a HAADF detector (Midgley and Dunin-Borkowski, 2009, Midgley and Weyland, 2003). HAADF STEM is well suited for tomography, as the intensity in the images is largely insensitive to diffraction contrast, fulfilling thereby the projection requirement (Hawkes, 1992). Moreover, due to its sensitivity to the atomic number it could be used to distinguish between different materials for optimized systems. Indeed, HAADF STEM provides contrast between materials which have sufficient difference in their atomic number, if the difference in atomic number is too small, the contrast is too low and therefore

HAADF STEM cannot be used to distinguish the different materials. In that case another contrast mechanism needs to be used.

EFTEM is based on detecting the energy loss of electrons due to inelastic interactions with the materials. Images are recorded at different energy losses, the range being fixed by an energy window width. This technique was proposed for tomography (Midgley and Weyland, 2003, Möbus et al., 2003, Weyland and Midgley, 2003) as it provides chemical sensitivity combined with reduced diffraction contrast. In core-loss EFTEM the intensity of ionization edges, which stem from the excitation of inner shell electrons is recorded. The possibilities of core-loss EFTEM tomography have been highlighted: it permits the identification of different chemical elements and could allow three-dimensional elemental quantification. The typical energy losses of the electrons recorded are in the range of few tens to two thousands of electron volts. The cross section of the excitation decreases with energy loss leading to a reduction of the recorded core-loss signal for high energies. The main effect is that only ionization edges at not too high energy losses (well below 1000 eV) can be used for core-loss EFTEM tomography to keep image acquisition time acceptable. However even then image acquisition times are in the range of several tens of seconds. As this technique needs at least two images close to ionization energy per tilt angle for each investigated element (Verbeeck et al., 2004), the total acquisition time is very long.

By contrast EFTEM imaging in the low-loss region (< 30 eV) requires only few seconds for image acquisition. If the different materials investigated exhibit differences in their plasmon energy, this technique can be used to distinguish them by using only a single or very few images taken at energies close to their plasmon energy (Herzing et al., 2010, Yurtsever et al., 2006). This allows the acquisition of a tomographic series in a similar timeframe as using HAADF STEM tomography. Tomography can be combined with spectral imaging all over the low-loss range and a spectral tomography series can be acquired within a few hours. In principle, such a dataset can then be used to reconstruct four-dimensional data, providing a low-loss spectrum at each voxel (Gass et al., 2006).

8.2 Investigated Samples

The experimental procedure for the fabrication of the silicon based capacitors is illustrated schematically in Fig. 8.2a. The devices have been prepared on 8 inch Si wafers using standard industrial tools. First, a multilayer reproducing today's interconnect technologies composed of a 70 nm titanium nitride layer, a 20 nm

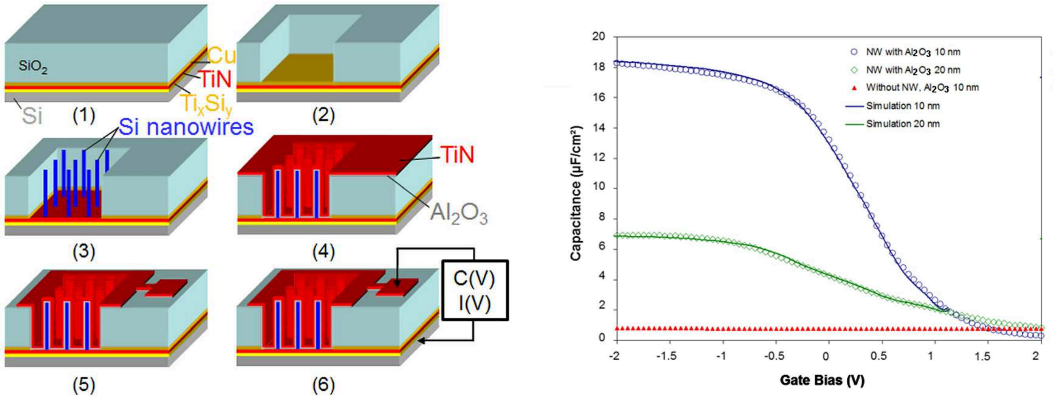

(a) **(b)**

Figure 8.2: (a) Integration flow for nanowires capacitor in the interconnect level: (1) Multilayer deposition stack composed of titanium silicide, titanium nitride, copper and silicon dioxide. (2) Photolithography and etching of the silicon dioxide to the copper. (3) Nanowire growth with copper as catalyst. (4) Optional nanowire cleaning followed by alumina and titanium nitride deposition. (5) Photolithography and etching to define the contact pads. (6) C(V) and I(V) measurements are performed between the top metal contact and the substrate backside. (b) Capacitance-voltage measurements and simulations of nanowire devices compared to a planar reference without nanowires. Measurements were acquired at ambient temperature and 1 kHz.

copper layer and a 1 µm silicon dioxide layer has been deposited on a silicon substrate (Fig. 8.2a(1)). The oxide was then patterned to open 100×100 µm^2 square windows toward the copper catalyst (Fig. 8.2a(2)). Silicon nanowire growth was then achieved at 425 °C in a chemical vapor deposition (CVD) reactor thanks to the oxidation of the copper catalyst as previously reported (Fig. 8.2a(3)) (Renard et al., 2009). Alumina (Al_2O_3) layers of 10 or 20 nm thickness were then deposited by atomic layer deposition (ALD) on different wafers to form the capacitor dielectric. For wafers with 10 nm thick alumina, a nanowire cleaning process (HF based) was performed before alumina deposition. A very conformal deposition of a 20 nm titanium nitride layer was achieved by using CVD, and was immediately followed by a 400 nm thick physical vapor deposition (PVD) of AlSi (Fig. 8.2a(4)). The last step of the process was the use of photolithography and etching to define electrical top contacts (Fig. 8.2a(5)). Devices were then ready for electrical characterizations using a backside electrical contact as shown in Fig. 8.2a(6). Fig. 8.2b shows results from electrical characterization for devices with 10 nm and 20 nm thick Al_2O_3 layers.

Electron tomography was performed on nanowires with a 20 nm thick Al_2O_3 layer. For the samples used for electron tomography the process described previously was stopped after deposition of TiN. The nanowires were sonicated in ethanol and trans-

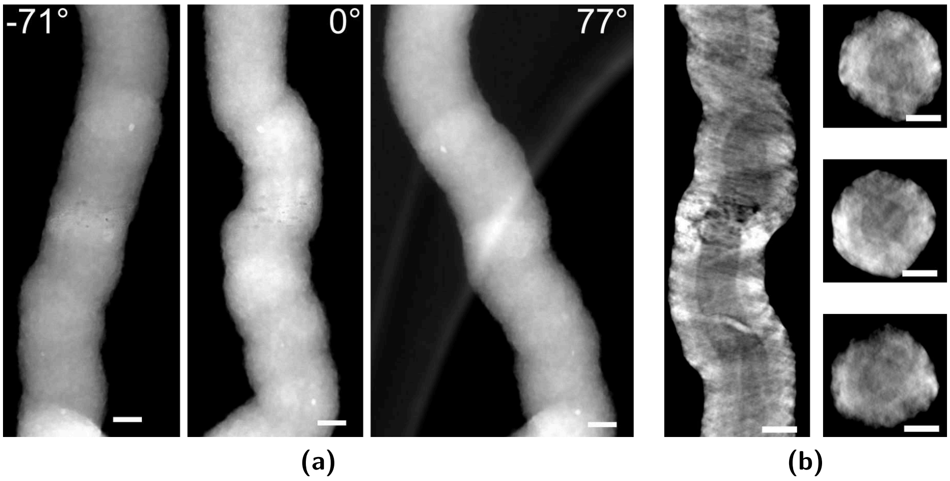

Figure 8.3: (a) Projections of a Si/Al_2O_3/TiN nanowire acquired in HAADF STEM mode and (b) slices through a SIRT reconstruction based on HAADF STEM images. Scale bars are 50 nm.

ferred onto a lacey-carbon grid. For 2D electron energy-loss spectroscopy (EELS) investigations, we prepared a thin lamella containing a transversal cross-section of a nanowire using a dual-beam FIB-SEM instrument.

8.3 Single-Window Low-Loss EFTEM Tomography

In a first experiment we tried using HAADF STEM tomography to reconstruct the interfaces between the different layers. Fig. 8.3 shows tilt series and reconstructions of the nanowires from these first experiments. While some small contrast is visible between the different materials, the differences in mass are much too small for a reliable segmentation. We therefore searched for other contrast mechanisms to use for tomography. Here low-loss EFTEM turned out to provide very good contrast between the different layers at suitable energy losses. We applied low-loss EFTEM in two experiments on the nanowires. First we acquired a tilt series at a single energy-loss of 13 eV. In a second experiment we did spectral low-loss EFTEM tomography, acquiring several energy-filtered series to reconstruct local low-loss spectra.

EFTEM tomography in the low-loss range was performed on a FEI Titan Cube microscope operating at 200 kV with a Gatan imaging filter (GIF) Tridiem. For single-window low-loss EFTEM tomography an energy window of 2 eV centered at 13 eV was chosen to acquire the tomography series over a tilt range of -70° to +80° with a step of 2°. Fig. 8.4 shows projections acquired in this tilt series. An energy loss of 13 eV was used, as for this energy contrast was visible for both the Si/Al_2O_3 interface as well as for the Al_2O_3/TiN interface. Three-dimensional reconstruction

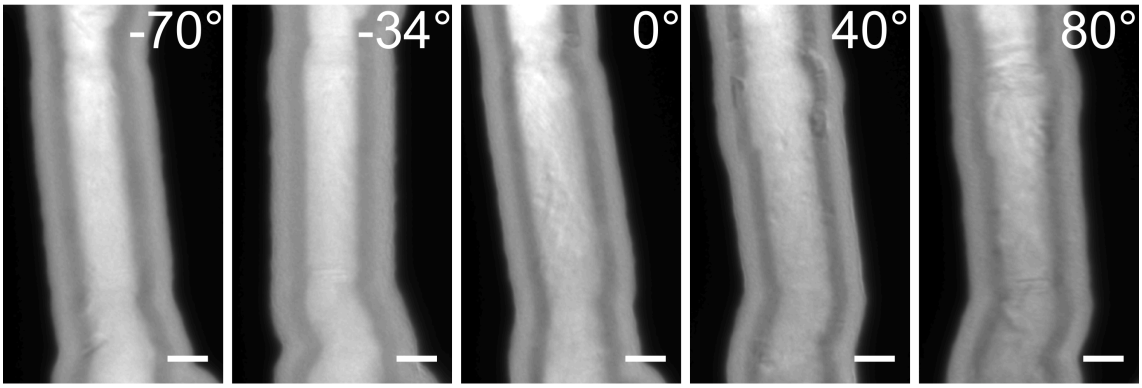

Figure 8.4: Projections of Si/Al_2O_3/TiN nanowire acquired in EFTEM mode at an energy loss of 13 eV. Scale bars are 50 nm.

was carried out using the simultaneous iterative reconstruction technique (SIRT). For visualization, the image was segmented using absolute threshold values. The result on Fig. 8.5 shows the conformity of the titanium nitride and alumina layers along the nanowire length with a uniform thickness following the nanowire roughness.

8.4 Spectral Low-Loss EFTEM Tomography

Motivated by the results from single-window low-loss EFTEM tomography we performed spectral low-loss EFTEM tomography experiments on the same nanowires, to explore whether tomography can be used to reliably reconstruct low-loss spectra and to see whether reconstructions at multiple energy losses can be used to get a better segmentation of the volume.

The principles of acquiring, aligning and reconstructing a spectral tomography series are shown in Fig. 8.6: a series of energy-filtered images with an energy window width of 2 eV centered from 7 eV to 27 eV was acquired every 2 eV. This was done for each tilt angle over a tilt range from -75° to +80° with a tilt step of 5°, giving a spectral series of eleven images for thirty-two tilt angles. The images at each energy loss were spatially aligned to each other using a cross-correlation algorithm and afterwards those image series were aligned over the whole tilt range. To perform this last step, the alignment over the tilt range is done at one single energy loss and the calculated shift is applied to all tilt series. This guarantees that the reconstructions at different energies are aligned to each other. After alignment each energy-filtered series was reconstructed using the SIRT method. Combination of the reconstructions provides a four-dimensional dataset consisting of a low-loss energy spectrum at each voxel.

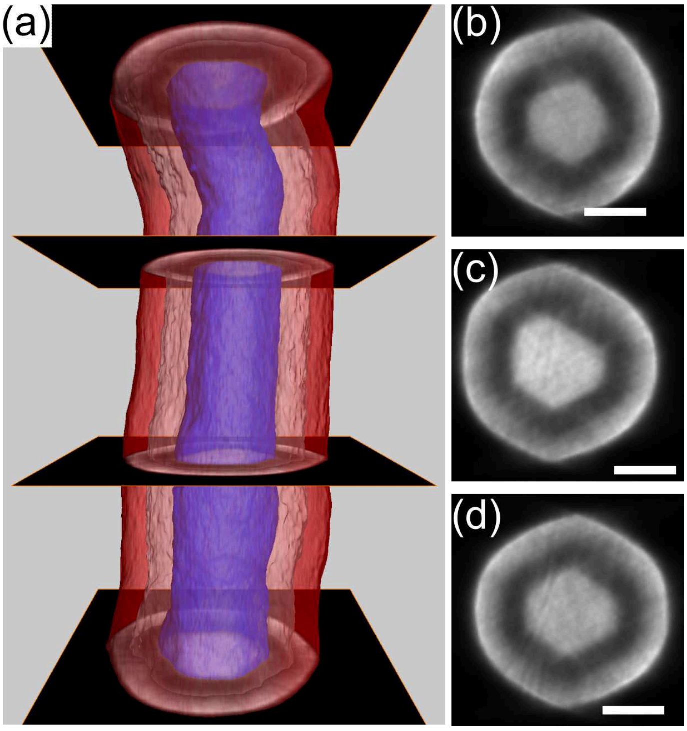

Figure 8.5: Tomographic reconstruction of energy-filtered TEM series acquired at an energy loss of 13 eV. (a) Surface rendered view of the reconstruction based on segmentation using absolute threshold values together with some slices through the reconstruction. (b-d) Slices through the reconstruction at different positions. Scale bars are 50 nm.

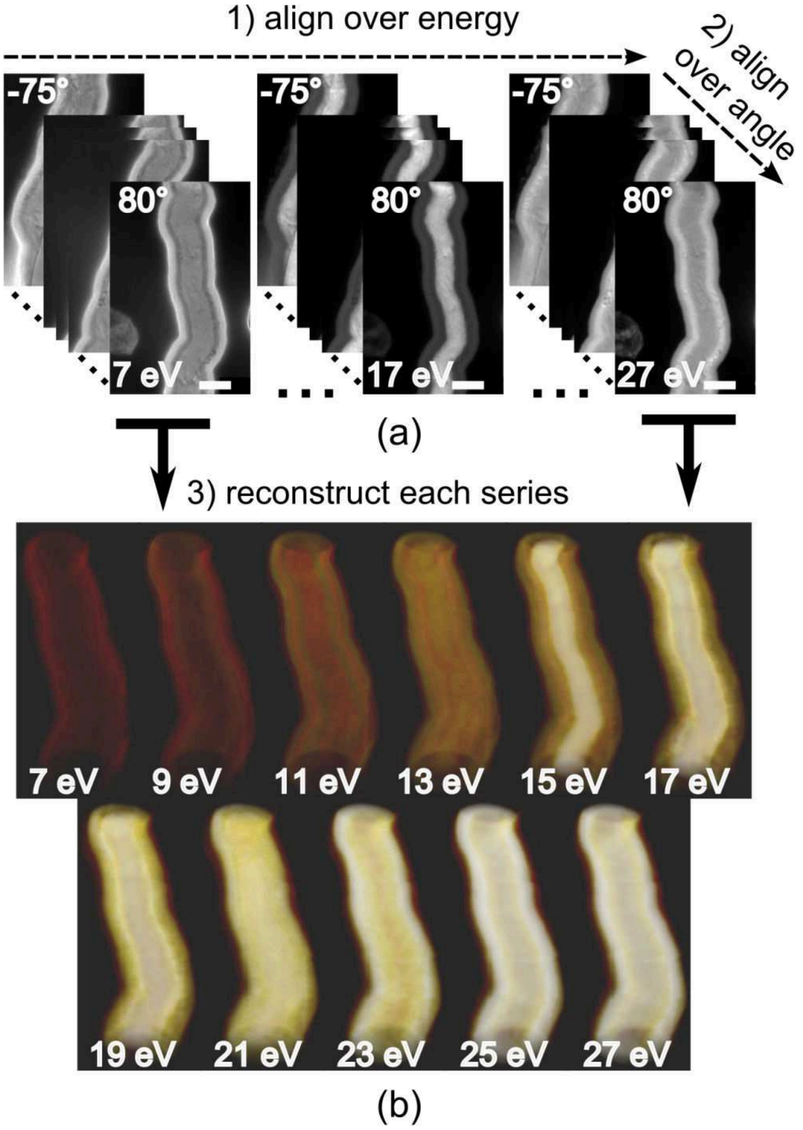

Figure 8.6: Principle of alignment and reconstruction of a spectral tomography series: (a) Energy filtered tilt series, (b) Volume rendered views of the reconstructed filtered volumes, scale bars are 100 nm.

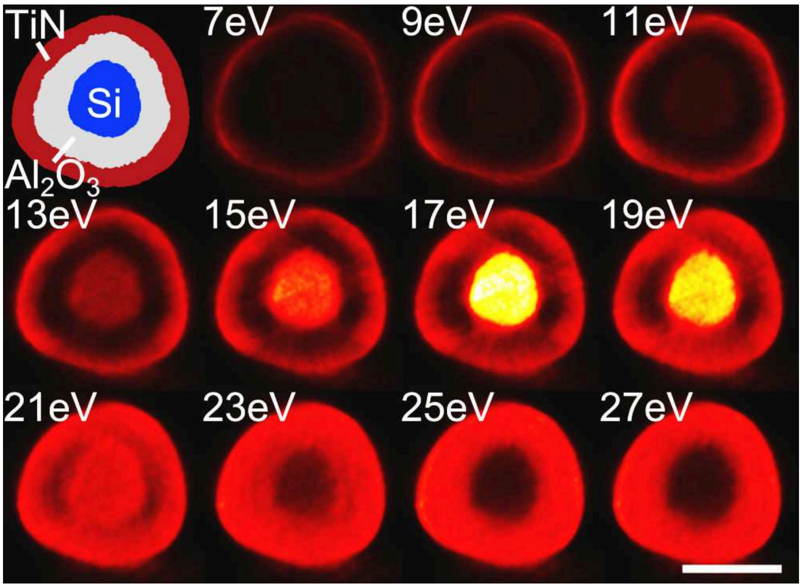

Figure 8.7: Slices through the reconstructed volume at all recorded energy losses, scale bar is 100 nm.

EELS experiments in the low-loss region were done on an FEI 80-300 kV Titan Ultimate microscope operated at 200 kV equipped with a GIF Quantum energy filter. EELS spectra were acquired along line-scans across a nanowire on a lacey-carbon grid and across the FIB prepared cross-section of a nanowire.

Fig. 8.7 shows a unique slice through the reconstructed volumes obtained at different energies. The interface between the central Si-core region and alumina is well visible in several of the reconstructions, in particular at an energy loss of 17 eV. By contrast the distinction between the alumina and TiN layer is less evident at this energy. Here the reconstruction at 13 eV exhibits best contrast and to a lesser extent also the reconstructions at energy losses up to 21 eV. We should also emphasize that at energy losses below 13 eV a large contribution to the contrast stems from surface plasmons. This clearly shows that the EFTEM reconstructions in the low loss energy region allow to get high contrast between the layers if one chooses optimum energy position.

Questions now arise to get a better understanding of the multiple contributions to the signal for each reconstruct voxel. For this purpose, we compared spectra across the three layers obtained along an EELS line scan across the entire wire Fig. 8.8a, from the reconstructed volume Fig. 8.8b and finally along an EELS line scan on a cross sectional FIB lamella Fig. 8.8c. In Fig. 8.8a, the spectra are strongly influenced by projection effects due to multiple materials, and also by interfaces along the beam path. This effect is particularly important for spectra acquired in the central region of the wire.

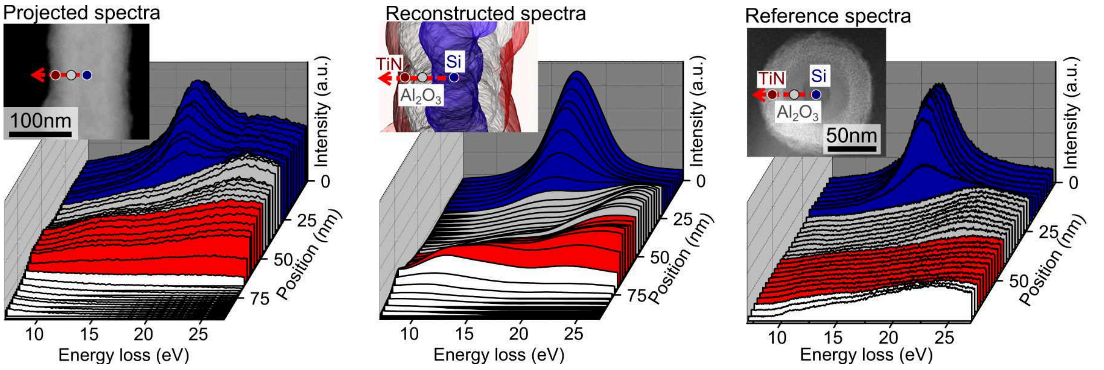

(a) **(b)** **(c)**

Figure 8.8: (a) HAADF STEM image of a nanowire on a lacey-carbon grid and EELS spectra acquired along the indicated line-scan. (b) Reconstructed volume and reconstructed spectra along the indicated cross-section through the reconstructed volume. (c) HAADF STEM image of the FIB prepared slice through the nanowire and EELS spectra acquired along the indicated line-scan.

Fig. 8.8b shows spectra along a cross-section through the reconstructed volume. These are local reconstructed spectra, each spectrum corresponds to one voxel. The benefit of the reconstruction is particularly significant in the central silicon part, where only the bulk plasmon peak of silicon remains while effects due to the contribution of the plasmon peaks of TiN and alumina are removed. Note that the reconstructed EELS spectra have only an energy resolution of 2 eV which corresponds to the energy slit used for the acquisition of the energy-filtered tilt series.

The third geometry of Fig. 8.8c permits to avoid superposition effects during the acquisition of the spectra so only interface contributions should still be present. We can then estimate that these spectra could serve as basis to evaluate the quality of the reconstructed spectra. Ideally, the comparison should exhibit similar features in both cases. Indeed, good agreement between the reconstructed and reference spectra is obtained in the central Si part. The plasmon peak of silicon shows a similar shape, however it appears shifted to a slightly higher energy in the reconstructed spectra. Moreover, the influence of the contributions of the plasmon peaks of the superimposed layers visible at energy losses around 25 eV are well removed in the reconstruction. In the alumina region the agreement between reference and reconstructed spectra is not as good as in the silicon core. We can observe discrepancies between the energy of the plasmon peak. Additionally the reconstructed spectra show an increased signal around 17 eV. Possible explanations for those discrepancies could be an influence of the strong plasmon peak of silicon on neighboring layers in the reconstruction process as well as energy drift of the energy filter over the duration of the experiment.

In the spectra reconstructed in the TiN region we observe an increasing signal towards the exterior boundary all over the spectral range and in particular at lower energies. This signal can be caused by contributions from surface plasmons and by effects of plural scattering. Though surface plasmons can generally not be reconstructed in three-dimensions as their intensity is angle dependent, the signal from surface plasmons will have the largest impact close to interfaces. Plural scattering has an impact on our experiment due to the relatively large sample diameter compared to the electron mean free path in the materials. This effect is particularly high at the center of the wires projections. Therefore the intensity of the reconstructed plasmon peaks should be lower close to the center of the wire and higher near the exterior boundaries. At the lowest energies also effects of delocalization are visible, which cause a signal in the surroundings of the nanowire. This shows finally that 3D reconstruction is possible and even if full interpretation is far from being obvious, interesting features could be extracted from the 3D reconstruction in the plasmon energy region.

On top of the spectral analysis, this work shows the 3D imaging capability of tomography to compute a 3D surface rendered reconstruction of the nanowire based on the low-loss contrast. Optimum energy windows give rise to optimum contrast between chemical layers and full 3D reconstruction and characterization of the morphology of the wire and its interfaces is then attainable. We used absolute threshold values for the segmentation of the volume intensities. Having the full volume reconstructed at all the energies authorizes to choose optimum energy conditions to highlight the contrast between the materials: for the Si/alumina interface the segmentation was done at 17 eV, for the alumina/TiN at 13 eV and for the outer surface at 27 eV. Fig. 8.9 shows surface rendered views of the nanowire using these conditions. This points out for example that the thicknesses of the alumina and TiN layers are homogeneous along the entire wire. This capital feature is essential for good device performance, to keep leakage currents low and to achieve high capacitances. To our knowledge, no other experiments could provide such a highly spatially resolved 3D volume showing similar chemical contrast and moreover it is a fairly rapid experiment with limited electron dose reducing radiation damage.

This method is of course not limited to the investigation of nanowires and has a wide range of applications. For example, in microelectronics, transistors, nanoelectromechanical systems (NEMS), interconnects and memories could in principle be studied with this tomographic scheme. More generally it can be applied also to materials for new energies showing strong 3D morphologies and even for biological applications, though radiation damage could be a limiting factor. With the advent

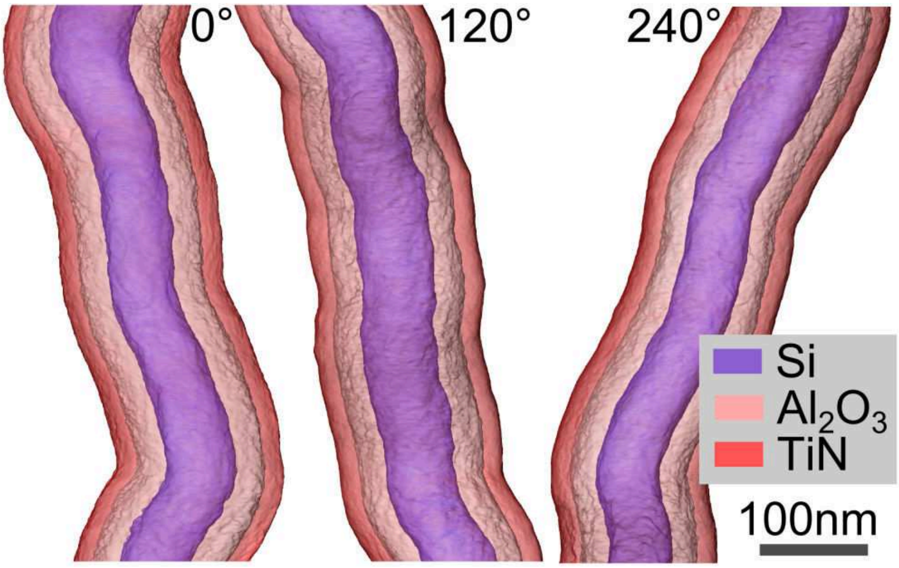

Figure 8.9: 3D reconstruction of the nanowire seen from three different viewing angles after segmentation

of high-brightness electron sources, monochromators and highly stable energy filters as well as with optimized experimental conditions and data analysis methods spectral low-loss tomography could be even extended to 3D nanoscale mapping of the bandstructure and optical properties (Lazar et al., 2003, Stöger-Pollach, 2008), using either densely sampled EFTEM or EELS tomography (Jarausch et al., 2009).

8.5 Conclusion

The application of electron tomography for the characterization of nanowire based devices has been shown. For materials with low difference in atomic mass, but differences in their bulk plasmon energies, low-loss EFTEM tomography has been shown to be a useful tool for three-dimensional nanoscale characterization by enhancing the contrast with respect to more conventional methods. In particular spectroscopic tomography has been applied and shown to provide valuable information in addition to single-window EFTEM tomography. It allows the reconstruction of an energy-loss spectrum for each single volume and provides thereby information about bulk plasmon peaks and allows reliable segmentation of the different materials. The agreement between reconstructed spectra and reference spectra is reasonably well. Limiting factors for the quality of the reconstructed spectra are the number of filtered images acquired at each tilt angle as well as the relatively low number of tilt angles used. Furthermore effects of surface plasmons and plural scattering were visible in the reconstruction. The number of projections could be in principle easily increased, however the tilt series acquisition time will increase accordingly and beam damage could become a problem. Plural scattering would have less impact on thinner samples and eventually deconvolution techniques could be used. Finally reconstructions at energies where surface plasmon excitation occurs need to be treated with care. In addition simulations could help to estimate the impact of all those factors on the reconstruction.

Part IV

Improving Resolution

9 Dual-Axis Tomography

This part of the thesis is concerned with methods towards improving spatial resolution of a reconstruction in electron tomography. Spatial resolution in electron tomography is generally limited by the number of projections and the available tilt range. Two basic methods exist for compensation for these limitations, which are the applications of dual- and multiple- axis tilt schemes (hardware methods) as well as the use of reconstruction algorithms, which include prior information (software methods).

In this chapter we investigate dual-axis tomography as a route towards improving resolution for the example of a tri-gate transistor. We are interested in particular in cases, which are not significantly affected by missing wedge artifacts and show that dual-axis tomography can improve the quality of a reconstruction also for such cases.[1]

9.1 Introduction

Dual-axis tomography has been used mostly for its capability of reducing missing wedge artifacts. These artifacts appear in tomography when the geometry of the sample or the sample holder does not allow rotation over a full tilt range of 180° (Mastronarde, 1997, Penczek et al., 1995). Such conditions occur frequently for biological samples (Messaoudi et al., 2006, Sousa et al., 2011, Xu et al., 2007) but also in materials science (Arslan et al., 2006, Sugimori et al., 2005). Missing wedge artifacts cause an elongation of sample features in the direction of the electron beam. The impact of these artifacts depends on the missing tilt range and is proportional to the size of features in the other directions. In materials science, in particular for focused ion beam (FIB)-based sample preparation, sample geometries and sample holders have been developed, which can eliminate the missing wedge (Kawase et al., 2007, Ke et al., 2010). For such FIB-prepared samples one might therefore get the impression of dual-axis tomography being useless.

---

[1] Devices have been elaborated by Sylvain Barraud, sample preparation and tomography investigation have been done together with Raphaël Serra. This chapter is reproduced from (Haberfehlner et al., 2013a).

Here we show that dual-axis tomography can also serve to improve the resolution of a reconstruction without or with a small missing wedge, in particular for samples containing features with high aspect-ratios being small in one dimension along a tilt axis and large in the other dimensions. In fact the resolution of the 3D reconstruction of such objects can become equal to the original two-dimensional (2D) resolution of the images, without the need for using any prior knowledge for the reconstruction.

Samples which fulfil these conditions are often encountered in nanotechnology, as many device concepts, also for complex three-dimensional (3D) structures are based on deposition of thin films. For such devices, it is then possible to adapt the tilt-axes accordingly to optimize the resolution perpendicular to these layers. Variations of thickness and roughness of these layers can then be measured with high accuracy.

In this work we investigate a tri-gate nanowire transistor using dual-axis tomography. Demonstrations of tri-gate nanowire transistors recently reported (Barraud et al., 2012, Coquand et al., 2012, Saitoh et al., 2010) highlight a better scalability of these structures with improved subthreshold slope and immunity to short channel effect for aggressively scaled complementary metal-oxide-semiconductor (CMOS) silicon devices. However, there are several key challenges in tri-gate devices for optimizing the device performance and the knowledge about variations in the geometry, in particular of the gate stack are essential. Here we use dual-axis electron tomography to get a high resolution 3D reconstruction of a tri-gate transistor, which allows detailed analysis of the gate stack for all surfaces of the transistor.

9.2 Materials and Methods

9.2.1 Investigated Samples

[110]-tri-gate nanowires (TGNWs) with high-κ/metal gate stack were fabricated on (100) silicon on insulator (SOI) wafers with a buried oxide (BOX) thickness of 145 nm. The SOI film thickness, which consequently defines the height of the TGNW, is of 11 nm. The silicon layer is patterned to create the nanowires by using a mesa isolation technique (Colinge, 2004). The nanowire pattern is defined by deep ultraviolet (DUV) optical lithography and followed by a resist trimming process (Coquand et al., 2012). It is performed to achieve nanowire structures with sizes down to 10 nm in width using HBr/O_2 plasma. The targeted thicknesses in gate stack deposition are 2 nm chemical vapor deposited (CVD) HfSiON, 5 nm atomic layer deposited (ALD) TiN finished by Poly-Silicon (50 nm) layers. A schematic of such a TGNW is shown in Fig. 9.1. As for the active patterning, the same photo-resist

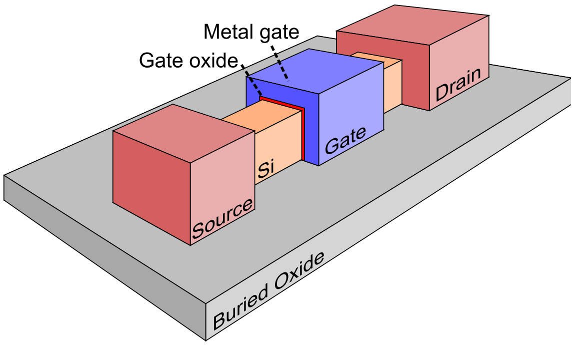

Figure 9.1: Schematic of a tri-gate transistor.

trimming is used providing gate lengths down to 20 nm. In the present study we investigated a device with a gate length of 10 µm. After gate patterning, a 15 nm thick nitride is deposited and etched to form the first spacer on source-drain (S/D). Then, low parasitic resistances are realized by S/D epitaxial silicon growth ($\Delta \mathrm{T}_{\mathrm{Si}} =$ 18 nm).

An important factor for the performance of such devices is the mobility of electrons or holes in the channel. One limit for the mobility is surface roughness scattering, which occurs due to interface roughness between the silicon and the gate oxide (Goodnick et al., 1985, Pirovano et al., 2000). Therefore it is important to be able to measure this roughness, however, experimental assessment is challenging and though high-resolution TEM images have been used to provide an idea about the roughness (Yi et al., 2009), they provide projections over the thickness of the sample and can therefore be misleading. Electron tomography however can be used to recover the full 3D information, if reconstructions with sufficiently high resolution can be acquired.

9.2.2 Sample Preparation

Samples were prepared using a FEI Strata dual-beam focused ion beam (FIB) instrument. We used a standard preparation method for electron tomography to prepare a needle-shaped sample containing the gate region of a single device (Bleuet et al., 2013, Haberfehlner et al., 2013b, Kawase et al., 2007, Ke et al., 2010, Yaguchi et al., 2008): first a protective stack was deposited on the region of interest consisting of electron-beam deposited silicon-dioxide, electron-deposited tungsten and ion-deposited tungsten. Then a lamella containing the device was extracted and glued to an Omniprobe TEM support grid. The lamella is milled to a circular shape to get a needle-shaped sample with a diameter of about 100 nm.

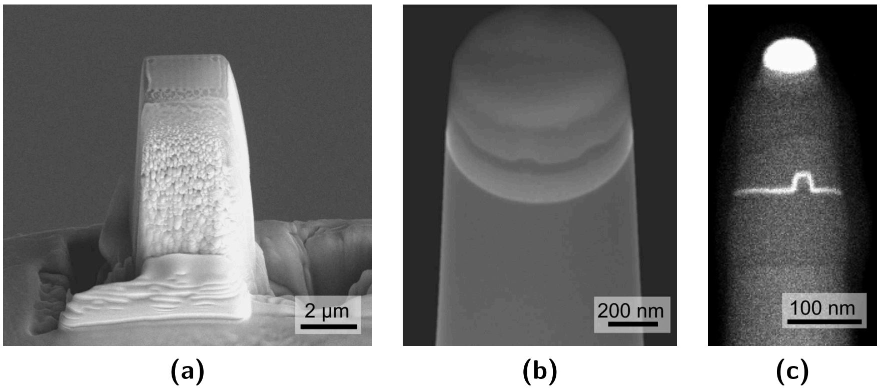

Figure 9.2: Sample preparation in the FIB: (a) SEM image of the sample glued to support after initial milling steps (b) SEM image after several steps of annular milling, (c) HAADF STEM image of the finished sample containing the gate region of the tri-gate device.

Annular milling was performed at a high tension of 30 kV in the FIB column using Ga$^+$-ions. The diameter of the needle-shaped sample is reduced in several steps, at each step the current in the FIB column is reduced to allow precise milling in the later stages of the preparation process. During the preparation process, care is taken to keep the device inside of the needle. Fig. 9.2 shows the sample during the preparation. In Fig. 9.2a the sample is glued to the support and some initial milling has been done to shape the sample as a pillar. Fig. 9.2b shows the pillar after several steps of annular milling and Fig. 9.2c shows the finished sample. The finished sample has a diameter of about 120 nm at the location of the region of interest.

9.2.3 Tilt Series Acquisition

Tilt series were acquired using a high-angle annular dark field (HAADF) detector in scanning transmission electron microscopy (STEM) mode on a probe-aberration corrected FEI Titan 80-300 microscope, operated at 200 kV. A convergence angle of 5 mrad and a camera length of 128 mm was used. A convergence angle of 5 mrad provides a probe size of 0.33 nm for a depth of field (DOF) of more than 80 nm. Images were acquired with at a size of 1024 × 1024 pixels with a pixel size of 0.26 nm. The probe size and the pixel size will ultimately limit the resolution of the reconstructed volume.

A standard single-tilt tomography holder (Fischione Advanced Tomography Holder Model 2020) was used for the experiment. Fig. 9.3a shows a schematic of the sample holder and the tilt scheme. For the acquisition of the first tilt series the sample was

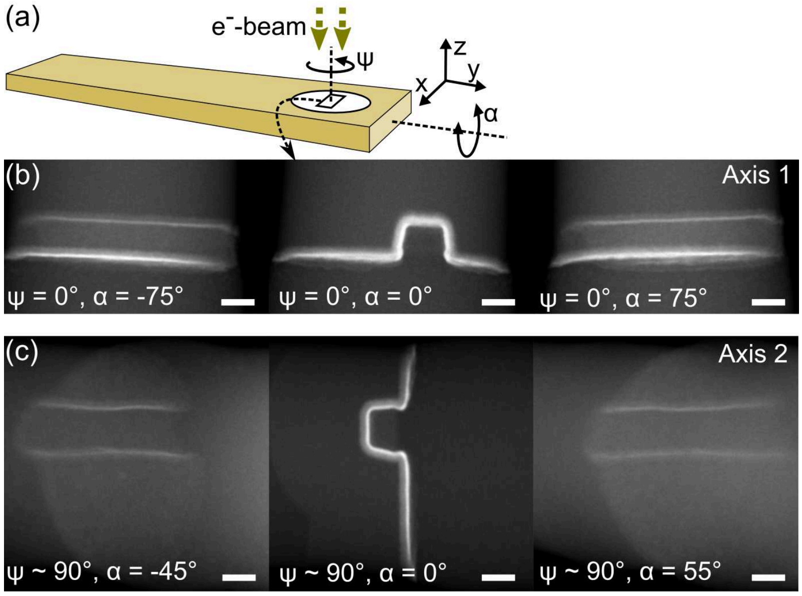

Figure 9.3: (a) Schematic of the sample holder showing the orientation and different rotation angles used for the sample. (b) Projections from the first tilt series taken with the needle-shaped sample oriented along the tilt axis ($\psi = 0°$). (c) Projections from the second tilt series taken with the needle-shaped sample oriented perpendicular to the tilt axis ($\psi = 90°$). Scale bars are 20 nm.

put on the holder oriented along the tilt axis of the microscope ($\psi = 0°$). Along this first tilt axis the needle-shape of the sample allows acquisition over a large tilt range from $\alpha = -78°$ to $\alpha = 78°$. Projections over this range were acquired every 1°. Projections from this first series are shown in Fig. 9.3b.

After acquisition of the first tilt series the sample was removed from the microscope and rotated manually by approximately 90° around ψ. We note that the exact value of rotation is not important as is will be determined in the alignment process. A second tilt series is taken around the new tilt axis. For this second series the maximum tilt range is limited from $\alpha = -46°$ to $\alpha = +59°$ as in this case the sample thickness along the beam path increases with the tilt angle. Images were again acquired every 1°. Projections from the second tilt series are shown in Fig. 9.3c.

9.2.4 Tilt Series Alignment

First the projections of each tilt series are aligned to each other using cross-correlation alignment methods (see Section 4.8) and the position of the tilt axis for each series is determined. The alignment of the two series to each other is done based on 3D cross correlation of volumes reconstructed from the two individual series. A similar approach was previously used by Messaoudi et al. (Messaoudi et al., 2006) and could be easily extended to more than two tilt axes. One key feature of this alignment

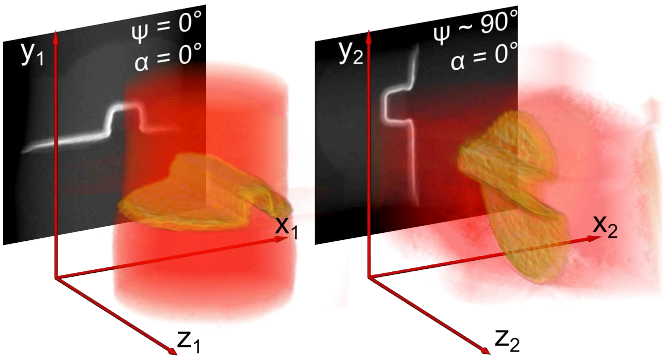

Figure 9.4: Definition of coordinate systems in the two individually reconstructed volumes for 3D cross-correlation alignment of the two tilt series.

routine is that it has no requirements about the exact angle between the two tilt axes and that for the alignment the two series do not need to have a common projection.

For the alignment of the two tilt series to each other, each of the two series is reconstructed independently using weighted backprojection. A coordinate system for each reconstruction is defined as shown in Fig. 9.4. The tilt axis defines the y-direction and the beam direction at 0° tilt angle the z-direction. The origin of the coordinate systems is put to the center of the reconstruction. Now the alignment of these two reconstructed volumes to each other requires the calculation of six parameters for the coordinate transformation between the two coordinate systems: the three Euler angles, giving the rotation between the coordinate systems and three shift parameters for the shift along the x-, y- and z-direction.

To find a suitable starting point for the alignment, the maximum of the cross-correlation between the projection taken at $\psi = 0°$ and $\alpha = 0°$ in the first tilt series and the projection taken at $\psi \approx 90°$ and $\alpha = 0°$ in the second tilt series is compared, while one of the two projections is rotated. We note that these projections may have been taken at slightly different tilt angles, as the rotation of the sample was done manually. However this does not affect the final alignment, as the value is used only as a first approximation for the rotation.

Starting from this initial rotational alignment the actual alignment is found by rotating one of the two volumes, while the second volume is used as reference. The quality of the alignment can be estimated by the maximum value of the 3D cross-correlation of the two volumes. Rotational values for all three Euler angles are tested iteratively, reducing the step after each iteration, until the desired accuracy for the alignment is reached. The alignment parameters, which provide the highest value for the maximum in the 3D cross-correlation, are used as results for these parameters.

In the present case we did the alignment to accuracy better than 0.1° for all Euler angles.

The calculation of the 3D cross-correlation provides additionally the three parameters for the shift alignment, which are given by the location of the maximum in the 3D cross-correlation. After the rotational alignment a final calculation of the cross-correlation between the two volumes is done and the shift alignment is improved to sub-voxel accuracy by doing a 3D cubic spline interpolation of the values around the maximum of the cross-correlation. The maximum of the interpolated values is used for the shift alignment.

Due to computation time and memory issues it can be advantageous to perform the calculations for the alignment at a lower resolution. In the present case we used a two times rebinned volume for the rotational alignment and took only the central part of each volume with half the size along each dimension into account. From the original volume with a size of $1024 \times 1024 \times 1024$ voxels this leads to calculations on volumes with a size of $256 \times 256 \times 256$ voxels. The final cross-correlation calculation for the shift values is refined at high resolution, using the central part of the original volume without rebinning, leading to a calculation on volumes with a size of $512 \times 512 \times 512$ voxels.

9.2.5 Reconstruction

Reconstruction is done with a new combined dual-axis SIRT (simultaneous iterative reconstruction technique) algorithm. The used algorithm has large similarities to the alternating dual-axis SIRT algorithm proposed in (Tong et al., 2006), with the exception that we did not use the two tilt series alternating, but used both series at the same time to correct the reconstruction in each iteration of the algorithm. Dual-axis SIRT algorithms have been shown to provide better reconstructions than real-space or Fourier-space combination of the individual reconstructed volumes (Arslan et al., 2006, Tong et al., 2006). We used the combined dual-axis SIRT algorithm as it provided better reconstructions for experimental data than an alternating dual-axis SIRT algorithm: the combined SIRT algorithm reduced artifacts which appeared in the coordinate transformation due to interpolation, which becomes necessary, when the rotation between the two tilt axes does not correspond exactly to 90°. These artifacts in the alternating dual-axis SIRT algorithm are shown in Fig. 9.5a for a slice through the reconstruction of the tri-gate transistor. Fig. 9.5b shows the same slice from the reconstructed with the combined algorithm, where the artifacts disappear.

The proposed combined dual-axis SIRT algorithm uses projection and backprojection operations and arithmetic operations to compare projections as well as recon-

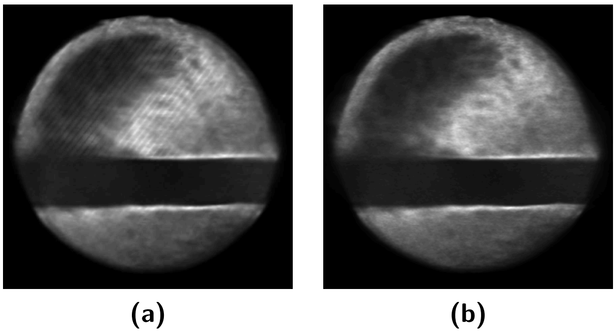

Figure 9.5: Slices through dual-axis reconstructions illustrating artifacts due to interpolation. (a) A slice from the reconstruction using the alternating dual-axis SIRT algorithms shows artifacts (stripes). (b) In the same slice from the reconstruction using the combined dual-axis SIRT algorithm these artifacts are removed.

structions. Additionally coordinate transformations are necessary using the alignment parameters previously calculated, to transform the volumes between their coordinate systems and a common reference coordinate system. In the present case, we used the coordinate system of the first tilt series as reference system, though in principle also another coordinate system could be used. For the rotations of the volume, which are required in the coordinate transformations, a linear interpolation scheme is used. Voxels in the transformed volume, which lie outside of the original volume, are filled with a small value (1×10^{-6}) to eliminate divisions by zero during the reconstruction process.

The principle of the used algorithm is shown in Fig. 9.6. First an initial reconstruction is calculated. In the present case, we used a Fourier space combination of reconstructions by backprojection from the two individual tilt series. This initial reconstruction is used as first temporary reconstruction in the iterative loop of the SIRT algorithm. It is transformed to the coordinate systems of the two tilt series and projected to the tilt angles of each of the two tilt series. These re-projections are compared to the original projections from the corresponding tilt series and difference projections are calculated. In the present case we used a division to calculate the difference projections, using a multiplicative update for the algorithm. The difference projections for both axes are backprojected to get a difference reconstruction for each tilt series. Each of the two difference reconstructions is transformed to the common reference coordinate system, where the mean value from both reconstructions for each voxel is calculated. The temporary reconstruction is corrected by this combined difference reconstruction. This corrected reconstruction is used as tem-

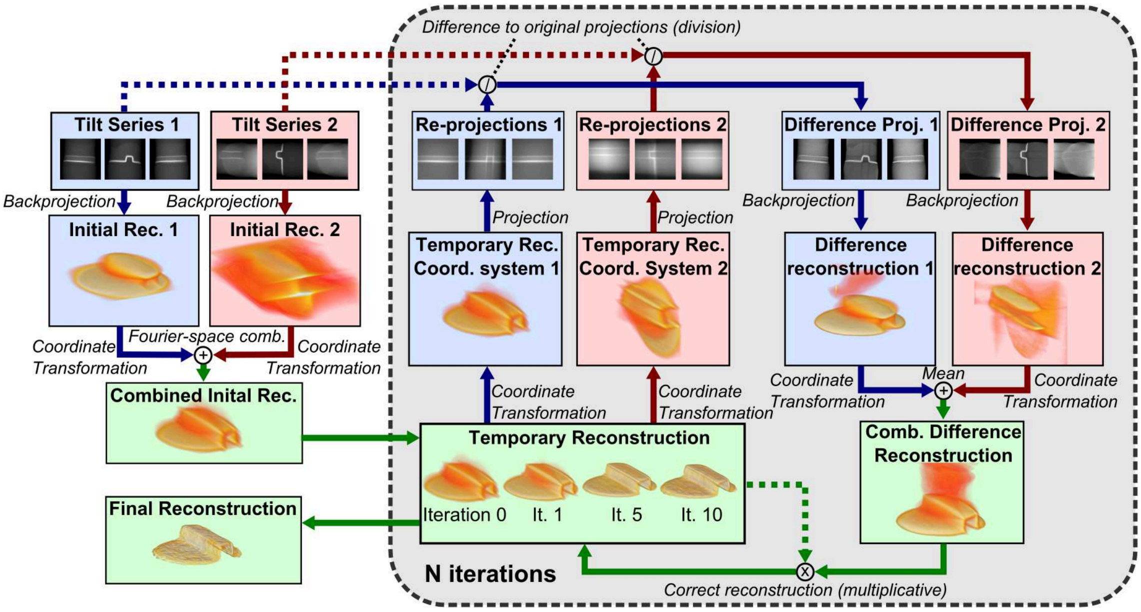

Figure 9.6: Principle of the proposed combined dual-axis SIRT reconstruction algorithm.

porary reconstruction in the next iteration until the desired number of iterations is reached.

In the present case we used 30 iterations for the dual-axis reconstruction. To evaluate the dual-axis reconstruction, the two tilt-series were also reconstructed independently using a single-axis SIRT algorithm with multiplicative update for 30 iterations.

9.2.6 Segmentation

To quantify results, segmentation was done in the central part of the reconstructed volume, to exclude areas close to the boundary of the needle-shaped samples, which can be affected by beam-damage from FIB preparation and by missing wedge artifacts. For the segmentation a gradient watershed algorithm was used (Adams and Bischof, 1994, Haberfehlner et al., 2013b, Volkmann, 2002). First a gradient volume is calculated. Transition regions between the different materials are masked using a threshold in the gradient volume. Outside of the masked volume, absolute threshold values are applied to define seed regions, which belong to a specific material. A watershed transform on the gradient volume is then used to set the interfaces between the materials (see Section 4.9.2). The watershed transform puts the interfaces to the location with the highest gradient.

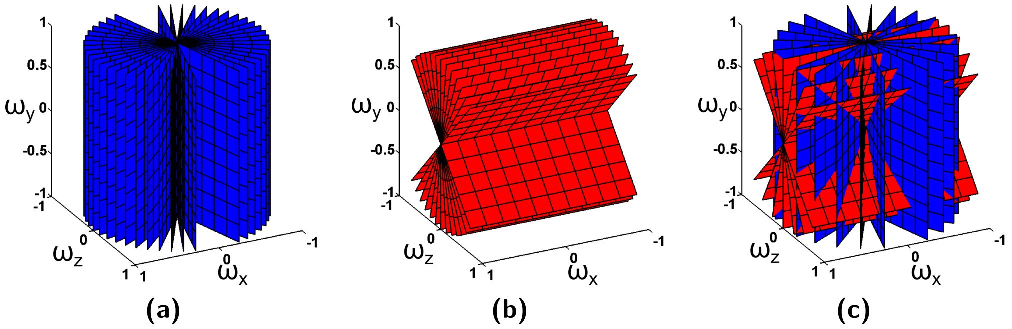

Figure 9.7: Sampling in the Fourier domain by dual-axis tomography: (a) Sampling in the 3D Fourier space by single-axis tomography around the first tilt-axis, (b) sampling in the 3D Fourier space around the second tilt axis, (c) sampling by dual-axis tomography.

9.3 Theory and Simulations

The advantages of dual-axis tomography, for the described type of application, can be better understood if we consider the sampling of information by the acquisition of projections in Fourier space. For the purpose of tomography, a TEM can be simplified as a source/detector system with parallel illumination. Therefore, for single-axis tomography, the reconstruction of a 3D object from its 2D projections can be done as reconstruction of multiple parallel 2D slices along the tilt axis, the resolution depends on the number of projections and on the available tilt range as has been discussed in Section 4.4.

Along the tilt axis however, each slice can be reconstructed independently, so the resolution in this direction can be equal to the original resolution of the images. In Figs. 9.7a&9.7b, sampling in the 3D Fourier domain for two different single-axis tilt series is shown. The Fourier space is sampled along central slices, which are represented as planes in 3D Fourier space. Information on each of these planes is densely sampled. It is visible from these schemes that in the direction of the tilt axis, high frequency components can be very well recovered, in particular if changes in the other two dimensions occur at low frequencies. Using a second tilt axis extends this capability to a second dimension, allowing retrieving the original 2D resolution along two dimensions of the reconstruction. This is illustrated in Fig. 9.7c, where the sampling in the Fourier domain by dual-axis tomography is shown. To demonstrate these capabilities of dual-axis tomography, we carried out simulations. As test object, a simplified structure similar to the investigated tri-gate transistor was used. The sizes of the object were derived from the nominal size of the transistor. For simplicity, we assume 90° angles between the gates. The size of

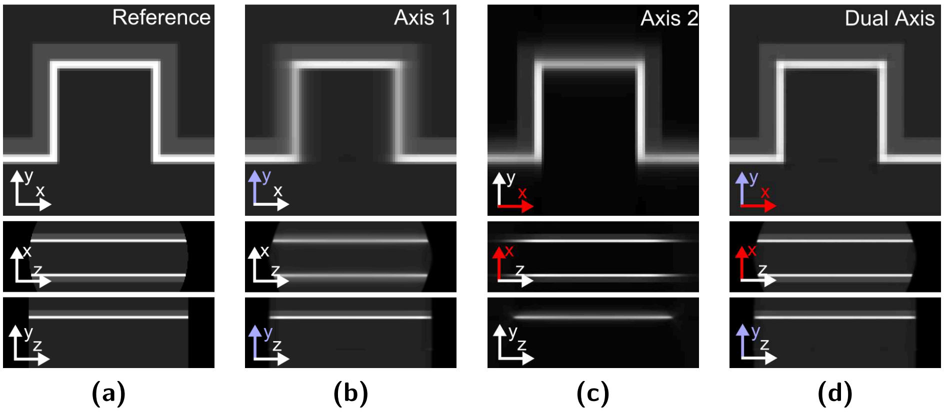

Figure 9.8: Slices along orthogonal planes through simulated reconstructions. (a) The test object used for the simulations. (b) Reconstruction from the tilt series around the first tilt-axis. (c) Reconstruction from the tilt series around the second tilt axis. (d) Dual-axis reconstruction using both tilt series. The first tilt axis corresponds to the y-direction (blue), the second tilt-axis to the x-direction (red).

the simulated volume is $512 \times 512 \times 512$ voxels with a voxel size of 0.52 nm, which corresponds to a volume rebinned by a factor of two compared to the experiment.

In Fig. 9.8 we compare single-axis SIRT reconstructions from simulated projections along the two tilt axes and a dual-axis SIRT reconstruction from a combined dataset. For the simulations of the single-axis reconstructions, the same conditions as in the experiment were used, using projections every 1°, between -78° and +78° for the first tilt axis (Fig. 9.8b) and between -46° and +59° for the second tilt axis (Fig. 9.8c). For the simulation of the dual-axis reconstruction (Fig. 9.8d), a tilt step of 2° for each series was used to have approximately the same number of projections for all reconstructions. In the single-axis reconstructions, the reduced resolution perpendicular to the tilt axis is clearly visible. The dual-axis reconstruction provides a reconstruction, which shows excellent resolution along both tilt axes, thus proving the capabilities of dual-axis tomography for the investigated application.

To closer investigate the influence of the missing wedge on these resolution improvements we did further simulations. In Fig. 9.9 we compare single-axis reconstructions from tilt series taken over different tilt ranges between ±50° and ±90° to dual-axis reconstructions from projections taken over the same tilt range around the first tilt axis and over a tilt range of ±50° around the second tilt axis. For the single-axis reconstructions projections are taken with steps of 1°, for the dual-axis reconstruction with steps of 2°. To quantify the quality of the reconstructions we

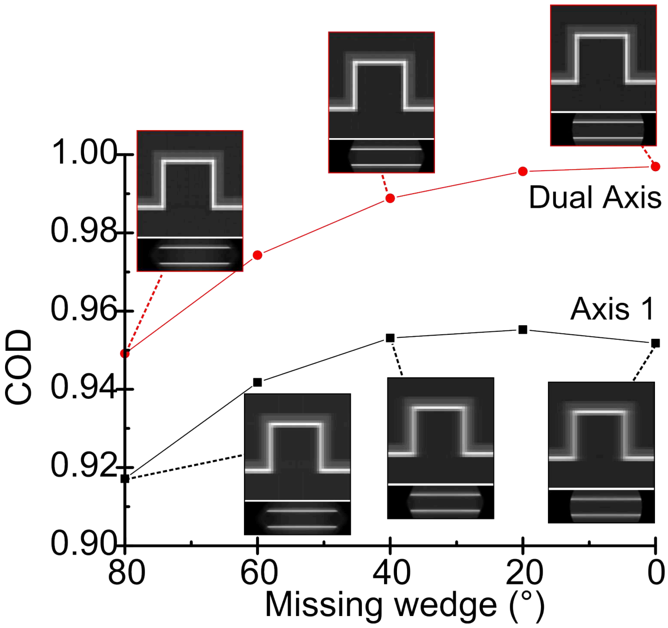

Figure 9.9: Comparison of simulations for different values of the missing wedge: The graph is showing the coefficient of determination (COD) for several values of the missing wedge ranging from 80° (±50° tilt range) to 0° (±90° tilt range). Results from the reconstructions around a single tilt axis (tilt axis 1) are shown in black, results from the dual-axis reconstruction are shown in red. The insets show slices along the xy- and xz-plane from the corresponding reconstruction.

calculated the coefficient of determination (COD), as proposed in (Tong et al., 2006). The COD is given as

$$COD = \frac{\left(\sum\left(\left(X_{i,j,k} - \bar{X}\right)\left(Y_{i,j,k} - \bar{Y}\right)\right)\right)^2}{\sum\left(X_{i,j,k} - \bar{X}\right)^2 \sum\left(Y_{i,j,k} - \bar{Y}\right)^2} \tag{9.1}$$

with $X_{i,j,k}$ being the reference data at a given voxel and $Y_{i,j,k}$ the value of the reconstructed data at the same voxel.

The results show that the quality of the reconstruction is improved by using a second tilt-axis irrespective of the missing wedge. For the dual-axis reconstruction, the COD improves slightly with reduction of the missing wedge, as this improves the quality of the reconstruction in the small areas affected by missing wedge artifacts. For the single-axis reconstruction, the same improvement is visible for a missing wedge between 80° and 20°, but when the missing wedge gets smaller than 20°, the COD is getting slightly lower. This effect is not larger and we did not investigate this effect closer, but we assume that errors due to the limited number of projections and the missing wedge may partially compensate each other and give grey values which are closer to the original object than without a missing wedge. These simulations

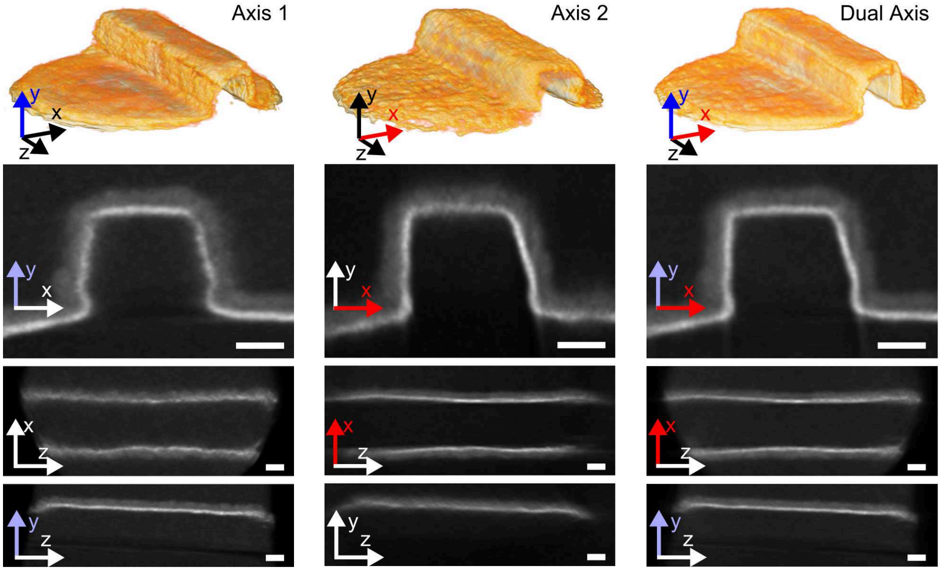

(a) (b) (c)

Figure 9.10: Volume rendered views of the reconstructions and slices along orthogonal planes through reconstructions of the tri-gate transistor. (a) Reconstruction from the tilt series around the first tilt-axis. (b) Reconstruction from the tilt series around the second tilt axis. (c) Dual-axis reconstruction using both tilt series. The first tilt axis corresponds to the y-direction (blue), the second tilt-axis approximately to the x-direction (red), scale bars are 10 nm.

prove the capabilities of dual-axis tomography for the investigated application and show that the improvement of the resolution is present with or without missing wedge, as was expected from the theoretical considerations.

9.4 Experimental Results

Fig. 9.10 shows volume rendered views of and slices through reconstructions from the experimental data, from the single tilt series and from the dual-axis reconstruction using both tilt series. In the single-axis reconstruction around the first tilt axis (Fig. 9.10a) the horizontal surface of the gate of the transistor, which is oriented perpendicular to the tilt axis (y-axis) is well reconstructed, allowing a clear distinction between the gate oxide, the metal gate on top of the gate oxide and other materials. By contrast the reconstruction of the two vertical surfaces of the gate, which are oriented perpendicular to the x-axis, suffers from the reduced resolution due to the limited number of projections. Though in the orthogonal slices the location and thickness of gate oxide and metal gate for the vertical surfaces can be roughly seen, the loss of resolution makes segmentation and estimation of their thickness impossible.

The single-axis reconstruction of the second series (Fig. 9.10b), taken around the second tilt axis, shows the same effects as the first series but for the orientation of the second tilt axis. For the two vertical surfaces of the gate, oriented perpendicular to the x-axis which corresponds to the tilt-axis in this case, the gate oxide and metal gate are well reconstructed, while now the resolution perpendicular to the y-axis is reduced.

The dual-axis reconstruction, using the combined dual-axis SIRT algorithm, allows the combination of advantages of both single-axis reconstructions and minimizes the drawbacks seen in the single-axis reconstructions (Fig. 9.10c). In the dual-axis reconstruction, all three surfaces of the gate are well reconstructed: the horizontal surface, which is perpendicular to the first tilt-axis (y-axis) preserves the resolution from the first single-axis reconstruction, while the two vertical surfaces of the gate on the side of the transistor, which are oriented perpendicular to the second tilt-axis (x-axis) preserve the resolution from the second tilt series. This confirms the simulated results and shows the usefulness of dual-axis tomography for high resolution applications, in particular also for applications, where the missing wedge does not play a significant role.

The resolution of the volume reconstructed from dual-axis tomography is influenced by several parameters. The first limit is the resolution of the original images linked to the probe size and to the pixel size. Another limitation is the alignment of the individual tilt series as well as the alignment between the two series. For the present case, the strong contrast of the gate oxide facilitated the alignment by cross-correlation, but errors could still be present and are difficult to quantify. Finally the detection of variations of the layers, which happen at high spatial frequencies along the layers will be still limited by the number of projections acquired. Though the simulations have shown that flat layers can be perfectly reconstructed, further investigations will be necessary to understand to which amount the roughness of the layers can be recovered in the reconstruction.

Dual-axis reconstruction of the transistor allows also segmentation of the reconstructed volume. As the gate stack is now well resolved for the full device the gate oxide and the metal gate can be separated from other materials. This segmentation would be not possible, if it were done from a single-axis series, due to the differences in resolution and contrast depending on the orientation of the gate surface. From the dual-axis reconstruction, the segmentation is quite easily possible and was done in a semiautomatic fashion, using a gradient watershed algorithm as described previously. Results of the segmentation using the dual-axis reconstruction are shown in Fig. 9.11.

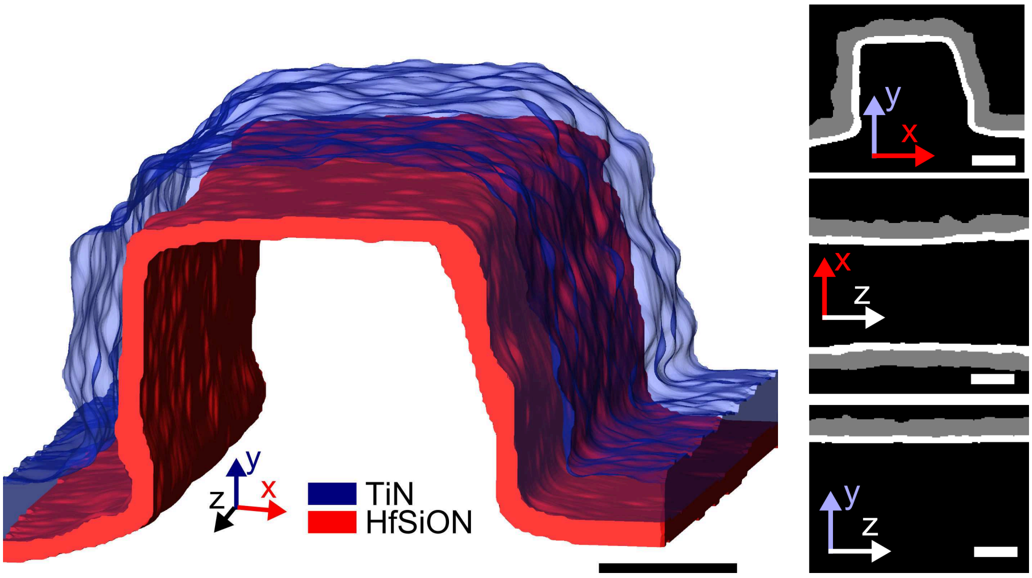

(a) (b)

Figure 9.11: (a) Surface rendered view of the segmented dual-axis reconstruction of the tri-gate transistor. (b) Orthogonal slices through the segmented data, scale bars are 10 nm.

From this segmented volume, it is now possible to extract information about the geometry of the device. As one example we use the segmented dataset to extract information about the gate thickness. For this purpose, we extract the distance from each voxel at the inner edge of the gate towards the nearest voxel in the metal gate. Fig. 9.12 shows a histogram with the distances extracted from all voxels. Peaks arise at multiples of the voxel size of 0.26 nm due to the discrete nature of the data. These peaks are shown independently from the histogram of all other distance values. From all extracted values the mean thickness can be calculated, which gives a value of 1.65 nm.

9.5 Conclusion

We have demonstrated the use of dual-axis tomography for applications requiring high resolution. Adapting the tilt axes to the sample geometry allows significant improvement of the 3D resolution even for structures not affected by missing wedge artifacts. We applied a 3D cross-correlation based alignment method, which poses no requirements on the positioning of the different tilt axes. This allowed a good alignment of the two tilt series even though a standard single-axis tomography sample holder was used. For the reconstruction a new combined dual-axis SIRT algorithm was developed, which reduced artifacts from interpolation in the reconstruction.

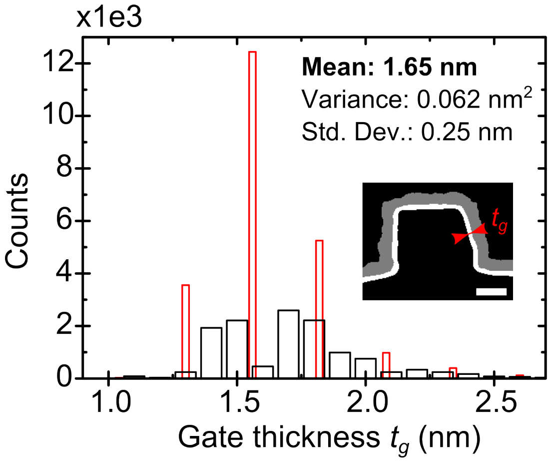

Figure 9.12: Measurement of gate thickness (t_g) from the segmented reconstruction. Peaks in the distribution occurring at multiples of the voxel size (0.26 nm) are shown in red. The histogram of all other thickness measurements is shown in black. Statistical values are calculated from all measurements. The inset illustrates the definition of the gate thickness.

Dual-axis tomography allowed extracting information about the geometry of the gate stack for all surfaces of the gate of a tri-gate transistor. The resolution compared to single-axis reconstructions was significantly improved for the gate surfaces, which were not oriented perpendicular to the tilt-axis in the single-axis tilt series. Dual-axis tomography permitted segmentation of the reconstruction, which was used to measure the local gate thickness for all surfaces of the gate of the transistor.

These results show the potential of dual-axis tomography for 3D characterization of advanced nanoscale devices. Many other transistor concepts like FinFETs or Gate-All-Around transistors have similar requirements on gate stack characterization and more generally all processes, which use thin films on a patterned geometry can profit from the presented approach. Additionally for more complex geometries, the alignment and reconstruction methods could be easily extended more than two tilt axes.

10 Multiple-Axis Tomography

In the previous chapter it was shown that dual-axis tomography can improve the resolution of a reconstruction as the object's 3D Fourier space is sampled differently than in a single-axis tilt scheme. This gives rise to the question, whether taking several tilt-series around different axes could be a route to optimizing resolution for a given number of projections. In this chapter we analyze such acquisition schemes, apply them to simulations and discuss the perspective of experimental application.

10.1 Introduction

Dual-axis tomography is an established way for reducing missing wedge artifacts in the case of a limited tilt range. It has been also extended to multiple-axis tomography to further reduce the missing Fourier data from a "missing pyramid" towards a "missing cone" (see Fig. 4.12) (Messaoudi et al., 2006). Even in the case of multiple-axis tomography though, the tilt-axes are located - at least approximately - in a common plane. This is due to practical reasons, as rotating a sample in the plane perpendicular to the beam direction can be done easily using a standard sample holder. Fig. 10.1 shows the orientation of tilt axes for such conventional single- dual- and multiple- axis tilt schemes.

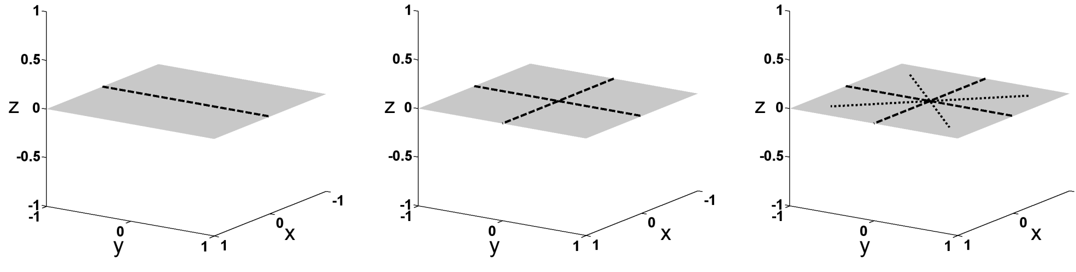

(a) (b) (c)

Figure 10.1: Location of the tilt axes in space for (a) single-axis tomography, (b) dual-axis tomography and (c) multiple-axis tomography with all tilt axes being located in a common plane.

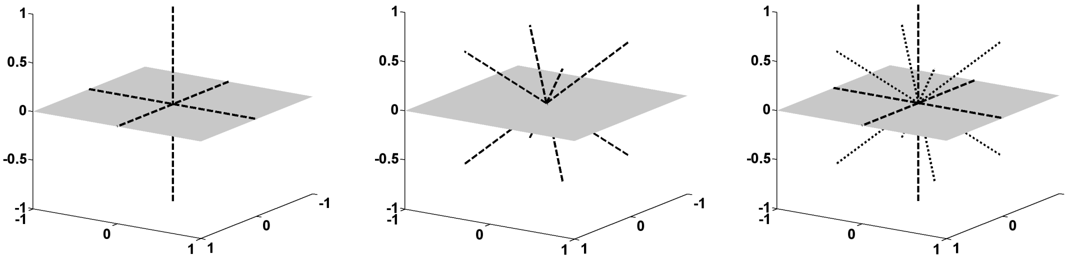

(a) (b) (c)

Figure 10.2: Location of tilt axis in (a) the proposed orthogonal triple-axis scheme (b) an example with four axes (c) an example for a multiple-axis scheme with seven tilt-axes out of a single common plane.

We propose using additional tilt series for tomographic reconstruction, which are acquired around tilt axes, located outside of a single common plane. In particular we propose using three tilt axes, which are located orthogonal to each other, but more generally also other schemes could be possible which use several tilt axes outside of a single plane. Fig.10.2a shows the orientation of the tilt axes for the proposed orthogonal triple-axis tilt scheme and Figs. 10.2b&10.2c show other possibilities for multiple-axis tilt schemes. Here we evaluate whether such schemes can provide advantages over conventional tilt schemes for a limited number of projections and discuss routes towards experimental application.

10.2 Principles

Fig. 10.3 shows the positioning and rotation of the sample in the source/detector system for orthogonal triple-axis tomography for the acquisition of the three series. If a cubic sample (or region of interest) is assumed, each tilt axis needs to be perpendicular to different surface planes of the cube, as illustrated in Fig. 10.3. For each of these tilt axes projections should be acquired over as large a tilt range as possible, ideally 180°. Practical application of such a scheme is evidently challenging. For now the discussion will be limited to theoretical considerations and simulations, approaches for experimental applications are discussed in Section 10.4.

To understand possible advantages of such an acquisition scheme, sampling of information in Fourier space can be considered. As discussed previously each acquired projection in a tomographic scheme contains the information of a central slice through the 3D Fourier transform of the object. On these slices the information is sampled with the original resolution of the acquired projection. Fig. 10.4a shows the sampling in 3D Fourier space using a tomographic scheme with a single tilt axis

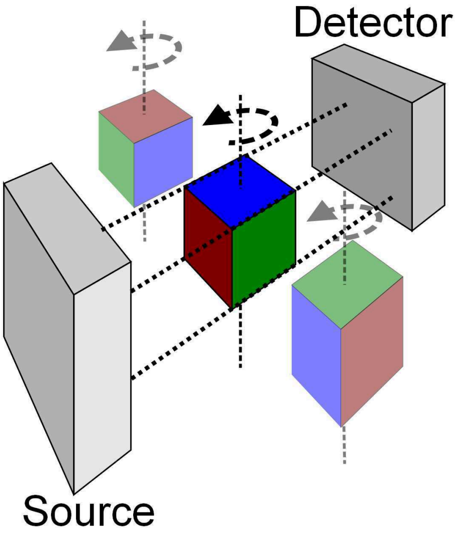

Figure 10.3: Scheme showing positioning and rotation of the sample with respect to the source/detector system for acquisition of tilt series around the three orthogonal tilt axes.

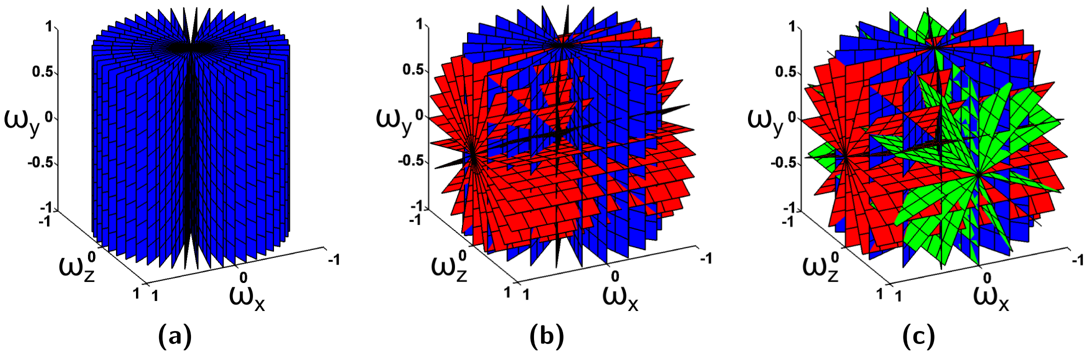

Figure 10.4: Information sampled by tomography in the 3D Fourier domain using (a) a single tilt axis (b) two orthogonal tilt axes, (c) three orthogonal tilt axes.

using N projections. On each of these central slices the data is densely sampled. This causes very dense sampling for frequencies along the tilt axis, while frequencies in directions perpendicular to the tilt axis are sampled more roughly, leading to the known anisotropy of the resolution in tomography, if the number of projections is limited.

Here we propose using multiple tilt axes to reduce this anisotropy by sampling the Fourier domain more equally. Fig. 10.4b shows the Fourier domain sampled by a dual-axis scheme using N projections in total: $N/2$ projections around each tilt axis. Fig. 10.4c shows the sampling by the proposed orthogonal triple-axis scheme. In total again N projections are used: $N/3$ projections around each tilt axis.

For the orthogonal triple-axis tilt scheme sampling of frequency components in the direction of each tilt-axis is dense. Spatial frequencies lying close to a tilt axis will therefore be well reconstructed. For frequencies further away from the three tilt axis the situation is more complicated. For spatial frequencies with large x- y- and z-components the spacing between different Fourier slices is relatively large, spacing between different slices is even larger for the triple-axis scheme than for single-axis tomography (see Fig. 10.4). However we assume that it can be advantageous that central slices are oriented along different directions in Fourier space. In this way a specific point in Fourier space, which lies between sampled slices has neighboring sampled spectral points in each direction.

10.3 Simulations

To test whether the proposed tilt scheme can provide better reconstructions than single- or dual-axis tomography we simulated reconstructions of a test object. As test object a model of a zinc-blende crystal lattice was created. At atomic positions we put spheres with constant grey values using different grey values and slightly different diameters for the two types of atoms. We created unit cells with a size of $12 \times 12 \times 12$ voxel, using a diameter of 3 voxel for the atoms. The unit cell is replicated along all three dimensions to a crystal containing of $30 \times 30 \times 30$ unit cells. The crystal is rotated by arbitrarily chosen values around the x-, y- and z-axis to avoid that tilt-axis coincide with crystallographic orientations. The crystal was put in a volume of $512 \times 512 \times 512$ voxels with a black background. It should be noted that these simulations consider no physical effects, such as the scattering mechanisms in a TEM and assume that the object is perfectly in focus over the full depth.

From this volume tilt series were simulated for a single-axis, a dual-axis and an orthogonal triple-axis scheme. For each scheme 90 projections were used in total, which were equally spaced over the full tilt range of 180° for each tilt axis. For the single-axis reconstruction one tilt series is used consisting of 90 projections (2° tilt step). For the dual-axis reconstruction two tilt series are used around two orthogonal tilt axes, each one consisting of 45 projections (4° tilt step). For the orthogonal triple-axis reconstruction three tilt series are used around three orthogonal tilt axes, each one consisting of 30 projections (6° tilt step).

The reconstruction of the single-axis dataset is done using SIRT. The dual-axis and triple-axis reconstructions are done using a multiple-axis SIRT algorithm similar to the dual-axis SIRT algorithm discussed in Section 9.2.5. Fig. 10.5 shows the original dataset (Fig 10.5a), and the reconstructions using the single-axis scheme (Fig. 10.5b), the dual-axis scheme (Fig. 10.5c) and the proposed triple-axis scheme (Fig. 10.5d). To evaluate the quality of the reconstruction numerically the COD was calculated for each reconstruction as defined in (9.1). For the single-axis scheme the COD of the simulated object was 0.51, for the dual-axis scheme 0.65 and for the triple-axis scheme 0.84, which shows the interest of the proposed scheme.

10.4 Practical Application

The practical application of the proposed orthogonal triple-axis tomography scheme in a TEM is challenging. Conventional TEM holders for tomography allow tilting the sample only around a single axis combined with manual rotation perpendicular to the beam direction, which can be used for acquiring tilt series around multiple axes located in a common plane. For the proposed scheme special sample holders or external manipulation of the sample is necessary. Here we discuss one possible method for external manipulation using a FIB and discuss requirements for sample holders, which could be used for the purpose of triple- or multiple-axis tomography.

10.4.1 FIB-Based Application

For an FIB-based method a standard Omniprobe FIB-grid is used as sample support. The basic idea of this method is that the sample needs to be rotated one time with respect to the sample support between acquisition of the different series. Fig. 10.6 shows the principle of the acquisition of three tilt series and the sample rotation using the FIB. For the purpose of orthogonal triple-axis tomography a needle-shaped sample, which contains the region of interest is prepared on an FIB grid as discussed in Section 6.1. The first two tilt series are acquired in the same way as for dual-axis tomography (Figs. 10.6a&10.6b). After acquisition of these two series the sample is rotated by 90° with respect to the sample support using an FIB (Fig. 10.6c) to allow acquisition of the third tilt series (Fig. 10.6d). It should be noted that it is equally possible to acquire tilt series 1 (Fig. 10.6a) after rotation of the sample in the FIB, which can be useful in order to reduce the effort necessary before the FIB manipulation.

Practically the rotation in the FIB is a challenging step. The sample needs to be manipulated without damaging the region of interest. In a first test we tried cutting the sample free relatively close to the region of interest. However in this case redeposition of material in the FIB affected the region of interest, making it

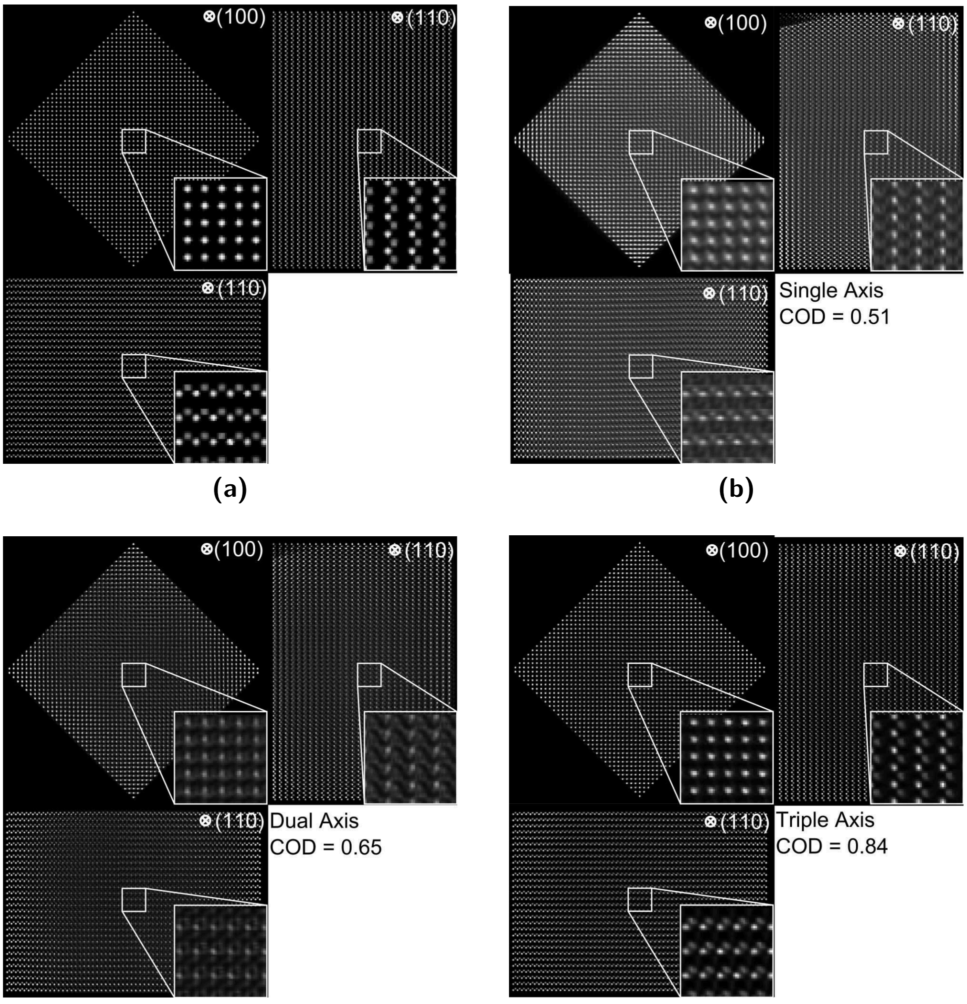

(a) (b)

(c) (d)

Figure 10.5: Simulated reconstructions of a zinc-blende crystal lattice. (a) Original test object seen along three orthogonal orientations. (b) Reconstruction from 90 projections taken around a single tilt axis. (c) Reconstruction from 90 projections taken around two orthogonal tilt axes (45 projections around each axis). (d) Reconstruction from 90 projections taken around three orthogonal tilt-axes (30 projections around each axis).

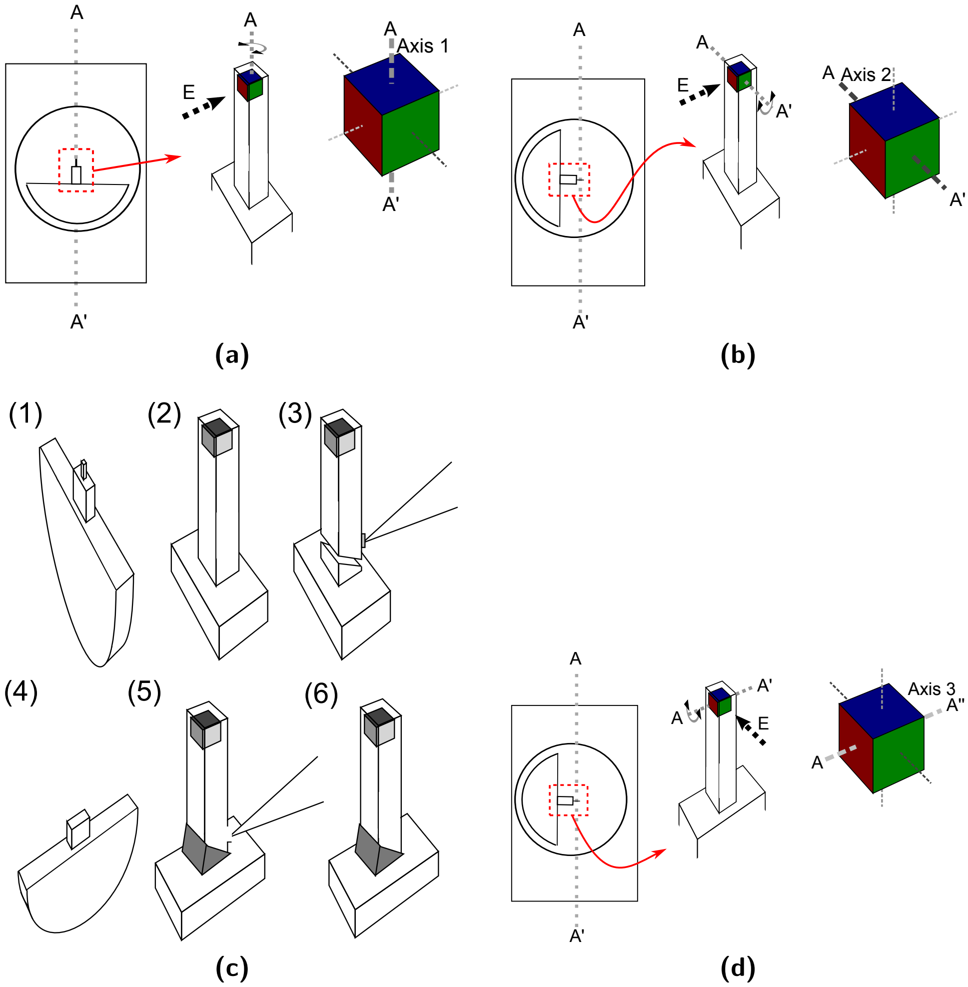

Figure 10.6: Acquisition of three orthogonal tilt series using FIB manipulation: (a) Acquisition of the first tilt series: A needle-shaped sample on a TEM support grid is oriented along the tilt-axis AA' of the microscope stage. E indicates the electron beam direction. (b) Acquisition of the second tilt series. The support grid is rotated by 90° with respect to the microscope stage. The second series is acquired with the needle-shaped sample oriented perpendicular to the tilt-axis. (c) Rotation of the sample in the FIB. (1)&(2) Sample is placed inside the FIB on its support, (3) The sample is glued to a micromanipulator and extracted. (4) The sample support is rotated by 90°. (5) The sample is glued to the rotated support. (6) Sample after rotation. (d) Acquisition of the third tilt series after rotation of the sample. The sample support is oriented similar as for acquisition of the second tilt series. The previous rotation of the sample with respect to the sample support allows acquisition of a third tilt series around a tilt axis perpendicular to the other two tilt axes.

unusable for further tomographic acquisition. Therefore we tried to do the necessary FIB manipulation far away from the region of interest. For this purpose an FIB support grid was manipulated in a plasma-FIB – which allows fast material removal – to reduce the size of supporting posts of the TEM grid. The sample was afterwards prepared in needle-shape on one of these posts. Now for rotation of the sample with respect to the support the whole supporting post can be rotated. The post is cut close to its base and extracted together with the sample. After rotation the whole post is glued to a new support rotated by 90°.

10.4.2 Sample Holder and Supports for Multi-Axis Tomography

The previously discussed FIB-based approach for orthogonal triple-axis tomography is challenging and consists of many steps which may go wrong. For practical routine application of the method specific sample holders or supports would be necessary, which allow acquisition of the three tilt-series without using the FIB between different series. There exist several possibilities for such devices. An approach, which would be compatible with most microscopes and standard tomography holders would be to design a support grid, which allows rotation of the sample around its axis.

Another way could be the use of a sample stage or sample holder, which allows tilting the sample to large tilt angles around both axis perpendicular to the electron beam axis, or an automated tilt-rotate sample stage, which allows automated rotation of the sample in the plane perpendicular to the electron beam and tilting around one axis. Both of these sample stages would allow to get arbitrary orientations between sample and electron beam and could be thereby used to acquire projections for any type of acquisition geometry. Such sample stages, which allow tilting and rotation in an electron microscope exists already, but are not yet commonly available.

10.5 Conclusion

In this chapter we analyzed multiple-axis tomography schemes as a route towards optimizing resolution. We proposed orthogonal triple-axis tomography and showed in simulations, that it can provide better reconstructions than single-axis tomography. We note however that from this single simulation we can not conclude that the proposed scheme will lead to resolution improvement for all types of problems. The practical application to electron tomography of this tilt scheme still remains to be demonstrated. This is a challenging task, which requires either a specific sample holder or support, or external manipulation of the sample between the tilt series, for example in an FIB.

11 Compressed Sensing-Based Reconstruction

Apart from adapting tilt schemes the second route towards improving resolution of a reconstruction for a limited number of projections is to include prior information in the reconstruction. Such methods have been discussed in Section 4.6. The first such technique, which was applied in electron tomography was discrete tomography and more recently also compressed sensing has gained significant attention. If applicable, it has been demonstrated that these techniques can improve the quality of reconstructions from a limited number of projections or for projections taken over a limited tilt range. In this chapter we apply a compressed-sensing based reconstruction method – total variation (TV) minimization – to several diameter-modulated GaAs nanowires. This is still a preliminary investigation and further work will be necessary to complete this study.[1]

11.1 Investigated Samples

On the investigated GaAs nanowires a flow-controlled approach for diameter modulation was demonstrated, similar to the approach used previously for diameter and composition modulation in (In,Ga)N nanowires (see Section 7.1).

GaAs nanowires were synthesized at atmospheric pressure in a cold walled horizontal flow metal-organic chemical vapor deposition (MOCVD) system. Substrates with 90 nm Au colloids on (111)B GaAs were placed on a graphite susceptor inside a quartz chamber. Prior to growth, the substrates were annealed to remove any oxides by heating the susceptor 600 °C using halogen lamps. Substrates were subsequently cooled down to 420 °C and trimethylgallium (TMG) was introduced to initiate growth. Diameter modulation was achieved by varying the flow of AsH_3 during growth, while TMG flow (0.36 sccm, standard cubic centimeter per minute) and H_2 flow (12 slpm, standard liter per minute) were kept constant. AsH_3 flows

---

[1] This work was done in collaboration with Sam Crawford and Silvija Gradečak (MIT). Nanowire growth was performed at MIT

used were 3.43 sccm, 1.15 sccm, 3.43 sccm and 0.69 sccm for 3 min, 1 min, 1 min and 1 min respectively. Reduction in AsH_3 flow led to lower growth rates and larger diameters.

Interestingly different nanowires oriented in the same direction ([111]B) showed significant differences in diameter modulation. It was suspected that these differences could be dependent on the nanowire cross section and its faceting. To investigate this behavior closer electron tomography is an unique tool as it allows reconstruction the local nanowire cross section and its evolution along the nanowire growth direction.

11.2 Tilt Series Acquistion

For electron tomography investigations GaAs nanowires were transferred on a lacey-carbon grid. Previous SEM and TEM investigations indicated three types of diameter modulated nanowires and possible intermediate types. For electron tomography these different types of nanowires were located and tilt-series were acquired on a diameter-modulated section for each nanowire over as large a tilt range as possible, with tilt steps of 2°. Images are acquired in HAADF STEM mode using a probe with a convergence angle of 7 mrad. Fig. 11.1 shows images from the tilt series for the different types of nanowires. Nanowires without diameter modulation are denoted as type 2 (Fig. 11.1a, tilt range -77° to +67°). Nanowires with weak diameter modulation are denoted as type 1 (Fig. 11.1b, tilt range -75° to +53°), with strong diameter modulation as type 3 (Fig. 11.1c, tilt range -77° to +59°), and an intermediate type as type 1b (Fig. 11.1d, tilt range -74° to +56°).

11.3 Reconstruction Methods

The principles of total-variation minimization have been discussed in Section 4.6.2. In the present example the problem was set up in the form

$$\min \|f\|_{TV} + \frac{\mu}{2} \|Af - p\|_2^2 \tag{11.1}$$

f is one slice of the reconstruction, where a single pixel is addressed as f_{ij}, p is a vector containing all projections (the sinogram) acquired from the slice f. A is the projection matrix which maps the image to its projections. μ is a regularization parameter. It can be adapted accordingly to the noise level of the projections, to

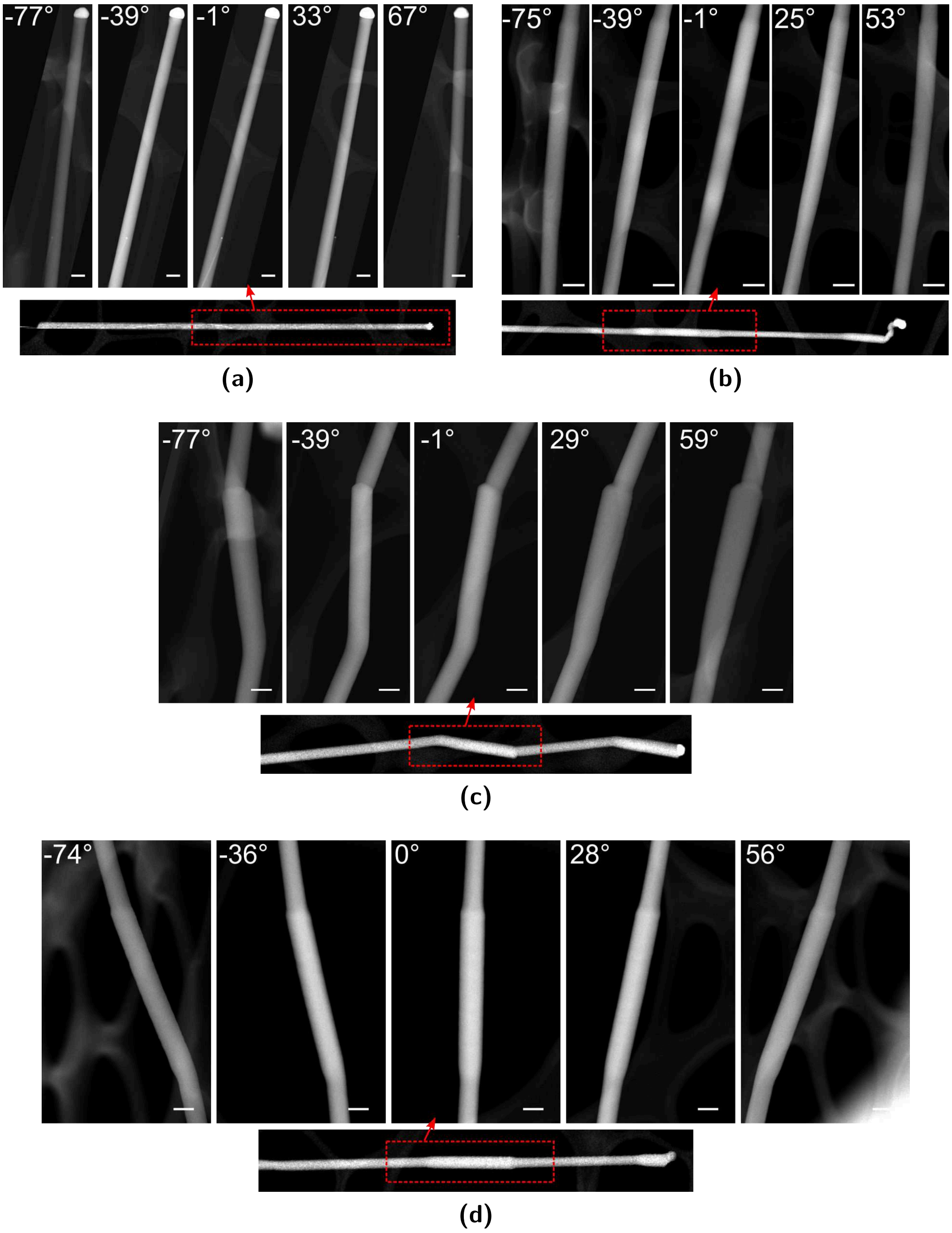

(a) (b) (c) (d)

Figure 11.1: Projections from the tilt series acquired from different types of diameter-modulated GaAs nanowires. (a) Nanowire without diameter modulation (Type 2). (b) Nanowire with weak diameter modulation (Type 1). (c) Nanowire with strong diameter modulation (Type 3). (d) Intermediate nanowire between type 1 and type 3 with diameter modulation (Type 1b). Images below the tilt series show a full view of the nanowires and indicate the region, where the tilt series was taken. Scale bars are 100 nm.

set the relation between minimization of the TV-norm of the image and the l_2 norm of the difference between measured projections and backprojections.

For the operator A and its adjoint operator graphics processing unit (GPU)-based implementations of the projection and backprojection operation from the ASTRA-toolbox were used (ASTRA-Toolbox, 2013, Palenstijn et al., 2011). To solve the TV-minimization problems the solver TVAL3 was used (Li, 2009, Li et al., 2013).

To evaluate the role of the normalization parameter μ single slices were reconstructed for different values for this parameter, while other solver parameters are kept constant. Fig. 11.2 compares reconstructions using TV-minimization of a slice through a GaAs nanowire (type 2) for different values of μ to reconstructions of the same slice using weighted backprojection (WBP) and SIRT. For each of the reconstructed slices the gradient image and the difference between the recorded projections and backprojections is shown.

Using a small value for μ (Fig. 11.2d) provides a very smooth reconstruction at the expense of a relatively large error in the difference projection (Fig. 11.2d(2)). A large value for μ (Fig. 11.2g) minimizes the error in the difference reconstruction, but noise from the projections is transferred to the reconstruction. Based on these observations parameters for the reconstruction of the nanowires were set to get a relatively smooth reconstruction.

11.4 Results and Discussion

Fig. 11.3 compares reconstructions using SIRT and TV-minimization for all different types of nanowires. Compared to the SIRT reconstruction, slices reconstructed using TV-minimization are more homogeneous, which simplifies segmentation of the volume. Missing wedge artifacts are slightly reduced, though this improvement is not enormous and segmentation from SIRT reconstructions would probably lead to similar results as from the TV-minimization reconstruction. The largest improvement can be seen for the reconstruction of the type 1-nanowire (Fig. 11.3b), which suffers most from missing wedge artifacts, as the available usable tilt range was smallest for this nanowire (-75° to +53°).

Fig. 11.4 shows slices through the reconstructed volumes. The reconstructions are rotated to orient the nanowires approximately in the growth direction and to facilitate comparison of their cross sections. Fig. 11.5 shows surface rendered views of the reconstructions of the nanowires.

Full interpretation of these results is still ongoing work, for now we will try summarizing some trends visible in the reconstructions of the different nanowires: The

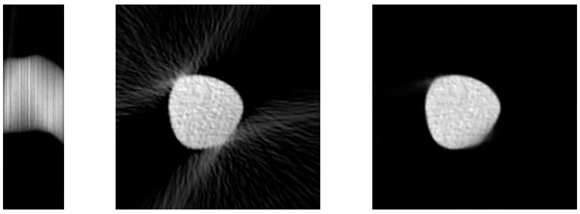

(a) **(b)** WBP **(c)** SIRT

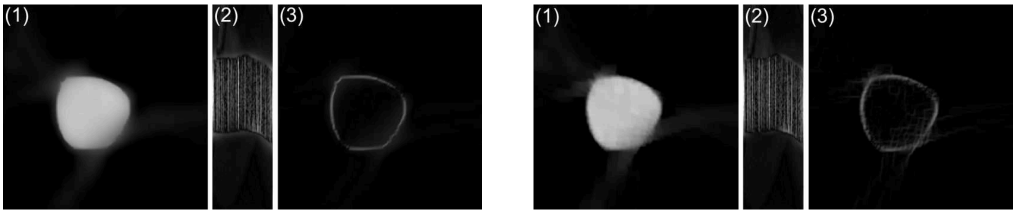

(d) $\mu = 2^5$ **(e)** $\mu = 2^9$

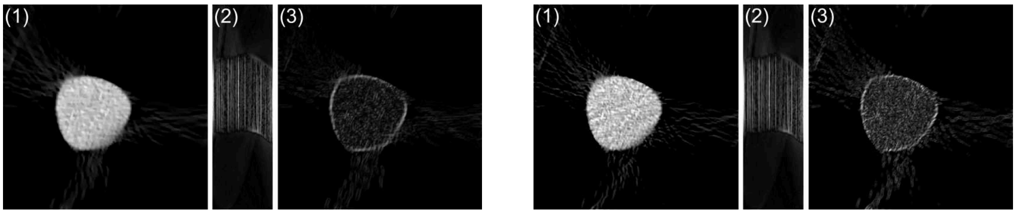

(f) $\mu = 2^{13}$ **(g)** $\mu = 2^{17}$

Figure 11.2: Evaluation of the impact of the regularization parameter μ in a TV-minimization reconstruction of a slice through a GaAs nanowire (type 2). (a) Measured projections (sinogram), (b) reconstruction using a weighted backprojection algorithm, (c) reconstruction using a multiplicative SIRT algorithm with 30 iterations. (d)-(g) Evaluation of TV-minimization based reconstructions for different values of μ. The images show (1) the reconstructed slice, (2) the difference between the recorded projections and re-projections of the reconstruction (3) the gradient image of the reconstructed slice. Images were oriented to locate the missing wedge in the upper left and lower right corners of the reconstructions.

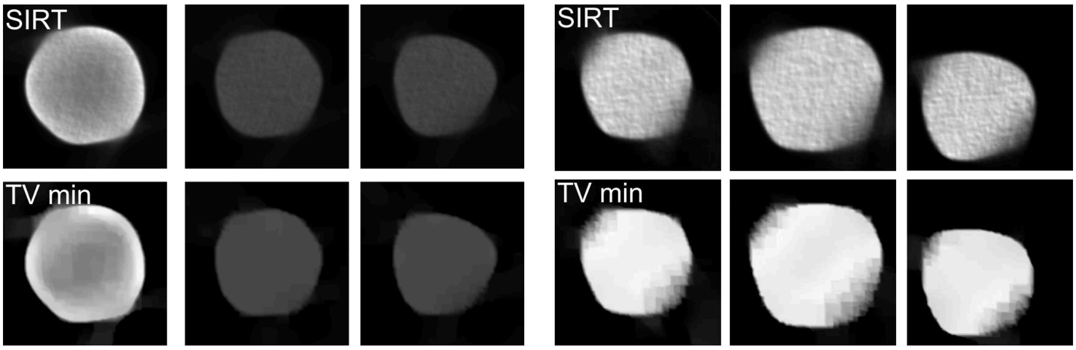

(a) Type 2 **(b)** Type 1

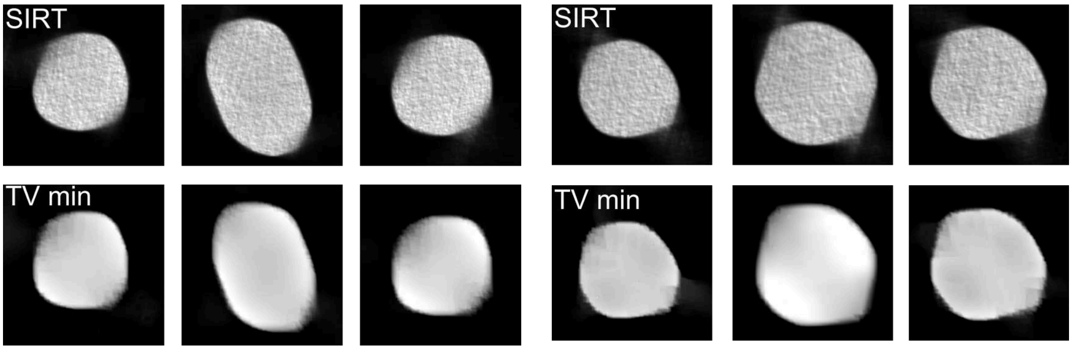

(c) Type 3 **(d)** Type 1b

Figure 11.3: Comparison of SIRT and TV-minimization reconstruction for the different types of GaAs nanowires. Images were oriented to locate the missing wedge in the upper left and lower right corners of the reconstructions.

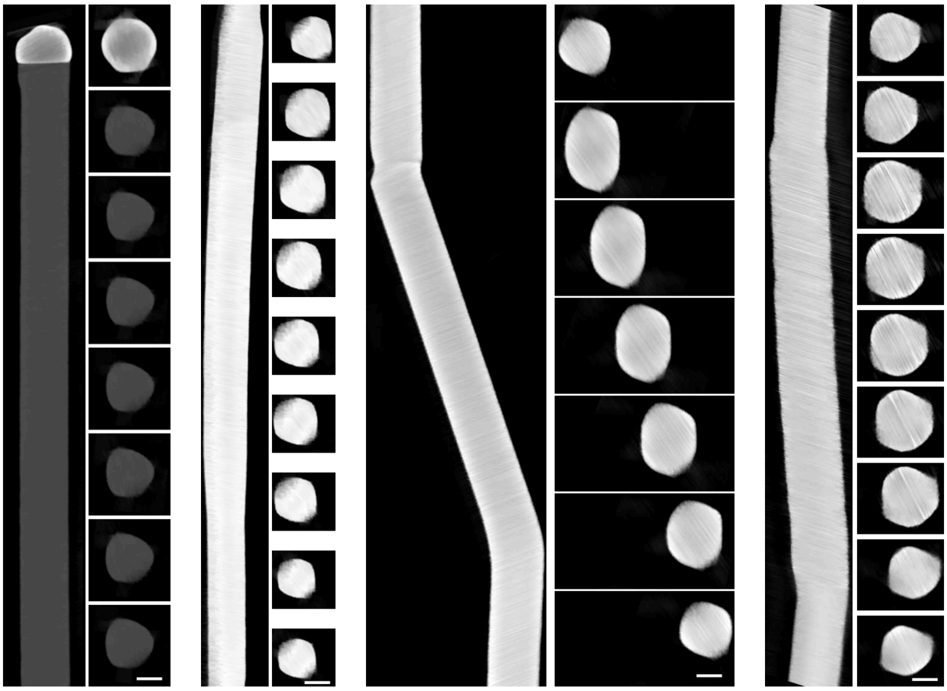

(a) Type 2 **(b)** Type 1 **(c)** Type 3 **(d)** Type 1b

Figure 11.4: Slices through TV-minimization reconstructions of the different types of GaAs nanowires. Growth direction is from bottom to top. Reconstructions are rotated to be approximately oriented along the growth direction, scale bars are 50 nm.

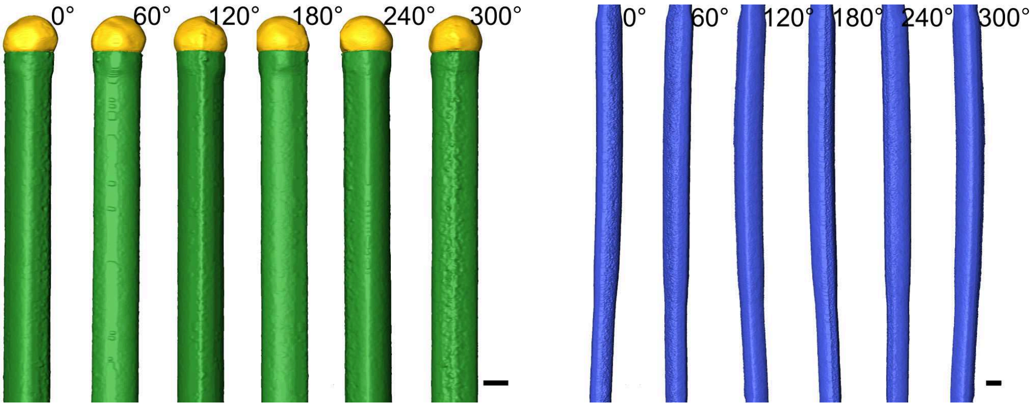

(a) Type 2

(b) Type 1

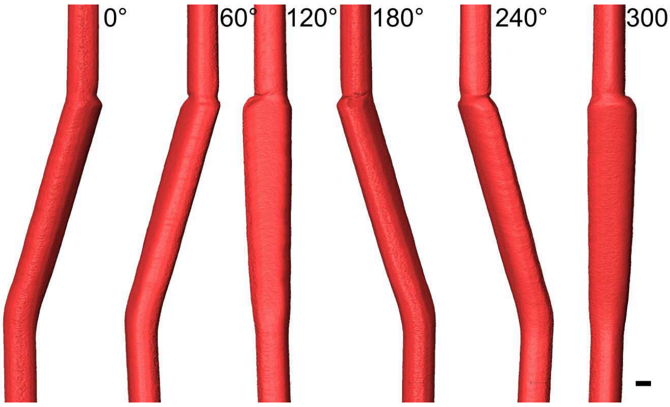

(c) Type 3

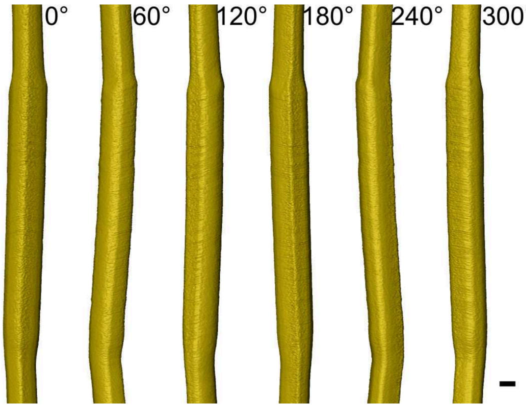

(d) Type 1b

Figure 11.5: Surface rendered views of the different types of GaAs nanowires. Scale bars are 50 nm.

type 2 nanowire, which does not show diameter modulation along its growth direction has a symmetric rounded triangular cross section. Only close to the seed particle the cross section changes to a hexagonal shape. For the type 3 nanowire, which shows the strongest diameter modulation this modulation is mostly due to the elongation of two opposite nanowire surfaces. Additionally the type 3 nanowire changes its growth direction quite significantly together with the diameter modulation. The thin diameter sections before and after the diameter modulated nanowire section show less symmetry than for the type 2 nanowires. For the type 1 nanowire the diameter modulation appears to happen more homogeneous, though less pronounced for the different nanowire surfaces than in the type 3 nanowire. The type 1b nanowire shows similar trends as the type 1 nanowire, but diameter modulation is more pronounced and stronger change of growth direction can be observed.

11.5 Conclusion

In this chapter TV-minimization was applied to tomographic reconstruction of nanowires. For the present case TV-minimization gives reconstructions, which can be easily segmented and some improvement regarding missing wedge artifacts was visible in the reconstructions. However the resolution improvement is not enormous. Further work will be necessary to evaluate the potential of TV-minimization. In particular systematic tests with different parameters for the algorithm and several numbers of projections for simulations and experimental data will be useful. Algorithm-based resolution improvement can be of interest in particular for beam-sensitive samples or for time-consuming imaging techniques, such as EELS, EFTEM or EDS.

Another perspective could be the combination of dual- and multiple-axis tilt schemes and compressed-sensing based reconstruction to combine resolution improvements from both approaches. However such an approach will require full 3D implementation of the reconstruction algorithm, which will be computationally intensive.

12 General Conclusion and Perspectives

In this thesis contributions to developing electron tomography and applications to semiconductor nanodevices and materials were presented. In terms of contrast techniques the feasibility of HAADF STEM tomography for investigations of concentration changes of heavy elements in a lighter environment has been shown, as well as the application of spectral low-loss EFTEM tomography in combination with experimental evaluation of the results as compared to reference spectra. Routes towards improving spatial resolution have been highlighted, in particular the potential of using two and more tilt axes, but also the use of compressed sensing based reconstruction algorithms. The techniques have been applied to answer scientific questions about several semiconductor materials and devices.

It should be mentioned that work on this thesis also included unsuccessful experiments. On such example has been the investigation of nanoparticles consisting of $AgInS_2$ and ZnS. Different preparations of these particles turned out either to be very sensitive to the electron beam or to suffer significantly from carbon contamination during the investigation, likely due to organic components in the solution the particles were prepared in. For such samples working under cryogenic conditions could be necessary as well as limitation of the number of projections – eventually in combination with TV minimization reconstruction or discrete tomography. In another trial, it was attempted to do tomography NEMS cantilevers with a functionalized surface layer. In this case the goal had been to extract a cantilever and glue the full cantilever to a TEM support using FIB tools. The extraction of the cantilever was tried first with a conventional micromanipulator and later with nano tweezers, but both approaches were not successful due to the large size or the manipulators as compared to the nanostructures, which hindered good access. A more conventional preparation, where the sample is protected before extraction could have been successful, but would have significantly limited the area, which can be investigated.

Allover electron tomography is today a mature technique for 3D characterization, though its application is still not routine work and extracting the desired information in challenging application can still fail – due to practical issues, or due to limited contrast or resolution. As such further development is necessary. HAADF STEM will remain the most important contrast technique in materials science, due to short image acquisition times and its relative simplicity. If it can provide contrast, low-loss EFTEM is of significant interest as well, as image acquisition times are also quite short. Concerning other contrast techniques EDS is a technique receiving significant attention recently, due to new detectors and the possibility of performing chemical identification relatively easily. It still suffers however from the long image acquisition times necessary and the consequent reduced spatial resolution due to the limited number of projections, which can be acquired. The same is true for core-loss EFTEM tomography or EELS tomography. Using these techniques is of interest, if other techniques fail, but will remain time-consuming and limited to samples little sensitive to the electron beam. An important contribution to making the application of time-consuming imaging techniques more feasible could be provided by the use of reconstruction algorithms, such as total-variation minimization, which can – at least for specific cases – compensate for the limited number of projections.

Spatial resolution improvement is the second important issue in electron tomography. Even though atomic resolution tomography has been demonstrated, it remains limited to very few specific cases. The large challenge still to overcome is to make atomic resolution electron tomography feasible for a wider range of samples: samples consisting of lighter materials and of larger size or beam-sensitive samples. Recent developments of reconstruction algorithms will be one piece necessary for achieving this goal, but not the only one. Multiple-axis tilt schemes or other tilt schemes adapted to the sample structure could provide another contribution. A further approach, which has been discussed recently is the combination of tomography with the acquisition through-focal series, where a series of images at different focus over the thickness of the sample are acquired for several tilt angles.

In the frame of spatial resolution improvement two important contributions will also stem from sample preparation and image alignment. Sample preparation in the FIB has already allowed overcoming the limitations of the missing wedge and – in particular for semiconductor devices – it is essential for the success of a tomography experiment. The ultimate goal of FIB sample preparation to optimize resolution for devices is to prepare a device without damaging it and with as little other material around it as possible.

Image alignment is a task, which is frequently neglected in electron tomography. While developments of reconstruction algorithms usually gain significant attention, alignment methods – though being maybe even more important – receive much less attention. Cross-correlation and marker based alignment methods, which have been developed quite some time ago are still the generally used methods. Cross-correlation methods in particular are however prone to errors, which can introduce errors in the reconstruction, regardless of the reconstruction algorithm used. One promising approach, which could be also automated, could be the combination of alignment and reconstruction to improve the image alignment by comparing backprojections to the recorded projections and adapt alignment parameters based on this comparison.

In conclusion electron tomography is now an indispensable technique for semiconductor characterization, providing information, which can not recovered by any other technique. Further developments are still necessary though to make it a technique with the same reliability as 2D TEM techniques.

13 Résumé en Français

13.1 Introduction

Compte tenu des tailles critiques rencontrées en micro et nanoélectronique, les procédés expérimentaux utilisés lors de la fabrication de dispositifs à semi-conducteurs doivent être contrôlés par des techniques ayant idéalement une résolution atomique. Cela explique l'essor des techniques de nanocaractérisation pour la compréhension et l'optimisation de ces dispositifs. Il s'agit notamment de la caractérisation électrique et optique de dispositifs fonctionnels afin de vérifier leurs comportements, mais aussi de la caractérisation morphologique, chimique et structurale (caractérisation dite « physique ») pour comprendre les origines de ces comportements et *in fine* d'optimiser les procédés de fabrication et de construction.

La plupart de ces techniques fournissent une information uni ou bidimensionnelle d'un objet qui est pourtant tridimensionnel ; il peut s'agir d'images 2D ou de profils en profondeur par exemple. Connaître la structure 3D est cependant fondamental pour correctement interpréter les phénomènes, ce qui explique l'essor de toutes les techniques 3D à différentes échelles, permettant notamment d'accéder à une imagerie morphologique, chimique et structurale 3D.

Le « TEM » (Transmission Electron Microscope – Microscope Electronique à Transmission) est l'un des outils les plus importants pour la nanocaractérisation de dispositifs à semi-conducteurs. En se basant sur les concepts de tomographie, les possibilités offertes par le « TEM » ont été étendues à la 3$^{\text{ème}}$ dimension, permettant d'ainsi d'obtenir des images 3D de dispositifs plus ou moins complexes, avec une résolution pouvant atteindre l'atome.

Dans ce contexte, ce travail de thèse vise à développer la tomographie électronique et à l'appliquer à des dispositifs à semi-conducteurs. Différents matériaux et dispositifs sont explorés, afin d'apporter des éléments de réponse à certaines questions encore ouvertes sur leur forme et leur distribution chimique 3D. En se basant sur un état de l'art complet, des développements sont proposés afin de répondre à ces questions. En particulier, différents modes de contraste sont étudiés, et des pistes visant à améliorer la résolution spatiale sont mises en œuvre.

13.2 Contexte

La première partie de cette thèse est une introduction générale à la physique des semi-conducteurs et aux techniques de nanocaractérisation 3D. Cette partie comprend aussi une introduction technologies employées. Les dispositifs fondamentaux les plus courants (transistors, optoélectronique, « NEMS » (Systèmes Electro-Mécaniques Nanométriques) sont abordés, afin d'exacerber le besoin en caractérisation 3D.

Les différentes techniques utilisées pour la nanocaractérisation 3D en science des matériaux sont détaillées et discutées. Il s'agit en particulier de la tomographie par rayons X, de la tomographie « destructrice » par faisceau d'ions, de la tomographie électronique et de la sonde atomique tomographique. Ce panel de technique couvre un large domaine d'échelles spatiales, de tailles d'échantillon et d'applications. Les techniques mettant en œuvre des modes de contraste avancés (morphologie, chimie, structure) sont discutées.

13.3 Méthodes Expérimentales

Les méthodes expérimentales sont expliquées dans la deuxième partie du manuscrit. Grossièrement, une « expérience de tomographie électronique » comprend 3 parties : la préparation d'échantillon, l'acquisition d'image sur le microscope électronique et le traitement de données.

Le traitement de données est abordé en premier lieu. Les principes fondamentaux de reconstruction en tomographie sont expliqués ainsi que différents algorithmes de reconstruction spécifiques à la tomographie. Les concepts de tomographie mettant en œuvre 2 voire 3 axes de rotation sont soulignés. Les méthodes de prétraitement (notamment l'alignement avant reconstruction) et de post-traitement (filtrage et segmentation) y sont discutées.

Le principe du microscope électronique à transmission (notamment le fonctionnement de l'instrument et l'interaction rayonnement matière) ainsi son utilisation dans le cas de la tomographie électronique sont abordés. Afin d'appliquer les algorithmes « classiques » de reconstruction à la tomographie électronique, il est important que les projections remplissent un certain nombre de conditions : en particulier, il est nécessaire que le signal mesuré par le détecteur soit une fonction monotone de la quantité physique à investiguer. Dans le cas de matériaux cristallins, les techniques répondant à ce critère sont :

- Le « HAADF STEM » (High-Angle Annular Dark Field Scanning Transmission Electron Microscope – microscopie électronique à transmission en balayage, en mode champ sombre annulaire à angle élevé),
- le « STEM-EELS » (STEM Electron Energy Loss Spectroscopy – spectroscopie à perte d'énergie des électrons),
- l' « EFTEM » (Energy Filtered TEM – microscopie électronique à transmission à énergie filtrée),
- l' « EDS » (Energy Dispersive Spectroscopy – spectroscopie dispersive).

Ces techniques sont toutes discutées dans cette partie.

13.4 Nouveaux Mode de Contraste

La troisième partie de cette thèse expose des résultats expérimentaux basés sur les différentes possibilités de contraste offertes par le TEM. En tout premier, nous étudions le mode « HAADF STEM » en tomographie, sur 2 types d'échantillon : il s'agit de nanofils InN/InGaN et de silicium sur-dopé. Ensuite, nous utilisé la tomographie « EFTEM » spectrale à faible perte d'énergie, appliquée à des capacités à base de nanofils.

Dans le cas des nanofils InN/InGaN, non seulement la forme des nanofils est reconstruite, mais aussi leur composition : il est en effet important de séparer les 2 matériaux, l'InN et l'InGaN, et donc de recourir à un contraste chimique. La tomographie électronique a permis de mieux comprendre l'évolution de la facettisation des nanofils pendant leur croissance (Lim et al., 2013).

Dans le cas du silicium sur-dopé, c'est une expérience de tomographie électronique ex-situ qui a été menée, afin de mettre en évidence l'effet du recuit sur la distribution du dopant (dans ce cas le sélénium). La sensibilité en masse de l' « HAADF-STEM » a permis de localiser les régions à forte concentration en sélénium et même de comparer qualitativement sa concentration en différents points et à différentes étapes du recuit (Haberfehlner et al., 2013b).

Enfin, des capacités à base de nanofils cœur-coquille, avec un cœur en silicium et une coquille en Al_2O_3 et TiN ont été sondées par tomographie « EFTEM » à faible perte d'énergie. Cette technique a été utilisée car le mode « HAADF-STEM » ne donnait pas un contraste suffisant entre les différents matériaux. En enregistrant des jeux de données de tomographie à différentes pertes d'énergie des électrons, des spectres locaux (c'est-à-dire en chaque voxel) ont pu être reconstruits et comparés à des spectres de référence mesurés sur chacun matériaux, pris individuellement (Haberfehlner et al., 2012, Morel et al., 2012).

13.5 Amélioration de la Résolution

La quatrième et dernière partie du manuscrit aborde la question de la résolution spatiale en tomographie électronique. Il s'agit en particulier d'optimiser l'échantillonnage en utilisant la tomographie double et triple axe, et d'utiliser des méthodes de reconstruction plus modernes. La tomographie double axe, c'est-à-dire utilisant 2 axes de rotation perpendiculaires, est mise en œuvre pour améliorer la résolution spatiale dans le cas de transistors « triple-grille ». Son avantage, même dans le cas de données complètes (sans projection manquantes), est démontré. L'orientation des axes de rotation est judicieusement choisie en fonction de celle du transistor (Haberfehlner et al., 2013a).

En se basant sur ces travaux, une idée originale basée sur l'utilisation d'un troisième axe de rotation (voire même plus) dans un troisième plan de l'espace est développée et mise en œuvre sur des simulations. Il est démontré qu'un tel schéma d'échantillonnage présente un certain nombre d'avantages par rapport à la méthode conventionnelle de tomographie électronique. Des pistes sont proposées pour l'implémentation pratique de la méthode.

Finalement, nous appliquons des méthodes de reconstruction plus récentes, basées la minimisation de la variation totale, à la reconstruction de la forme de nanofils GaAs de diamètre modulable. La paramétrisation de cet algorithme est en particulier étudiée ; il apparaît qu'un travail plus profond serait nécessaire pour réellement appréhender le potentiel de ces algorithmes.

13.6 Conclusion

La tomographie électronique est aujourd'hui une technique mûre et sûre pour la caractérisation 3D à l'échelle nanométrique. Cependant, son application n'est pas encore triviale pour faire ressortir certaines informations dans les cas scientifiques complexes tels que ceux abordés ici. Ceci est principalement dû à un contraste ou une résolution parfois insuffisants. Des développements plus poussés sont donc toujours pleinement justifiés. La tomographie « HAADF-STEM » restera certainement la technique la plus couramment utilisée en science des matériaux, car elle bénéficie de 2 atouts majeurs : sa simplicité et un temps de mesure relativement rapide. La tomographie « EFTEM » à faible perte d'énergie est également intéressante pour faire ressortir un contraste chimique, et reste une technique rapide. D'autres méthodes, notamment basées sur l' « EDS », sont aujourd'hui d'actualité car elles bénéficient des nouvelles technologies de détection et permettent d'effectuer une réelle imagerie chimique tridimensionnelle. Elles sont cependant limitées par des temps de mesure encore rédhibitoires, et une résolution spatiale moindre à cause d'un échantillonnage angulaire sous-optimal. C'est également le cas de la tomographie « EFTEM » ou de la tomographie « EELS ». Ces techniques restent intéressantes dans le cas où les autres techniques ne fonctionnent pas, mais sont néanmoins plus lourdes à mettre en œuvre car plus longues et plus irradiantes.

La résolution spatiale est une limitation en tomographie électronique : même si des résolutions atomiques ont été démontrées, cela reste confiné à certaines applications très spécifiques et sur des objets de très petite taille. Un challenge est de parvenir à atteindre une résolution atomique pour des échantillons plus complexes et variés : matériaux légers, matériaux sensibles aux dégâts d'irradiation, et surtout échantillons de taille « raisonnable ». Le développement de nouveaux algorithmes de reconstruction est fondamental pour atteindre ce but, mais n'est pas le seul. D'autres approches, tels que la tomographie utilisant plusieurs jeux de données en confocal, c'est-à-dire se focalisant sur différents plans, sont en plein essor. Un point clef pour atteindre une meilleure résolution spatiale est la préparation d'échantillon, toujours critique malgré des outils performants, et l'alignement des images.

Pour conclure, il apparaît clairement que la tomographie électronique est devenue un outil indispensable pour la nanocaractérisation des dispositifs à semi-conducteurs car elle permet d'accéder à une information non atteignable par les autres méthodes. Elle doit maintenant être rendue aussi routinière que les techniques bidimensionnelles.

Appendices

A Supplementary Information for Chapter 2

A.1 Properties of Semiconductors

Semiconductors are defined by their bandgap. While metals have no bandgap and insulators typically have a large bandgap of 6 eV or more, semiconductors have bandgaps of smaller energy. In their intrinsic state semiconductors are typically weakly conducting materials, but their properties can be adapted by introducing impurities and by applying electric fields.

The most frequently occurring crystal structure of semiconductors are the diamond lattice for group IV semiconductors (e.g. Ge, Si) and the zinc-blende lattice for compound semiconductors (e.g. GaAs, GaP). Other important crystal structures for compound semiconductors are the wurzite (e.g. GaN, CdS, ZnS) and rock-salt lattices (e.g. PbS, PbTe).

A.1.1 Bandstructure

The bandstructure of a semiconductor gives information about its electrical and optical properties. It is the energy-momentum ($E(k)$) relationship, which can be obtained by solving the Schrödinger equation for electrons in the crystal lattice. Fig. A.1 shows the bandstructure for Ge, Si and GaAs, Table A.1 lists some important properties. For every semiconductor there is a forbidden energy region in which no states are allowed. The energy bands below this region are called valence bands, the energy bands above are called conduction bands. The distance between the lowest allowed energy in the conduction bands and the highest allowed energy in the valence bands gives the bandgap E_g of the semiconductor.

If the maximum of the valence bands and the minimum of the conduction band are located at the same momentum, the semiconductor is called direct semiconductor (e.g. GaAs), if they are located at different positions, it is called an indirect semiconductor (e.g. Ge, Si). This is of importance for optical properties.

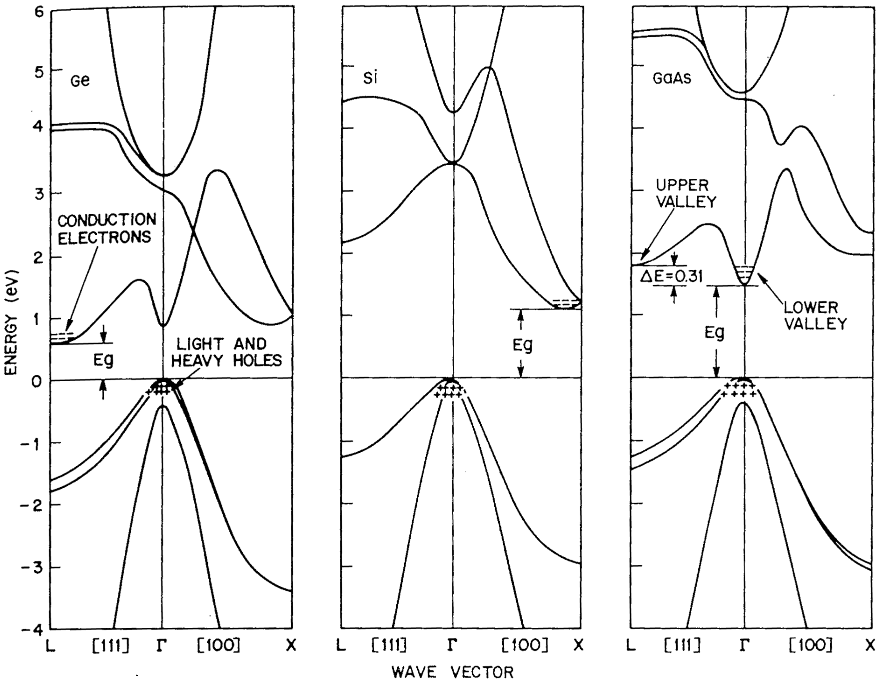

Figure A.1: Bandstructure of germanium, silicon and gallium-arsenide (Sze, 1981).

	Ge	Si	GaAs
Band gap at 300 K (eV)	0.66	1.12	1.424
Effective Mass m^*/m_0			
Electrons	$m_l^* = 1.64$	$m_l^* = 0.98$	0.067
	$m_t^* = 0.082$	$m_t^* = 0.19$	
Holes	$m_{lh}^* = 0.044$	$m_{lh}^* = 0.16$	$m_{lh}^* = 0.082$
	$m_{hh}^* = 0.28$	$m_{hh}^* = 0.49$	$m_{hh}^* = 0.45$
Mobility at 300 K (cm^2/Vs)			
Electrons	3900	1500	8500
Holes	1900	450	400
Dielectric constant	16	11.9	13.1

Table A.1: Some properties of important semiconductors, $m_0 = 9.11 \times 10^{-31}$kg is the electron rest mass (Sze, 1981).

Another important property, which can be derived from the bandstructure is the mobility of free carriers μ_c in the crystal. The mobility depends on the effective mass of carriers, electrons or holes in the crystal. The effective mass m^* is given as

$$\frac{1}{m^*} = \frac{1}{\hbar^2}\frac{d^2E(k)}{dk^2} \tag{A.1}$$

where $\hbar = 2\pi h = 1.054 \times 10^{-34}$J s is the reduced Planck constant. m^* is actually a tensor, depending on orientation and energy. Practically for free carriers located in the minimum of an energy band, it can be however often approximated as constant. It can be seen that the effective mass is inversely proportional to the curvature of the band. A high curvature gives a low effective mass and thereby high carrier mobility. For the materials shown in Fig. A.1 this means that the mobility of holes is higher for Ge than for Si and GaAs (see Table A.1). The mobility of electrons is highest for GaAs, as the curvature of the Γ-minimum is particularly high. The mobility of electrons in Ge is lower and again lower for Si. Generally the mobility of electrons is higher than the mobility of holes.

A.1.2 Carrier Statistics

The statistics of electrons in a semiconductor are given by the density of states and by the Fermi-Dirac distribution function. The Fermi-Dirac function gives the probability of the occupation of a state as a function of energy. It is given as

$$f(E) = \frac{1}{1 + \exp\left(\frac{E-E_F}{kT}\right)} \tag{A.2}$$

with E_F being the Fermi level, T the temperature (in K) and the Boltzmann constant $k = 8.62\times10^{-5}$eV K^{-1} = 1.38×10^{-23}J K^{-1}. At zero temperature all states up to the Fermi level would be occupied while all states above would be free. With increasing temperature the probability of free states below the Fermi level and occupied states above the Fermi level increases.

The density of states can be calculated given as

$$N(E) = \frac{1}{(2\pi)^2}\frac{4\pi}{\hbar^3}\sqrt{(2m^*)^3}E^{1/2} \tag{A.3}$$

for a three-dimensional (3D) system, where electrons can move freely along all three dimensions of space. In this case the density of states increases with the square-root of the energy, so there are only few states available close to the band edges, while further away from the edges the density of states increases.

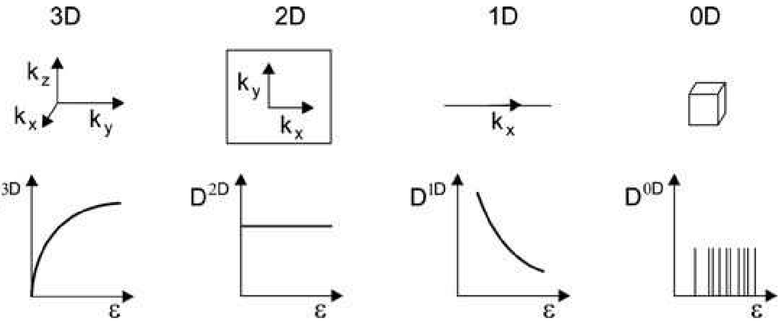

Figure A.2: Density of states in a 3D, 2D, 1D and 0D system (Renk, 2012)

When the size of a semiconductor is reduced below the de Broglie wavelength of the electrons, the number of dimensions in which electrons can freely move are reduced. This changes the density of states as shown in Fig. A.2. In the two-dimensional (2D) case (small in one dimension) the density of states remains constant with energy giving discrete steps in the shape of the function. In a one-dimensional (1D) system (small in two dimensions) the density of states is inversely proportional to the square-root of the energy, giving steps, which decrease with energy. Finally in a zero-dimensional (0D) case (small in three dimensions) only discrete energy levels are allowed, giving Dirac peaks for the density of states. Such 0D systems are referred to as quantum dots, 1D systems as quantum wires, 2D systems as quantum films. Examples of materials with reduced dimensionality are nanowires, quantum dots, carbon nanotubes or graphene.

The actual number of occupied states can be found by integrating the density of states with the Fermi-Dirac distribution function. Unoccupied states in the valence band remain as holes, which can serve as positively charged free carriers, occupied states in the conduction band give electrons, which serve as negatively charged free carriers. In a pure, undoped semiconductor these statistics give the intrinsic concentration of carriers, which is higher for semiconductors with a small bandgap and depends strongly on temperature.

To adapt the parameters of these statistics and increase the number of free carriers, semiconductors can be doped. Dopants are divided into acceptors, elements with three or less outer shell electrons and donators, elements with five or more outer shell electrons. Acceptors remove electrons from the crystal (p-doping), providing a hole, donators provide additional electrons (n-doping). Doping reduces the distance between the Fermi level and the edges of conduction and valence bands. P-doping reduces the distance between valence band and Fermi level, while n-doping reduces the distance between conduction band and Fermi level.

A.1.3 Electrical Properties

As previously discussed the mobility of free carriers μ_c (in cm s^{-1}) is an important property of a semiconductor, which governs its electrical properties. The mobility is the proportionality constant between the drift velocity v_d (in cm^2 V^{-1} s^{-1}) of carriers and an applied electric field $\mathbf{E}$ (in V cm^{-1}). This relation is given as

$$v_d = \mu_c \mathbf{E} \tag{A.4}$$

The mobility is significantly influenced by scattering from phonons and ionized impurities. Therefore higher temperature and higher concentrations of dopants reduce the mobility.

The resistivity ρ (in Ω cm) of a material is defined as the proportionality constant between an electric field and the current density J (in A cm^{-2}) as

$$\mathbf{E} = \rho J \tag{A.5}$$

The resistivity depends on the mobility and on the number of electrons and holes, which are available as carrier. It can be obtained as

$$\rho = \frac{1}{e\left(\mu_n n + \mu_p p\right)} \tag{A.6}$$

with the unit charge $e = 1.602 \times 10^{-19}$C and the number of electrons n and holes p and their corresponding mobilities μ_n and μ_p. In doped semiconductors usually one type of carriers is dominant, so one of the two terms can be ignored.

The carrier transport, which takes place under an electric field is called drift current. In addition to the drift current there is a second contribution to the electrical current in semiconductors, which is the diffusion current. The diffusion current is caused by thermal movement of carriers. Thermal diffusion of carriers is always present, but leads to an observable current only if an inhomogeneous carrier distribution is present. This inhomogeneous distribution will be reduced by the diffusion current.

The diffusion current along a direction x can be written as

$$J_n = e D_n \frac{dn}{dx} \tag{A.7}$$

for electrons and for holes as

$$J_p = -e D_p \frac{dp}{dx} \tag{A.8}$$

with the diffusion coefficients D_n and D_p for electrons and holes (in cm^2 s^{-1}). Those are given as

$$D_n = U_t \mu_n \tag{A.9}$$

and

$$D_p = U_t \mu_p \tag{A.10}$$

U_t is the thermal voltage, which is given as

$$U_t = \frac{kT}{e} \tag{A.11}$$

with the temperature T and the Boltzmann constant k. At 300 K its value is 25.85 mV.

Combining the drift and diffusion components gives the drift-diffusion equations, which can be used to calculate the current density in a semiconductor. For holes it is written as

$$J_p = ep\mu_p E - eD_p \frac{dp}{dx} \tag{A.12}$$

for electrons as

$$J_n = en\mu_n E + eD_n \frac{dn}{dx} \tag{A.13}$$

A.1.4 Optical Properties

Photons can interact with the electrons in a semiconductor, which gives rise to several optical applications of semiconductors. Three types of interaction between photons and electrons are possible:

- Absorption: A photon can transfer its energy to an electron which is elevated to a higher energy state. This process forms the basis for devices like solar cells and optical detectors.
- Spontaneous emission: An excited electron can loose energy, moving to a lower energy state. From the excess energy a photon is created. This process is the basis for light emitting diodes.
- Stimulated emission: A photon interacting with an excited electron can create a second identical photon. In the process the excited electron looses energy, moving to a lower energy state. This process is of importance for semiconductor laser diodes.

Transitions of electrons in semiconductors can happen between different bands (in particular between valence and conduction band) or within one band. The first type is called interband transition, the second type intraband transition. For most optical application interband transitions are used. In these transitions photons with an energy larger than the band gap can be absorbed or emitted.

For the optical properties of a semiconductor it is important, whether a semiconductor is direct or indirect. In an electron-photon interaction energy and momentum need to be conserved. As the momentum of a photon is negligible compared to the momentum of the electron, optical transitions always happen vertically in the $E(k)$ diagram. In an indirect semiconductor therefore additionally another particle, most frequently a phonon needs to participate in the interaction. These transitions are much less probable than direct transitions, which is why for optical devices, in particular for light emitting devices mostly direct semiconductors are used.

In a direct semiconductor the probabilities for absorption and emission depend on the occupation of states at the lower and higher energy level, between which the transition takes place. For absorption the lower level needs to be occupied by an electron and in the upper level there needs to be a free state to which the electron can be transferred. For emission the situation is exactly opposite. A higher level needs to be occupied, while a lower level needs to be free. While in thermodynamical equilibrium the number of free states in the higher energy level is always higher than in the lower state in an excited semiconductor this situation can be inverted. In this case stimulated emission becomes more probable than absorption, which leads to amplification of light. This is the basis for semiconductor lasers.

B Supplementary Information for Chapter 7

B.1 Evaluation of the Gradient Watershed Segmentation Method

To get a better understanding of the behavior of the proposed segmentation method and in particular on the influence of missing wedge artifacts on the results, simulations have been performed. For this purpose we compared the gradient watershed segmentation algorithm to segmentation using absolute threshold values. For the simulations a two-dimensional phantom object with a size of 512×512 pixels has been created. The phantom is shown in Fig. B.1a. It consists of a grey circle (pixel value = 152) on a black background (pixel value = 0). Inside the grey circle we created 13 "precipitates" represented as white circles and ellipses (pixel value = 255) of different sizes. Ellipses are oriented either horizontally or vertically. The horizontally oriented ellipses will be affected strongest by missing wedge artifacts.

Two datasets of one-dimensional projections of the object were calculated. The first dataset for a tilt range from -78° to +78° with a step of 1° corresponding to the tilt range used in the experiments, the second dataset for a full tilt range of -90° to +89° again with a step of 1°. The second dataset will therefore not suffer from missing wedge artifacts. To the projections white Gaussian noise was added. The two sets of projections with and without missing wedge are shown in Figs. B.1b&B.1c respectively.

Each of the two datasets is reconstructed using a SIRT algorithm with 20 iterations. The reconstruction of the dataset with missing wedge is shown in Supplementary Fig. B.2a, without missing wedge in Fig. B.2b. Before segmentation of the reconstructions anisotropic diffusion filtering is applied on the reconstructions, the filtered reconstructions are shown in Figs. B.2c&B.2d. On the filtered reconstructions watershed segmentation and segmentation using an absolute threshold value are performed. Watershed segmentation was done as described in the main text.

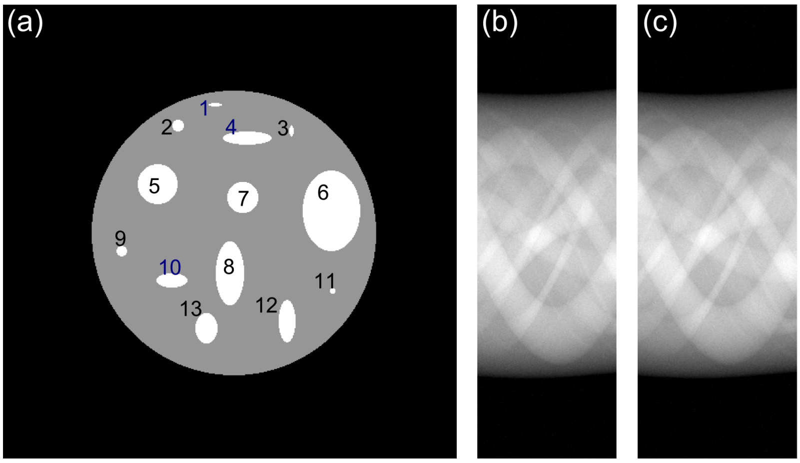

Figure B.1: (a) Simulated phantom with 13 precipitates. Precipitates are indexed from 1 to 13. Numbers of precipitates, which are prone to missing wedge artifacts (1, 4, 10) are colored blue. (b) Noisy projections of the phantom for a tilt range from -78° to +78°. (c) Noisy projections of the phantom for a tilt range of -90° to +89°.

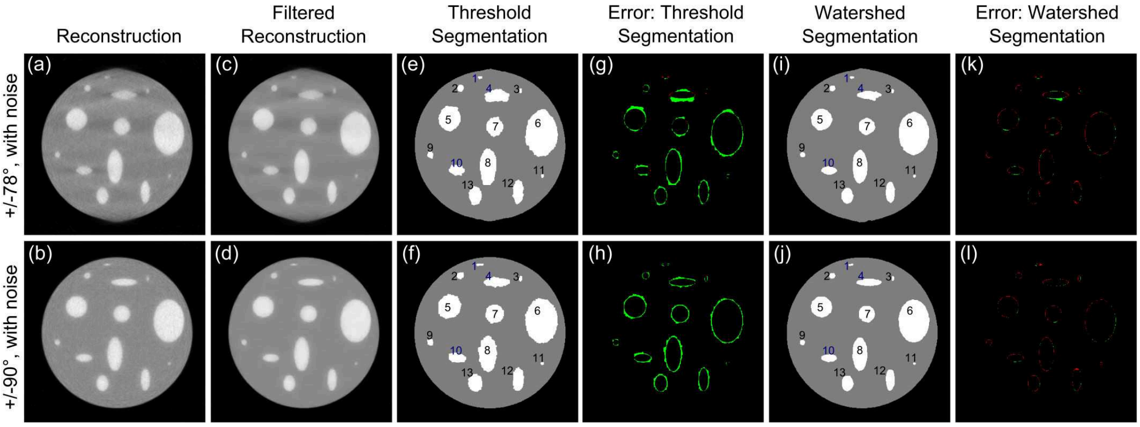

Figure B.2: Reconstruction and segmentation of the phantom from noisy datasets with and without missing wedge: Original reconstruction (a) with missing wedge and (b) without missing wedge. Filtered reconstruction using anisotropic diffusion filtering (c) with missing wedge and (d) without missing wedge. Results from the segmentation using an absolute threshold (e) with missing wedge and (f) without missing wedge. (g) Erroneous pixels of the segmentation shown in (e). (h) Erroneous pixels of the segmentation shown in (f). Results using watershed segmentation (i) with missing wedge and (j) without missing wedge. (k) Erroneous pixels of the segmentation shown in (i). (l) Erroneous pixels of the segmentation shown in (l). In the error images pixels missing in the segmentation are shown in red, while additional pixels are shown in green.

For the segmentation using absolute threshold values the threshold was set manually. It was chosen low enough to allow segmentation of the smallest precipitates, which have lost contrast in the reconstruction due to resolution limits imposed by the number of projections.

Figs. B.2e&B.2f show the results of the segmentation for both datasets using an absolute threshold, Figs. B.2g&B.2h show images with erroneous pixels for both segmentations. Supplementary Figs. B.2i-k show results of the watershed segmentation for both datasets and the corresponding images with erroneous pixels. For segmentation using an absolute threshold value, we observe a systematic overestimation of the size of the precipitates, which increases with particle size, for both datasets, with and without missing wedge. This is due to the chosen threshold value, which was selected to include also small precipitates. Using a lower threshold would reduce this effect for large precipitates, but would lead to the loss of the smallest precipitates in the segmentation. The errors using watershed segmentation are significantly lower, in particular for large particles. For the dataset without missing wedge erroneous pixels are constrained to very thin layers on the surface of the precipitates. Such errors are to be expected due to discrete steps at interfaces of the phantom object. Concerning missing wedge artifacts, the ellipses oriented horizontally are affected by such artifacts for both segmentation methods, though the impact is limited due to the relatively large tilt range of +/-78°. Missing wedge artifacts can be seen for example precipitate #4: Pixels are missing in the segmentation on two sides of the precipitates, while the precipitate is elongated on the two other sides. Though these artifacts are visible for both segmentation methods, their impact is significantly smaller using watershed segmentation.

In Table B.1 and Fig. B.3 measurements and measurement errors for all precipitates for each segmentation are given.

The results show a smaller error for the watershed algorithm compared to segmentation using a threshold value. While in these measurements the particles affected by missing wedge artifacts do not show systematically a larger error for the reduced dataset, we note that this is also due to a partial compensation of errors from the different sides of the particles. This can however not be generally expected for all particle shapes.

These simulations indicate that while the missing wedge has an impact on the measurement results its effect is limited by the relatively small missing tilt range. For the simulated object the watershed segmentation method performs significantly better than thresholding of the reconstruction. The segmentation method also limits the effects of missing wedge artifacts on the results. For larger particles the error

Index	Size (px^2)	±78° watershed	±78° threshold	±90° watershed	±78° threshold
11	32	20 (-37.5%)	24 (-25.0%)	20 (-37.5%)	32 (0.0%)
1	**48**	**40 (-16.7%)**	**21 (-56.3%)**	**44 (-8.3%)**	**55 (+14.6%)**
3	49	33 (-32.7%)	37 (-24.5%)	37 (-24.6%)	49 (0.0%)
9	112	96 (-14.3%)	122 (+8.9%)	96 (-14.3%)	135 (+20.5%)
2	137	117 (-14.6%)	144 (+5.1%)	117 (-14.6%)	166 (+21.2%)
10	**444**	**443 (-0.2%)**	**489 (+10.1%)**	**413 (-7.0%)**	**524 (+18.0%)**
4	**653**	**702 (+7.5%)**	**787 (+20.5%)**	**615 (-5.8%)**	**772 (+18.2%)**
13	674	646 (-4.2%)	719 (+6.7%)	645 (-4.3%)	783 (+16.2%)
12	720	685 (-4.9%)	791 (+9.9%)	688 (-4.4%)	852 (+18.3%)
7	973	944 (-3.0%)	1015 (+4.3%)	936 (-3.8%)	1108 (+13.9%)
5	1597	1575 (-1.4%)	1714 (+7.3%)	1563 (-2.1%)	1765 (+10.5%)
8	1812	1762 (-2.8%)	1932 (+6.6%)	1766 (-2.5%)	2053 (+13.3%)
6	4647	4608 (-0.8%)	4839 (+4.1%)	4596 (-1.1%)	4943 (+6.4%)

Table B.1: Measured size of precipitates and relative error for the noisy phantom with and without missing wedge, using gradient watershed segmentation and thresholding. The precipitates are sorted by size. Values for precipitates prone to missing wedge artifacts are shown in bold font.

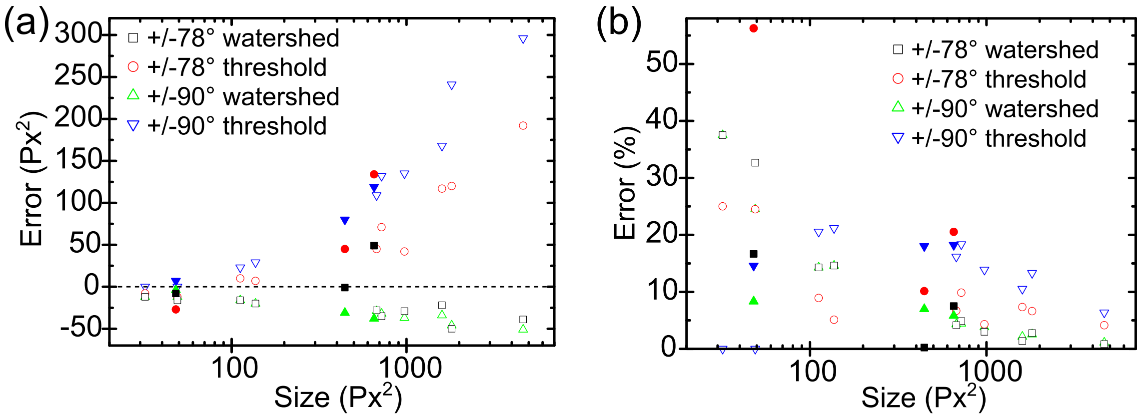

Figure B.3: (a) Absolute error for the different segmentation methods with and without missing wedge for all particles as a function of particle size. (b) Relative error for the different segmentation methods with and without missing wedge for all particles. The error of precipitates prone to missing wedge artifacts is displayed with filled symbols.

using the proposed method is well below 10% for datasets with and without missing wedge. For smaller particles the ratio of surface pixels compared to the total area of the precipitates increases and leads to a larger error in the simulations for both datasets with and without missing wedge.

Bibliography

Adams, R. and Bischof, L. (1994). Seeded region growing. *IEEE Transactions on Pattern Analysis and Machine Intelligence*, 16(6):641–647.

Algra, R. E., Verheijen, M. A., Borgstrom, M. T., Feiner, L.-F., Immink, G., van Enckevort, W. J. P., Vlieg, E., and Bakkers, E. P. A. M. (2008). Twinning superlattices in indium phosphide nanowires. *Nature*, 456(7220):369–372.

Allibert, F., Ernst, T., Pretet, J., Hefyene, N., Perret, C., Zaslavsky, A., and Cristoloveanu, S. (2001). From SOI materials to innovative devices. *Solid-State Electronics*, 45(4):559–566.

Anderson, L., Halary, S., Lechaire, J.-P., Boudier, T., Frébourg, G., Marco, S., Zbinden, M., and Gaill, F. (2008). Tomography of bacteria-mineral associations within the deep-sea hydrothermal vent shrimp rimicaris exoculata. *Comptes Rendus Chimie*, 11(3):268–280.

Arden, W., Brillouët, M., Cogez, P., Graef, M., Huizing, B., and Mahnkopf, R. (2010). “More-than-Moore” white paper.

Arico, A. S., Bruce, P., Scrosati, B., Tarascon, J.-M., and van Schalkwijk, W. (2005). Nanostructured materials for advanced energy conversion and storage devices. *Nature Materials*, 4(5):366–377.

Arslan, I., Marquis, E. A., Homer, M., Hekmaty, M. A., and Bartelt, N. C. (2008). Towards better 3-D reconstructions by combining electron tomography and atom-probe tomography. *Ultramicroscopy*, 108(12):1579–1585.

Arslan, I., Tong, J. R., and Midgley, P. A. (2006). Reducing the missing wedge: High-resolution dual axis tomography of inorganic materials. *Ultramicroscopy*, 106(11-12):994–1000.

ASTRA-Toolbox (2013). http://code.google.com/p/astra-toolbox/.

Atalla, M. M., Tannenbaum, E., and Scheibner, E. J. (1959). Stabilization of silicon surfaces by thermally grown oxides. *The Bell System Technical Journal*, 38(3):749–783.

Azevedo, S. G., Daniel J. Schneberk, Fitch, J. P., and Martz, H. E. (1990). Calculation of the rotational centers in computed tomography sinograms. *IEEE Transactions on Nuclear Science*, 37(4):1525–1540.

Bajolet, A., Giraudin, J. C., Rossato, C., Pinzelli, L., Bruyere, S., Cremer, S., Jagueneau, T., Delpech, P., Montès, L., and Ghibaudo, G. (2005). Three-dimensional 35 nF/mm^2 MIM capacitors integrated in BiCMOS technology. In *Proceedings of 35th European Solid-State Device Research Conference*, pages 121–124.

Balandin, A. A. and Wang, K. L. (2009). *Handbook of Semiconductor Nanostructures and Nanodevices*. American Scientific Publishers.

Baliga, B. J. (1991). An overview of smart power technology. *IEEE Transactions on Electron Devices*, 38(7):1568–1575.

Bals, S., Batenburg, K. J., Liang, D., Lebedev, O., Van Tendeloo, G., Aerts, A., Martens, J. A., and Kirschhock, C. E. A. (2009). Quantitative three-dimensional modeling of zeotile through discrete electron tomography. *Journal of the American Chemical Society*, 131(13):4769–4773.

Bals, S., Batenburg, K. J., Verbeeck, J., Sijbers, J., and Van Tendeloo, G. (2007). Quantitative three-dimensional reconstruction of catalyst particles for bamboo-like carbon nanotubes. *Nano Letters*, 7(12):3669–3674.

Bals, S., Casavola, M., van Huis, M. A., Van Aert, S., Batenburg, K. J., Van Tendeloo, G., and Vanmaekelbergh, D. (2010). Three-dimensional atomic imaging of colloidal core-shell nanocrystals. *Nano Letters*, 11(8):3420–3424.

Banerjee, P., Perez, I., Henn-Lecordier, L., Lee, S. B., and Rubloff, G. W. (2009). Nanotubular metal-insulator-metal capacitor arrays for energy storage. *Nature Nanotechnology*, 4(5):292–296.

Barnard, J. S., Eggeman, A. S., Sharp, J., White, T. A., and Midgley, P. A. (2010). Dislocation electron tomography and precession electron diffraction – minimising the effects of dynamical interactions in real and reciprocal space. *Philosophical Magazine*, 90(36–36):4711–4730.

Barnard, J. S., Sharp, J., Tong, J. R., and Midgley, P. A. (2006a). High-resolution three-dimensional imaging of dislocations. *Science*, 313(5785):319.

Barnard, J. S., Sharp, J., Tong, J. R., and Midgley, P. A. (2006b). Three-dimensional analysis of dislocation networks in GaN using weak-beam dark-field electron tomography. *Philosophical Magazine*, 86(29–31):4901–4922.

Barraud, S., Coquand, R., Casse, M., Koyama, M., Hartmann, J. M., Maffini-Alvaro, V., Comboroure, C., Vizioz, C., Aussenac, F., Faynot, O., and Poiroux, T. (2012). Performance of omega-shaped-gate silicon nanowire MOSFET with diameter down to 8 nm. *IEEE Electron Device Letters*, 33(11):1526–1528.

Baruchel, J., Buffiere, J.-Y., Cloetens, P., Di Michiel, M., Ferrie, E., Ludwig, W., Maire, E., and Salvo, L. (2006). Advances in synchrotron radiation microtomography. *Scripta Materialia*, 55(1):41–46.

Batenburg, K. J., Bals, S., Sijbers, J., Kübel, C., Midgley, P. A., Hernandez, J. C., Kaiser, U., Encina, E. R., Coronado, E. A., and Van Tendeloo, G. (2009). 3D imaging of nanomaterials by discrete tomography. *Ultramicroscopy*, 109(6):730–740.

Baumeister, W., Grimm, R., and Walz, J. (1999). Electron tomography of molecules and cells. *Trends in Cell Biology*, 9(2):81–85.

Bender, H., Richard, O., Kalio, A., and Sourty, E. (2007). 3D-analysis of semiconductor structures by electron tomography. *Microelectronic Engineering*, 84(11):2707–2713.

Benlekbir, S., Epicier, T., Bausach, M., Aouine, M., and Berhault, G. (2009). STEM HAADF electron tomography of palladium nanoparticles with complex shapes. *Philosophical Magazine Letters*, 89(2):145–153.

Biskupek, J., Leschner, J., Walther, P., and Kaiser, U. (2010). Optimization of STEM tomography acquisition – a comparison of convergent beam and parallel beam STEM tomography. *Ultramicroscopy*, 110(9):1231–1237.

Black, C. T., Guarini, K. W., Ying, Z., Kim, H., Benedict, J., Sikorski, E., Babich, I. V., and Milkove, K. R. (2004). High-capacity, self-assembled metal-oxide-semiconductor decoupling capacitors. *IEEE Electron Device Letters*, 25(9):622–624.

Black, J., Lockwood, H., and Mayburg, S. (1963). Recombination radiation in GaAs. *Journal of Applied Physics*, 34(1):178–180.

Black, M. J., Sapiro, G., Marimont, D. H., and Heeger, D. (1998). Robust anisotropic diffusion. *IEEE Transactions on Image Processing*, 7(3):421–432.

Blavette, D., Bostel, A., Sarrau, J. M., Deconihout, B., and Menand, A. (1993). An atom probe for three-dimensional tomography. *Nature*, 363(6428):432–435.

Blavette, D., Duval, P., Letellier, L., and Guttmann, M. (1996). Atomic-scale APFIM and TEM investigation of grain boundary microchemistry in astroloy nickel base superalloys. *Acta Materialia*, 44(12):4995–5005.

Bleuet, P., Audoit, G., Barnes, J.-P., Bertheau, J., Dabin, Y., Dansas, H., Fabbri, J.-M., Florin, B., Gergaud, P., Grenier, A., Haberfehlner, G., Lay, E., Laurencin, J., Serra, R., and Villanova, J. (2013). Specifications for hard condensed matter specimens for three-dimensional high-resolution tomographies. *Microscopy and Microanalysis*, 19(3):726–739.

Bleuet, P., Cloetens, P., Gergaud, P., Mariolle, D., Chevalier, N., Tucoulou, R., Susini, J., and Chabli, A. (2009). A hard x-ray nanoprobe for scanning and projection nanotomography. *Review of Scientific Instruments*, 80(5):056101–3.

Bleuet, P., Welcomme, E., Dooryhee, E., Susini, J., Hodeau, J.-L., and Walter, P. (2008). Probing the structure of heterogeneous diluted materials by diffraction tomography. *Nature Materials*, 7(6):468–472.

Brandt, S., Heikkonen, J., and Engelhardt, P. (2001). Multiphase method for automatic alignment of transmission electron microscope images using markers. *Journal of Structural Biology*, 133(1):10–22.

Brescia, R., Miszta, K., Dorfs, D., Manna, L., and Bertoni, G. (2011). Birth and growth of octapod-shaped colloidal nanocrystals studied by electron tomography. *The Journal of Physical Chemistry C*, 115(41):20128–20133.

Bruel, M. (1995). Silicon on insulator material technology. *Electronics Letters*, 31(14):1201–1202.

Candes, E. J., Romberg, J., and Tao, T. (2006). Robust uncertainty principles: exact signal reconstruction from highly incomplete frequency information. *IEEE Transactions on Information Theory*, 52(2):489–509.

Candes, E. J. and Wakin, M. B. (2008). An introduction to compressive sampling. *IEEE Signal Processing Magazine*, 25(2):21–30.

Carey, J. E., Crouch, C. H., Shen, M., and Mazur, E. (2005). Visible and near-infrared responsivity of femtosecond-laser microstructured silicon photodiodes. *Optics Letters*, 30(14):1773–1775.

Caroff, P., Dick, K. A., Johansson, J., Messing, M. E., Deppert, K., and Samuelson, L. (2009). Controlled polytypic and twin-plane superlattices in III-V nanowires. *Nature Nanotechnology*, 4(1):50–55.

Castro, R., Coates, M., Liang, G., Nowak, R., and Yu, B. (2004). Network tomography: Recent developments. *Statistical Science*, 19(3):499–517.

Chan, C. K., Peng, H., Liu, G., McIlwrath, K., Zhang, X. F., Huggins, R. A., and Cui, Y. (2008). High-performance lithium battery anodes using silicon nanowires. *Nature Nanotechnology*, 3(1):31–35.

Chang, Y. F., Chou, Q. R., Lin, J. Y., and Lee, C. H. (2007). Fabrication of high-aspect-ratio silicon nanopillar arrays with the conventional reactive ion etching technique. *Applied Physics A*, 86(2):193–196.

Cherns, P. D., Lorut, F., Dupré, C., Tachi, K., Cooper, D., Chabli, A., and Ernst, T. (2010). Electron tomography of gate-all-around nanowire transistors. *Journal of Physics: Conference Series*, 209(1):012046.

Chiaramonte, T., Tizei, L. H. G., Ugarte, D., and Cotta, M. A. (2011). Kinetic effects in InP nanowire growth and stacking fault formation: The role of interface roughening. *Nano Letters*, 11(5):1934–1940.

Choi, Y., Mosley, L. E., Min, Y., and Amaratunga, G. A. J. (2010). Carbon nanotube capacitors arrays using high-k dielectrics. *Diamond and Related Materials*, 19(2-3):221–224.

Choy, K. L. (2003). Chemical vapour deposition of coatings. *Progress in Materials Science*, 48(2):57–170.

Chuntonov, L., Bar-Sadan, M., Houben, L., and Haran, G. (2012). Correlating electron tomography and plasmon spectroscopy of single noble metal core-shell nanoparticles. *Nano Letters*, 12(1):145–150.

Clement, L., Borowiak, C., Galand, R., Lepinay, K., Lorut, F., Pantel, R., Servanton, G., Thomas, R., Vannier, P., and Bicais, N. (2011). Microscopy needs for next generation devices characterization in the semiconductor industry. *Journal of Physics: Conference Series*, 326(1):012008.

Cloetens, P., Barrett, R., Baruchel, J., Guigay, J.-P., and Schlenker, M. (1996). Phase objects in synchrotron radiation hard x-ray imaging. *Journal of Physics D: Applied Physics*, 29(1):133.

Cloetens, P., Ludwig, W., Baruchel, J., Van Dyck, D., Van Landuyt, J., Guigay, J. P., and Schlenker, M. (1999). Holotomography: Quantitative phase tomography with micrometer resolution using hard synchrotron radiation x-rays. *Applied Physics Letters*, 75(19):2912–2914.

Coates, M., Hero, A. O., Nowak, R., and Bin, Y. (2002). Internet tomography. *IEEE Signal Processing Magazine*, 19(3):47–65.

Colinge, J. (2004). *Silicon-on-Insulator technology: materials to VLSI.* Kluwer Academic Publishers.

Colinge, J. P. (2007). Multi-gate SOI MOSFETs. *Microelectronic Engineering*, 84(9-10):2071–2076.

Coquand, R., Barraud, S., Casse, M., Leroux, P., Vizioz, C., Comboroure, C., Perreau, P., Ernst, E., Samson, M., Maffini-Alvaro, V., Tabone, C., Barnola, S., Munteanu, D., Ghibaudo, G., Monfray, S., Boeuf, F., and Poiroux, T. (2012). Scaling of high-k/metal-gate trigate SOI nanowire transistors down to 10nm width. In *13th International Conference on Ultimate Integration on Silicon (ULIS)*, pages 37–40.

Cormack, A. M. (1963). Representation of a function by its line integrals, with some radiological applications. *Journal of Applied Physics*, 34(9):2722–2727.

Crowther, R. A., Amos, L. A., Finch, J. T., De Rosier, D. J., and Klug, A. (1970a). Three dimensional reconstructions of spherical viruses by Fourier synthesis from electron micrographs. *Nature*, 226(5244):421–425.

Crowther, R. A., DeRosier, D. J., and Klug, A. (1970b). The reconstruction of a three-dimensional structure from projections and its application to electron microscopy. *Proceedings of the Royal Society A*, 317(1530):319–340.

Cui, Y., Wei, Q., Park, H., and Lieber, C. M. (2001). Nanowire nanosensors for highly sensitive and selective detection of biological and chemical species. *Science*, 293(5533):1289–1292.

Czochralski, J. (1918). Ein neues Verfahren zur Messung der Kristallisationsgeschwindigkeit der Metalle. *Zeitschrift für Physikalische Chemie*, 92:219.

de Jong, K. P. and Koster, A. J. (2002). Three-dimensional electron microscopy of mesoporous Materials—Recent strides towards spatial imaging at the nanometer scale. *ChemPhysChem*, 3(9):776–780.

de Jonge, M. D. and Vogt, S. (2010). Hard x-ray fluorescence tomography - an emerging tool for structural visualization. *Current Opinion in Structural Biology*, 20(5):606–614.

De Rosier, D. J. and Klug, A. (1968). Reconstruction of three dimensional structures from electron micrographs. *Nature*, 217(5124):130–134.

Detalle, M., Barrenetxea, M., Muller, P., Potoms, G., Phommahaxay, A., Soussan, P., Vaesen, K., and De Raedt, W. (2010). High density, low leakage backend 3D capacitors for mixed signals applications. *Microelectronic Engineering*, 87(12):2571–2576.

Dierksen, K., Typke, D., Hegerl, R., and Baumeister, W. (1993). Towards automatic electron tomography II. Implementation of autofocus and low-dose procedures. *Ultramicroscopy*, 49(1-4):109–120.

Dierksen, K., Typke, D., Hegerl, R., Koster, A. J., and Baumeister, W. (1992). Towards automatic electron tomography. *Ultramicroscopy*, 40(1):71–87.

Dierolf, M., Menzel, A., Thibault, P., Schneider, P., Kewish, C. M., Wepf, R., Bunk, O., and Pfeiffer, F. (2010). Ptychographic x-ray computed tomography at the nanoscale. *Nature*, 467(7314):436–439.

Doering, R. and Nishi, Y. (2008). *Handbook Semiconductor Manufactoring Technology*. CRC Press.

Donoho, D. L. (2006). Compressed sensing. *IEEE Transactions on Information Theory*, 52(4):1289–1306.

Duguay, S., Colin, A., Mathiot, D., Morin, P., and Blavette, D. (2010). Atomic-scale redistribution of dopants in polycrystalline silicon layers. *Journal of Applied Physics*, 108(3):034911.

Dupuis, R. D. (1987). An introduction to the development of the semiconductor laser. *IEEE Journal of Quantum Electronics*, 23(6):651–657.

Egerton, R. F. (2009). Electron energy-loss spectroscopy in the TEM. *Reports on Progress in Physics*, 72(1):016502.

Egerton, R. F. and Malac, M. (2005). EELS in the TEM. *Journal of Electron Spectroscopy and Related Phenomena*, 143(2-3):43–50.

Ekinci, K. L. and Roukes, M. L. (2005). Nanoelectromechanical systems. *Review of Scientific Instruments*, 76(6):061101.

Eom, K., Park, H. S., Yoon, D. S., and Kwon, T. (2011). Nanomechanical resonators and their applications in biological/chemical detection: Nanomechanics principles. *Physics Reports*, 503(4-5):115–163.

Ercius, P., Gignac, L. M., Hu, C. K., and Muller, D. A. (2009). Three-dimensional measurement of line edge roughness in copper wires using electron tomography. *Microscopy and Microanalysis*, 15(3):244–250.

Ercius, P., Weyland, M., Muller, D. A., and Gignac, L. M. (2006). Three-dimensional imaging of nanovoids in copper interconnects using incoherent bright field tomography. *Applied Physics Letters*, 88(24):243116.

Ersen, O., Werckmann, J., Houllé, M., Ledoux, M.-J., and Pham-Huu, C. (2007). 3D electron microscopy study of metal particles inside multiwalled carbon nanotubes. *Nano Letters*, 7(7):1898–1907.

Faggin, F. and Klein, T. (1969). A faster generation of MOS devices with low thresholds is riding crest of new wave, silicon-gate IC's. *Electronics*, 42(20):88.

Faist, J., Capasso, F., Sivco, D. L., Sirtori, C., Hutchinson, A. L., and Cho, A. Y. (1994). Quantum cascade laser. *Science*, 264(5158):553–556.

Fan, Z., Kapadia, R., Leu, P. W., Zhang, X., Chueh, Y.-L., Takei, K., Yu, K., Jamshidi, A., Rathore, A. A., Ruebusch, D. J., Wu, M., and Javey, A. (2010). Ordered arrays of dual-diameter nanopillars for maximized optical absorption. *Nano Letters*, 10(10):3823–3827.

Feng, Z. Q., Yang, Y. Q., Huang, B., Luo, X., Li, M. H., Chen, Y. X., Han, M., Fu, M. S., and Ru, J. G. (2011). STEM-HAADF tomography investigation of grain boundary precipitates in Al-Cu-Mg alloy. *Materials Letters*, 65(17-18):2808–2811.

Ferain, I., Colinge, C. A., and Colinge, J.-P. (2011). Multigate transistors as the future of classical metal-oxide-semiconductor field-effect transistors. *Nature*, 479(7373):310–316.

Fernández, J.-J. (2012). Computational methods for electron tomography. *Micron*, 43(10):1010–1030.

Fernández, J.-J., Gordon, D., and Gordon, R. (2008). Efficient parallel implementation of iterative reconstruction algorithms for electron tomography. *Journal of Parallel and Distributed Computing*, 68(5):626–640.

Fernández, J. J. and Sam, L. (2005). Anisotropic nonlinear filtering of cellular structures in cryoelectron tomography. *Computing in Science & Engineering*, 7(5):54–61.

Fernández-Busnadiego, R., Zuber, B., Maurer, U. E., Cyrklaff, M., Baumeister, W., and Lučić, V. (2010). Quantitative analysis of the native presynaptic cytomatrix by cryoelectron tomography. *The Journal of Cell Biology*, 188(1):145–156.

Fischetti, M. V. and Laux, S. E. (1996). Band structure, deformation potentials, and carrier mobility in strained Si, Ge, and SiGe alloys. *Journal of Applied Physics*, 80(4):2234–2252.

Florea, I., Ersen, O., Hirlimann, C., Roiban, L., Deneuve, A., Houlle, M., Janowska, I., Nguyen, P., Pham, C., and Pham-Huu, C. (2010). Analytical electron tomography mapping of the SiC pore oxidation at the nanoscale. *Nanoscale*, 2:2668–2678.

Franchi, S., Trevisi, G., Seravalli, L., and Frigeri, P. (2003). Quantum dot nanostructures and molecular beam epitaxy. *Progress in Crystal Growth and Characterization of Materials*, 47(2-3):166–195.

Frangakis, A. S. and Hegerl, R. (2001). Noise reduction in electron tomographic reconstructions using nonlinear anisotropic diffusion. *Journal of Structural Biology*, 135(3):239–250.

Frank, J. (2005). *Electron Tomography: Methods for Three-Dimensional Visualization of Structures in the Cell.* Springer, 2nd edition.

Frank, J., Wagenknecht, T., McEwen, B. F., Marko, M., Hsieh, C.-E., and Mannella, C. A. (2002). Three-dimensional imaging of biological complexity. *Journal of Structural Biology*, 138(1-2):85–91.

Gass, M. H., Koziol, K. K. K., Windle, A. H., and Midgley, P. A. (2006). Four-dimensional spectral tomography of carbonaceous nanocomposites. *Nano Letters*, 6(3):376–379.

Gault, B., Vella, A., Vurpillot, F., Menand, A., Blavette, D., and Deconihout, B. (2007). Optical and thermal processes involved in ultrafast laser pulse interaction with a field emitter. *Ultramicroscopy*, 107(9):713–719.

Giannuzzi, L. A. and Stevie, F. A. (1999). A review of focused ion beam milling techniques for TEM specimen preparation. *Micron*, 30(3):197–204.

Gilbert, P. (1972). Iterative methods for the three-dimensional reconstruction of an object from projections. *Journal of Theoretical Biology*, 36(1):105–117.

Goetzberger, A., Hebling, C., and Schock, H.-W. (2003). Photovoltaic materials, history, status and outlook. *Materials Science and Engineering: R: Reports*, 40(1):1–46.

Goldberger, J., Hochbaum, A. I., Fan, R., and Yang, P. (2006). Silicon vertically integrated nanowire field effect transistors. *Nano Letters*, 6(5):973–977.

Goodnick, S. M., Ferry, D. K., Wilmsen, C. W., Liliental, Z., Fathy, D., and Krivanek, O. L. (1985). Surface roughness at the Si(100)-SiO_2 interface. *Physical Review B: Condensed Matter*, 32(12):8171–8186.

Gordon, R., Bender, R., and Herman, G. T. (1970). Algebraic reconstruction techniques (ART) for three-dimensional electron microscopy and x-ray photography. *Journal of Theoretical Biology*, 29(3):471–481.

Goris, B., Bals, S., Van den Broek, W., Carbó-Argibay, E., Gómez-Graña, S., Liz-Marzán, L. M., and Van Tendeloo, G. (2012a). Atomic-scale determination of surface facets in gold nanorods. *Nature Materials*, 11(11):930–935.

Goris, B., Bals, S., Van den Broek, W., Verbeeck, J., and Van Tendeloo, G. (2011). Exploring different inelastic projection mechanisms for electron tomography. *Ultramicroscopy*, 111(8):1262–1267.

Goris, B., Van den Broek, W., Batenburg, K. J., Heidari Mezerji, H., and Bals, S. (2012b). Electron tomography based on a total variation minimization reconstruction technique. *Ultramicroscopy*, 113:120–130.

Grenier, A., Duguay, S., Barnes, J.-P., Serra, R., Haberfehlner, G., Cooper, D., Bertin, F., Barraud, S., Audoit, G., Arnoldi, L., Cadel, E., Chabli, A., and Vurpillot, F. (2013). 3D analysis of advanced devices using electron and atom probe tomography. *Ultramicroscopy*, accepted.

Grimm, R., Bärmann, M., Häckl, W., Typke, D., Sackmann, E., and Baumeister, W. (1997). Energy filtered electron tomography of ice-embedded actin and vesicles. *Biophysical Journal*, 72(1):482–489.

Grimm, R., Singh, H., Rachel, R., Typke, D., Zillig, W., and Baumeister, W. (1998a). Electron tomography of ice-embedded prokaryotic cells. *Biophysical Journal*, 74(2):1031–1042.

Grimm, R., Typke, D., and Baumeister, W. (1998b). Improving image quality by zero-loss energy filtering: quantitative assessment by means of image cross-correlation. *Journal of Microscopy*, 190(3):339–349.

Groeber, M. A., Haley, B. K., Uchic, M. D., Dimiduk, D. M., and Ghosh, S. (2006). 3D reconstruction and characterization of polycrystalline microstructures using a FIB-SEM system. *Materials Characterization*, 57(4-5):259–273.

Grothausmann, R., Zehl, G., Manke, I., Fiechter, S., Bogdanoff, P., Dorbandt, I., Kupsch, A., Lange, A., Hentschel, M. P., Schumacher, G., and Banhart, J. (2011). Quantitative structural assessment of heterogeneous catalysts by electron tomography. *Journal of the American Chemical Society*, 133(45):18161–18171.

Gubbens, A. J., Kraus, B., Krivanek, O. L., and Mooney, P. E. (1995). An imaging filter for high voltage electron microscopy. *Ultramicroscopy*, 59(1-4):255–265.

Günes, S., Neugebauer, H., and Sariciftci, N. S. (2007). Conjugated polymer-based organic solar cells. *Chemical Reviews*, 107(4):1324–1338.

Guo, W., Banerjee, A., Bhattacharya, P., and Ooi, B. S. (2011). InGaN/GaN disk-in-nanowire white light emitting diodes on (001) silicon. *Applied Physics Letters*, 98(19):193102–3.

Gusev, E. P., Cabral Jr, C., Copel, M., D’Emic, C., and Gribelyuk, M. (2003). Ultrathin HfO_2 films grown on silicon by atomic layer deposition for advanced gate dielectrics applications. *Microelectronic Engineering*, 69(2-4):145–151.

Haberfehlner, G., Bayle-Guillemaud, P., Audoit, G., Lafond, D., Morel, P. H., Jousseaume, V., Ernst, T., and Bleuet, P. (2012). Four-dimensional spectral low-loss energy-filtered transmission electron tomography of silicon nanowire-based capacitors. *Applied Physics Letters*, 101(6):063108.

Haberfehlner, G., Serra, R., Cooper, D., Barraud, S., and Bleuet, P. (2013a). 3D spatial resolution improvement by dual-axis electron tomography: Application to tri-gate transistors. *Ultramicroscopy*, accepted.

Haberfehlner, G., Smith, M. J., Idrobo, J.-C., Auvert, G., Sher, M.-J., Winkler, M. T., Mazur, E., Gambacorti, N., Gradečak, S., and Bleuet, P. (2013b). Dopant segregation in femtosecond laser-doped silicon revealed by electron tomography. *Microscopy and Microanalysis*, 19(3):716–725.

Hamzaoui, H., Bouazzi, A. S., and Rezig, B. (2005). Theoretical possibilities of $\mathrm{In_xGa_{1-x}N}$ tandem PV structures. *Solar Energy Materials and Solar Cells*, 87(1-4):595–603.

Hart, R. G. (1968). Electron microscopy of unstained biological material: The polytropic montage. *Science*, 159(3822):1464–1467.

Hata, S., Kimura, K., Gao, H., Matsumura, S., Doi, M., Moritani, T., Barnard, J. S., Tong, J. R., Sharp, J. H., and Midgley, P. A. (2008). Electron tomography imaging and analysis of γ' and γ domains in Ni-based superalloys. *Advanced Materials*, 20(10):1905–1909.

Hawkes, P. W. (1992). The electron microscope as a structure projector. In Frank, J., editor, *Electron Tomography*, pages 17–38. Plenum, New York.

Hayden, O., Agarwal, R., and Lu, W. (2008). Semiconductor nanowire devices. *Nano Today*, 3(5-6):12–22.

Hemesath, E. R., Schreiber, D. K., Gulsoy, E. B., Kisielowski, C. F., Petford-Long, A. K., Voorhees, P. W., and Lauhon, L. J. (2012). Catalyst incorporation at defects during nanowire growth. *Nano Letters*, 12(1):167–171.

Herman, G. T. and Davidi, R. (2008). Image reconstruction from a small number of projections. *Inverse Problems*, 24(4):045011.

Herman, G. T. and Kuba, A. (1999). *Discrete Tomography: Foundations, Algorithms and Applications*. Birkhäuser, Boston.

Herman, G. T. and Lent, A. (1976). Iterative reconstruction algorithms. *Computers in Biology and Medicine*, 6(4):273–294.

Herzing, A. A., Richter, L. J., and Anderson, I. M. (2010). 3D nanoscale characterization of thin-film organic photovoltaic device structures via spectroscopic contrast in the TEM. *The Journal of Physical Chemistry C*, 114(41):17501–17508.

Hiramatsu, K., Nishiyama, K., Onishi, M., Mizutani, H., Narukawa, M., Motogaito, A., Miyake, H., Iyechika, Y., and Maeda, T. (2000). Fabrication and characterization of low defect density GaN using facet-controlled epitaxial lateral overgrowth (FACELO). *Journal of Crystal Growth*, 221(1-4):316–326.

Hofer, F., Grogger, W., Kothleitner, G., and Warbichler, P. (1997). Quantitative analysis of EFTEM elemental distribution images. *Ultramicroscopy*, 67(1-4):83–103.

Hofer, F. and Warbichler, P. (1996). Improved imaging of secondary phases in solids by energy-filtering TEM. *Ultramicroscopy*, 63(1):21–25.

Holonyak, N. and Bevacqua, S. F. (1962). Coherent (visible) light emission from Ga($\mathrm{As}_{1-\mathrm{x}}\mathrm{P}_{\mathrm{x}}$) junctions. *Applied Physics Letters*, 1(4):82–83.

Hoppe, W. (1974). Zur elektronenmikroskopisch dreidimensionalen Rekonstruktion eines Objektes. *Naturwissenschaften*, 61(12):534–536.

Hoppe, W., Gassmann, J., Hunsmann, N., Schramm, H. J., and Sturm, M. (1974). 3-dimensional reconstruction of individual negatively stained yeast fatty-acid synthetase molecules from tilt series in electron-microscope. *Hoppe-Seylers Zeitschrift für Physiologische Chemie*, 355(11):1483–1487.

Hoppe, W., Langer, R., Knesch, G., and Poppe, C. (1968). Protein-Kristallstrukturanalyse mit Elektronenstrahlen. *Naturwissenschaften*, 55(7):333–336.

Huang, Z., Geyer, N., Werner, P., de Boor, J., and Gösele, U. (2011). Metal-assisted chemical etching of silicon: A review. *Advanced Materials*, 23(2):285–308.

Huolin, L. X., Peter, E., Kevin, J. H., James, R. E., and David, A. M. (2010). Three-dimensional imaging of pore structures inside low-kappa dielectrics. *Applied Physics Letters*, 96(22):223108.

Hyun, J. K., Ercius, P., and Muller, D. A. (2008). Beam spreading and spatial resolution in thick organic specimens. *Ultramicroscopy*, 109(1):1–7.

Inoue, K., Yano, F., Nishida, A., Takamizawa, H., Tsunomura, T., Nagai, Y., and Hasegawa, M. (2009). Dopant distributions in n-MOSFET structure observed by atom probe tomography. *Ultramicroscopy*, 109(12):1479–1484.

Iwai, H., Shikazono, N., Matsui, T., Teshima, H., Kishimoto, M., Kishida, R., Hayashi, D., Matsuzaki, K., Kanno, D., Saito, M., Muroyama, H., Eguchi, K., Kasagi, N., and Yoshida, H. (2010). Quantification of SOFC anode microstructure based on dual beam FIB-SEM technique. *Journal of Power Sources*, 195(4):955–961.

Jain, A., Weng, X., Raghavan, S., VanMil, B. L., Myers, T., and Redwing, J. M. (2008). Effect of polarity on the growth of InN films by metalorganic chemical vapor deposition. *Journal of Applied Physics*, 104(5):053112–7.

Jarausch, K., Thomas, P., Leonard, D. N., Twesten, R., and Booth, C. R. (2009). Four-dimensional STEM-EELS: enabling nano-scale chemical tomography. *Ultramicroscopy*, 109(4):326–337.

Jin, S., Jones, K. S., Law, M. E., and Camillo-Castillo, R. (2012). B segregation to grain boundaries and diffusion in polycrystalline Si with flash annealing. *Journal of Applied Physics*, 111(4):044508.

Jin-Phillipp, N. Y., Koch, C. T., and van Aken, P. A. (2011). Toward quantitative core-loss EFTEM tomography. *Ultramicroscopy*, 111(8):1255–1261.

Jinschek, J. R., Batenburg, K. J., Calderon, H. A., Kilaas, R., Radmilovic, V., and Kisielowski, C. (2008). 3-D reconstruction of the atomic positions in a simulated gold nanocrystal based on discrete tomography: Prospects of atomic resolution electron tomography. *Ultramicroscopy*, 108(6):589–604.

Joyce, H. J., Gao, Q., Hoe Tan, H., Jagadish, C., Kim, Y., Zou, J., Smith, L. M., Jackson, H. E., Yarrison-Rice, J. M., Parkinson, P., and Johnston, M. B. (2011). III-V semiconductor nanowires for optoelectronic device applications. *Progress in Quantum Electronics*, 35(2-3):23–75.

Kak, A. C. and Slaney, M. (1987). *Principles of Computerized Tomographic Imaging.* IEEE Press.

Kambham, A. K., Mody, J., Gilbert, M., Koelling, S., and Vandervorst, W. (2011). Atom-probe for FinFET dopant characterization. *Ultramicroscopy*, 111(6):535–539.

Kaneko, K., Inoke, K., Sato, K., Kitawaki, K., Higashida, H., Arslan, I., and Midgley, P. A. (2008). TEM characterization of Ge precipitates in an Al-1.6 at% Ge alloy. *Ultramicroscopy*, 108(3):210–220.

Kawase, N., Kato, M., Nishioka, H., and Jinnai, H. (2007). Transmission electron microtomography without the "missing wedge" for quantitative structural analysis. *Ultramicroscopy*, 107(1):8–15.

Ke, X., Bals, S., Cott, D., Hantschel, T., Bender, H., and Van Tendeloo, G. (2010). Three-dimensional analysis of carbon nanotube networks in interconnects by electron tomography without missing wedge artifacts. *Microscopy and Microanalysis*, 16(2):210–217.

Kelly, T. and Miller, M. (2007). Invited review article: Atom probe tomography. *Review of Scientific Instruments*, 78(3):031101.

Klootwijk, J. H., Jinesh, K. B., Dekkers, W., Verhoeven, J. F., Van Den Heuvel, F. C., Kim, H. D., Blin, D., Verheijen, M. A., Weemaes, R. G. R., Kaiser, M., Ruigrok, J., and Roozeboom, F. (2008). Ultrahigh capacitance density for multiple ALD-Grown MIM capacitor stacks in 3-D silicon. *IEEE Electron Device Letters*, 29(7):740–742.

Ko, W. H. (2007). Trends and frontiers of MEMS. *Sensors and Actuators A: Physical*, 136(1):62–67.

Kobayashi, A., Fujigaya, T., Itoh, M., Taguchi, T., and Takano, H. (2009). Technical note: A tool for determining rotational tilt axis with or without fiducial markers. *Ultramicroscopy*, 110(1):1–6.

Kociak, M., Stéphan, O., Walls, M. G., Tencé, M., and Colliex, C. (2011). Spatially resolved EELS: the spectrum-imaging technique and its applications. In Pennycook, S. J. and Nellist, P. D., editors, *Scanning Transmission Electron Microscopy*, pages 163–205. Springer New York.

Koester, R., Hwang, J.-S., Salomon, D., Chen, X., Bougerol, C., Barnes, J.-P., Dang, D. L. S., Rigutti, L., de Luna Bugallo, A., Jacopin, G., Tchernycheva, M., Durand, C., and Eymery, J. (2011). M-plane core-shell InGaN/GaN multiple-quantum-wells on GaN wires for electroluminescent devices. *Nano Letters*, 11(11):4839–4845.

Kolb, U., Gorelik, T., Kübel, C., Otten, M. T., and Hubert, D. (2007). Towards automated diffraction tomography: Part I - data acquisition. *Ultramicroscopy*, 107(6-7):507–513.

Kolb, U., Gorelik, T., and Otten, M. T. (2008). Towards automated diffraction tomography. Part II - cell parameter determination. *Ultramicroscopy*, 108(8):763–772.

Kolb, U., Mugnaioli, E., and Gorelik, T. E. (2011). Automated electron diffraction tomography – a new tool for nano crystal structure analysis. *Crystal Research and Technology*, 46(6):542–554.

Koster, A. J., Chen, H., Sedat, J. W., and Agard, D. A. (1992). Automated microscopy for electron tomography. *Ultramicroscopy*, 46(1-4):207–227.

Koster, A. J., Grimm, R., Typke, D., Hegerl, R., Stoschek, A., Walz, J., and Baumeister, W. (1997). Perspectives of molecular and cellular electron tomography. *Journal of Structural Biology*, 120(3):276–308.

Koster, A. J., Ziese, U., Verkleij, A. J., Janssen, A. H., and de Jong, K. P. (2000). Three-dimensional transmission electron microscopy: A novel imaging and characterization technique with nanometer scale resolution for materials science. *The Journal of Physical Chemistry B*, 104(40):9368–9370.

Kotula, P. G., Brewer, L. N., Michael, J., and Giannuzzi, L. (2007). Computed tomographic spectral imaging: 3D STEM-EDS spectral imaging. *Microscopy and Microanalysis*, 13(Supplement S02):1324–1325.

Kotula, P. G., Keenan, M. R., and Michael, J. R. (2006). Tomographic spectral imaging with multivariate statistical analysis: Comprehensive 3D microanalysis. *Microscopy and Microanalysis*, 12(1):36–48.

Krivanek, O. L., Lovejoy, T. C., Dellby, N., and W., C. R. (2013). Monochromated STEM with a 30 meV-wide atom-sized electron probe. *Microscopy*, 62(1):3–21.

Kuzmik, J. (2001). Power electronics on InAlN/(In)GaN: prospect for a record performance. *IEEE Electron Device Letters*, 22(11):510–512.

Landis, E. N. and Keane, D. T. (2010). X-ray microtomography. *Materials Characterization*, 61(12):1305–1316.

Lang, W. (1996). Silicon microstructuring technology. *Materials Science and Engineering: R: Reports*, 17(1):1–55.

Larson, B. C., Yang, W., Ice, G. E., Budai, J. D., and Tischler, J. Z. (2002). Three-dimensional x-ray structural microscopy with submicrometre resolution. *Nature*, 415(6874):887–890.

Lauhon, L. J., Adusumilli, P., Ronsheim, P., Flaitz, P. L., and Lawrence, D. (2009). Atom-probe tomography of semiconductor materials and device structures. *MRS Bulletin*, 34(10):738–743.

Lazar, S., Botton, G. A., Wu, M. Y., Tichelaar, F. D., and Zandbergen, H. W. (2003). Materials science applications of HREELS in near edge structure analysis and low-energy loss spectroscopy. *Ultramicroscopy*, 96(3-4):535–546.

Leapman, R. D., Kocsis, E., Zhang, G., Talbot, T. L., and Laquerriere, P. (2004). Three-dimensional distributions of elements in biological samples by energy-filtered electron tomography. *Ultramicroscopy*, 100(1-2):115–125.

Lepinay, K., Lorut, F., Pantel, R., and Epicier, T. (2013). Chemical 3D tomography of 28nm high k metal gate transistor: STEM XEDS experimental method and results. *Micron*, 47:43–49.

Li, C. (2009). An efficient algorithm for total variation regularization with applications to the single pixel camera and compressive sensing. Master's thesis, Rice University, Houston, Texas.

Li, C., Yin, W., and Zhang, Y. (2013). http://www.caam.rice.edu/~optimization/L1/TVAL3/.

Li, J., Papadopoulos, C., Xu, J. M., and Moskovits, M. (1999). Highly-ordered carbon nanotube arrays for electronics applications. *Applied Physics Letters*, 75(3):367–369.

Li, Y., Qian, F., Xiang, J., and Lieber, C. M. (2006a). Nanowire electronic and optoelectronic devices. *Materials Today*, 9(10):18–27.

Li, Y., Xiang, J., Qian, F., Gradečak, S., Wu, Y., Yan, H., Blom, D. A., and Lieber, C. M. (2006b). Dopant-free GaN/AlN/AlGaN radial nanowire heterostructures as high electron mobility transistors. *Nano Letters*, 6(7):1468–1473.

Lim, S. K., Brewster, M., Qian, F., Li, Y., Lieber, C. M., and Gradečak, S. (2009). Direct correlation between structural and optical properties of III-V nitride nanowire heterostructures with nanoscale resolution. *Nano Letters*, 9(11):3940–3944.

Lim, S. K., Crawford, S., Haberfehlner, G., and Gradečak, S. (2013). Controlled modulation of diameter and composition along individual III-V nitride nanowires. *Nano Letters*, 13(2):331–336.

Lu, J.-Q. (2009). 3-D hyperintegration and packaging technologies for micro-nano systems. *Proceedings of the IEEE*, 97(1):18–30.

Lu, W. and Lieber, C. M. (2006). Semiconductor nanowires. *Journal of Physics D: Applied Physics*, 39(21):R387.

Lu, W. and Lieber, C. M. (2007). Nanoelectronics from the bottom up. *Nature Materials*, 6(11):841–850.

Mastronarde, D. N. (1997). Dual-axis tomography: An approach with alignment methods that preserve resolution. *Journal of Structural Biology*, 120(3):343–352.

Messaoudi, C., de Loubresse, N. G., Boudier, T., Dupuis-Williams, P., and Marco, S. (2006). Multiple-axis tomography: applications to basal bodies from paramecium tetraurelia. *Biology of the Cell*, 98(7):415–425.

Midgley, P. A. and Dunin-Borkowski, R. E. (2009). Electron tomography and holography in materials science. *Nature Materials*, 8(4):271–280.

Midgley, P. A. and Weyland, M. (2003). 3D electron microscopy in the physical sciences: the development of z-contrast and EFTEM tomography. *Ultramicroscopy*, 96(3-4):413–431.

Midgley, P. A., Weyland, M., Thomas, J. M., and Johnson, B. F. G. (2001). Z-contrast tomography: a technique in three-dimensional nanostructural analysis based on rutherford scattering. *Chemical Communications*, (10):907–908.

Miller, M. K. and Forbes, R. G. (2009). Atom probe tomography. *Materials Characterization*, 60(6):461–469.

Miller, M. K., Hoelzer, D. T., Kenik, E. A., and Russell, K. F. (2005a). Stability of ferritic MA/ODS alloys at high temperatures. *Intermetallics*, 13(3-4):387–392.

Miller, M. K., Russell, K. F., and Thompson, G. B. (2005b). Strategies for fabricating atom probe specimens with a dual beam FIB. *Ultramicroscopy*, 102(4):287–298.

Miller, M. K., Wirth, B. D., and Odette, G. R. (2003). Precipitation in neutron-irradiated Fe-Cu and Fe-Cu-Mn model alloys: a comparison of APT and SANS data. *Materials Science and Engineering: A*, 353(1-2):133–139.

Mimura, T., Hiyamizu, S., Fujii, T., and Nanbu, K. (1980). A new field-effect transistor with selectively doped GaAs/n-$Al_xGa_{1-x}As$ heterojunctions. *Japanese Journal of Applied Physics*, 19(5):L225–L227.

Mishra, U. K., Parikh, P., and Yi-Feng, W. (2002). AlGaN/GaN HEMTs-an overview of device operation and applications. *Proceedings of the IEEE*, 90(6):1022–1031.

Möbus, G., Doole, R. C., and Inkson, B. J. (2003). Spectroscopic electron tomography. *Ultramicroscopy*, 96(3-4):433–451.

Möbus, G. and Inkson, B. J. (2001). Three-dimensional reconstruction of buried nanoparticles by element-sensitive tomography based on inelastically scattered electrons. *Applied Physics Letters*, 79(9):1369–1371.

Momose, A. (2003). Phase-sensitive imaging and phase tomography using x-ray interferometers. *Optics Express*, 11(19):2303–2314.

Momose, A., Takeda, T., Itai, Y., and Hirano, K. (1996). Phase-contrast x-ray computed tomography for observing biological soft tissues. *Nature Medicine*, 2(4):473–475.

Moore, G. E. (1965). Cramming more components onto integrated circuits. *Electronics*, 38(8):114–117.

Morel, P. H., Haberfehlner, G., Lafond, D., Audoit, G., Jousseaume, V., Leroux, C., Fayolle-Lecocq, M., Baron, T., and Ernst, T. (2012). Ultra high density three dimensional capacitors based on Si nanowires array grown on a metal layer. *Applied Physics Letters*, 101(8):083110.

Morton, K. J., Nieberg, G., Bai, S., and Chou, S. Y. (2008). Wafer-scale patterning of sub-40 nm diameter and high aspect ratio (>50:1) silicon pillar arrays by nanoimprint andâ etching. *Nanotechnology*, 19(34):345301.

Müller, G. (2007). The Czochralski method - where we are 90 years after Jan Czochralski's invention. *Crystal Research and Technology*, 42(12):1150–1161.

Nam, S., Jiang, X., Xiong, Q., Ham, D., and Lieber, C. M. (2009). Vertically integrated, three-dimensional nanowire complementary metal-oxide-semiconductor circuits. *PNAS*, 106(50):21035–21038.

Newman, B., Sullivan, J., Winkler, M., Sher, M., Marcus, M., Fakra, S., Smith, M., Gradečak, S., Mazur, E., and Buonassisi, T. (2009). Illuminating the mechanism for sub-bandgap absorption in chalcogen doped silicon materials for PV applications. In *24th European Photovoltaic Solar Energy Conference*, pages 236–238.

Northrup, J. E. and Neugebauer, J. (1999). Indium-induced changes in GaN(0001) surface morphology. *Physical Review B*, 60(12):R8473–R8476.

Ohser, J. and Schladitz, K. (2009). *3D Images of Material Structures.* Wiley-VCH.

Otsu, N. (1979). A threshold selection method from gray-level histograms. *IEEE Transactions on Systems, Man and Cybernetics*, 9(1):62–66.

Owen, C. H. and Landis, W. J. (1996). Alignment of electron tomographic series by correlation without the use of gold particles. *Ultramicroscopy*, 63(1):27–38.

Palenstijn, W. J., Batenburg, K. J., and Sijbers, J. (2011). Performance improvements for iterative electron tomography reconstruction using graphics processing units (GPUs). *Journal of Structural Biology*, 176(2):250–253.

Pan, N., Xue, H., Yu, M., Cui, X., Wang, X., Hou, J. G., Huang, J., and Deng, S. Z. (2010). Tip-morphology-dependent field emission from ZnO nanorod arrays. *Nanotechnology*, 21(22):225707.

Penczek, P., Marko, M., Buttle, K., and Frank, J. (1995). Double-tilt electron tomography. *Ultramicroscopy*, 60(3):393–410.

Pennycook, S. J. and Nellist, P. D. (2011). *Scanning Transmission Electron Microscopy.* Springer New York.

Perassi, E. M., Hernandez-Garrido, J. C., Moreno, M. S., Encina, E. R., Coronado, E. A., and Midgley, P. A. (2010). Using highly accurate 3D nanometrology to model the optical properties of highly irregular nanoparticles: A powerful tool for rational design of plasmonic devices. *Nano Letters*, 10(6):2097–2104.

Perea, D. E., Allen, J. E., May, S. J., Wessels, B. W., Seidman, D. N., and Lauhon, L. J. (2005). Three-dimensional nanoscale composition mapping of semiconductor nanowires. *Nano Letters*, 6(2):181–185.

Perea, D. E., Wijaya, E., Lensch-Falk, J. L., Hemesath, E. R., and Lauhon, L. J. (2008). Tomographic analysis of dilute impurities in semiconductor nanostructures. *Journal of Solid State Chemistry*, 181(7):1642–1649.

Perona, P. and Malik, J. (1990). Scale-space and edge detection using anisotropic diffusion. *IEEE Transactions on Pattern Analysis and Machine Intelligence*, 12(7):629–639.

Persson, A. I., Larsson, M. W., Stenstrom, S., Ohlsson, B. J., Samuelson, L., and Wallenberg, L. R. (2004). Solid-phase diffusion mechanism for GaAs nanowire growth. *Nature Materials*, 3(10):677–681.

Pirovano, A., Lacaita, A. L., Zandler, G., and Oberhuber, R. (2000). Explaining the dependences of the hole and electron mobilities in Si inversion layers. *IEEE Transactions on Electron Devices*, 47(4):718–724.

Ponce, F. A. and Bour, D. P. (1997). Nitride-based semiconductors for blue and green light-emitting devices. *Nature*, 386(6623):351–359.

Porter, A. E., Gass, M., Muller, K., Skepper, J. N., Midgley, P. A., and Welland, M. (2007). Direct imaging of single-walled carbon nanotubes in cells. *Nature Nanotechnology*, 2(11):713–717.

Puurunen, R. L. (2005). Surface chemistry of atomic layer deposition: A case study for the trimethylaluminum/water process. *Journal of Applied Physics*, 97(12):121301.

Qian, F., Gradečak, S., Li, Y., Wen, C.-Y., and Lieber, C. M. (2005). Core/Multishell nanowire heterostructures as multicolor, high-efficiency light-emitting diodes. *Nano Letters*, 5(11):2287–2291.

Qian, F., Li, Y., Gradečak, S., Park, H.-G., Dong, Y., Ding, Y., Wang, Z. L., and Lieber, C. M. (2008). Multi-quantum-well nanowire heterostructures for wavelength-controlled lasers. *Nature Materials*, 7(9):701–706.

Radermacher, M. (1988). Three-dimensional reconstruction of single particles from random and nonrandom tilt series. *Journal of Electron Microscopy Technique*, 9:359–394.

Radjenović, B. and Radmilović-Radjenović, M. (2010). Top down nano technologies in surface modification of materials. *Central European Journal of Physics*, 9(2):265–275.

Radon, J. (1917). Über die Bestimmung von Funktionen durch ihre Integralwerte längs gewisser Mannigfaltigkeiten. *Berichte der Sächsischen Akadamie der Wissenschaft*, 69:262–277.

Radtke, G. and Botton, G. A. (2011). Energy loss near-edge structures. In Pennycook, S. J. and Nellist, P. D., editors, *Scanning Transmission Electron Microscopy*, pages 207–245. Springer New York.

Randolph, S. J., Fowlkes, J. D., and Rack, P. D. (2006). Focused, nanoscale electron-beam-induced deposition and etching. *Critical Reviews in Solid State and Materials Sciences*, 31(3):55–89.

Rawlinson, N., Pozgay, S., and Fishwick, S. (2010). Seismic tomography: A window into deep earth. *Physics of the Earth and Planetary Interiors*, 178(3-4):101–135.

Reimer, L. and Kohl, H. (2008). *Transmission Electron Microscopy: Physics of Image Formation*. Springer.

Renard, V. T., Jublot, M., Gergaud, P., Cherns, P., Rouchon, D., Chabli, A., and Jousseaume, V. (2009). Catalyst preparation for CMOS-compatible silicon nanowire synthesis. *Nature Nanotechnology*, 4(10):654–657.

Renk, K. F. (2012). *Basics of Laser Physics*. Springer.

Ress, D., Harlow, M. L., Schwarz, M., Marshall, R. M., and McMahan, U. J. (1999). Automatic acquisition of fiducial markers and alignment of images in tilt series for electron tomography. *Journal of Electron Microscopy*, 48(3):277–287.

Revol-Muller, C., Peyrin, F., Carrillon, Y., and Odet, C. (2002). Automated 3D region growing algorithm based on an assessment function. *Pattern Recognition Letters*, 23(1-3):137–150.

Ridler, T. W. and Calvard, S. (1978). Picture thresholding using an iterative selection method. *IEEE Transactions on Systems, Man and Cybernetics*, 8(8):630–632.

Rigutti, L., Tchernycheva, M., De Luna Bugallo, A., Jacopin, G., Julien, F. H., Zagonel, L. F., March, K., Stephan, O., Kociak, M., and Songmuang, R. (2010). Ultraviolet photodetector based on GaN/AlN quantum disks in a single nanowire. *Nano Letters*, 10(8):2939–2943.

Ronsheim, P. A., Hatzistergos, M., and Jin, S. (2010). Dopant measurements in semiconductors with atom probe tomography. *Journal of Vacuum Science and Technology B*, 28(1):C1E1–C1E4.

Roozeboom, F., Elfrink, R., Verhoeven, J., van den Meerakher, J., and Holthuysen, F. (2000). High-value MOS capacitor arrays in ultradeep trenches in silicon. *Microelectronic Engineering*, 53(1-4):581–584.

Ross, F. M., Tersoff, J., and Reuter, M. C. (2005). Sawtooth faceting in silicon nanowires. *Physical Review Letters*, 95(14):146104.

Saghi, Z., Holland, D. J., Leary, R., Falqui, A., Bertoni, G., Sederman, A. J., Gladden, L. F., and Midgley, P. A. (2011). Three-dimensional morphology of iron oxide nanoparticles with reactive concave surfaces. a compressed sensing-electron tomography (CS-ET) approach. *Nano Letters*, 11(11):4666–4673.

Saghi, Z., Xu, X., Peng, Y., Inkson, B., and Mobus, G. (2007). Three-dimensional chemical analysis of tungsten probes by energy dispersive x-ray nanotomography. *Applied Physics Letters*, 91(25):251906.

Saitoh, M., Nakabayashi, Y., Ota, K., Uchida, K., and Numata, T. (2010). Understanding of short-channel mobility in tri-gate nanowire MOSFETs and enhanced stress memorization technique for performance improvement. In *IEEE International Electron Devices Meeting (IEDM)*, pages 34.3.1–34.3.4.

Salvi, E., Cantele, F., Zampighi, L., Fain, N., Pigino, G., Zampighi, G., and Lanzavecchia, S. (2008). JUST (java user segmentation tool) for semi-automatic segmentation of tomographic maps. *Journal of Structural Biology*, 161(3):287–297.

Schierning, G., Theissmann, R., Stein, N., Petermann, N., Becker, A., Engenhorst, M., Kessler, V., Geller, M., Beckel, A., Wiggers, H., and Schmechel, R. (2011). Role of oxygen on microstructure and thermoelectric properties of silicon nanocomposites. *Journal of Applied Physics*, 110(11):113515.

Schift, H. (2008). Nanoimprint lithography: An old story in modern times? A review. *Journal of Vacuum Science and Technology B*, 26(2):458–480.

Schmidt, V., Riel, H., Senz, S., Karg, S., Riess, W., and Gösele, U. (2006). Realization of a silicon nanowire vertical surround-gate field-effect transistor. *Small*, 2(1):85–88.

Schmidt, V., Wittemann, J. V., Senz, S., and Gösele, U. (2009). Silicon nanowires: A review on aspects of their growth and their electrical properties. *Advanced Materials*, 21(25-26):2681–2702.

Scott, M. C., Chen, C.-C., Mecklenburg, M., Zhu, C., Xu, R., Ercius, P., Dahmen, U., Regan, B. C., and Miao, J. (2012). Electron tomography at 2.4-angstrom resolution. *Nature*, 483(7390):444–447.

Seisyan, R. P. (2011). Nanolithography in microelectronics: A review. *Technical Physics*, 56(8):1061–1073.

Sezgin, M. and Sankur, B. (2004). Survey over image thresholding techniques and quantitative performance evaluation. *Journal of Electronic Imaging*, 13(1):146–155.

Sheehy, M. A., Tull, B. R., Friend, C. M., and Mazur, E. (2007). Chalcogen doping of silicon via intense femtosecond-laser irradiation. *Materials Science and Engineering: B*, 137(1-3):289–294.

Shen, S., Gu, T., Mao, D., Xiao, X., Yuan, P., Yu, M., Xia, L., Ji, Q., Meng, L., Song, W., Yu, C., and Lu, G. (2012). Synthesis of nonspherical mesoporous silica ellipsoids with tunable aspect ratios for magnetic assisted assembly and gene delivery. *Chemistry of Materials*, 24(1):230–235.

Sher, M. J., Winkler, M. T., and Mazur, E. (2011). Pulsed-laser hyperdoping and surface texturing for photovoltaics. *MRS Bulletin*, 36(6):439–445.

Smith, J. R., Chen, A., Gostovic, D., Hickey, D., Kundinger, D., Duncan, K. L., DeHoff, R. T., Jones, K. S., and Wachsman, E. D. (2009). Evaluation of the relationship between cathode microstructure and electrochemical behavior for SOFCs. *Solid State Ionics*, 180(1):90–98.

Smith, M., Winkler, M., Sher, M.-J., Lin, Y.-T., Mazur, E., and Gradečak, S. (2011a). The effects of a thin film dopant precursor on the structure and properties of femtosecond-laser irradiated silicon. *Applied Physics A: Materials Science & Processing*, 105(4):795–800.

Smith, M. J., Lin, Y.-T., Sher, M.-J., Winkler, M. T., Mazur, E., and Gradečak, S. (2011b). Pressure-induced phase transformations during femtosecond-laser doping of silicon. *Journal of Applied Physics*, 110(5):053524.

Smith, M. J., Sher, M.-J., Franta, B., Lin, Y.-T., Mazur, E., and Gradečak, S. (2012). The origins of pressure-induced phase transformations during the surface texturing of silicon using femtosecond laser irradiation. *Journal of Applied Physics*, 112:083518.

Sousa, A. A., Azari, A. A., Zhang, G., and Leapman, R. D. (2011). Dual-axis electron tomography of biological specimens: Extending the limits of specimen thickness with bright-field STEM imaging. *Journal of Structural Biology*, 174(1):107–114.

Speck, J. S. and Chichibu, S. F. (2009). Nonpolar and semipolar group III nitride-based materials. *MRS Bulletin*, 34(05):304–312.

Stagg, S. M., Knappenberger, K. L., Dowgiallo, A.-M., and Chandra, M. (2011). Three-dimensional interfacial structure determination of hollow gold nanosphere aggregates. *The Journal of Physical Chemistry Letters*, 2(23):2946–2950.

Stark, H., Woods, J. W., Paul, I., and Hingorani, R. (1981). Direct Fourier reconstruction in computer tomography. *IEEE Transactions on Acoustics, Speech and Signal Processing*, 29(2):237–245.

Stöger-Pollach, M. (2008). Optical properties and bandgaps from low loss EELS: pitfalls and solutions. *Micron*, 39(8):1092–1110.

Sugimori, H., Nishi, T., and Jinnai, H. (2005). Dual-axis electron tomography for three-dimensional observations of polymeric nanostructures. *Macromolecules*, 38(24):10226–10233.

Sze, S. M. (1981). *Physics of Semiconductor Devices.* John Wiley & Sons.

Takagi, S., Iisawa, T., Tezuka, T., Numata, T., Nakaharai, S., Hirashita, N., Moriyama, Y., Usuda, K., Toyoda, E., Dissanayake, S., Shichijo, M., Nakane, R., Sugahara, S., Takenaka, M., and Sugiyama, N. (2008). Carrier-transport-enhanced channel CMOS for improved power consumption and performance. *IEEE Transactions on Electron Devices*, 55(1):21–39.

Teal, G. K. and Little, J. B. (1950). Growth of germanium single crystals. *Physical Review*, 78(5):647–647.

Thelander, C., Agarwal, P., Brongersma, S., Eymery, J., Feiner, L. F., Forchel, A., Scheffler, M., Riess, W., Ohlsson, B. J., Gösele, U., and Samuelson, L. (2006). Nanowire-based one-dimensional electronics. *Materials Today*, 9(10):28–35.

Thomas, P. J. and Midgley, P. A. (2001a). Image-spectroscopy - I. The advantages of increased spectral information for compositional EFTEM analysis. *Ultramicroscopy*, 88(3):179–186.

Thomas, P. J. and Midgley, P. A. (2001b). Image-spectroscopy - II. The removal of plural scattering from extended energy-filtered series by fourier deconvolution. *Ultramicroscopy*, 88(3):187–194.

Thompson, G. B., Miller, M. K., and Fraser, H. L. (2004). Some aspects of atom probe specimen preparation and analysis of thin film materials. *Ultramicroscopy*, 100(1-2):25–34.

Thompson, K., Booske, J. H., Larson, D. J., and Kelly, T. F. (2005). Three-dimensional atom mapping of dopants in Si nanostructures. *Applied Physics Letters*, 87(5):052108.

Thompson, K., Lawrence, D., Larson, D. J., Olson, J. D., Kelly, T. F., and Gorman, B. (2007). In situ site-specific specimen preparation for atom probe tomography. *Ultramicroscopy*, 107(2-3):131–139.

Tiemeijer, P. (2005). Titan condenser manual. *FEI Company.*

Tong, J., Arslan, I., and Midgley, P. (2006). A novel dual-axis iterative algorithm for electron tomography. *Journal of Structural Biology*, 153(1):55–63.

Tourbot, G., Bougerol, C., Grenier, A., Hertog, M. D., Sam-Giao, D., Cooper, D., Gilet, P., Gayral, B., and Daudin, B. (2011). Structural and optical properties of InGaN/GaN nanowire heterostructures grown by PA-MBE. *Nanotechnology*, 22(7):075601.

Trier, O. D. and Jain, A. K. (1995). Goal-directed evaluation of binarization methods. *IEEE Transactions on Pattern Analysis and Machine Intelligence*, 17(12):1191–1201.

Tull, B., Winkler, M., and Mazur, E. (2009). The role of diffusion in broadband infrared absorption in chalcogen-doped silicon. *Applied Physics A: Materials Science & Processing*, 96(2):327–334.

Tull, B. R., Carey, J. E., Mazur, E., McDonald, J. P., and Yalisove, S. M. (2006). Silicon surface morphologies after femtosecond laser irradiation. *MRS Bulletin*, 31(8):626–633.

Uchic, M. D., Holzer, L., Inkson, B. J., Principe, E. L., and Munroe, P. (2007). Three-dimensional microstructural characterization using focused ion beam tomography. *MRS Bulletin*, 32(5):408–416.

Van Aert, S., Batenburg, K. J., Rossell, M. D., Erni, R., and Van Tendeloo, G. (2011). Three-dimensional atomic imaging of crystalline nanoparticles. *Nature*, 470(7334):374–377.

Van Aert, S., Verbeeck, J., Erni, R., Bals, S., Luysberg, M., Dyck, D. V., and Tendeloo, G. V. (2009). Quantitative atomic resolution mapping using high-angle annular dark field scanning transmission electron microscopy. *Ultramicroscopy*, 109(10):1236–1244.

Van den Broek, W., Rosenauer, A., Goris, B., Martinez, G. T., Bals, S., Van Aert, S., and Van Dyck, D. (2012). Correction of non-linear thickness effects in HAADF STEM electron tomography. *Ultramicroscopy*, 116:8–12.

Van den Broek, W., Verbeeck, J., De Backer, S., Scheunders, P., and Schryvers, D. (2006). Acquisition of the EELS data cube by tomographic reconstruction. *Ultramicroscopy*, 106(4-5):269–276.

Verbeeck, J., Van Dyck, D., and Van Tendeloo, G. (2004). Energy-filtered transmission electron microscopy: an overview. *Spectrochimica Acta Part B: Atomic Spectroscopy*, 59(10-11):1529–1534.

Verheijen, M. A., Algra, R. E., Borgström, M. T., Immink, G., Sourty, E., van Enckevort, W. J. P., Vlieg, E., and Bakkers, E. P. A. M. (2007). Three-dimensional morphology of GaP-GaAs nanowires revealed by transmission electron microscopy tomography. *Nano Letters*, 7(10):3051–3055.

Vila-Comamala, J., Pan, Y., Lombardo, J. J., Harris, W. M., Chiu, W. K. S., David, C., and Wang, Y. (2012). Zone-doubled fresnel zone plates for high-resolution hard x-ray full-field transmission microscopy. *Journal of Synchrotron Radiation*, 19(5):705–709.

Vincent, L. and Soille, P. (1991). Watersheds in digital spaces: an efficient algorithm based on immersion simulations. *IEEE Transactions on Pattern Analysis and Machine Intelligence*, 13(6):583–598.

Volkmann, N. (2002). A novel three-dimensional variant of the watershed transform for segmentation of electron density maps. *Journal of Structural Biology*, 138(1-2):123–129.

Vydyanath, H. R., Lorenzo, J. S., and Kroger, F. A. (1978). Defect pairing diffusion, and solubility studies in selenium-doped silicon. *Journal of Applied Physics*, 49(12):5928–5937.

Wagner, R. S. and Ellis, W. C. (1964). Vapor-liquid-solid mechanism of single crystal growth. *Applied Physics Letters*, 4(5):89–90.

Waltereit, P., Brandt, O., Trampert, A., Grahn, H. T., Menniger, J., Ramsteiner, M., Reiche, M., and Ploog, K. H. (2000). Nitride semiconductors free of electrostatic fields for efficient white light-emitting diodes. *Nature*, 406(6798):865–868.

Wang, Y., Schmidt, V., Senz, S., and Gosele, U. (2006). Epitaxial growth of silicon nanowires using an aluminium catalyst. *Nature Nanotechnology*, 1(3):186–189.

Ward, E. P. W., Yates, T. J. V., Fernández, J.-J., Vaughan, D. E. W., and Midgley, P. A. (2007). Three-dimensional nanoparticle distribution and local curvature of heterogeneous catalysts revealed by electron tomography. *The Journal of Physical Chemistry C*, 111(31):11501–11505.

Weickert, J., Romeny, B. M. T. H., and Viergever, M. A. (1998). Efficient and reliable schemes for nonlinear diffusion filtering. *IEEE Transactions on Image Processing*, 7(3):398–410.

Weyland, M. and Midgley, P. A. (2003). Extending energy-filtered transmission electron microscopy (EFTEM) into three dimensions using electron tomography. *Microscopy and Microanalysis*, 9(6):542–555.

Wikipedia (2013). http://en.wikipedia.org/wiki/Moore%27s_law.

Wilk, G. D., Wallace, R. M., and Anthony, J. M. (2001). High-kappa gate dielectrics: Current status and materials properties considerations. *Journal of Applied Physics*, 89(10):5243–5275.

Williams, D. B. and Carter, C. B. (2009). *Transmission Electron Microscopy - A Textbook for Materials Science*. Springer.

Wilson, J. R., Gameiro, M., Mischaikow, K., Kalies, W., Voorhees, P. W., and Barnett, S. A. (2009). Three-dimensional analysis of solid oxide fuel cell Ni-YSZ anode interconnectivity. *Microscopy and Microanalysis*, 15(1):71–77.

Withers, P. J. (2007). X-ray nanotomography. *Materials Today*, 10(12):26–34.

Wong, H.-S. P., Frank, D. J., Solomon, P. M., Wann, C. H. J., and Welser, J. J. (1999). Nanoscale CMOS. *Proceedings of the IEEE*, 87(4):537–570.

Wu, C., Crouch, C. H., Zhao, L., Carey, J. E., Younkin, R., Levinson, J. A., Mazur, E., Farrell, R. M., Gothoskar, P., and Karger, A. (2001). Near-unity below-band-gap absorption by microstructured silicon. *Applied Physics Letters*, 78(13):1850–1852.

Wu, M., Alivov, Y. I., and Morkoç, H. (2008a). High-k dielectrics and advanced channel concepts for Si MOSFET. *Journal of Materials Science: Materials in Electronics*, 19(10):915–951.

Wu, Y. H., Chang, L., Chen, L. C., Chen, H. S., and Chen, F. R. (2008b). Geometrical correlations of quantum dots in InAs/GaAs superlattice structure from electron tomography. *Applied Physics Letters*, 93(15):153108.

Xiang, J., Lu, W., Hu, Y., Wu, Y., Yan, H., and Lieber, C. M. (2006). Ge/Si nanowire heterostructures as high-performance field-effect transistors. *Nature*, 441(7092):489–493.

Xin, H. L. and Muller, D. A. (2010). Three-dimensional imaging in aberration-corrected electron microscopes. *Microscopy and Microanalysis*, 16(04):445–455.

Xu, P., Donaldson, L., Gergely, Z., and Staehelin, L. (2007). Dual-axis electron tomography: a new approach for investigating the spatial organization of wood cellulose microfibrils. *Wood Science and Technology*, 41(2):101–116.

Yaguchi, T., Konno, M., Kamino, T., Hashimoto, T., Ohnishi, T., and Watanabe, M. (2004). 3D elemental mapping using a dedicated FIB/STEM system. *Microscopy and Microanalysis*, 10(SupplementS02):1030–1031.

Yaguchi, T., Konno, M., Kamino, T., and Watanabe, M. (2008). Observation of three-dimensional elemental distributions of a Si device using a 360°-tilt FIB and the cold field-emission STEM system. *Ultramicroscopy*, 108(12):1603–1615.

Yan, R., Gargas, D., and Yang, P. (2009). Nanowire photonics. *Nature Photonics*, 3(10):569–576.

Yedra, L., Eljarrat, A., Arenal, R., Pellicer, E., Cabo, M., López-Ortega, A., Estrader, M., Sort, J., Baróe, M. D., Estradé, S., and Peiró, F. (2012). EEL spectroscopic tomography: Towards a new dimension in nanomaterials analysis. *Ultramicroscopy*, 122:12–18.

Yi, Z., Takenaka, M., and Takagi, S. (2009). On surface roughness scattering-limited mobilities of electrons and holes in biaxially tensile-strained Si MOSFETs. *IEEE Electron Device Letters*, 30(9):987–989.

Younkin, R., Carey, J. E., Mazur, E., Levinson, J. A., and Friend, C. M. (2003). Infrared absorption by conical silicon microstructures made in a variety of background gases using femtosecond-laser pulses. *Journal of Applied Physics*, 93(5):2626–2629.

Yu, P. Y. and Cardona, M. (2004). *Fundamentals of Semiconductors : Physics and Materials Properties*. Springer.

Yurtsever, A., Weyland, M., and Muller, D. A. (2006). Three-dimensional imaging of nonspherical silicon nanoparticles embedded in silicon oxide by plasmon tomography. *Applied Physics Letters*, 89(15):151920.

Zaefferer, S., Wright, S. I., and Raabe, D. (2008). Three-dimensional orientation microscopy in a focused ion beam-scanning electron microscope: A new dimension of microstructure characterization. *Metallurgical and Materials Transactions A*, 39(2):374–389.

Zianni, X. (2010). Diameter-modulated nanowires as candidates for high thermoelectric energy conversion efficiency. *Applied Physics Letters*, 97(23):233106–3.

Ziegler, J. F., Ziegler, M. D., and Biersack, J. P. (2010). SRIM - the stopping and range of ions in matter (2010). *Nuclear Instruments and Methods in Physics Research Section B: Beam Interactions with Materials and Atoms*, 268(11-12):1818–1823.

Zschech, D., Kim, D. H., Milenin, A. P., Scholz, R., Hillebrand, R., Hawker, C. J., Russell, T. P., Steinhart, M., and Gösele, U. (2007). Ordered arrays of <100>-oriented silicon nanorods by CMOS-Compatible block copolymer lithography. *Nano Letters*, 7(6):1516–1520.

Communications during this thesis

Peer-reviewed journal articles

- Morel, P. H., Haberfehlner, G., Lafond, D., Audoit, G., Jousseaume, V., Leroux, C., Fayolle-Lecocq, M., Baron, T., and Ernst, T. (2012). Ultra high density three dimensional capacitors based on Si nanowires array grown on a metal layer. *Applied Physics Letters*, 101(8):083110
- Haberfehlner, G., Bayle-Guillemaud, P., Audoit, G., Lafond, D., Morel, P. H., Jousseaume, V., Ernst, T., and Bleuet, P. (2012). Four-dimensional spectral low-loss energy-filtered transmission electron tomography of silicon nanowire-based capacitors. *Applied Physics Letters*, 101(6):063108
- Lim, S. K., Crawford, S., Haberfehlner, G., and Gradečak, S. (2013). Controlled modulation of diameter and composition along individual III-V nitride nanowires. *Nano Letters*, 13(2):331–336
- Haberfehlner, G., Smith, M. J., Idrobo, J.-C., Auvert, G., Sher, M.-J., Winkler, M. T., Mazur, E., Gambacorti, N., Gradečak, S., and Bleuet, P. (2013b). Dopant segregation in femtosecond laser-doped silicon revealed by electron tomography. *Microscopy and Microanalysis*, 19(3):716–725
- Bleuet, P., Audoit, G., Barnes, J.-P., Bertheau, J., Dabin, Y., Dansas, H., Fabbri, J.-M., Florin, B., Gergaud, P., Grenier, A., Haberfehlner, G., Lay, E., Laurencin, J., Serra, R., and Villanova, J. (2013). Specifications for hard condensed matter specimens for three-dimensional high-resolution tomographies. *Microscopy and Microanalysis*, 19(3):726–739
- Haberfehlner, G., Serra, R., Cooper, D., Barraud, S., and Bleuet, P. (2013a). 3D spatial resolution improvement by dual-axis electron tomography: Application to tri-gate transistors. *Ultramicroscopy*, accepted
- Grenier, A., Duguay, S., Barnes, J.-P., Serra, R., Haberfehlner, G., Cooper, D., Bertin, F., Barraud, S., Audoit, G., Arnoldi, L., Cadel, E., Chabli, A., and

Vurpillot, F. (2013). 3D analysis of advanced devices using electron and atom probe tomography. *Ultramicroscopy*, accepted

Patents

- Haberfehlner, G., and Bleuet, P. (2013). Procédé d'imagerie en trois dimensions à resolution améliorée, French patent application no. 13 51442.

Conferences

- Haberfehlner, G., Grenier, A., Cooper, D. Auvert, G., Gambacorti, N., Smith, M., Gradečak, S., and Bleuet, P. (2011). Status And Trends In 3D Nanodevices: Inspection by Electron Tomography. In *Frontiers in Characterization and Metrology for Nanoelectronics (FCMN), Grenoble, France* (poster presentation).

- Haberfehlner, G., Smith, M.J., Cooper, D. Auvert, G., Sher, M.J., Winkler, M.T., Mazur, E., Gradečak, S., Gambacorti, N., and Bleuet, P (2011). 3D dopant concentration in femtosecond laser-doped silicon investigated by HAADF STEM nanotomography. In *Material Research Society (MRS) Fall Meeting, Boston, United States* (oral presentation).

- Haberfehlner, G., Bayle-Guillemaud, P., Audoit, G., Serra, R., Lafond, D., Morel, P.H., Ernst, T., and Bleuet, P. (2012). Four-dimensional spectral low-loss EFTEM tomography of core-shell nanowires. In *European Microscopy Congress (EMC), Manchester, Great Britain* (oral presentation).

- Haberfehlner, G., Serra, R., Cooper, D., Audoit, G., Barraud, S., and Bleuet, P. (2013). Optimizing Sampling Schemes for Electron Tomography: Dual- and Multiple-Axis Tomography. In *Microscopy and Microanalysis (M&M), Indianapolis, United States* (poster presentation).

- Haberfehlner, G., Bayle-Guillemaud, P., Audoit, G., Smith, M., Crawford, S., Gradečak, S., Morel, P.H., Ernst, T., Gambacorti, N., and Bleuet, P. (2013). Electron Tomography for 3D Nanoscale Characterization of Semiconductor Materials Devices. In *Microscopy and Microanalysis (M&M), Indianapolis, United States* (poster presentation).

Workshops and Summerschools

- Haberfehlner, G. (2011). Electron tomography for semiconductor materials. In *Réunion de Groupe des Utilisateurs en Microscopie électronique Philips-FEI (GUMP)* (oral presentation).
- Haberfehlner, G., and Bleuet, P (2012). Electron tomography: A technique for 3D nanoscale materials characterization. In *Microelectronics for Society - More than Moore expands More Moore, Bad Honnef, Germany* (poster presentation), best poster award.
- Haberfehlner, G., Bayle-Guillemaud, P., Audoit, G., Lafond, D., Morel, P.H., Jousseaume, V., Ernst, T., and Bleuet, P (2012). Four-dimensional spectral low-loss EFTEM tomography of nanowire-based capacitors. In *Journées EELS (JEELS), Aix les Bains, France* (poster presentation).

Abbreviations

0D zero-dimensional.

1D one-dimensional.

2D two-dimensional.

2DEG two-dimensional electron gas.

3D three-dimensional.

ADF annular dark field.

AFM atomic force microscope (microscopy).

ALD atomic layer deposition.

ART algebraic reconstruction technique.

BF bright-field.

BOX buried oxide.

CBED convergent beam electron diffraction.

CCD charge-coupled device.

CMOS complementary metal-oxide-semiconductor.

COD coefficient of determination.

CVD chemical vapor deposition.

DF dark-field.

DMOS double-diffused metal-oxide-semiconductor.

DOF depth of field.

DUV deep ultraviolet.

EBID electron-beam induced deposition.

EBSD electron backscatter diffraction.

EDS energy-dispersive x-ray spectroscopy.

EELS electron energy-loss spectroscopy.

EFTEM energy-filtered transmission electron microscopy.

ELNES energy-loss near-edge spectroscopy.

EUV extreme ultra-violet.

EXAFS extended x-ray absorptance fine structure.

FBP filtered backprojection.

FEG field-emission gun.

FET field-effect transistor.

FIB focused ion beam.

fs femtosecond.

GIF Gatan imaging filter.

GPU graphics processing unit.

HAADF high-angle annular dark field.

HEMT high-electron mobility transistor.

IBID ion-beam induced deposition.

IC integrated circuit.

IR infrared.

LED light-emitting diode.

MAADF medium-angle annular dark field.

MBE molecular beam epitaxy.

MEMS microelectromechanical systems.

MOCVD metal-organic chemical vapor deposition.

MOS metal-oxide-semiconductor.

MOSFET metal-oxide-semiconductor field-effect transistor.

NBED nanobeam electron diffraction.

NEMS nanoelectromechanical systems.

NMOS negative metal-oxide-semiconductor.

PECVD plasma-enhanced chemical vapor deposition.

PMOS positive metal-oxide-semiconductor.

PVD physical vapor deposition.

SAD selected area diffraction.

SART simultaneous algebraic reconstruction technique.

SEM scanning electron microscope (microscopy).

SIRT simultaneous iterative reconstruction technique.

SOI silicon on insulator.

STEM scanning transmission electron microscope (microscopy).

TEM transmission electron microscope (microscopy).

TGNW tri-gate nanowire.

TMG trimethylgallium.

TV total variation.

UHV ultra-high vacuum.

VLS vapor-liquid-solid.

WBP weighted backprojection.

List of Notations

Γ	Plasmon damping
α_c	Convergence semi-angle (mrad)
ε	Permittivity (F m^{-1})
λ	Mean free path (m)
λ_e	Electron wavelength (nm)
μ_c	Carrier mobility (cm^2 V^{-1} s^{-1})
μ_n	Mobility of electrons (cm^2 V^{-1} s^{-1})
μ_p	Mobility of holes (cm^2 V^{-1} s^{-1})
ω	angular frequency (s^{-1})
ρ	Density (kg m^{-3})
ρ	Resistivity (Ω cm)
σ_{atom}	Atomic scattering cross section (m^2)
σ_{total}	Total scattering cross section (m^{-1})
θ	Scattering angle (mrad)
A	Atomic weight (kg m^{-3})
$\mathbf{B}$	Magnetic field (T)
D_n	Electron diffusion coefficient (cm^2 s^{-1})
DOF	Depth of field (nm)
D_p	Hole diffusion coefficient (cm^2 s^{-1})
d_x	resolution in x-direction (nm)

d_y	resolution in y-direction (nm)
d_z	resolution in z-direction (nm)
$\mathbf{E}$	Electric field (V cm^{-1})
E	Energy (eV)
E_0	Electron beam energy (eV)
E_F	Fermi level (eV)
E_g	Bandgap energy (eV)
E_p	Plasmon energy (eV)
E_s	Surface plasmon energy (eV)
$\mathbf{F}$	Force (N)
f	frequency (Hz)
$F\left(u, v\right)$	2D Fourier transform
$f\left(x, y\right)$	2D object function
J	Current density (A cm^{-2})
J_n	Electron current density (A cm^{-2})
J_p	Hole current density (A cm^{-2})
k	Wave number (m^{-1})
m^*	Effective mass (kg)
n	Number of holes
$N(E)$	Density of states
n_{proj}	number of projections
p	Number of holes
$Q\left(\theta, t\right)$	filtered projection or sinogram
$R(\theta, t)$	projection, sinogram

$S(\theta, w)$	1D Fourier transform of projections
T	Temperature (K)
U_t	Thermal voltage (V)
v	Velocity (m s^{-1})
v_d	Drift velocity (cm s^{-1})
Z	Atomic number

Physical constants

Name	**Symbol**	**Value**	**Unit**
Unit charge	e	1.602177×10^{-19}	C
Vacuum permittivity	ε_0	8.854187×10^{-12}	$\mathrm{F\ m^{-1}}$
Planck constant	h	6.626070×10^{-34}	J s
		4.135668×10^{-15}	eV s
Reduced Planck constant	$\hbar = h/(2\pi)$	1.054572×10^{-34}	J s
		6.582119×10^{-16}	eV s
Avogadro number	N_A	6.022141×10^{23}	$\mathrm{mol^{-1}}$
Boltzmann constant	k	1.380649×10^{-23}	$\mathrm{J\ K^{-1}}$
Electron mass	m_e	9.109382×10^{-31}	kg

List of Figures

Abstract

In this thesis electron tomography is developed and applied as a tool for three-dimensional nanoscale characterization of semiconductor materials and devices. The major contributions of this thesis are the exploration and application of transmission electron microscopy (TEM) contrast techniques for specific semiconductor applications and the exploration of routes towards improving spatial resolution, in particular by adapting tomographic acquisition schemes. As contrast techniques we apply high-angle annular dark-field (HAADF) scanning TEM (STEM) for investigations of heavy dopants in a lighter environment and we combine spectral low-loss energy-filtered TEM (EFTEM) with tomography and explore the features of reconstructed low-loss spectra. For resolution improvement we experimentally apply dual-axis electron tomography and investigate the potential of multiple-axis tomography based on simulations. Furthermore reconstruction algorithms based on total-variation minimization are applied to electron tomography. Samples investigated in this work include tri-gate transistors, III-V nanowire heterostructures and silicon nanowire-based capacitors as well as selenium-hyperdoped silicon, a material for optoelectronic applications.

Keywords: electron tomography, semiconductor, HAADF STEM, EFTEM, nanowire, reconstruction

Résumé

Ces travaux de doctorat concernent le développement de la tomographie électronique appliquée à la nano-caractérisation tridimensionnelle de dispositifs à semi-conducteurs et de matériaux pour la micro et la nanoélectronique. Les contributions les plus significatives de ces travaux sont (i) l'exploration et l'application de différents modes de contraste en microscopie électronique à transmission (TEM) pour des applications spécifiques liées au semi-conducteurs et (ii) l'investigation de nouvelles pistes pour améliorer encore la résolution spatiale, en particulier en adaptant les schémas d'acquisition en tomographie. Le TEM en balayage (STEM), basé sur des mesures annulaires aux forts angles et en champ sombre (HAADF) a été mis en œuvre pour observer des dopants dont le numéro atomique est typiquement largement supérieur à celui de la matrice (en silicium), et nous avons combiné le TEM résolu en énergie (EFTEM) dans un régime de faible perte d'énergie des électrons avec les techniques de tomographie afin de reconstruire les spectres de perte d'énergie locaux, en chaque voxel. La tomographie double-axe a été expérimentalement mise en œuvre pour améliorer la résolution spatiale, et le potentiel de la tomographie à axe multiple a été démontré, grâce aux simulations. Enfin, des algorithmes de reconstruction basés sur la minimisation de la variation totale ont été appliqués à la tomographie électronique. Les analyses effectuées comprennent les transistors triple-grille, les nanofils III-V, les capacités à base de nanofils de silicium et le silicium sur-dopé au sélénium, un matériau utilisé pour des applications optoélectroniques.

Mots clefs : Tomographie électronique, semi-conducteurs, HAADF STEM, EFTEM, nanofil, reconstruction

3D nanoimaging of semiconductor devices and materials by electron tomography

In this thesis electron tomography is developed and applied as a tool for three-dimensional nanoscale characterization of semiconductor materials and devices. The major contributions of this thesis are the exploration and application of transmission electron microscopy (TEM) contrast techniques for specific semiconductor applications and the exploration of routes towards improving spatial resolution, in particular by adapting tomographic acquisition schemes. As contrast techniques we apply high-angle annular dark-field (HAADF) scanning TEM (STEM) for investigations of heavy dopants in a lighter environment and we combine spectral low-loss energy-filtered TEM (EFTEM) with tomography and explore the features of reconstructed low-loss spectra. For resolution improvement we experimentally apply dual-axis electron tomography and investigate the potential of multiple-axis tomography based on simulations. Furthermore reconstruction algorithms based on total-variation minimization are applied to electron tomography. Samples investigated in this work include tri-gate transistors, III-V nanowire heterostructures and silicon nanowire-based capacitors as well as selenium-hyperdoped silicon, a material for optoelectronic applications.

Keywords : electron tomography, semiconductor, HAADF STEM, EFTEM, nanowire, reconstruction

---

Imagerie tridimensionnelle nanométrique de matériaux et dispositifs à semi-conducteurs par tomographie électronique

Ces travaux de doctorat concernent le développement de la tomographie électronique appliquée à la nano-caractérisation tridimensionnelle de dispositifs à semi-conducteurs et de matériaux pour la micro et la nanoélectronique. Les contributions les plus significatives de ces travaux sont (i) l'exploration et l'application de différents modes de contraste en microscopie électronique à transmission (TEM) pour des applications spécifiques liées au semi-conducteurs et (ii) l'investigation de nouvelles pistes pour améliorer encore la résolution spatiale, en particulier en adaptant les schémas d'acquisition en tomographie. Le TEM en balayage (STEM), basé sur des mesures annulaires aux forts angles et en champ sombre (HAADF) a été mis en œuvre pour observer des dopants dont le numéro atomique est typiquement largement supérieur à celui de la matrice (en silicium), et nous avons combiné le TEM résolu en énergie (EFTEM) dans un régime de faible perte d'énergie des électrons avec les techniques de tomographie afin de reconstruire les spectres de perte d'énergie locaux, en chaque voxel. La tomographie double-axe a été expérimentalement mise en œuvre pour améliorer la résolution spatiale, et le potentiel de la tomographie à axe multiple a été démontré, grâce aux simulations. Enfin, des algorithmes de reconstruction basés sur la minimisation de la variation totale ont été appliqués à la tomographie électronique. Les analyses effectuées comprennent les transistors triple-grille, les nanofils III-V, les capacités à base de nanofils de silicium et le silicium sur-dopé au sélénium, un matériau utilisé pour des applications optoélectroniques.

Mots clefs : Tomographie électronique, semi-conducteurs, HAADF STEM, EFTEM, nanofil, reconstruction